SEARCHING FOR SLOW-DEVELOPING COSMIC-RAY SHOWERS:

LOOKING FOR EVIDENCE OF EXOTIC PRIMARIES AT THE

PIERRE AUGER OBSERVATORY

by

Eric William Mayotte

A thesis submitted to the Faculty and the Board of Trustees of the Colorado School of Mines in partial fulfillment of the requirements for the degree of Doctorate of Science (Applied Physics).

Golden, Colorado

Date _____

Signed: _____
Eric William Mayotte

Signed: _____
Dr. Frederic Sarazin
Thesis Advisor

Golden, Colorado

Date _____

Signed: _____
Dr. Jeff Squier
Professor and Head
Department of Physics

ABSTRACT

The central purpose of this research was to add the event propagation velocity to the list of shower parameters that the Florescence Detector of Pierre Auger Observatory is capable of measuring. This capability was then leveraged to differentiate exotic slow moving events from the rest of the cosmic ray flux. Clearly, by relativistic necessity, all known cosmic ray primaries can only cause a measurable extensive air shower at velocities indistinguishably close to the speed of light. Therefore any accurate observation of an event propagating slower than the speed of light would provide an unmistakable indicator of new physics.

A particle must possess very specific characteristics in order to be capable of producing a slow shower. High mass Strangelets, macroscopic dark matter, and super-symmetric Q-Balls were identified as strong candidates. Theory supporting high mass Strangelets and macroscopic dark matter appeared too late for full inclusion in this work, however super-symmetric Q-Balls were thoroughly examined. CORSIKA simulations were used to show that the fluorescence detector of the Pierre Auger Observatory has sensitivity to Q-Balls with a mass $M_Q > 3.25 \times 10^{27} GeV\ c^{-2}$ while the surface detector is sensitive at a mass $M_Q > 1.15 \times 10^{27} GeV\ c^{-2}$.

The Pierre Auger Observatory was shown to be capable of accurately measuring a wide range of velocities with two independent methods. These methods were applied to 7 years of data and one candidate slow event was identified. This candidate measurement proved to be due to a rare and interesting, but ultimately, non-exotic effect, which when accounted for resulted in the event being measured normally. As a result of this, no exotic candidate events were found in the search. Recommendations are made for improving the result and promising alternative search methods are presented.

TABLE OF CONTENTS

v

LIST OF FIGURES

LIST OF TABLES

LIST OF SYMBOLS

Cosmic Microwave Background.. CMB

The Δ baryon resonance .... Δ^+

A Pi Meson with Positive, Negative or No Charge .... π^+, π^- and π^0

Cosmic ray deflection from source .... $\theta_{scatter}$

Net Charge .... Q

Atomic Number .... Z

Particle Mass... M

Neutron Number .... N

A Muon.. μ

Longitudinal particle density profile.. $N(X)$

The atmospheric slant depth... X

Particle count at shower maximum... N_{max}

The Depth of Shower Maximum .... X_{max}

The RMS for X_{max} Values Within an Energy Bin...................................... X_{max} RMS

Gaisser-Hillas composition fit parameter.. λ

Gaisser-Hillas energy fit parameter.. X_0

The SD's five trigger levels T1-T5

TLT multiplicity zero value counter... n_{gap}

TLT multiplicity step counter .... n_{step}

The integrated TLT multiplicity signal... int_{all}

LIST OF ABBREVIATIONS

Active Galactic Nuclei .... AGN

Greisen-Zatsepin-Kuzmin ....GZK

Ultra-High Energy Cosmic Ray .... UHECR

Lateral Distribution Function..LDF

PhotoMultiplier Tube .... PMT

Los Leones LL

Los Morados... LM

Coihueco...CO

Loma Amarrilla...LA

High Elevation Auger Telescopes ....HEAT

First Level Trigger .... FLT

Second Level Trigger ....SLT

Balloon Launch Station .... BLS

Global Data Assimilation System..GDAS

Geostationary Operational Environmental Satellite..GOES

Central Laser Facility .... CLF

eXtreme Laser Facility..XLF

Real-time Environmental Applications and Display sYstem .... READY

Aerosol Phase Function...APF

Vertical Aerosol Optical Depth .... VAOD

ACKNOWLEDGMENTS

To my advisor and friend Frederic Sarazin, without your enthusiastic support, unfailing accessibility and sagacious advice the task of this thesis would have been insurmountable. Somehow you've managed to take the confused, willful and procrastinating student I used to be and painstakingly mold me into the confused, willful and procrastinating scientist I am today. I've enjoyed every one of my numerous years under your guidance.

To Lawrence Wiencke, David Schuster, Kathleen Gesterling, Martin Will, Keri Kuhn, Carlos Medina, Johannes Esser, each of my lab mates, the Mines Physics Faculty and Staff and the Pierre Auger Collaboration, without you I would certainly have been unable to do what I have done. Working with you has been an absolute pleasure. Everyone should be so lucky as to work with people of your quality.

To my family- my mother, my father, my brother, my sister, my son and his mother, Mémère, Pépère, Nanny, Papa, the Byrds, the Falloons, the Lathams, the Rachwitzs and the Ruizs- without you I would simply not be here. You are the solidity of the earth and the rope that catches the fall. Without your support I could never have left the ground.

To those who have inspired me to try to be greater than I alone would have aimed to be-Jean-Marc, Leah, Rick Fetters, John Latham, Warren Pettine, Ryan Dunn, Sean Sargent, Christopher Kelso, Jeff Goldanloo, Kate Charlton, Ben Jackson, John Spear, Jay Straker, Ed Cecil, Alex Flournoy, Brennan Sprinkle, Sam Gangess, Rachel Ryan, Cat Green, Jim Bernard, Lauren Zemp, Dane Linblad, Chris Runyan, Audrey May Briel, Jamie Korte, the Undisputed King Of Cribbage, Lauren Parker and Gene Tafoya- I would be far from who I am and farther still from who I want to be if you each hadn't shared your time with me.

And finally, to the reader, for showing me the meaning of patience and understanding.

Thank You

For Caleb,

the most delightful human I've ever had the pleasure of knowing.

CHAPTER 1

INTRODUCTION: EXOTIC ASTROPARTICLE PHYSICS

Particle Astrophysics, or rather, Astroparticle Physics, is the study of any particle phenomena of extraterrestrial origin and has been an active field of research for over 100 years. Currently, astroparticle physics focuses on a wide range of fundamental physics topics. The following are generally seen as the most urgent topics of the field today [1].

- Dark Matter

- Charged Cosmic Radiation (Cosmic Rays)

- Gamma-Ray Astronomy

- Neutrino Astrophysics

- Neutrino Oscillation and Properties

- Gravitational Waves

- Theoretical Astroparticle Physics

- Nuclear Astrophysics

Within these subjects stand some of the most pressing and important unanswered questions in modern physics.

- Why is there a surplus of observed gravity as compared to visible matter?

- Why and how does the Neutrino change its flavor and mass, seemingly in isolation?

- Can gravitational systems radiate their energy?

- Why is there surplus of matter as compared to antimatter?

- How do quantum field theories behave at the extreme energy limit?

Answering these questions will take a focused effort from all aspects of high energy physics, and astroparticle physics is well positioned to provide insights as it leverages the entire universe and its history as a source of phenomena to study. To be sure, many of these questions may find their answers safely within the confines of established physical theories, however there is mounting evidence that much of this phenomena is beyond what current theories are capable of describing. This necessitates a willingness to play with new theories, examine established assumptions and look for the unexpected.

Working in this field of study, often called exotic physics, requires special care be lent to objectivity and skepticism. It is attractive to focus on the aspects of an observation that point to exciting and new results while ignoring the more practical and logical explanations. Furthermore, the supremely well tested and supported theories of physics, mainly the Standard Model and General Relativity should not and indeed can not be ignored. Balancing the need to search in unique and new directions with the absolute necessity of maintaining a solid ground in objectivity and accepted physics is a difficult task. Undertaking a study in exotic physics requires a clear statement of assumptions, goals and planned methods.

This thesis explores new possibilities in physics by looking for evidence of exotic particles and interactions within the flux of Ultra-High Energy Cosmic Rays using the Pierre Auger Observatory. This goal is approached by developing and implementing a method of isolating exotic events from traditional cosmic ray events by measuring the velocity at which each event moves through the atmosphere. This event velocity serves as a simple and robust segregation criteria as any particle capable of producing a bright, coherent and measurable event without relying on ultra relativistic speeds and kinetic energies, necessitates interaction mechanisms beyond those available to traditional cosmic ray primaries. More simply put, if any event is seen to evolve slowly and energetically, then it is potentially exotic and merits significant further study.

In order to pursue this research, the following assumptions are being worked under:

1. Within the universe there exist stable particles that will interact energetically with the atmosphere at velocities significantly below the speed of light in a way that allows for the creation of events bright enough to meet the observation criteria of the Pierre Auger Observatory.

2. That it is possible to reconstruct the speed at which cosmic ray events evolve in the atmosphere using the data already collected by the Pierre Auger Observatory.

3. That these exotic particles have already been measured by the Pierre Auger Observatory and can be differentiated from the rest of the cosmic ray flux by their velocity.

Through the course of this thesis, the validity of these assumptions will be tested and evaluated with as much certainty as this line of inquiry and the experimental techniques available to it are capable of.

In Chapter 2, Ultra-High Energy Cosmic Rays, the history, phenomena, processes and characteristics of charged cosmic radiation at extremely high energies will be covered. This is to provide a firm base to understand the field, as well as, the instrumentation and search techniques explained and used in later chapters.

In Chapter 3, the Pierre Auger Observatory, the instrumentation and general detection methods to be used in this search are covered in depth. A firm grasp of the instrumentation is critical to understand the research, however this section is not an exhaustive description of the Observatory, but rather focuses solely on the components used in the study. This research relies most heavily on the Observatory's Fluorescence Detector so it is given considerable space in this section. However, because of the wide range of factors that must be considered later in this work, nearly all the major components of the array are covered.

In Chapter 4, Exotic Slow Events and Candidate Phenomena, the intricacies of slow events will be presented. The beginning of this chapter outlines why these events are of interest. It then moves to the requirements any phenomena would have to meet to be considered as a candidate for a search at the Pierre Auger Observatory. The super Symmetric

Q-Ball is highlighted as a strong candidate and given a theoretical overview. The viability of detecting Q-Ball induced showers is then tested through CORSIKA shower and $\overline{\text{Off}}$ $\underline{\text{line}}$ detector simulations.

In Chapter 5, the Velocity Sensitivity of the Pierre Auger Observatory, the capability of making a measurement of shower velocity with the Observatory's Fluorescence Detector is evaluated. First, the simple core model of the method is developed. This model is then used to understand how the ability of the Fluorescence Detector to record events changes with velocity and event geometry. These predictions are then tested with toy slow events thrown into the full Observatory detector simulations. From here a more accurate velocity dependent model, accounting for most atmospheric effects, is developed and real world laser events are analyzed to set expectations on the velocity resolution of the real observatory. The results of this sub-study are interesting on their own as the reconstructed velocities of the laser events systematically deviate from the expected result of the speed of light in air and change based on which telescope is observing the event. To ascertain the cause of these differences the results of the study are thoroughly explored and compared to simulations. The core method of the work is shown not to be responsible for the offsets, suggesting possible problems in the instrumentation, standard analysis software or both. Due to the scale of the instrumentation, specific causes of the offsets could not be conclusively identified. Regardless, the Fluorescence Detector is shown to be accurate to $\sim 1.5\%$ of c, which is more than sufficient for the study at hand.

In Chapter 6, Stereo Velocity Reconstruction, a method using simultaneous observations from multiple fluorescence telescopes to reconstruct the geometry and velocity of cosmic ray events is developed by interlacing the signals from each telescope. This stereo reconstruction technique is applied to vertical and inclined laser events showing that the effects observed in the previous laser studies are confined only to vertical events. The stereo reconstruction method is then altered to include the absorption and reemission effects and directly applied to cosmic ray events measured at the Observatory. Because the reconstruction of velocity

demands a high quality signal, quality cuts are applied and a final stereo velocity distribution is produced for analysis in Chapter 8.

In Chapter 7, Hybrid Velocity Reconstruction, the method is altered to incorporate the signals from both the Fluorescence Detector and the signals from the array of particle detectors on the ground. This hybrid reconstruction is then applied to lasers showing that the offsets seen in the laser studies are again confined only to vertical events. The absorption and emission corrections are then added and the hybrid reconstruction is applied to the shower event dataset. Quality cuts are again applied and final distributions are produced for analysis in Chapter 8.

In Chapter 8, Candidate Selection, the final distributions in Chapters 5 and 6 are parsed for candidate slow events. Because each method's velocity reconstruction has an inherent error rate, a second selection criteria is introduced. This quantity, called the χ^2 improvement factor, compares quality of fit with the measured velocity as compared to a fit at the expected cosmic ray velocity of the speed of light. Both of these criteria are considered simultaneously and a probability distribution is formed for each method and observing telescope. Events that are found to have a probability of less than 3×10^{-7} of being a statistical fluctuation are selected as candidates and given individual attention. Each selected candidate, while interesting can be traced back to rare special cases that were unforeseen during the development of the reconstruction algorithms and quality cuts.

In Chapter 9, Conclusions and Perspectives, the full work and its results are summarized. Then, the assumptions made above are examined in the context of the findings of the research. Finally, future work, suggested improvements to the method, as well as promising leads and alternative search techniques are then presented.

CHAPTER 2

ULTRA-HIGH ENERGY COSMIC RAYS

The first concrete evidence pointing to the existence of cosmic rays came in the form of Theodor Wulf's 1909 air ionization measurements at the Eiffel tower. He showed, contrary to expectations, that the ionization of the air at the top of the tower was greater than half of that at the bottom. If terrestrial radiation sources were solely responsible for the ionization, the decrease should have been much more severe pointing to a secondary radiation source [2]. However, Victor Hess' high altitude balloon flights between 1911 and 1913 are widely regarded as the true starting point of the field.

Hess thought that it was likely that a radiation source in the sky was the cause for Wulf's odd ionization profile. To investigate this idea, he first greatly improved the accuracy of the electroscopes used at the time to measure the air's ionization. He then, at great personal risk, flew the instruments to various altitudes up to 5.3 km and very carefully recorded the atmosphere's radiation profile. Over the course of the following few years he flew at both day and night, and during a near total solar eclipse. From these measurements he noticed that there was a sharp increase in radiation at high altitudes and that there was no significant difference in the radiation levels during the solar eclipse. From this information he correctly reasoned that there must be a very strong extraterrestrial radiation source and that it likely originated from a region of space more distant than the Sun[3]. For this discovery Victor Hess was awarded the 1936 Nobel Prize in physics.

For the first few years, scientist generally believed the phenomena to be a form of electromagnetic radiation (likely gamma rays) and therefore named them cosmic rays. However, in 1927 Jacob Clay was able to show that small variations in measured fluxes and intensities correlate with the latitudes of the measurement locations. He noticed that the variation mirrored the strength of the earth's magnetic field and correctly postulated that this effect

was indicative of cosmic rays being mainly composed of charged particles [4]. In 1930, Bruno Rossi predicted that, given that cosmic rays are generally of the same charge, there should be a measurable difference in the flux of particles coming from the east as compared to the west due to the orientation of the earths magnetic field, the so called East-West effect [5]. Immediately following this prediction, studies [6], [7], and [8] found the number of events incident from the west to be greater than the count from the east. This excess effectively showed cosmic rays to be mainly positively charged. After this, between 1930 and 1945 in many independent studies, cosmic rays were identified as being mainly composed of protons with 10% being ionized Helium, 1% being mixed heavy nuclei and a small portion being gamma rays and other particles.

During his work on the East-West effect, Rossi noticed that two distantly separated Geiger counters trigger in coincidence far above the rate expected due to random noise. In an aside, in his field report he postulated that this could be due to very extensive particle showers, but did not pursue the matter further [9]. The subject was neglected until 1937 when Pierre Auger, unaware of Rossi's report, noticed the same effect in his instrumentation. Auger, then proceeded to investigate the phenomena in detail and concluded that the effect was in fact due to extensive particle showers precipitated by very energetic cosmic ray primaries. He concluded that upon entering the earth's atmosphere, very high energy cosmic rays interact with nuclei in the air and spawn a large number of secondary particles. He also proposed that the signals that are being measured at all but the highest altitudes and lowest energies were in fact due to these secondary particles [10]. These hypothesis proved correct and thus the field of high energy astroparticle physics was born.

2.1 Cosmic Ray Spectrum

Cosmic Rays have been detected with energies ranging from a few hundred MeV ($10^8 eV$) to more than $10^{20} eV$. The high energy end of this range, the so called Ultra High Energy Cosmic Rays (UHECRs), far surpass the maximum energies of any man-made accelerator. UHECR particle energies are at least 40 million times higher than what the current genera-

tion of particle accelerators can produce. However, because they interact with nuclei in the air which are at rest when compared to the cosmic rays, their center of mass collision energy only exceeds the LHC collision's by a factor of 40 [11].

As the energy increases to these extreme levels, the number of particles incident on the earth falls dramatically from $\sim 10^3 m^{-2} s^{-1}$ to less than $\sim 0.01 km^{-2} yr^{-1}$ per century. The energy spectrum of cosmic rays (energy vs flux) roughly follows an inverse power law with a differential flux well described by

$$\frac{dN}{dE} \propto E^{-\alpha}, \tag{2.1}$$

but with a few regions, as seen in Figure 2.1. Up to $\sim 3 \times 10^{15} eV$, the spectrum is well described with $\alpha \approx 2.7$. At this point, called the "Knee", the spectrum steepens to $\alpha \approx 3$. At $\sim 3 \times 10^{18} eV$ there is a very slight flattening called the "Ankle". As the energy reaches extreme levels the signal drops and agreement between experiments becomes much less certain. There does seem to be significant drop in flux around $\sim 5 \times 10^{19} eV$ as statistics start to thin. The origins of this drop-off is currently a matter of debate and is an active subject in UHECR physics [12].

2.2 Cosmic Ray Sources, Composition and Acceleration

The composition and source of cosmic rays is of fundamental interest to astroparticle physics. By correctly identifying sources and composition many of the uncertainties about how cosmic rays are accelerated would be cleared up. With all of this information in hand, much more would be known about the nature of the high energy universe. Unfortunately, at all but the highest energies, the trajectories of cosmic rays are completely scrambled by the omnipresent magnetic fields of our galaxy and more generally our universe. This in turn makes the influx cosmic rays look isotropic erasing any correlation with sources. Also, because cosmic rays interact and break up in the upper atmosphere, their composition is very difficult to determine. We do know that cosmic rays are mainly ionized atomic nuclei, but the exact composition and sources for much of the spectrum remains largely unknown.
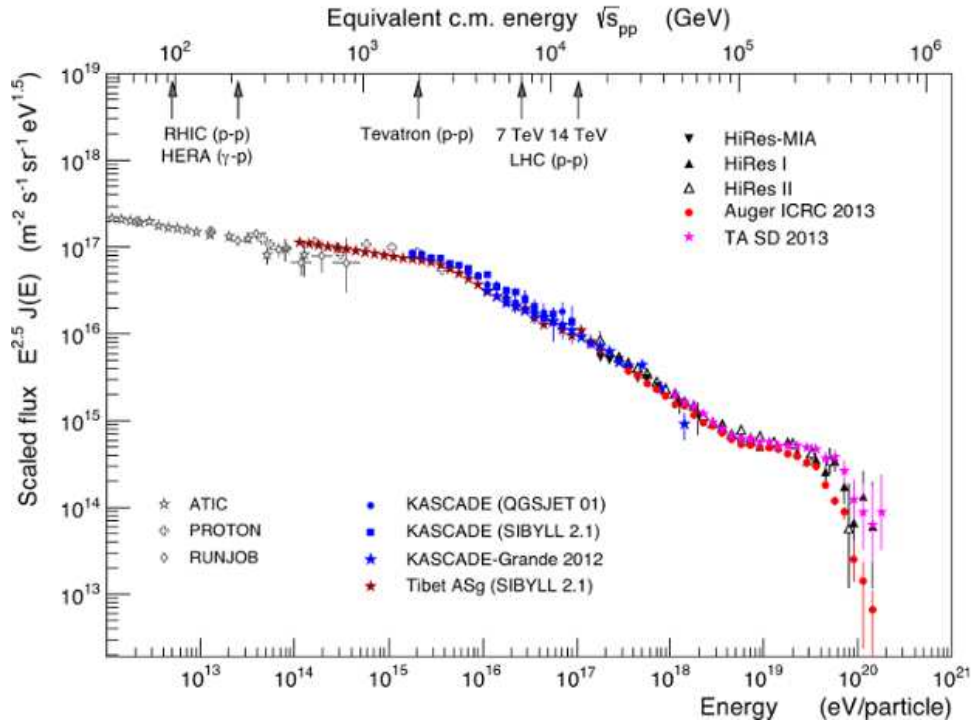
Figure 2.1: The Latest Energy Spectrum of Cosmic Rays [13].

At energies below the Knee the flux of particles is high enough, and their energy is low enough for their exact composition to be directly observed by detectors on high altitude balloons or based in space. From these measurements the composition of low energy cosmic rays is known to closely resemble the atomic abundances seen in stars, but with a slight over abundance of lighter elements. This slightly lighter composition can be understood as the heavier elements should fracture into lighter ones through nuclear decay processes or interactions with dust particles on their long meandering journeys through space [14].

At the lowest energies cosmic rays would have difficulty escaping local magnetic fields and are mostly free protons or ionized helium. From this information it is known that these low energy cosmic rays are likely ejected locally either from our sun or other similar stars, though some may be the leftover products of higher energy cosmic rays interacting with dust. As the observed energy increases, the probable origin transitions from local sources to more distant galactic sources and the particle type shifts to heavier mixed nuclei [15]. Due

9

to this heavier composition, local supernova are singled out as a likely source of the original cosmic ray particles up to $10^{15}eV$. As energy increases past this point, local galactic sources gradually drop off as higher energy extra-galactic sources take over. At these energies the question of where these particle are created becomes less interesting than identifying the astrophysical accelerators that produced these extreme energies.

There are many possible acceleration mechanisms for cosmic rays with energies up to the Knee. The two types of *bottom-up*[1] models for cosmic ray production are direct acceleration and stochastic acceleration. Basically, direct acceleration is the acceleration of charged particles in very strong electric fields in one shot. This E-field could be sourced from sunspots on stars at the lowest level to pulsars and Active Galactic Nuclei (AGN) at the highest energies. Unfortunately, this type of acceleration would not create the power law we see in the spectrum and generally can only take place where the cross section for deceleration mechanisms would also be high. Stochastic models rely on cosmic rays repeatedly encountering slow accelerators. These acceleration processes, called Fermi mechanisms, usually take the form of moving magnetized plasmas that would cause an acceleration when met head on. These are very slow to accelerate, but would naturally produce a power law spectrum. The most powerful stochastic mechanism is a process within supernova remnants called shock acceleration. Shock acceleration, or second order Fermi acceleration, relies on moving magnetized plasmas as well, but in this case the plasma takes the form of the rapidly expanding shock front of a supernova explosion. This plasma structure has the added benefit of strongly confining the cosmic ray to a region of high acceleration [16].

At the end of the Knee, exact composition, source and acceleration mechanisms become very foggy. This is both because direct observation of primary composition is no longer possible and the maximum possible energies producible via shock acceleration are thought to be reached. Somewhere between the Knee and the Ankle the galactic component of the cosmic ray spectrum falls off in favor of the rarer extragalactic component, though whether

---

[1]A bottom-up model refers to an acceleration mechanism where the cosmic ray starts with a low energy and is accelerated. The alternative is for cosmic rays to be the result of high energy decays (top-down).

this transition takes place at the Knee or at still higher energies is another matter of open research. It is known that galactic magnetic fields are too weak to confine cosmic rays in this energy range leading to the loss of locally accelerated particles and expectations of a flux of externally produced cosmic rays. Further on, the Ankle is even less well understood. Currently it is described as either another source transition, or possibly a pile up of formally higher energy cosmic rays decelerated by either the GZK interaction, pair production processes or both as outlined in Section 2.3.

Much of the nature of cosmic rays beyond the Ankle is unknown. This is because direct observation is all but impossible and indirect observation becomes extremely difficult for two reasons: First, the extreme scarcity of events with this energy $< 1 km^{-2} yr^{-1}$ makes opportunities for their observation rare; Second, the energies are so high that the particle interaction models needed to describe processes at this point are highly extrapolated from the regions where particle accelerator data does exist, giving these models huge uncertainties. This in turn means that the indirect observations that can be made are very difficult to interpret.

In Pierre Auger Observatory data there are hints of a composition starting light and moving to heavy with increasing energy [17]. However, the Telescope Array (TA), a competing cosmic ray observatory in the northern hemisphere with sensitivity to this energy range, sees a constantly light composition at these energies [18]. The discrepancy is a matter of hot debate will not be touched on here, except to say that the difference may be due to detector calibration, differences in statistics or data analysis, or simply a different spectrum of sources. In any case it is far too early to speak with certainty as much more work needs to be done on the subject. Hopefully planned upgrades for both observatories meant to increase the statistics and quality of composition measurements will be funded, allowing the composition and source question to be answered.

2.3 The GZK and Ultra-High Energy Cosmic Rays

In 1966, shortly after the discovery of the cosmic microwave background (CMB), Greisen [19], and Zatsepin and Kuzmin [20] independently predicted that due to interactions with the CMB there would be a cutoff in the cosmic ray spectrum at $5 \times 10^{19} eV$, now called the Greisen-Zatsepin-Kuzmin limit, or GZK cutoff. This is because above this energy blue-shifted CMB photons are energetic enough to create the Δ^+ baryon resonance[2]. The Δ quickly decays thereby producing pions (π^0 or π^+) and either a neutron or proton. As seen in Figure 2.2, the π^+ arm of the Δ^+ particle cascade, this process creates a large number of secondary particles. These particles derive their momenta and rest mass energy from the kinetic energy of the cosmic ray proton, slowing the proton down. Given enough time/distance, this process of energy loss would continue until the proton's energy falls below $5 \times 10^{19} eV$, the minimum threshold necessary for photo-pion production [21].
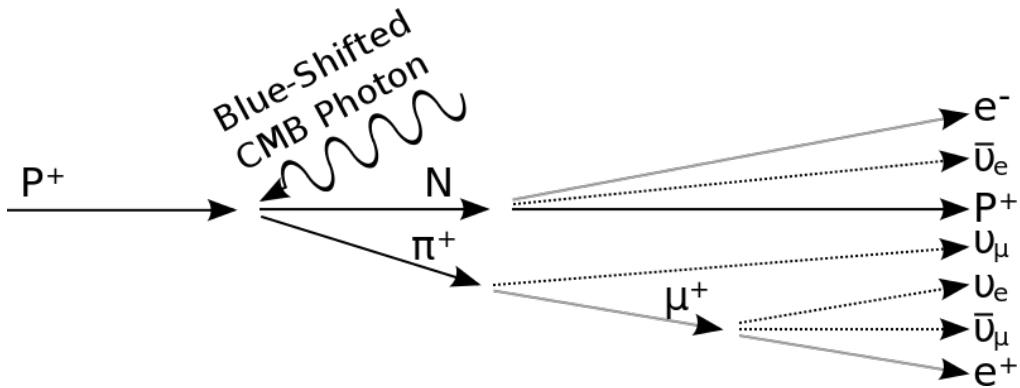
Figure 2.2: The GZK Interaction: A diagram of the π^+ path of the GZK particle interaction.

As shown in Figure 2.3, because the CMB is relatively sparse and multiple interactions are required to fully reduce a super GZK proton's energy below the threshold, a proton needs to traverse extremely large distances for the effect to be fully felt. This means that the GZK cutoff does not outlaw the observation of protons above $5 \times 10^{19} eV$, but instead states that

---

[2]The Δ^+ is (uud) and decays as $\Delta^+ \rightarrow n + \pi^+$ or $p + \pi^0$.

it is statistically unlikely that any super GZK proton was initially accelerated more than about 100 Mpc away.
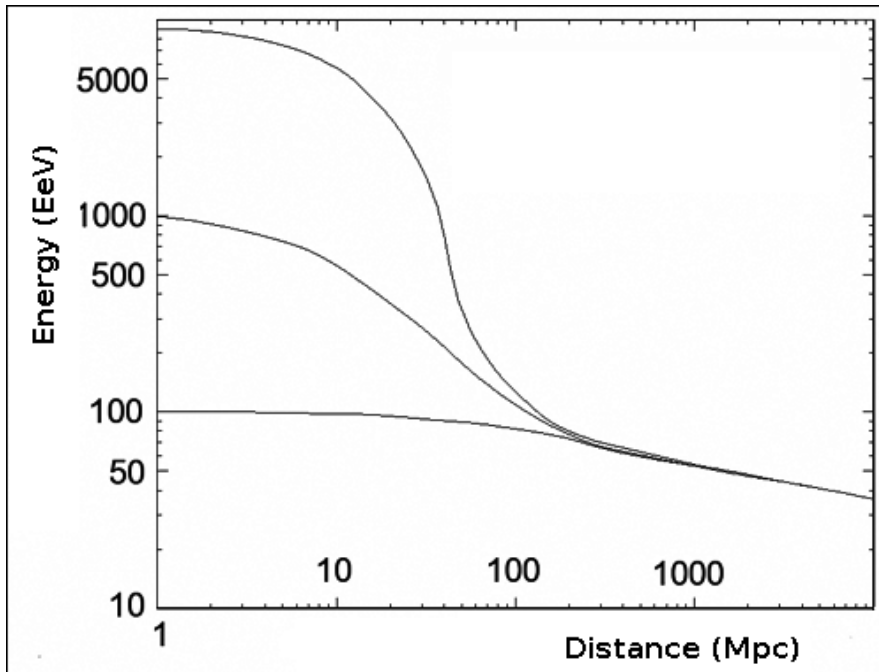
Figure 2.3: The GZK Suppression: the lines indicate the energy evolution of a proton starting with $10^{20}eV$, $10^{21}eV$ and $10^{22}eV$ as it propagates through space and is attenuated by the GZK process. Note that after enough time, each particle reaches an identical energy [21].

For heavier primaries, due to their higher mass, their energy per nucleon is lower and therefore so is their γ factor and the energies of the blue shifted CMB photons. This in turn means, that the GZK does not effect high mass particles at anywhere near the same energy range as it does for protons. However, a very similar process, called photo-dissociation does provide a similar limit. In photo-dissociation blue shifted CMB photons are able to exceed the nucleon binding energy of a high mass primary ($\sim 8.8MeV$ for Fe). Therefore, when one of these blue shifted photons strike a high mass primary, they are capable of removing a nucleon thus lowering its mass and removing some of the primaries original kinetic energy. Photo-dissociation provides a less hard limit as binding energies and cross-sections vary with nucleon count, but is expected to apply at a similar energy range.

On the 22nd of February, 1962, the Volcano Ranch experiment in New Mexico recorded the cosmic ray event shown in Figure 2.6(b). This observation corresponds to an air shower caused by a parent particle with an energy of $E_{total} \simeq 1 \times 10^{20} eV$. At the time this observation constituted the highest single particle energy ever observed, and was the first energy measurement to exceed the theoretical GZK Limit of $5 \times 10^{19} eV$. Though single particle energies of up to $3 \times 10^{20} eV$ have been measured [22], the Volcano Ranch measurement stands out as it spawned the field of Ultra-High Energy Cosmic Ray (UHECR) physics [23]. Since this initial observation, due to a rapid investment in instrumentation, there have been many more detections of particle energies above $1 EeV$ ($1 \times 10^{18} eV$), the limit that generally defines a UHECR.

As shown in Figure 2.1, a GZK-like drop in flux has been independently observed by HiRes [24], TA [25] and the Pierre Auger Observatory [26]. However, each experiment reports the cutoff to have different magnitudes and to take effect at different energies, although they are consistent within measurement uncertainty. Furthermore, because of the hint in the Pierre Auger Observatory's data that the primaries at the highest energies may be at least partially composed of heavy ions, the impact of the GZK could be somewhat dulled. This means that the observed drop-off could be the GZK for protons supplemented by the onset of photo disintegration of the heavy ions at these energies. Again, this is a region of debate and high uncertainty in the field that may be answered by upgrades to Auger and TA or a proposed ISS based observatory with a massive aperture called the Extreme Universe Space Observatory to be hosted on the Japanese owned JEM module (JEM-EUSO) [27].

Backtracking cosmic rays to their source is difficult since the degree to which galactic magnetic fields scatter cosmic rays depends on the cosmic ray primary's charge to kinetic energy ratio. Because of this, the paths of all low energy cosmic rays are heavily scrambled and therefore appear to arrive isotropically. In UHECR protons, however, the kinetic energy per unit charge is high enough that the expected deflection from the source is small ($\theta_{scatter} \approx 3°$), meaning, given our current knowledge of both galactic and extragalactic magnetic fields,

the arrival direction of a UHECR proton should point back to its source.

If the highest energy particles contain a significant portion of heavy nuclei primaries any correlation with sources would be suppressed. This is both because the heavy particles have a higher charge associated with their higher proton count ($Q = Z$), and have a higher rest mass ($M \approx Z + N$). Say a heavy nuclei and a proton have the same net energy of $5 \times 10^{19} eV$. Though their velocities would be nearly identical, $E_{net} = \gamma mc^2$ shows that the nuclei's higher mass leads to a proportionally lower Lorentz-factor ($\gamma_{heavy} \approx \gamma_{p+}/(M_{heavy}/M_{p+})$). Additionally, the heavy nuclei experiences a larger force that is proportional to its additional charge, $F_{heavy} = Z * F_{p+}$.

Though the calculation is somewhat involved, the effect of a constant magnetic field on relativistic particles of identical energy but different charges and masses turns out to be strikingly simple. Conveniently, the reduction in the Lorentz-factor directly compensates for the increased inertia of the heavier particle. Therefore, the acceleration experienced by the heavy nuclei is increased by a factor equal to the particle's proton count and the radius of curvature is reduced by the same amount, aka $a_{heavy} = Z * a_{p+}$ and $R_{heavy} = R_{p+}/Z$. This means heavy nuclei cosmic rays are scattered more easily on their trip to earth, and therefore their arrival direction will appear much more isotropic than protons of the same energy. This in turn has the effect of washing out the overall correlation rate at the highest energies.

Early on, the Pierre Auger collaboration was able to correlate a statistically significant portion of these super GZK particles with nearby Active Galactic Nuclei (AGN) [28]. When the finding was published, there was a very high degree of correlation for events over 50EeV, but interestingly as the UHECR event count went up, the originally strong correlation began to fall dramatically [29]. This began raising questions about the validity of the original results. However, if the hints seen in recent studies are true and at the highest energies a large fraction of primaries do consist of higher mass atomic nuclei, the correlation rate should be much lower than that for a purely proton flux and/or may only exist for certain

energy bands [30].

2.4 Extensive Air Showers

Under the current hadronic interaction models at this energy, when a highly energetic cosmic ray particle first enters the atmosphere and interacts with an air molecule, it can produce up to 50 secondary particles in the first interaction alone. As seen in Figure 2.4 the majority of these secondary particles are π mesons or pions. Pions come in three varieties, π^-, π^0 and π^+ which are produced in roughly equal numbers. The charged pion varieties ($\pi^\pm$), have relatively large decay times and often survive long enough to interact with another atmospheric nuclei, thus generating more pions. Any charged pions or kaons that fail to interact further will decay into muons (μ). These muons are relatively inert and often survive all the way to the ground. Therefore, muons represent the majority of the particles representing this interaction chain when the shower reaches the ground. This whole process leads to a cascade of particles which is generally referred to as the hadronic shower.
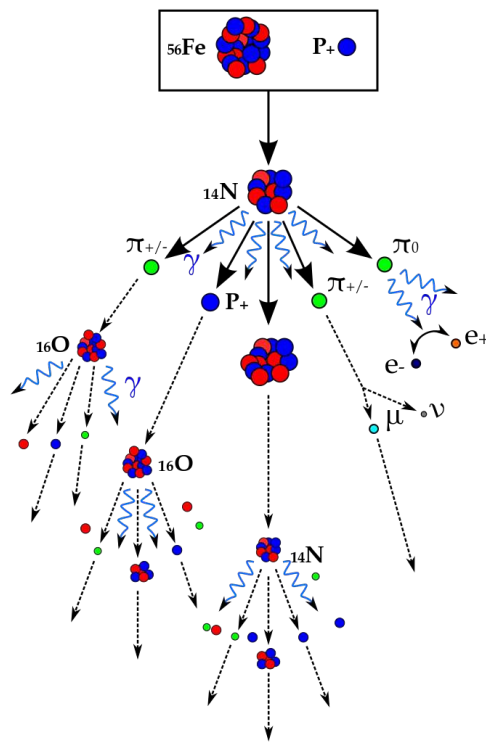
Figure 2.4: Diagram of EAS Interactions

One third of all produced pions are of the short-lived neutral variety (π^0). Neutral pions seldom survive long enough to interact with the atmosphere, quickly decaying into a pair of gamma rays. These gamma rays couple with atmospheric nuclei producing electron positron pairs, which in turn, interact to produce more photons. Additionally, as charged particles in the shower propagate through the atmosphere, nitrogen molecules are excited along the shower axis. Upon relaxing down to their original state they fluoresce isotropically, emitting UV light at an intensity roughly proportional to the number of charged particles present. This portion of the particle cascade is referred to as the electromagnetic shower. The electromagnetic and hadronic components together are collectively known as an extensive air shower (EAS).

As the shower pushes into the atmosphere, all of the above interactions continue until the average energy of its particles is insufficient to produce more secondaries. Once this happens, the rate at which particles are produced in the shower is outpaced by the rate at which they are absorbed by the atmosphere. Because at this point the particle count of the shower is at its highest, it is generally referred to as the shower maximum. At maximum, a shower on average consists of a little more than one particle for every GeV of primary energy. This means that for a primary with energy of 10^{19} eV, the shower maximum contains around 10^{10} particles. Because particle count directly relates to the amount of light emitted from a EAS, the shower maximum is also the brightest point in the shower [31].

Traditionally, the evolution of an EAS is described by the longitudinal density profile $N(X)$. N is the number of particles present in the shower and X, the slant depth, is the amount of atmosphere the shower has traveled through in g/cm^2 from the top of the atmosphere. X is calculated from the zenith angle of the incoming cosmic ray θ and the atmospheric density profile $\rho(h)$ via

$$X = \frac{X_\nu}{cos\theta},$$ (2.2)
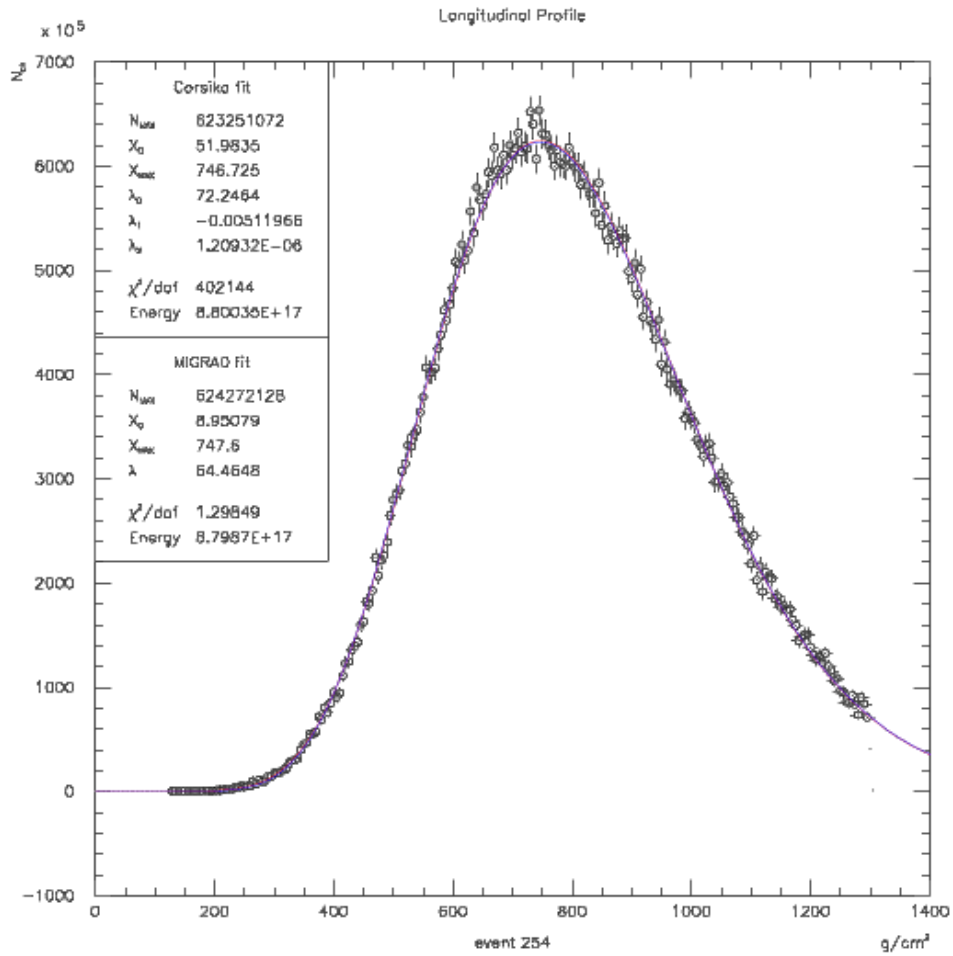
Figure 2.5: A Simulated EAS Longitudinal Density Profile Fit by a Gaisser-Hillas [32].

where X_ν is total vertical atmosphere passed through and is given by

$$X_\nu = \int_\infty^h \rho(h')dh'. \tag{2.3}$$

As seen in Figure 2.5, $N(X)$ in an EAS is well described by the Gaisser-Hillas function. The Gaisser-Hillas function empirically relates $N(X)$ to the particle count at shower maximum (N_{max}), the depth of maximum (X_{max}) and two fit parameters, λ and X_0 related to primary composition and energy as

$$N(X) = N_{max} \left(\frac{X - X_0}{X_{max} - X_0} \right)^{\frac{X_{max} - X_0}{\lambda}} \mathrm{Exp}\left(\frac{X_{max} - X}{\lambda} \right). \tag{2.4}$$

.

The amount of particles in a shower is directly determined by the quantity of kinetic energy in the primary available to be converted to particle rest mass. This means that the area under the Gaisser-Hillas curve, which is essentially a count of the number of particles in the entire shower, is indicative of primary energy. Also, the cross-section of a primary generally grows with its mass and the mean atmospheric depth of first interaction is inversely proportional to primary cross section. This means that showers caused by heavy primaries, start earlier in the atmosphere than those caused by lighter primaries. Additionally, the principal of shower universality states that all showers develop at about the same rate regardless of primary energy or composition. Because of this, the information on the primary cosmic ray's composition available at the unobservable first interaction is mostly preserved to the easily observable point X_{max}. $N(X)$ is directly related to the intensity of the UV light emitted by the shower. A measurement of this light and its geometry, is sufficient to completely describe the nature of the incoming cosmic ray primary.

Because all of the particles produced in a shower have high kinetic energy, they are essentially traveling at the speed of light. Also, all particles in the shower are offspring of the same first interaction. These two facts taken together mean that the leading edge of an EAS, called the shower front and shown in Figure 2.6(a), is well represented by a relatively thin shelled expanding sphere. The particle density in this shell however, is not evenly

(a) A Diagram of an EAS Shower Front

(b) The First UHECR
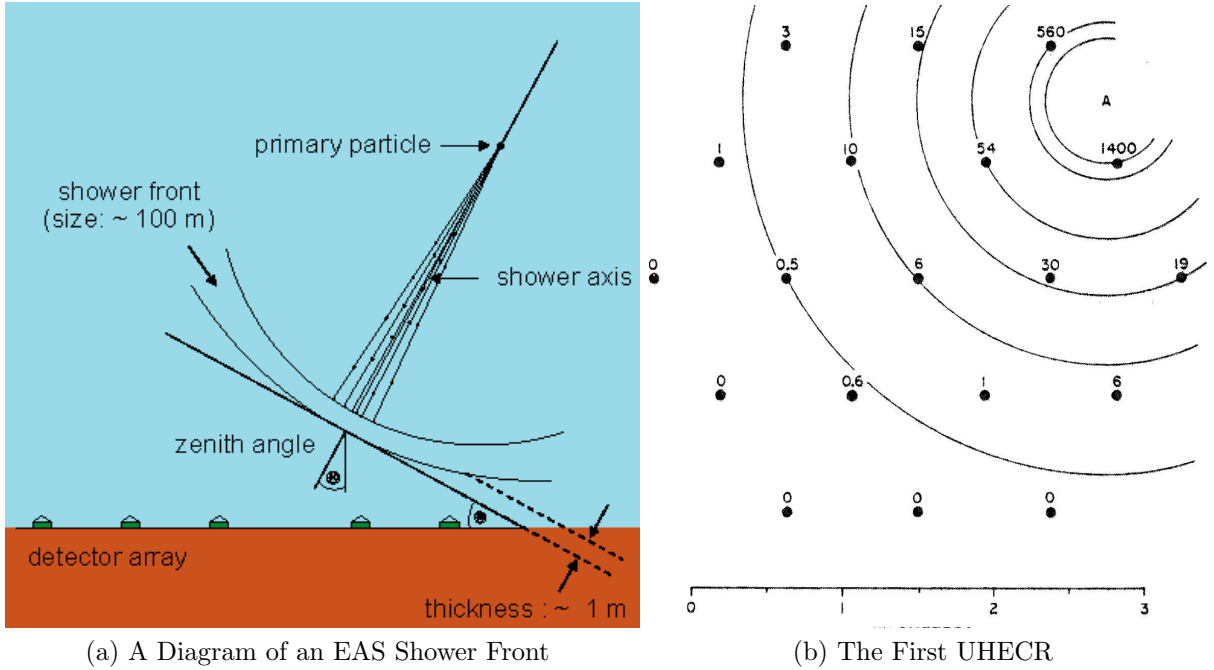
Figure 2.6: Left: A Diagram of an EAS Shower Front. Right: The Volcano Ranch experiment surface measurement of a $1 \times 10^{20} eV$ event [23].

distributed. It is heavily weighted in the direction of the cosmic ray's original trajectory by the incident primary's kinetic energy. As a result of this uneven distribution, when the EAS reaches the ground, it does so in a spherical disc consisting of mostly muons. This disc, has a total particle count related to primary energy and generally has a high density near the shower axis that quickly decreases with distance. The timing, shape and density at the ground is referred to as the shower footprint and is shown in Figure 2.6(b) for the Volcano Ranch Experiment. If recorded, the timing and shape of the footprint is indicative of the showers arrival direction, while a function fit to the footprint's particle distribution, called the Lateral Distribution Function (LDF), can be used to infer the primary's initial energy.

CHAPTER 3

THE PIERRE AUGER OBSERVATORY

Any experimental search for new and interesting physics is strongly dependent on the instrumentation that is used. Small details and fundamentals of the detector design will make or break a study. This research is no different. The instrumentation and software of the Pierre Auger Observatory is huge and staggeringly complex. What follows is a distillation of cosmic ray detection techniques, the Pierre Auger Observatory instrumentation and the software that are critical to the study. It is not a general overview of the whole observatory, and with the exception of the following short introduction, it is focused solely to the information necessary to understand the topic at hand.

Since the 1962 Volcano Ranch observation, UHECRs have been a subject of interest in the astroparticle physics community. Over the years the instrumentation built for their study has grown both larger and more sophisticated. Many techniques and methods have been employed for their study. The main methods thus far used are surface arrays, atmosphere fluorescence telescopes and Cerenkov telescopes. Each of these methods has its advantages and disadvantages.

Surface arrays are simple, durable and work well in a wide range of conditions. Unfortunately, they also depend strongly on models or calibration and can only provide a limited amount of information on individual events. Cerenkov telescopes can also operate in a wide range of environments and can provide useful information about the individual showers, but are not well-suited to scaling to the very large apertures necessary to make statistically strong UHECR studies. Fluorescence telescopes, on the other hand, do well in providing a large amount of information on each shower and scale in size, but are very delicate and can only operate in very dark and clear environments. These weaknesses, coupled with the extreme rarity of UHECRs, means despite the large number of observatories built to study

them there is still much to discover about the nature of these extreme particles.

The Pierre Auger Observatory was designed to answer the open questions of UHECR physics and has proven to be well-suited to do so. When it was designed it was clear that both high statistics and highly detailed shower by shower measurements were required. To satisfy this need and avoid the individual weaknesses of each observation method, the Pierre Auger Observatory was designed as a hybrid detector. This means it is able to measure both the signals on the ground and a shower's evolution in the atmosphere simultaneously. Additionally, due to the low UHECR event rate at the highest energy ($\Phi < 1 \times km^{-2} \times 100yr^{-1}$) and the need for a large number of measurements, the array was designed with a massive aperture.

Thanks to the generous contributions of many funding agencies around the world, the Pierre Auger Observatory was officially commissioned in 2008. It covers an area of over 3000 km^2 near the town of Malargüe, Mendoza, Argentina, and if you include its calorimeter, the column of atmosphere above it, it is the largest detector in the world. As seen in Figure 3.1, the heart of the Observatory is its 1600 ground-based water Cerenkov detectors, together called the Surface Detector (SD), and its 27 fluorescence telescopes split into 4 detector sites overseeing the SD, together called the Fluorescence Detector (FD). Additionally, because the instrumentation uses the atmosphere as an integral part of its detector, the atmosphere above the Observatory is among the most well-measured in the world [33].

3.1   The Surface Detector

Represented by the dots in figure Figure 3.1, the Pierre Auger Observatory surface detector is made up of roughly 1600 water Cerenkov detector tanks (stations) spaced in a 1.5 km triangular grid. In addition to the regular 1.5 km grid, there is also the more densely packed region with 0.75 km spacing seen in Figure 3.1. This is referred to as the in-fill and was designed as a low energy extension to the array. The in-fill is unused in this analysis.

As shown in Figure 3.2, each SD station is essentially a cylindrical tank measuring 1.7 m in radius by 1.5 m in height which is filled with 12 m^3 of highly purified water. This water
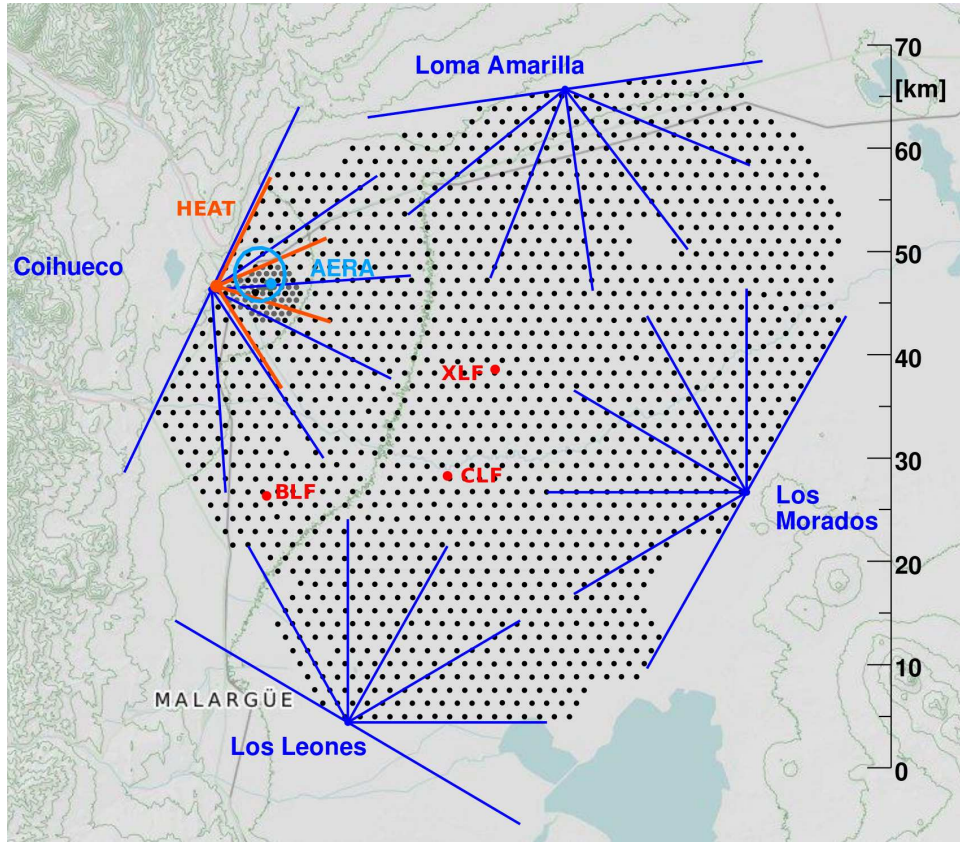
Figure 3.1: The Pierre Auger Observatory: Dots represent Surface Detector stations. Red dots represent the atmospheric monitoring facilities. Lines, both orange and blue, represent the field of view of each Fluorescence Telescope for each Eye of the FD. The light blue circle represents AERA, an R&D radio detector [34].

is encased in an opaque and highly internally reflective Tyvek© liner, and is monitored by 3 photomultiplier tubes (PMT). Due to the nature of the tank and liner, this water sits in near perfect darkness and can be considered optically isolated from external light sources. This allows the SD to take measurements in a wide variety of conditions.

The core principle on which these detectors operate is called Cerenkov radiation. Cerenkov radiation is the flash of light produced when a charged particle travels at a velocity that exceeds the speed of light in the media in which it is traveling. This light flash can be quite bright on a per particle basis and is produced in a manner similar to a sonic boom. By recording the number, intensity and timing of these flashes, each station constantly monitors the flux and intensity of high energy charged particles passing through it at any given

time.
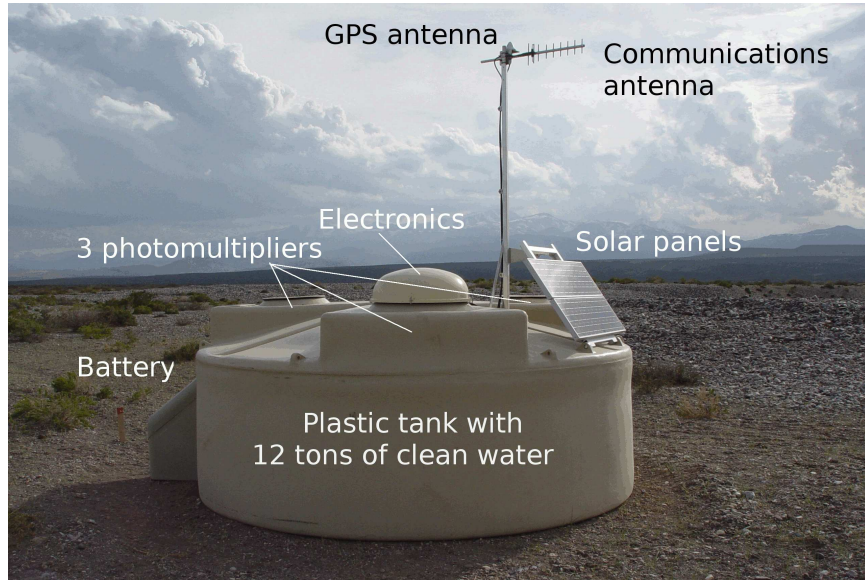
Figure 3.2: An Pierre Auger Observatory Surface Detector [13].

Electronically, each of these stations is completely self-sufficient and operates autonomously. As shown in Figure 3.2, each separate station possesses its own on-board photo-voltaic array, battery, GPS clock, micro-controller, and radio broadcast antenna. Over the years, they have be proven to be both robust and reliable. However, in measuring UHECRs events, an isolated station observation is neither useful nor trustworthy. In order to make a measurement of the energy or trajectory of an incoming cosmic ray event, the shower must strike many stations taking synchronized measurements. Furthermore, due to the large number of random energetic particles passing through the air at any given time, each station is constantly recording particle flashes. In order to ensure that each station measurement corresponds to an actual cosmic ray event and that these measurements occur in coincidence, each tank is strongly reliant on an internal filtering or triggering system as well as triggering from the rest of the Observatory [35].

The triggering system for the SD array has five levels, T1 through T5. The first two levels are internally processed on each individual station's micro-controller. The first trigger, T1, requires that at least two of the three PMTs in a station, each record a signal that exceeds

either a minimum signal strength threshold concurrently, or a minimum length of time. T1 is tuned to be passed at a rate of $\sim 100Hz$ for each tank, the rate at which cosmic rays are expected to strike a $10m^2$ area. T2 is a more computationally intensive and stricter form of T1. It also asks for one of two conditions to be met. Basically, the signal in each PMT must either exceed a very high threshold with all three PMTs concurrently, or two PMTs must fire coincidentally for a minimum duration over a high, but somewhat lower threshold. T2 is met at a rate of about $20Hz$ for condition 1 and $1Hz$ for condition 2. If T2 is met, the tank transmits data via its radio antenna to a receiving tower located at the nearest FD. From here it is then relayed to the Central Data Acquisition System (CDAS) at the main campus in Malargüe for further analysis.

The T3-5 triggers are carried out at CDAS and rely on the signals from multiple detectors at the Observatory. T3 is the coincidence trigger and acts as the first gateway to storing the event in the Pierre Auger Observatory data stream. T3 looks for coincident measurements in the SD and/or the FD. In the case of the SD, T3 asks that at least one T2 station in the event has at minimum two nearby stations also triggering at the T2 level coincidently. These can either be two of its closest neighbor stations or one of its closest neighbors and one of its second closest neighbors, as shown in Figure 3.3. If the station's measurement is isolated, but the FD also triggers during the SD event, then the FD T3 trigger takes over to evaluate the significance of the station's signal. If an event meets the FD's T3 filter its data is stored as a hybrid measurement. If the event only passes the SD's T3 it is passed along to the T4 trigger.

T4 is the first SD physics trigger and requires that the event timing and geometry correspond to a real EAS. This trigger was specifically designed to filter out rare, but expected, random T3s due to atmospheric muons striking a tank at the same time that a very low energy shower lands nearby. T4 specifically requires either three adjacent, non-aligned tanks each have signals passing a time over threshold trigger, or the tank with the highest signal (the Hot Tank) must have three of its closest neighbors also fire. In all cases, T4 also re-
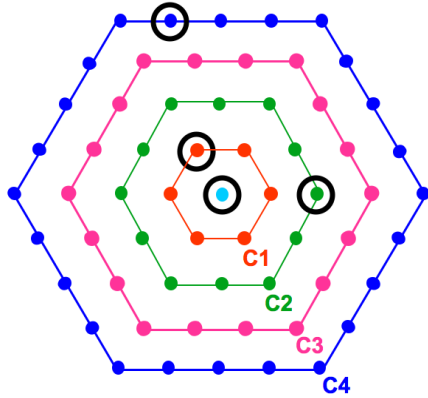
Figure 3.3: The T3 SD Trigger. Only the center tank has a complete T3 trigger. The C4 ring tank's data is stored as the event had at least one tank pass T3 [36].

quires that the signal start times for all tanks lay within the timing difference defined by the distance between the tanks divided by the speed of light. This ensures each event that passes the T4 trigger corresponds to a physically realizable cosmic ray shower.

The final trigger, T5, does not need to be passed for the event to be recorded, but is necessary to ensure that events that fall close to the edge of the array are properly considered. T5 essentially requires the hot tank to have all six tanks surrounding it to be fully functional. In the case of the center tank in Figure 3.3, all of C1 must be present and fully functional during the event. The functionality of surrounding tanks is included in the data packets sent to CDAS [36].

The performance of the SD is almost completely independent of environmental conditions. It is able to take data day or night, rain or shine. Because of this 100% duty cycle, the SD array is the statistical workhorse of the Observatory. Unfortunately, since the SD doesn't measure the shower's development profile, but only the particle count at ground, it has a few shortcomings. It is generally less accurate in its measurements. It is only indirectly sensitive to primary composition. Finally, because the particle count at ground is only empirically related to primary energy, it must be calibrated by the FD in a process described in Section 3.3 [13].

3.2   The Fluorescence Detector

The Fluorescence Detector (FD) of the Pierre Auger Observatory consists of four detector sites (Eyes) housing a total of 24 UV telescopes trained on the air above the SD. The location of each Eye is labeled on the observatory map, Figure 3.1. The field of view of the housed telescopes is represented by the radiating lines. The four sites, Los Leones (LL) (shown in Figure 3.4), Los Morados (LM), Coihueco (CO) and Loma Amarilla (LA) occupy high points overlooking the flat plain occupied by the SD. Each of the individual telescopes have a 30° elevation × 30° azimuth field of view and are carefully aligned for seamless telescope-to-telescope transition. This gives each Eye, an uninterrupted total viewing angle of nearly 180°. In addition, there is a low energy extension called the High Elevation Auger Telescopes (HEAT) meant to compliment the SD'd in-fill array. HEAT consists of three more UV telescopes trained between 30° and 60° above the horizon. HEAT is not used in this analysis.

Figure 3.4: The Los Leones Detector [37].

Though the instrumentation is similar in design, Fluorescence telescopes operate in a way that is unlike the more familiar optical telescopes that directly produce images. A

Fluorescence telescope does not directly observe cosmic rays, but only their effects on its calorimeter, the atmosphere. In this way, Fluorescence telescopes are much more similar to detectors in nuclear or particle physics than they are to the Hubble. In 2.4, the section covering a cosmic ray's interactions in the atmosphere and the production of an EAS, the electromagnetic shower component was described. In an electromagnetic shower, the numerous charged particles produced excite the valence electrons in atmospheric nitrogen causing them to fluoresce isotropically. The FD's telescopes are calibrated to specifically look at, and record, the timing, intensity and evolution of this emission. This UV light is far too dim and of the wrong wavelength to be seen by the naked eye and can be easily rendered imperceivable to instrumentation by small amounts of atmospheric background light or haze. This means that the FD can only operate in extremely dark, very clear and cloudless environments, and therefore has $\sim 14\%$ duty cycle, severely limiting its statistical power [38].
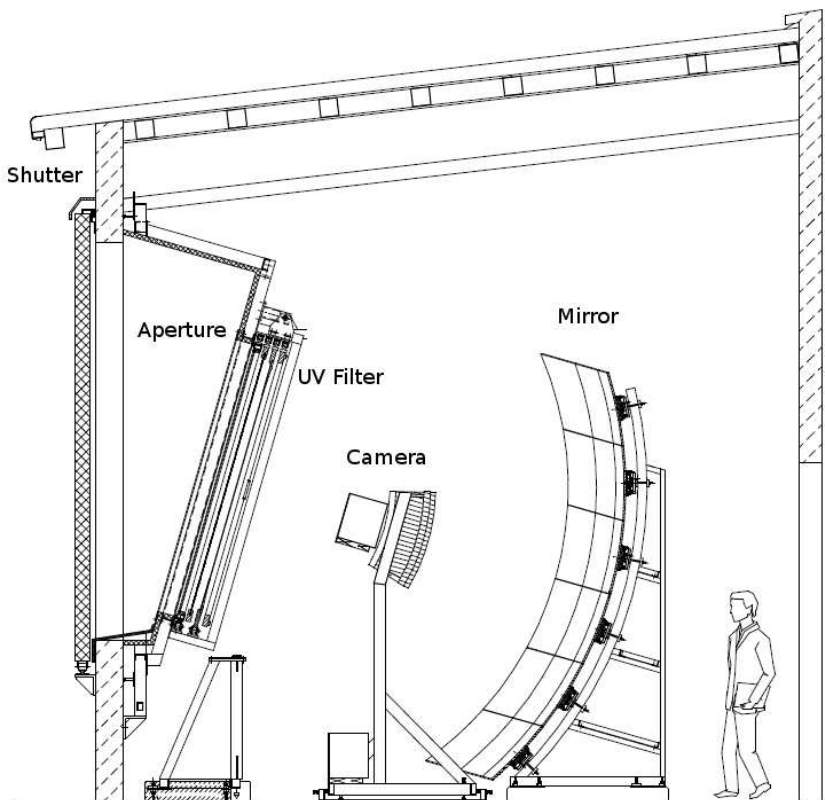
Figure 3.5: Auger Fluorescence Telescope Schematic [39].

As shown in Figure 3.5, each telescope consists of a shutter, a 1.1 m aperture, a narrow band UV light filter, a corrector ring, and a segmented 3.4 m radius spherical mirror which focuses photons on the camera [39]. Seen in Figure 3.6, the camera is made up of 440 PMTs in a hexagonal grid of 20 rows of 22 PMTs each. As illustrated in Figure 3.7, each PMT is also equipped with a head electric unit, which collects the electrical signal and sends it to one of 20 analog boards for filtering and amplification. The 22 programmable potentiometers on each analog board control the gain of 22 corresponding PMTs, ensuring uniform amplitude and response time. The result of this is a coordinated array of detectors each capable of counting individual photons with a $100ns$ resolution. This photon count per time-bin is called its ADC trace [40]. This instrumentation gives the FD superb accuracy and resolution, but also leaves it susceptible to noise and background light. Like the SD, the FD is constantly recording signals from background light sources and small random atmospheric light flashes. Also, like the SD, the FD is outfitted with a robust trigger system in order to ensure that only cosmic ray observations make it into the final data stream.

The FD trigger system consists of four separate trigger levels of increasing complexity. Like the SD, the first two levels are processed internally by each telescope on its trigger board [40]. The First Level Trigger (FLT) is a threshold filter. The FLT requires that the integrated signal for 10 consecutive time bins ($10 \times 100ns$) in all triggered pixels combined is above the minimum adjustable threshold. This demand is designed to cut out short noise signals and is set to maintain an $100Hz$ trigger rate per telescope. Upon passing, the data is evaluated by the Second Level Trigger (SLT).

The SLT evaluates the geometry of triggered pixels and cuts out events that could not possibly have been caused by a cosmic ray. Essentially, it reads in all PMT signals and looks for the 4 to 5 pixel minimum base geometries shown in Figure 3.8. If one of these pixel geometries is found and 4 out of the 5 pixels triggered in a 20 μs window then the event passes the SLT. This 20 μs limit will cutoff sensitivity to very low velocity events at large distances and will be examined later. This step reduces the trigger rate down to about
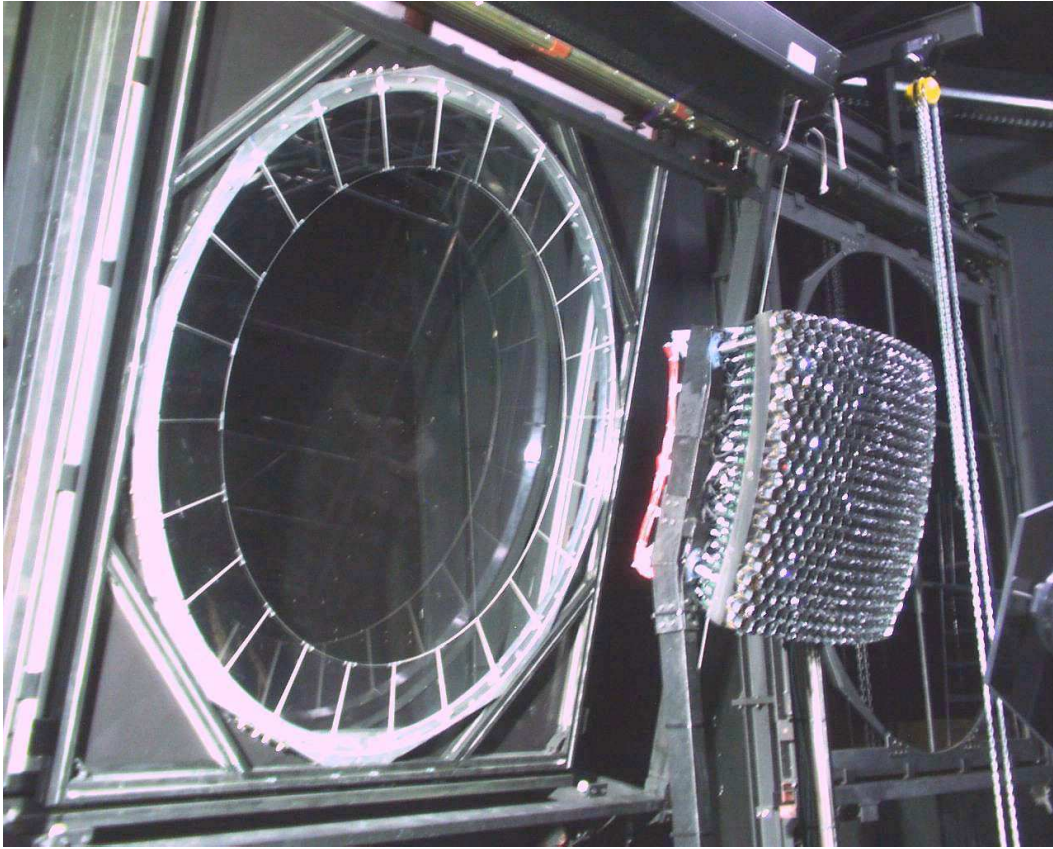
Figure 3.6: FD Camera and Aperture [39].

$1Hz$ per mirror. When SLT is passed, all of the camera data from the 30 μs proceeding the trigger time as well as the following 70 μs are copied from the buffer and saved as a potential event. From this point the data is moved from the internal telescope electronics to the more capable EyePC housed at each detector site. The buffer is now cleared and is able to capture a new 100 μs event window. If an event lasts longer than one 100 μs window is able to record, the next 100 μs of the event will be stored in the next time window if it independently passes both the FLT and SLT [41]. Cosmic ray events that are close enough to be detected by the FD are not predicted to approach this maximum time, however slow exotic events and atmospheric phenomena can.

On the EyePC two additional triggers are implemented. The first is the Third Level Trigger (TLT). The TLT is designed to remove the lightning and background events that
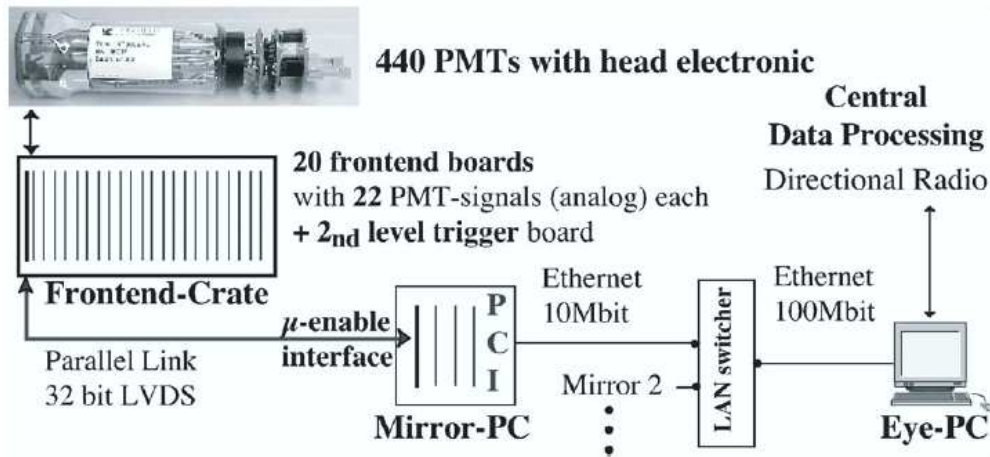
Figure 3.7: Auger Fluorescence Telescope Electronics [40].

fulfill the first two triggers, while passing the vast majority of cosmic ray events. Originally, the TLT made cuts by reading out the entire camera and examining the ADC traces of each triggered pixel in order to remove background and lightning events. This proved far too computationally intensive and resulted in a long down time in the FD. This was fixed by splitting the TLT into two separate levels. The first level, called the multiplicity trigger, focuses on quickly removing very large background events in order to reduce the data load for the second, more effective ADC based trigger level.

The TLT multiplicity trigger is able to quickly cut large background events without reading out the camera by examining the multiplicity signal. Shown in Figure 3.9, the multiplicity signal is simply the time ordered count of the number of pixels triggered in a camera for each of the one thousand 100 ns time-bins during an event. The maximum value that the multiplicity signal can reach for any one time-bin is 63 as that fills the data buffer for that 100 ns and therefore the camera is considered saturated. The multiplicity signal is calculated during the FLT and SLT and is directly accessible from the hardware making it ideal for the fast rejection of background events. The first step of the multiplicity trigger is to convert the multiplicity signal into the following five variables which easily distinguish
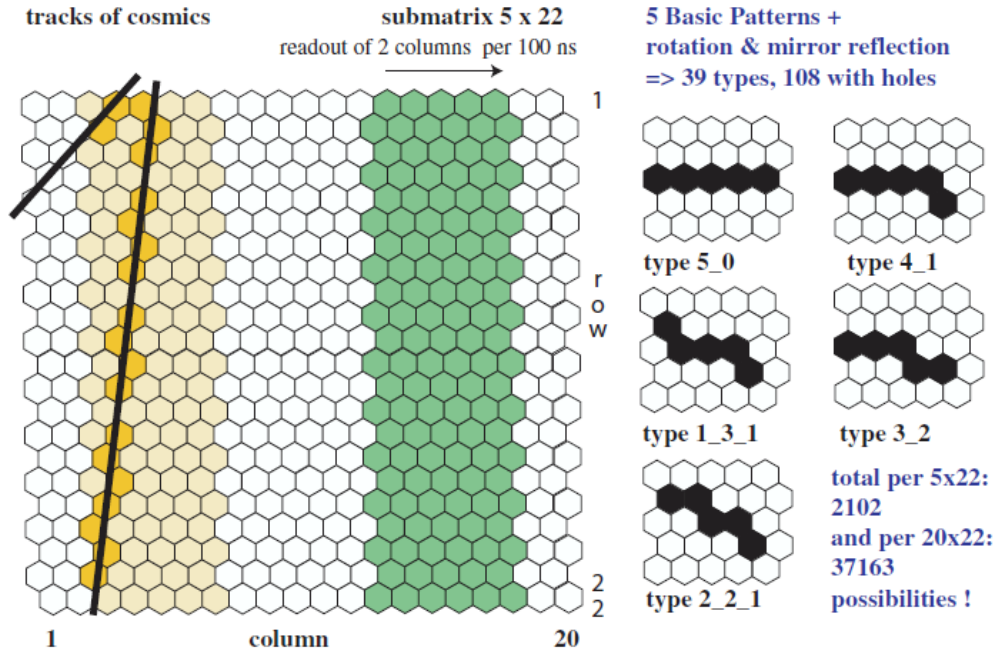
Figure 3.8: T2 FD Trigger Minimum Pixel Geometries [40].

cosmic ray events from background:

n_gap The number of times that the multiplicity signal reaches a zero value and then rebounds. The right side of Figure 3.9(a) has a n_{gap} value of two, one preceding the event and one after the main peak.

n_step A count of any changes in the multiplicity signal. Both upward and downward changes and their magnitudes are added positively to the count. This keeps track of how many and how often pixels gain and lose their trigger.

int_all The integrated multiplicity signal throughout the 1000 time-bins of an event. This value is a count of the total number of triggered pixels multiplied by the number of time-bins each pixel was active for which can be seen as the area under the the right side plot in Figure 3.9.

n_pix The total number of triggered pixels. Each pixel is only counted once.

32
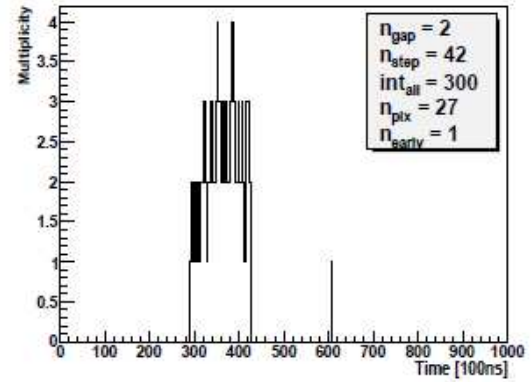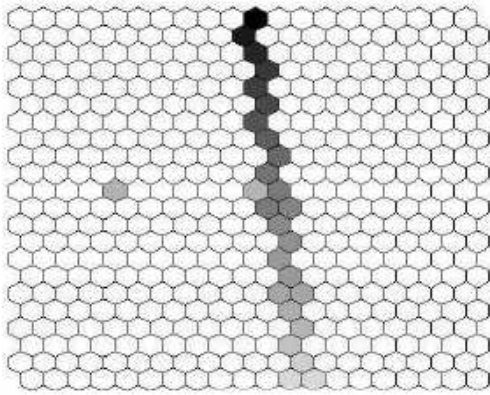
(a) A Cosmic Ray Shower Event
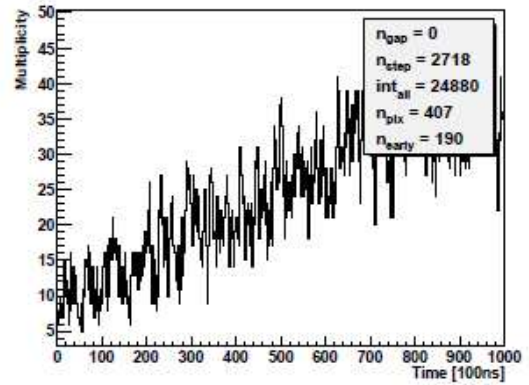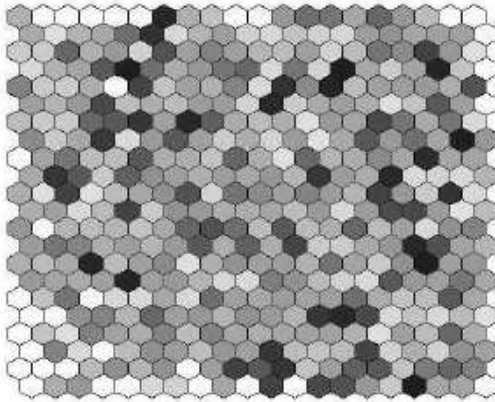
(b) A Lightning Event

Figure 3.9: The left side of each figure shows the integrated camera responses to the event. The right show a plot of the event's multiplicity signal as well as the values for each of the five multiplicity parameters [41].

n_{early} he number of pixels which trigger in the first 5 μs of an event. Each pixel is only counted once.

These values are then checked against the following five requirements, each targeting a difference between shower and background events:

1. $n_{early} < 6$

   Showers always have fewer than 6 pixels trigger in the first 5 μs, but lightning and background events often have many. This is well-illustrated by Figure 3.9 as the lightning event triggered 190 early pixels, but the shower only triggered one.

2. $int_{all} > 8 \cdot n_{pix} - 100$

   This cut has the effect of removing events where the average trigger time of pixels over the whole event is 0.8 μs or less. This is effective because background events often consist of many pixels triggering for very short durations and therefore easily cut. Showers on the other hand always trigger pixels for at least 1 μs regardless of their geometry or distance to the detector.

3. $n_{gap} < 40$

   This cut targets background events as their pixel signals rapidly fluctuate and often leave gaps in the camera response. Showers, however, tend to trigger pixels one after another with significant overlap as shown in Figure 3.9(a).

4. $n_{step} < 2 \cdot (n_{pix} + 25)$

   This cut has the effect of removing any event where 25 or more pixels are triggered at least twice. As seen in Figure 3.9(b), lightning and background events often have large number of their pixels trigger repeatedly. This does not occur in showers.

5. $int_{all} < 10000$

   This cut removes any events that are too bright for too long. As seen in Figure 3.9, this happens often in lightning events and practically never in cosmic rays. This could

34

potentially cut a cosmic ray if it was very very bright and very very slow (triggering 10 or more pixels throughout the event 1000 time bins of the event). Real events of this magnitude are not expected.

After passing these five conditions only cosmic ray events and noise events with manageable data streams are left. At this point the ADC traces for each of the event's triggered pixels can be read out without contributing to FD down time and the second stage of the TLT trigger takes over.

The second stage of the TLT trigger focuses on rejecting fast muon hits, direct cosmic ray strikes and random triggers. It does this by checking to see if the event's camera response is both time-ordered and geometrically consistent with a shower event. The first step in this process is to identify the center of the shower in the camera. This is done by looking for the largest group of pixels, allowing for a maximum gap of one pixel between pixels in a group. In the second step, a straight line is fit to the pixel trace via a least-square regression using the pixel exposures as a weight. The pixels are then ordered, from start to finish, by their projected position on this line. The trigger then marches down this ordered list comparing the centroid time of each pixel with that of the pixel immediately preceding it in the list. If the value is positive then the counter n_{up} is increased by one otherwise the counter n_{down} is added to. After all pixels are checked the value of n_{up} is compared to n_{down}. If $\mid n_{up} - n_{down} \mid\geq 3$ then the event is passed as a probable shower event [41].

The final trigger is the array trigger level T3. In this trigger the FD searches for correlated measurements in the SD and then combines any passed measurements as a Hybrid Event. To do this the EyePC performs a fast, rudimentary reconstruction of the event in order to determine the event's core location and timing in the SD array. This information is then relayed to CDAS to be compared to incoming SD events and in rare cases, other FD events. These events that are coincidently measured in the FD and SD are called hybrid and are vitally important for the observatory. They represent the most plentiful high accuracy measurements made by the Observatory and are critical to the energy calibration of the

SD array. The rare events that are measured at two or more independent FD sites (and usually the SD) are called Stereo events and are the most well-observed and therefore, most constrained measurements made at the Observatory [40].
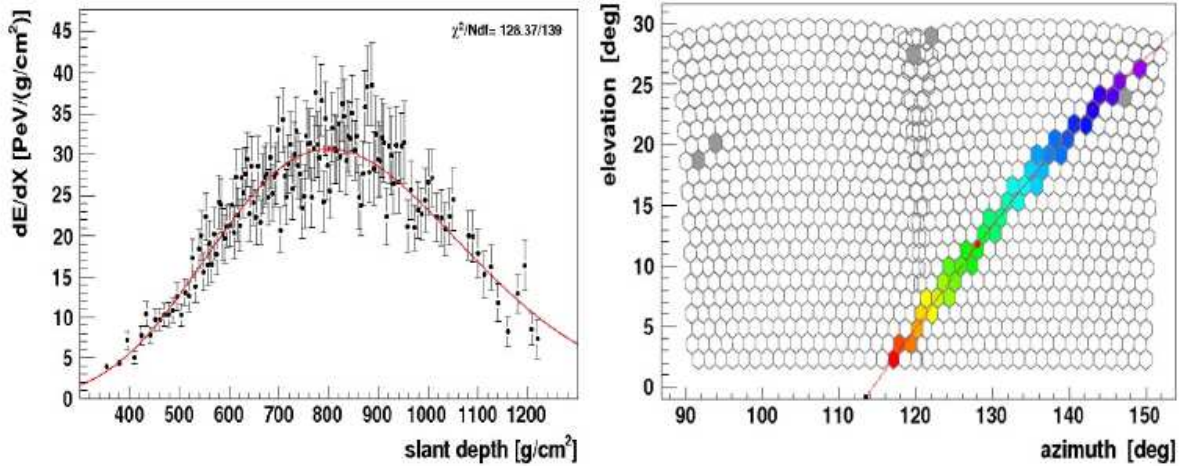
Figure 3.10: An Example of a FD measurement. Left: A typical FD light profile. Right: FD pixel trace and timing (blue: early, red: late)

As explained in Section 2.4, the pattern of the triggered pixels, shown in Figure 3.10, the timing evolution of the signal across the camera and the light intensity profile recorded by the FD together represent the most complete signature of a individual cosmic ray shower available at the Observatory. With this information, the geometry and energy of cosmic ray showers can be estimated directly with reasonable errors, while many observations of the shower profile can be used to infer information on primary composition. When the concurrent measurements on the SD or other FD sites is added in, these errors are significantly reduced. This high sensitivity more than compensates for complexity of running fluorescence telescopes and their low duty cycle.

3.3 FD-SD Cross Calibration

The relationship between the SD's particle count distribution at the ground and shower energy is non-exact due to a heavy dependence on the SD station geometry, random fluctuations in shower evolution, and variations in the expectations of the signal at ground based

on primary composition. Because of this, the methods used to translate the SD response to energy are necessarily empirical. This means that SD measurements must be calibrated in order for its observations to physically correspond to the actual values of the shower's observables. This is one of the primary reasons that the Pierre Auger Observatory was designed as a hybrid detector.
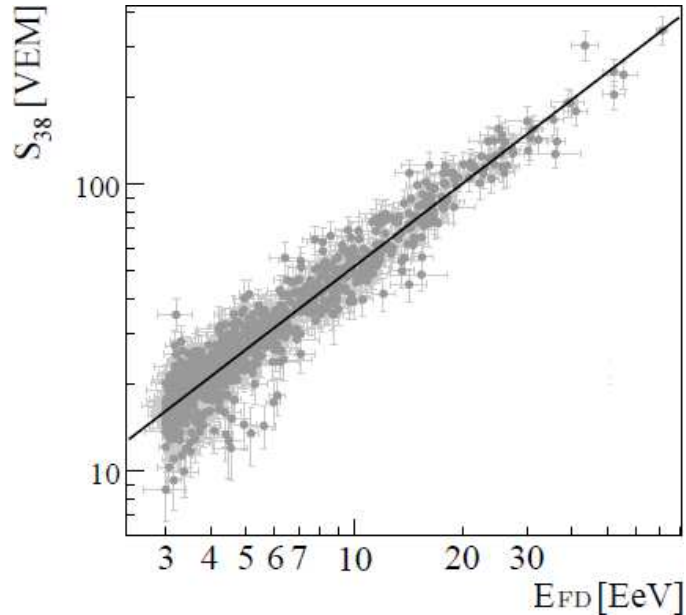
Figure 3.11: Calibration of the SD using FD energy measurements. On the X axis is the energy measured by the FD, on the Y-axis S_{38}, a reliable zenith angle normalized energy indicator. The distribution is fit via the equation $S_{38} = (E_{FD}/A)^{1/B}$. The SD energy is then calculated as $E_{SD} = A\, S_{38}^{B}$ [42].

As explained in Section 3.2, the FD is capable of nearly model independent measurement of cosmic ray primary energy using the light profile the EAS leaves in the atmosphere. Because of this, events which fully and independently trigger both the FD and SD, called Golden Hybrid events, can be used to calibrate the SD without the model dependencies required in simulations. Basically, the energy reconstruction of the SD can be compared to the energy measurement done by the FD in order to empirically calibrate the SD response. Ideally the SD energy will closely match the FD energy for all events, but this is not the case because of the aforementioned shower-to-shower fluctuations and uncertainties. How-

ever, as shown in Figure 3.11, the SD response can be calibrated to correspond to the FD measurement on average. This greatly reduces the errors in the SD energy measurements and provides a real measurement of the SD detector efficiency and its changes relative to the FD over time [42].

3.4 Atmospheric Monitoring

Because the FD uses the atmosphere as a calorimeter, the condition of the air above the Observatory greatly effects the measurements made at the Observatory. This is especially relevant to this work as the profile of the atmosphere is critical to high accuracy timing studies and because hazy or cloudy atmospheric conditions will render possible candidates untrustable. The most important atmospheric factors are the density profile, the temperature profile, the cloud height and coverage above the array and the atmospheric aerosol content. In order to track each of these properties, the Observatory uses a wide range of methods and instrumentation.

Until 2012, the density and temperature profiles were sampled via radiosonde balloon launches from the Balloon Launch Station (BLS). This proved to be burdensome and impractical. The regular balloon launches were far too infrequent to provide a reliable data set for shower reconstruction. This was addressed by a program that launched a balloon immediately after any FD observation of a high energy shower, but this program was costly, labor intensive and left large holes in the data. Due to these factors, atmospheric profiles are now pulled for free from the Global Data Assimilation System (GDAS), which has proven to be much more consistent, reliable and accurate [43].

Clouds are able to scramble the shower timing data, obscure the UV emission of a shower or, by scattering the intense and highly directional Cerenkov light toward the eye, amplify the apparent UV light. This means cloud coverage readings are crucial to FD analysis as any FD observation involving a cloud is unreliable and needs to be carefully addressed. Because of its importance, the Observatory uses several systems to gather cloud coverage information. The Geostationary Operational Environmental Satellite system (GOES) provides a very reliable

cloud coverage probability measurement. This data is always present and is updated every 15 minutes. Unfortunately, it can only provide probabilities of cloud coverage [44]. On site, the cloud coverage in the field of view of the Eyes is primarily by the IR cloud cameras and Lidars placed at each Eye. These work well and give precise measurements, but because of down time on the instrumentation there are holes in the IR camera data [45].

The Central Laser Facility (CLF) and the eXtreme Laser Facility (XLF) also provide cloud height measurements, but are primarily responsible for measuring the aerosol content in the air above the array. Their aerosol readings are supplemented by the Raman Lidars, optical telescopes and other specialized equipment located around the array.

3.4.1 The Geostationary Operational Environment Satellite

The GOES satellite system is an array of weather satellites that monitors the conditions of the atmosphere above north and south America as well as the Atlantic and eastern Pacific oceans. First launched in 1974, the GOES constellation is an integral part of U.S weather forecasting and atmospheric study. Though 15 satellites have been launched, only 4 (GOES 12-15) are still used for weather atmospheric monitoring. The Pierre Auger Observatory takes data mainly from GOES-12, the satellite tasked with monitoring south American weather. GOES-12 is outfitted with two main instruments, the Imager and the Sounder.

The Imager is an optical camera that measures the radiated infrared and reflected visible solar emissions from the earth's surface and atmosphere. With this data, it monitors cloud coverage and surface temperature [46] with a spacial resolution of $\sim 1km$. The Sounder, is a sweeping high accuracy IR scanner that is capable of many of the same readings as a balloon born radiosondes. With the data it collects, it is capable of recording the atmospheric temperature, moisture and density profile, surface and cloud top temperature and ozone distribution [47]. The Sounder data is not directly used by the Observatory in its raw form, instead it is incorporated into the GDAS predictions which are then used by the Observatory. The Imager data, however serves as an important source for cloud coverage data.

3.4.2 The Global Data Assimilation System

The Global Data Assimilation System is a weather forecasting method that combines observations from a wide range of atmospheric monitoring equipment placed in space (including GOES) and around the world with the most up-to-date atmospheric and weather forecasting models. By combining observation and forecasting, GDAS is able to provide real-time accurate estimations of atmospheric profiles, corrected by real measured values 4 times a day. This data is calculated on a 1° Lat/Long grid covering the earth, and is made available to the Observatory free of charge using the Real-time Environmental Applications and Display sYstem (READY).
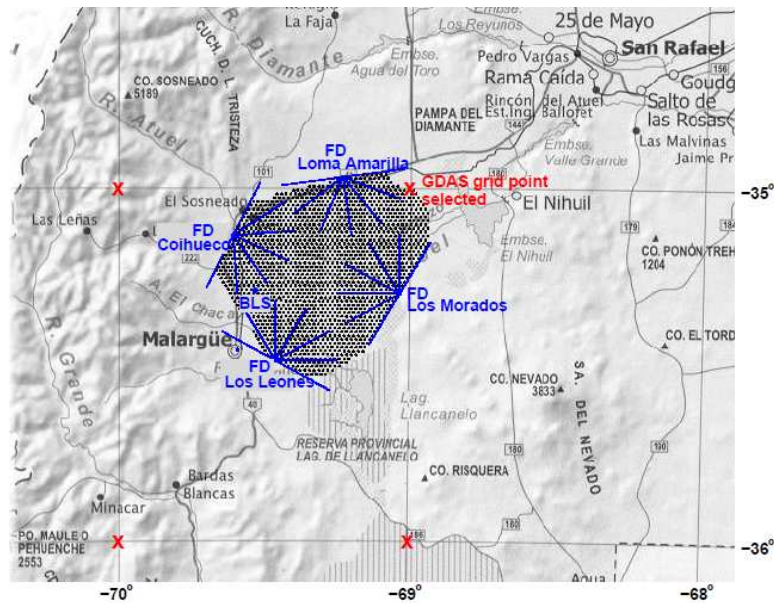
Figure 3.12: GDAS Grid Points Near the Observatory. The grid points (the **Xs are spaced every** $1°$ **of latitude and longitude at each degree** [43].

As seen in Figure 3.12, the grid point selected for the Observatory's profile measurements is located at the north-east corner of the array. There is an assumption that the atmospheric profile has reasonable horizontal uniformity over distances on the scale of the Observatory. This means that atmospheric profiles calculated for the marked GDAS point should approximate well the profiles over the whole array. By comparing GDAS data to the data collected

40

by the BLS radiosonde launches made at the array from 2005 to 2010, very good agreement was found, vindicating the accuracy of the GDAS dataset and the assumption of horizontal uniformity. Furthermore, because the regular balloon launches could only provide a monthly average for atmospheric profiles at the array, GDAS improves the accuracy of reconstructions at the array as it is sensitive to changes on the scale of a few hours [43].

3.4.3   At Eye Atmospheric Monitoring Instruments

As seen in Figure 3.16 and Table 3.1, each Eye is equipped with a wide range of atmospheric monitoring tools.

Table 3.1: The distribution of atmospheric monitoring equipment at each Eye

Instrument	Los Leones	Los Morados	Loma Amarilla	Coihueco / HEAT
Lidar	x	x	x	x
Raman	-	-	-	x
Weather Station	x	x	x	x
IR Cloud Camera	x	x	x	x
APF	-	x	-	x
Optical Telescope	x	-	-	-

In order to monitor for the presence of clouds in each Eye's field of view at any given time, each Eye is equipped with a IR cloud camera and Lidar station. The IR camera scans the full field of view of each Eye every 15 minutes, while the Lidars monitor the height of the clouds above the array at regular and frequent intervals. By combining the two readings, the presence of clouds in any pixel's field of view, as well as the distance to that cloud can be approximated. By comparing the cloud's calculated location with the reconstructed geometry of an observed shower, the probability that the shower passed through a cloud can be reported [45].

The Raman Lidar located at Coihueco is capable of monitoring the aerosol and vapor content of the atmosphere in any direction. However, because it dumps a large amount of light into the atmosphere, all FDs observing in the direction of the Raman must be shut down for the duration of the measurement. This means that this Raman is only used to

make a quick measurement of the atmosphere after very energetic showers are observed. The Optical Telescopes, called the F/(Ph)otometric Robotic Atmospheric Monitor (FRAM) and the Horizontal Attenuation Monitor (HAM), measure the intensity of light from stars with a known luminosity in order to calculate its attenuation due to aerosols. By doing this they serve a purpose similar to that of the Raman but with a lower accuracy. The benefit to this method is that it does not require the FD's to be shut down during its measurements [48].

The Aerosol Phase Function monitor (APF) located at Coihueco and Los Morados fire horizontal beams of light (330nm, 350nm and 390nm) across the field of view of all the telescopes in the Eye in order to measure the APF. The APF describes the rate at which aerosols scatter light in any given direction. This information is critical in correcting for multiple scattering during FD measurement. The weather stations at each Eye simply record the temperature, wind speed and direction, cloud height and precipitation rate. This information is used to decide if the weather is safe for operating the delicate FD telescopes [45].

3.4.4   Aerosol Monitoring and the Laser Facilities

The single largest time dependent source of error for the FD measurement technique is the aerosol content of the air in which the cosmic ray EAS evolves. The aerosols in the air do not change the nature of the particle interactions or their deposition of energy in the atmosphere, but the presence of particulate matter in the air can strongly attenuate the UV light the FD relies on for its observations. Because the FD uses a precise evaluation of the light profile of any given EAS in order to properly estimate its energy and composition, changes in the strength of this attenuation cause changes of equal magnitude in the measured shower parameters.

To properly account for this effect, the aerosol content of the air, personified by a quantity called the Vertical Aerosol Optical Depth (VAOD), needs to be actively measured throughout FD operation. This is difficult as the techniques for making this measurement that are considered the standard in atmospheric physics are poorly suited to the needs of the Observatory. They all either dump far too much light into the atmosphere to allow for use

during FD operation, or are not sensitive enough for the needs of the array. To solve these problems, the bi-static method was developed.
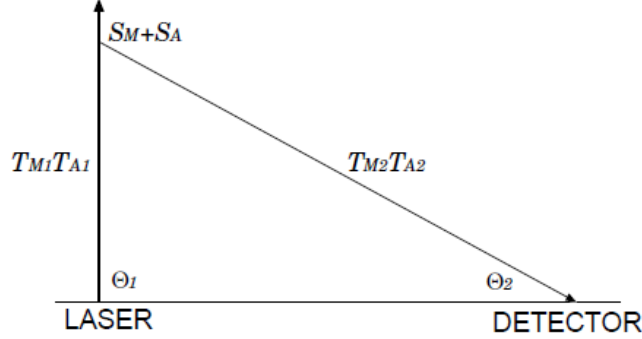
Figure 3.13: The Bi-static Aerosol Measurement Technique. A simple illustration of the Bi-static VAOD measurement technique [49]. T_{M1} and T_{M2} are the pre and post scattering molecular transmission coefficients, while T_{A1} and T_{A2} are the aerosol transmission coefficients before and after scattering. S_{M2} and S_{A2} are the scattering cross sections for molecular and areosols respectively. Θ_1 is the angle the laser makes with horizontal and Θ_2 is the observation angle of the incoming light.

Shown in Figure 3.13, the bi-static method, so called because of the separation of its emission and measurement instrumentation, uses a distant UV laser as a controlled light source and the FD itself as the measurement instrumentation. By observing the intensity of the laser light arriving at an Eye (N_{Obs}) at a given angle and then comparing it to the expected intensity had the laser light traveled that path through an atmosphere free of aerosols and was only attenuated by molecular scattering (N_{Mol}), the VAOD can be calculated as

$$\text{VAOD} = \frac{\sin\theta_1 \sin\theta_2}{\sin\theta_1 + \sin\theta_2} \ln\left(\frac{N_{Obs}}{N_{Mol}}\right). \tag{3.1}$$

The quantity N_{Mol} can either be taken from laser measurements made on an extremely clear night with no measurable aerosols, or calculated via simulation. The VAOD can then be used, assuming horizontal uniformity of aerosols and without accounting for multiple scattering, to calculate the UV light transmission (T_A) at any observation angle (θ_{Obs}) as

$$T_A = exp\left(\frac{-\text{VAOD}}{\sin\theta_{Obs}}\right). \tag{3.2}$$

This transmission is then used to correct the observed UV light profiles of cosmic ray air showers made at times near the VAOD measurement.

This technique is particularly well-suited for cosmic ray observatories for many reasons. First, the magnitude and nature of the light in each laser shot closely mirrors the actual UV emission of cosmic rays. This means the light is ideal for measurement with the FDs and is very telling of the atmosphere's effect on EAS profiles. Secondly, because each separate laser shot provides a strong measurement with a low signal to noise ratio, relatively few of these shots are needed to properly measure the VAOD. This means that this measurement only very slightly reduces the FD runtime ($<< 1\%$) and only for a few of its telescopes. Lastly, the signals used for the VAOD measurement themselves are extremely useful as a real world control sample for a wide range of FD centric studies as they are very well understood, very regular and permeate the entire FD data set [49] [50] .

Figure 3.14: The Central Raman Laser Facility. A photo of the CRLF shortly after its completion.

In order to make these bi-static measurements, the Pierre Auger Observatory is equipped with two high powered automated laser facilities, the Central Raman Laser Facility (CRLF) and the eXtreme Laser Facility (XLF). The CRLF shown in Figure 3.14 was completed in

May 2013 and can operate in either the bi-static FD calibration mode or can steer its laser to an internally housed Raman system capable of making an independent measurement of the VAOD. It was built by Lawrence Wiencke, Carlos Medina and myself to replace the aging Central Laser facility (CLF) which operated from 2004 until its replacement. Shown in Figure 3.15, the XLF was finished by our group in 2008, and served as the model for the CRLF. The construction, programming and upkeep of these facilities, as well as the processing of the data they collected, was a service responsibility of mine for both the Mines group and the Pierre Auger collaboration and added valuable instrumentation experience to my PhD. For a more detailed overview of the CRLF construction and my contributions to it, see Appendix: A.

Figure 3.15: The Central Raman Laser Facility. A photo of the CRLF shortly after its completion.

As seen in Figure 3.16, the laser facilities are separated by approximately 10 km and are placed symmetrically in the array, with each being roughly 30 km from three of the Eyes and 40 km from the fourth. Each laser facility consists of a frequency-tripled YAG laser emitting at a wavelength of 355nm capable of pulse energies up to $8mJ$. The specifications of these lasers were chosen to mimic the cosmic ray fluorescence tracks in the FD. These beams,

fired several hundred times during each night of FD activity, can either be shot vertically or steered to any trajectory. The primary purpose of each laser facility is measurement of the VAOD as explained above. However, these facilities usefulness for a wide range of applications, and, particularly for this work, as an FD control sample, can not be overstated.
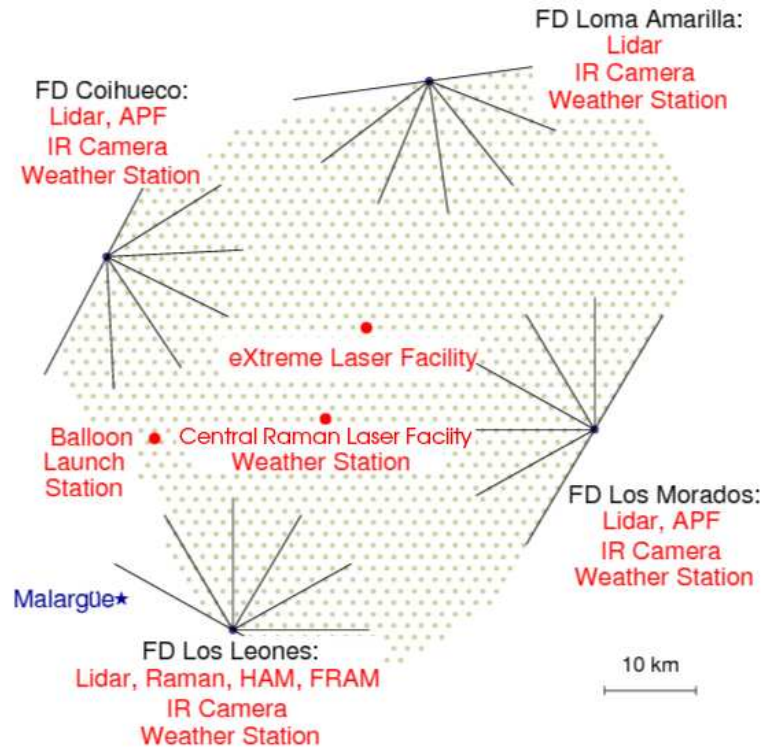
Figure 3.16: Map of Observatory Atmospheric Monitoring Instrumentation[45].

Each facility consists of a laser house situated near a sister tank used for hybrid shots and for measuring the SD/FD timing offset. When the CRLF is in FD calibration mode, the optical setup of the two facilities is very similar. As can be seen in Figure 3.17, the first piece of optics that the laser pulse enters is a 3x beam expander. This serves mainly to further collimate the beam to ensure it stays compact, but also widens the beam to lessen the intensity of light to protect the optics. The beam is then sent through a 1% pick-off optic, with a majority of the light passing through it to the firing optics. The picked off 1% is sent to the tank fiber channel. Here, another pick-off probe steers a small amount of the beam to an energy probe providing real time energy information for each laser pulse. The

46

rest of this beam is sent to the sister tank via a fiber optic cable.

The component of the beam that continues to the firing optics is either allowed to prop-
agate to the vertical beam channel or deflected to steered optics via an optical switch. The
on table vertical and steered optics are identical, each consisting of a depolarizing filter and
a steering mirror. The steering mirror is careful aligned to send the beam vertically with
respect to gravity with greater than 0.1° accuracy. Each beam then either passes to the roof
or is measured for calibration purposes.
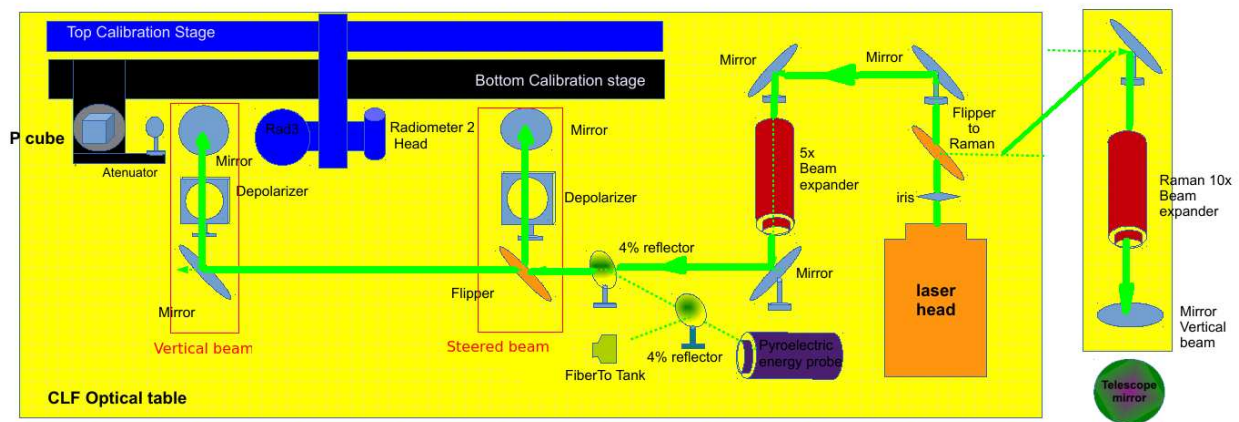
Figure 3.17: Optical Schematic of the Central Raman Laser Facility. This schematic also
accurately depicts the XLF facility if the Raman components are removed.

Both the CRLF and XLF are equipped with calibration systems capable of measuring
both the energy and polarization of the laser. The energy calibration system consists of
two probes, each with a different optimal energy range, mounted on computer controlled
precision movable stages. To sample the pulse energy, the probe with the proper energy
range for the current laser energy setting is moved in-line with the steered or vertical beam
path. The laser is then fired several times and the intensity of each shot, as well as the
average measured energy, is recorded. If the polarization of the laser is to be measured, a
linear beam splitter is moved into the beam path upstream of the probe. The beam splitter
either passes or diverts light based on its orientation as compared to the polarization of
the incoming light. To measure the polarization, the beam is fired through the splitter and

the intensity of the passed light is measured by the probe. The splitter is rotated in 45°
increments with a set of shots at each stop for a full rotation. If the measured energy is the
same for each position of the cube, then the beam is depolarized. Any divergence from this
can be analyzed to determine the extent and direction of the laser's polarization.

If the laser is to be fired into the sky for FD observation, it passes the calibration stages
and is sent to the roof. On the roof there are two hatches, one for the vertical beam and
one for the steered beam. The vertical hatch has no additional optics allowing the beam to
pass vertically into the sky. The steered beam, however, enters the steering head which is
capable of sending the beam to any above horizon trajectory. Both laser systems only fire
at specific GPS nanoseconds ($GPSns$) to eliminate real data contamination. The CLF fires
at the $250 \times 10^6 GPSns$ for laser only and $500 \times 10^6 GPSns$ for sister tank hybrid, while the
XLF fires at $350 \times 10^6 GPSns$ for laser only and $700 \times 10^6 GPSns$ for sister tank hybrid. The
firing time (in GPS second and nanosecond), energy, and, if steered, the firing trajectory are
all recorded for every fired shot in the Laser station data files referred to as the Autologs.
Thus, with the Autologs in hand, the data generated by FD observation of the laser can be
used as a control sample for a wide range of studies.

3.5 FD Reconstruction

Of central importance to this thesis is the reconstruction of an event's geometry and
timing from the signals recorded by the FD. In order to fully describe the geometry and
timing of any FD event, five separate shower parameters need to be calculated. These
parameters are:

$(\theta_{\hat{\mathbf{S}}}, \phi_{\hat{\mathbf{S}}})$ The polar variables that define the trajectory of the event's axis of evolution, called
the shower axis ($\hat{\mathbf{S}}$)).

(x_{core}, y_{core}) The x and y coordinates describing the location of the event's axis at an
altitude level with the observing Eye. In reality any point on the shower axis is sufficient
to constrain it spacially.

$\boldsymbol{T_0}$ The time the shower passed or would pass the point of closest approach to the Eye. This is chosen out of convenience, any point of time on the shower axis would do.

A simultaneous five parameter fit is often too difficult to be practical. In order to make the calculation of these five parameters easier, an FD reconstruction is traditionally done in two separate steps:

1. The determination of the plane in which the event had to occur using only the geometry of the FD pixels triggered during the event. This plane is called the shower detector plane (SDP).

2. The determination of the axis on which the core of shower traveled within the SDP, called the shower axis. This is mainly done using the angular and timing data from the FD pixels triggered during the event which was not used during the determination of the SDP.

By first constraining the event to the SDP, the geometric reconstruction is reduced from a 3D problem to a 2D problem. This in turn reduces the parameter count from five to three. After this plane is found there are three methods that can be used to constrain the shower axis. The lowest quality method is called a Monocular reconstruction and is the reconstruction of an event from only the measurements made by one Eye. The next level in terms of quality is Hybrid reconstruction which uses both the data from one eye and the measurements of the event made by the SD. The highest quality method is Stereo reconstruction, which uses the simultaneously observations made of one event by two or more separate Eyes.

3.5.1 The Reconstruction of the Shower Detector Plane

The SDP, illustrated in Figure 3.18(a), is simply the plane containing the shower axis and the center of the observing Eye. The reconstruction of SDP relies on the geometry of the triggered pixels in an event (shown in Figure 3.18(b)) and each pixel's total exposure.

(a) Illustration of the SDP   (b) SDP Projection on the Camera
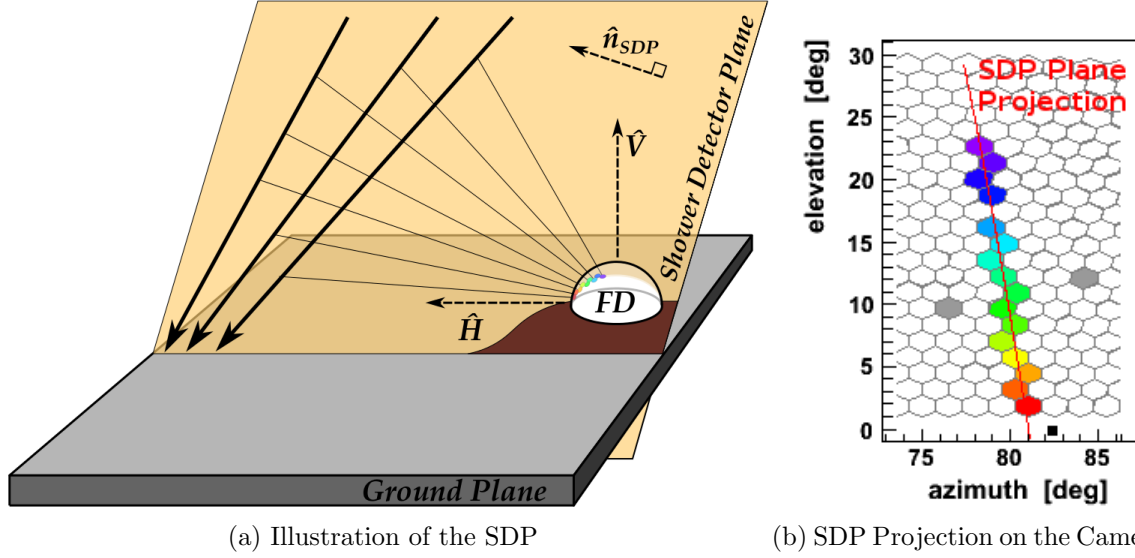
Figure 3.18: The Shower Detector Plane. The SDP constrains the event to a plane in which it had to occur using only the geometry of the pixels triggered by the event. Though constrained, there are many possible event geometries in the SDP (as shown by the multiple axes in (a).

The SDP reconstruction, however, does not use every triggered pixel. Only pixels that pass a filter meant to clean the pixel traces of any randomly triggered pixels are considered for the reconstruction. In order to be used, each selected pixel, called a SDP pixel, must meet the following two requirements:

1. It must be within 4 pixels of another SDP pixel and the centroid time of its ADC trace must lay within $6\mu s$ of another SDP pixel's centroid time.

2. The SDP pixel must have a time ordering that correlates with a physically realizable event.

Once these requirements are met, a plane is fit to the SDP pixels' pointing directions ($\hat{\mathbf{r}}_i$). The geometry of the plane is specified by its normal vector ($\hat{\mathbf{n}}_{SDP}$). Since any plane can have two normal vectors, $\hat{\mathbf{n}}_{SDP}$ is defined as the normal vector that when crossed with the vector pointing vertically from the observing eye ($\hat{\mathbf{V}}$), results in the horizontal vector ($\hat{\mathbf{H}}$) pointing from the eye to the shower core. This means that the SDP will be identical for

events that propagate downward like a shower event or upward like a laser event.

The event SDP corresponds to the one plane whose $\hat{\mathbf{n}}_{SDP}$ is most perpendicular to all of the SDP pixels' $\hat{\mathbf{r}}_i$ vectors as weighted by their total exposure a_i. This plane is found by minimizing the value χ^2_{SDP} defined as

$$\chi^2_{SDP} = \sum_i \left(\hat{\mathbf{n}}_{SDP} \cdot \hat{\mathbf{r}}_i\right) a_i, \tag{3.3}$$

where i iterates through the SDP pixels. To find the plane, the normal vector $\hat{\mathbf{n}}_{SDP}$ is tweaked until the minimum value of χ^2_{SDP} is found. This method of fitting, from here on referred to as a χ^2 minimization by collaboration tradition, is in reality a weighted least-square fit. This general method of fitting the observatory data to models is used throughout $\overline{\text{Off}}\underline{\text{line}}$ and this research. Once the χ^2 fit is complete, for a track length of 30° the resulting SDP plane has been shown to be very accurate, with a 0.08° uncertainty in the position of SDP in the Eye and a 0.5° uncertainty in its angle[3] [51].

3.5.2 Monocular Axis Reconstruction

As said earlier, by constraining the event to the SDP, the geometric reconstruction is essentially reduced from a 3D problem to a 2D problem. This reduces the number of parameters needed to fully describe the event from five to three. T_0 is still needed, however the geometry, as illustrated in Figure 3.19, can now be fully described by:

Rp The distance to the point of closest approach to the Eye. The vector between the Eye and this point is always perpendicular to the shower axis.

χ_0 The angle in the SDP between the shower axis and the vector $\hat{\mathbf{H}}$ which points horizontally out from the Eye.

The process of finding these three parameters is referred to as the axis reconstruction. If an event is seen by at least one FD and passes the TLT trigger, its axis can be reconstructed

---

[3]These uncertainties are for an ideal case. In reality they vary with the nature of the pixel traces. The error in the SDP is maximized when the event has a 30° inclination in the Eye. This is because a 30° inclination results in a single line of pixels being triggered, which in turn maximizes both uncertainties.

monocularly. In essence, a monocular reconstruction is a reconstruction performed with only the data provided by the cameras in one Eye.
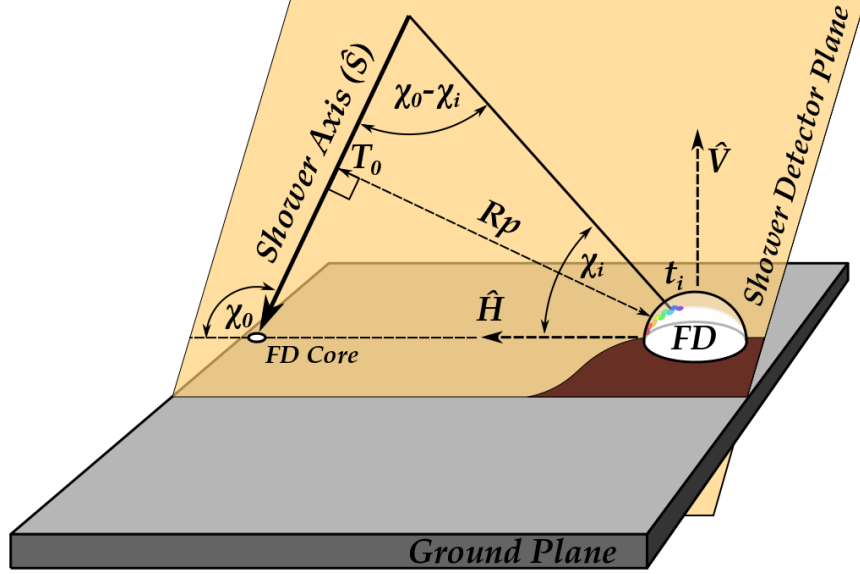
Figure 3.19: The Geometry of a Monocular Event.

The first step of a monocular fit is to build a model of the event's geometry in order to make a prediction of what the event's timing and signal will look like in the Eye. Using the parameters and geometry shown in Figure 3.19 the expected time at the camera for the ith pixel that observed the event (t_i^{exp}) can be expressed as

$$t_i^{exp} = T_0 + \frac{Rp}{c} tan\left(\frac{\chi_0 - \chi_i}{2}\right). \tag{3.4}$$

The variable χ_i is measured from $\hat{\mathbf{H}}$ and is just the ith pixel's pointing direction, r_i, projected into the SDP plane. The constant c is of course the speed of light.

As shown in Figure 3.20, (3.4) is fit to the data recorded by the observing Eye via a χ^2 minimization. First, initial best guess values for Rp, χ_0 and T_0 are plugged into (3.4) along with each pixel's χ_i to get a t_i^{exp} value. The difference between each pixel's t_i^{exp} and the centroid time of that pixel's ADC trace (t_i) is then squared and weighted by the square of the uncertainty of pixel's centroid time t_i^{err}. The weighted differences for all the pixels are
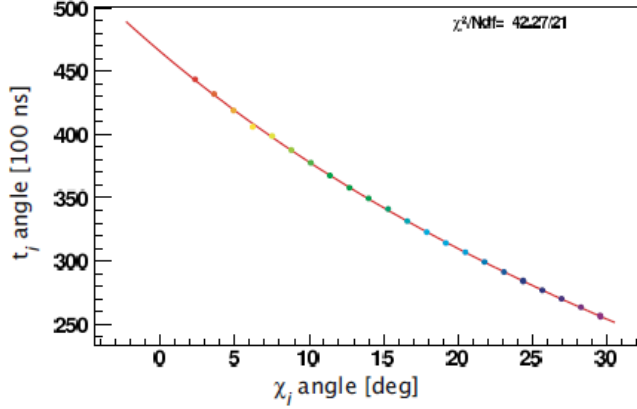
Figure 3.20: Monocular χ^2 Fit to Laser Data.

then summed resulting in the FD only χ^2 equation,

$$\chi^2_{FD} = \sum_i \frac{(t_i - t_i^{exp})^2}{(t_i^{err})^2}. \qquad (3.5)$$

To find the shower axis, the values Rp, χ_0 and T_0 are tweaked following the gradient of the parameter space and the above process is repeated until the shower parameters that minimize χ^2_{FD} are found.

The χ^2 method is powerful, but can only be as accurate as the data you provide it and as correct as the model you are fitting. If (3.4) correctly represents the system, the values of Rp, χ_0 and T_0 that minimize the χ^2_{FD} value should represent the real parameters of the observed event [52]. However, because of the relatively large number of fitted parameters compared to the small set of available data, monocular reconstructions suffer from a depth problem not unlike the issue you encounter when observing things with just one eye. Overcoming this depth problem relies on the event having a very strong curvature in it timing data. This means monocular reconstructions are fairly inaccurate in all but a few geometries and extremely susceptible to event conditions.

3.5.3 Hybrid Reconstruction

As stated earlier, one of the most important aspects of the Pierre Auger Observatory is that it is a hybrid detector. This means it is capable of measuring one event with both

the FD and SD simultaneously. These hybrid events are useful beyond their capacity for calibration of the SD. By taking advantage of the spacial and timing constraints that are added to the event data through the signal in the SD, the reconstruction of the location of the shower can be decoupled from its trajectory. Because of this, a hybrid reconstruction avoids the pitfalls that plague a monocular reconstruction. The net result, as seen in Figure 3.21, is a far more accurate and robust geometric reconstruction than what monocular can alone provide.
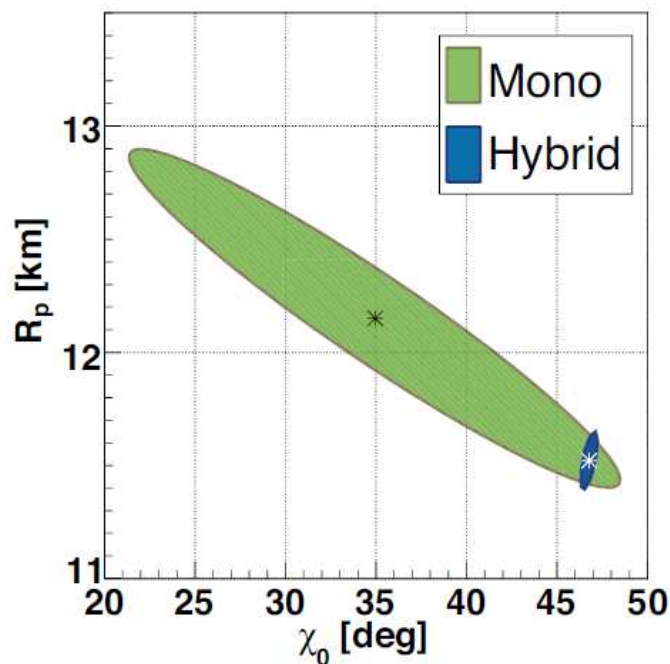
Figure 3.21: Hybrid Accuracy Improvement Over Monocular. The solution errors (1σ) for an event's in SDP geometry from both the Monocular (green) and Hybrid (blue) reconstructions. The star in each ellipse represents the parameter values that minimize the χ^2 fit for the event's shower axis. The event was simulated with an Rp of 11.5 km and a χ_0 of 47° [53].

A hybrid reconstruction is simply the monocular reconstruction with the added constraint of the location and signal start time of the SD tank with the highest signal- the hot tank. This simple addition of an independent detection considerably improves the geometric, as compared to monocular only. The new information is incorporated into the process by adding a term to the χ^2 fit that aims to ensure that the reconstructed geometry agrees with

both the FD pixel data and the signal in the SD. The additional term, χ^2_{SD}, like χ^{FD}, is the squared comparison of an expected time and the measured time weighted by the error in the measurement. Specifically χ^2_{SD} takes the form

$$\chi^2_{SD} = \frac{(t_{SD} - t_{SD}^{exp})^2}{\left(t_{SD/FD}^{err}\right)^2},\tag{3.6}$$

where t_{SD} is the signal start time in the hot tank, t_{SD}^{exp} is the time the shower should reach the tank as predicted by our geometric fit, and $t_{SD/FD}^{err}$ is the expected error in synchronization of the FD and SD. $t_{SD/FD}^{err}$ is used because the error in the FD/SD synchronization is expected to be much larger than the uncertainty in the SD signal start time. Adding (3.6) to (3.5) results in a hybrid χ^2 function χ^2_{hy} given by

$$\chi^2_{hy} = \chi^2_{SD} + \chi^2_{FD} = \frac{(t_{SD} - t_{SD}^{exp})^2}{\left(t_{SD/FD}^{err}\right)^2} + \sum_i \frac{(t_i - t_i^{exp})^2}{(t_i^{err})^2}.\tag{3.7}$$

Figure 3.22: The Geometry of a Hybrid Event.

To actually improve the reconstruction accuracy and stability, t_{SD}^{exp} needs to be calculated using only our geometric parameters, Rp, χ_0 and T_0, the SDP and the known location of the hot tank and Eyes. Figure 3.22 illustrates how this is done. First, two vectors are defined:

$\overrightarrow{r}_{SD}$, the vector that points from the eye to the hot tank, and $\overrightarrow{r}_{axis}$, the vector pointing from the SD Core to the hot tank. The next step is to calculate the time that the shower will reach the FD core (t_{coreFD}), represented by the green line in Figure 3.22. By starting at the point of closest approach to the Eye and the time at that point, T_0, t_{coreFD} is defined as

$$t_{coreFD} = T_0 + \frac{Rp}{c} \cot(\pi - \chi_0). \tag{3.8}$$

From here, the time that it will take the shower to move from the FD core to the SD core (t_{coreSD}), represented by the length of purple line in Figure 3.22 over c, or

$$t_{coreSD} = -\frac{\overrightarrow{r}_{SD} \cdot \hat{\mathbf{S}}}{c}. \tag{3.9}$$

t_{coreSD} is negative because $\hat{\mathbf{S}}$ always points up by Pierre Auger Collaboration convention. The last component that needs to be accounted for is the time it will take the curved shower front to reach the hot tank (t_{front}), represented in dark blue in Figure 3.22. Assuming a general two parameter description of the wavefront, t_{front} can be described by

$$t_{front} = \frac{a_1|\overrightarrow{r}_{axis}| + a_2|\overrightarrow{r}_{axis}|^2}{c}, \tag{3.10}$$

where a_1 and a_2 are theoretical constants that describe the shape of the shower front. By summing together these terms, the expected time at the t_{SD}^{exp} is predicted by

$$t_{SD}^{exp} = T_0 + \frac{Rp}{c} \cot(\pi - \chi_0) - \frac{\overrightarrow{r}_{SD} \cdot \hat{\mathbf{S}}}{c} + \frac{a_1|\overrightarrow{r}_{axis}| + a_2|\overrightarrow{r}_{axis}|^2}{c}. \tag{3.11}$$

Like the monocular case, to find the shower axis, the values Rp, χ_0 and T_0 are tweaked until the shower parameters that minimize χ_{hy}^2 are found.

Because a hybrid reconstruction only uses the location and signal timing of the station with the largest signal (the hot tank). This means that all hybrid events, regardless of the strength of the SD response, are treated the same by the hybrid reconstruction, and equally improve upon monocular reconstruction. All hybrid events however are not equal in quality and usefulness. There are in fact two levels of hybrid events:

Simple Hybrid A simple hybrid event refers to any FD event with at least one station that passes both the SD T2 and FD T3 triggers.

Golden Hybrid A golden hybrid event are a subclassifications of simple hybrid. A golden hybrid event is any FD event with a simultaneous SD event that passes at minimum the SD T4 and FD T3 triggers.

Though all hybrid events are reconstructed identically, because golden hybrid events fully trigger both the SD and FD, their geometry and energy can be independently reconstructed with both the FD and SD. This property of golden hybrid events makes them particularly useful to the Observatory in several ways:

- The highly accurate geometric hybrid reconstruction can be used to crosscheck the SD's geometric and angular resolution; a step which is crucial for arrival direction anisotropy studies.

- As explained in Section 3.3, because the FD is able to make a nearly model independent measurement of the event's energy, in golden hybrid events the energy reconstruction of the FD can be calibrate the SD's energy reconstruction.

- Because the FD is sensitive to X_{max} and therefore primary composition, golden hybrid events that have X_{max} in the field of view of their cameras can be used to search for composition sensitive indicators in the SD.

3.5.4 Stereo Axis Reconstruction

Very rarely, one event is observed by two or more distantly separated Eyes simultaneously. By using the information gathered by both Eyes to fit a single axis, the quality of the geometric reconstruction can be improved greatly. Unlike monocular events, the SDP isn't fit separately, instead both the pixel geometry and timing are used from every Eye to find the shower axis. This results in the stereo reconstruction χ^2 fit equation χ^2_{stereo} taking the

57

form

$$\chi^2_{Stereo} = \chi^2_t + 4\chi^2_{geo}. \tag{3.12}$$

χ^2_t is the term that focuses on making sure the reconstructed axis agrees with each camera's pixel timing profile. χ^2_{geo} minimizes against the pixel geometry and is weighted by 4 to reflect the fact that the pixel geometry is much more reliable than the pixel timing. The timing term, χ^2_t, is the same as the monocular χ^2_{fl} except with the added complexity of summing over all the Eyes and therefore takes the form

$$\chi^2_t = \sum_{Eyes} \sum_i \left(\frac{(T_i^{Eye} - Texp_i^{Eye})^2}{(Terr_i^{Eye})^2} \right), \tag{3.13}$$

where T_i^{Eye}, $Texp_i^{Eye}$ and $Terr_i^{Eye}$ are the same as the terms in (3.5), but with the additional Eye index. The geometric term, χ^2_{geo} is functionally very similar to χ^2_{SDP}, however, as the shower axis is expected to lay at different distances to each Eye, therefore, the pixel charge a_i is no longer a reliable weighting term. If a_i were still used, a poorly measured pixel at a close distance could be given more weight than a well-measured pixel at far distance messing up the fit. Instead, the angular uncertainty in the pointing direction of each pixel ($\hat{\mathbf{r}}_i err$), which for the Pierre Auger Observatory FD is a constant $0.35°$, is used. χ^2 equations must be dimensionless so the numerator of χ^2_{geo} must also be an angle. Therefore, the angular difference between between a_i and $\hat{\mathbf{n}}_{SDP}$ is used resulting in χ^2_{geo} equation of the form

$$\chi^2_{geo} = \sum_{Eyes} \sum_i \left(\frac{(\pi/2 - \arccos{(\hat{\mathbf{r}}_i^{Eye} \bullet \hat{\mathbf{n}}_{SDP}^{Eye}))^2}}{(\hat{\mathbf{r}}_i^{Eye} err)^2} \right), \tag{3.14}$$

where $\hat{\mathbf{r}}_i^{Eye}$ and $\hat{\mathbf{n}}_{SDP}^{Eye}$ are the same as the terms in (3.3), but with the additional Eye index.

Instead of minimizing against Rp, χ_0 and T_0 for later conversion to the shower parameters $[\theta_{\hat{\mathbf{S}}}, \phi_{\hat{\mathbf{S}}}, x_{core}, y_{core}$ and $T_0]$ like a monocular reconstruction, the stereo reconstruction directly minimizes against these parameters with two small changes. As seen in Figure 3.23, the core location (x_{core}, y_{core}) is replaced by (N_{1400}, E_{1400}) which define location of the shower core at an elevation of 1400m in UTM coordinates (Northing and Easting). The core is now defined in UTM because a universal coordinate system is needed to relate the Eyes to each
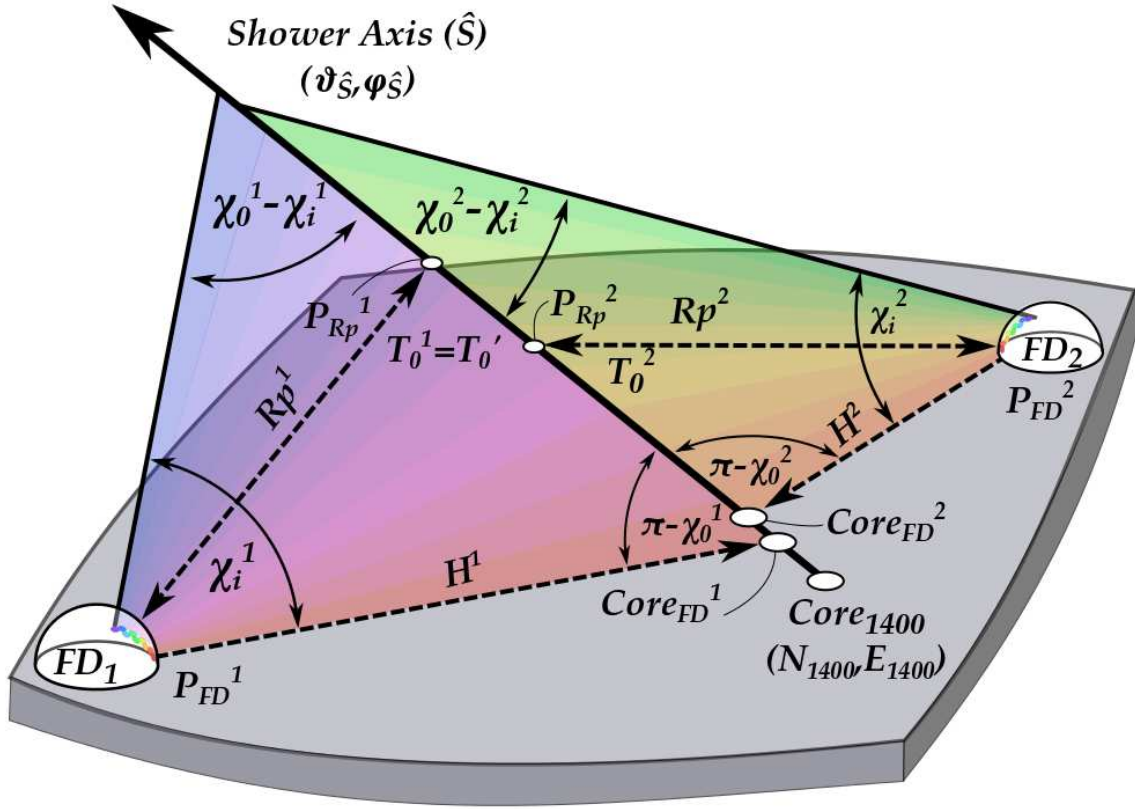
Figure 3.23: The Geometry of the Multi-Eye Stereo Method: FD_1 is the lowest indexed observing Eye so it is regarded as Eye'. The SDP of each Eye is represented by the colored portion. The white dots represent important geometric points.

other. An elevation of 1400m is used because the average elevation of the SD is 1400m above sea level. Also, T_0 is replaced by T_0', the time of closest approach for the lowest indexed observing Eye ($LL = 1$, $LM = 2$, $LA = 3$ and $CO = 4$), here on denoted as Eye'. This again is to accommodate the fact that there are now multiple Eyes, each of which would have a different T_0. Because the observations of all of the Eyes are from the same event, there is only one value for each of these parameters per shower. Using the geometry shown in Figure 3.23, $Texp_i^{Eye}$ can be calculated as

$$Texp_i^{Eye} = T_0^{Eye} + \frac{Rp^{Eye}}{c} tan\left(\frac{\chi_0^{Eye} - \chi_i^{Eye}}{2}\right), \tag{3.15}$$

59

where Rp^{Eye}, χ_0^{Eye} and T_0^{Eye} are all calculated for each Eye using the shower parameters ($\theta_{\hat{\mathbf{S}}}$, $\phi_{\hat{\mathbf{S}}}$, N_{1400}, E_{1400} and T_0'). χ_0^{Eye} is calculated as

$$\chi_0^{Eye} = \arccos\left(\frac{\overrightarrow{H}^{Eye} \cdot \hat{\mathbf{S}}}{|\overrightarrow{H}^{Eye}|}\right) \tag{3.16}$$

where $\overrightarrow{H}^{Eye}$ is

$$\overrightarrow{H}^{Eye} = FD_{core}^{Eye} - P_{FD}^{Eye}, \tag{3.17}$$

where P_{FD}^{Eye} defined as $(N_{FD}^{Eye}, E_{FD}^{Eye}, Z_{FD}^{Eye})$ is the location of each Eye in UTM coordinates and FD_{core}^{Eye} is the location of the shower core at the same elevation as the Eye in UTM coordinates. FD_{core}^{Eye} consists of the components $(X_{core}^{Eye}, Y_{core}^{Eye}, Z_{core}^{Eye})$ which are found via,

$$
\begin{align}
X_{core}^{Eye} &= E_{1400} - \left((1400 - Z_{FD}^{Eye}) * \tan\phi_{\hat{\mathbf{S}}} \sin\theta_{\hat{\mathbf{S}}}\right), \tag{3.18} \\
Y_{core}^{Eye} &= N_{1400} - \left((1400 - Z_{FD}^{Eye}) * \tan\phi_{\hat{\mathbf{S}}} \cos\theta_{\hat{\mathbf{S}}}\right) \text{ and} \tag{3.19} \\
Z_{core}^{Eye} &= Z_{FD}^{Eye}. \tag{3.20}
\end{align}
$$

Rp^{Eye} is calculated as

$$Rp^{Eye} = |\overrightarrow{H}^{Eye}| \sin(\pi - \chi_0^{Eye}). \tag{3.21}$$

While T_0^{Eye} is calculated as

$$T_0^{Eye} = T_0' + \frac{P_{Rp}^{Eye} - (P_{Rp}')}{c}, \tag{3.22}$$

where P_{Rp}' is the point of closest approach for the lowest indexed observing eye and P_{Rp}^{Eye}, the point of closest approach for the current observing eye. Both P_{Rp}' and P_{Rp}^{Eye} are calculated via

$$Point_{Rp}^{Eye} = P_{FD}^{Eye} + Rp^{Eye}(\hat{\mathbf{n}}_{SDP}^{Eye} \times \hat{\mathbf{S}}), \tag{3.23}$$

using $Eye = Eye'$ for the P_{Rp}' value. Finally, $\hat{\mathbf{n}}_{SDP}^{Eye}$ is calculated as

$$\hat{\mathbf{n}}_{SDP}^{Eye} = \hat{\mathbf{S}} \times \left(\frac{\overrightarrow{H}^{Eye}}{|\overrightarrow{H}^{Eye}|}\right), \tag{3.24}$$

again using $Eye = Eye'$ when appropriate..

The values for $\theta_{\hat{\mathbf{S}}}$, $\phi_{\hat{\mathbf{S}}}$, N_{1400}, E_{1400} and T_0' are then adjusted until a minimum value for χ^2_{Stereo} is found. These values that minimize the χ^2_{Stereo} function now correspond to the most probable shower geometry and timing for the observed event. Because in stereo both the pixel geometry and timing profile independently and fully constrain the geometry of the event, stereo reconstructions have the highest accuracy of any event reconstruction available to the Pierre Auger Observatory.

3.6   The $\overline{\text{Off}\underline{\text{line}}}$ Framework

In large scale experiments, the job of coordinating thousands of detector responses, accounting for hundreds of time dependent variables and translating them all into useful and interesting information about phenomena is always difficult. Given the complexity of keeping track of all this data, mistakes and therefore erroneous findings are common. Furthermore, if analyses aren't standardized across a collaboration, it is difficult to talk about the results of an experiment rather than just those analyses. Unfortunately, attempts to standardize an analysis often fail to provide the flexibility and customization necessary to facilitate rather than inhibit science. To avoid these pitfalls and to optimize productivity, the Pierre Auger Collaboration invested in building a rigorous, robust and fully customizable cosmic ray analysis package, $\overline{\text{Off}\underline{\text{line}}}$.

$\overline{\text{Off}\underline{\text{line}}}$ is simply a C++ framework built around open-source tool-sets for the purpose of facilitating the reconstruction or simulation of cosmic ray events and other data at the Pierre Auger Observatory. As is shown in Figure 3.24, there are three main components to $\overline{\text{Off}\underline{\text{line}}}$. There are the analysis modules, event data structure and detector description.

Analysis Modules

Analysis modules are the building blocks of an $\overline{\text{Off}\underline{\text{line}}}$ analysis. A module is a subprogram that deals with a specific step in the overall cosmic ray analysis. Each module is dedicated to a specific analysis task and is written and administered by an Auger collaborator with a high level of expertise in that facet of the analysis. Each module
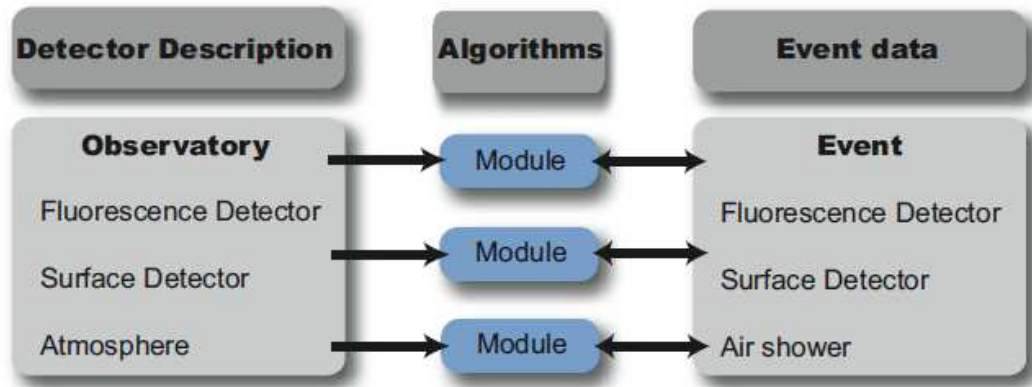
Figure 3.24: The $\overline{\text{Offline}}$ Framework Structure. The core of the analysis, whether it be a simulation or data reconstruction is handled by interchangeable and compartmentalized algorithms called modules. Each module simply reads data from variables in Event Data structure and/or detector description, performs its analysis and then updates the information in the Event Data structure for the next module [54].

only interacts with the detector description and event data structure. This isolation ensures each module is compatible with every other and that changes or improvements to one module do not necessitate changes in others. To build a full $\overline{\text{Offline}}$ analysis, a user only needs to pick which modules are to be used and in what order, called a Module Sequence, and then specify the settings of each module in the user friendly XML cards associated with each module or in a single file called the Bootstrap. The $\overline{\text{Offline}}$ program can then be compiled via a makefile and is ready to analyze the data pointed to in the EventFileReader. This flexible design assures that the analysis can be quickly tailored to any collaborator's needs with little or no need for the user to directly interact with code. A set of standard modules and module sequences are built to deal with event simulation, reconstruction and analysis. This set of standard programs is called Observer and is often used unaltered by most members of the Pierre Auger Collaboration for their cosmic ray studies.

Event Data Structure

The event data is a data structure containing a variable for each quantity that $\overline{\text{Off}}$

line needs or is capable of filling. It has a field for everything ranging from raw detector response, simulation parameters and atmospheric conditions, to reconstructed shower observables like energy, X_{max} and event geometry. By separating the data storage from the data processing and preallocating all the variables that could be used by the modules, the job of making sure each module is interchangeable and can still work as intended is made much simpler. In the case of real showers, the event data starts with just the detector response and is then filled with reconstructed data by the proper modules. For simulation, the first module used is always an event builder, which makes the event data class. A detector response is then fabricated and placed in the structure. Finally, this the event data structure contains everything in it that a real shower's datafile would contain, along with the information of the simulation parameters used to make that data.

Detector Description

The detector description is pretty self explanatory. It is simply a structure that ties together all the various data sources needed to describe the layout and nature of the detector, conditions and environment at the Observatory and the functionality of the instrumentation at the time an event is measured. This description can be real information from the Observatory, simulated ideal or extreme conditions or a combination of both. Handling the detector information in this way is very powerful. By simply changing the detector description and tweaking the modules, entirely different observatories can be simulated and studied.

In addition to the overarching structure and framework, $\overline{\text{Off}}\underline{\underline{\text{line}}}$ also provides a robust tool-set which greatly simplifies the process of analyzing Observatory data and simulation studies. Among the more useful tools included are:

- The MySQL database handlers: As stated earlier, properly accounting for the time dependent conditions of the atmosphere and the minute by minute status of each of the

more than 10,000 separate pieces of instrumentation at the array is vitally important to correctly interpreting any data. To facilitate this, $\overline{\text{Off}\underline{\text{line}}}$ has included several high and low level MySQL database handlers. These are extremely useful as they streamline the process of querying and pulling data from the atmospheric and calibration databases. Without these handlers, accessing this data would be a very difficult, error prone and time consuming process.

- The Geometry packages: In the process of making calculations at the array it is almost always necessary to carry out complex geometric calculations in several different coordinate systems. Because of the size of the array, and the scale of the phenomena it seeks to observe, this is made extremely difficult. Describing phenomena across the array and calculating its expected trajectory and timing in distantly separated instrumentation demands that factors like the exact curvature of the Earth and its rotation be accounted for precisely. To deal with this, $\overline{\text{Off}\underline{\text{line}}}$ includes a novel geometry package which automatically accounts for these effects simply through coordinate system definition and reference frame tracking.

- The Visualization and Plotting packages: It is often difficult to interpret results simply through distributions of measured variables and their errors. To address this, $\overline{\text{Off}}$ $\underline{\text{line}}$ includes a suite of visualization and plotting packages to help present measurements and reconstructions in a meaningful way.

$\overline{\text{Off}\underline{\text{line}}}$ also includes the full tool-set available through Cern's ROOT analysis software [55]. This facilitates Monte-Carlo simulation, data storage, fitting and interpretation and the importation and exportation of results from external analysis [54].

CHAPTER 4

EXOTIC SLOW EVENTS AND CANDIDATE PHENOMENA

The detectors of the Pierre Auger Observatory become fully efficient around a primary energy of $\approx 10^{18}eV$. This means that in order for the FD or SD to reliably record any event, that event must deposit at least as much energy in the atmosphere as a $1EeV$ cosmic ray shower. Currently, except for the as-of-yet unobserved Strangelet, under the Standard Model (SM), cosmic ray primary rest masses are, at maximum, restricted to a couple hundred GeV/c^2. These two facts combined lead naturally to the expectation that all cosmic ray events recorded by the Pierre Auger Observatory will be caused by primary particles traveling very close to the speed of light. This is simply justified through relativistic imperative.

Assuming a cosmic ray of the minimum observable energy of $E_{min} = 10^{18}eV$ with a mass of $200GeV/c^2$, which is well above the expected mass of any cosmic ray candidate, relativity states that

$$
\begin{aligned}
E_{total} &= \gamma \times m \times c^2, \text{ so for Auger} & (4.1) \\
E_{min} = 10^{18}eV &\leq \gamma \times 200GeV/c^2 \times c^2 \text{ and therefore} & (4.2) \\
5 \times 10^6 &\leq \gamma. & (4.3)
\end{aligned}
$$

So, at the minimum detectable energy and using a mass far beyond the expected mass of a cosmic ray primary, the Lorentz factor of a Standard Model cosmic ray detected at the Observatory must be at least 5×10^6. A Lorentz factor of 5×10^6 corresponds to a minimum velocity of about 99.9999999999995% of c. This velocity is greater than the speed of light in air and far too close to c to matter in any analysis done at the Pierre Auger Observatory [56].

Extremely massive macroscopic conglomerate objects like Micrometeorites could circumvent this issue as objects with a high mass can have large kinetic energy at low speeds. Micrometeorites, in particular, can cause events that are bright enough to be observed by

the FD. However, due to their low density and high surface area, the luminous portion of their descent to the earth's surface is constrained to altitudes of 80 km or higher [57]. HEAT is the only Eye that could realistically see these events. However, even so, in order to pass the SLT of the FD the event would have to traverse a minimum 5.7° (Sections 3.2 and 5) in one of HEAT's cameras in a 20 μs time window. Assuming the very generous parameters[4] of 80 km for the minimum distance to the event and a trajectory that is perpendicular to the HEAT in its field of view, then the minimum event velocity required is

$$V_{min} = \frac{80km \cdot Tan(5.7°)}{20\mu s} \approx 4 \times 10^8 m/s, \tag{4.4}$$

or $\sim 133\%$ of the speed of light, clearly rendering observation unlikely.

Lastly, a large slow moving exotic primary could cause a measurable EAS through energetic decay or by interacting strongly and breaking up, however, the created shower will still propagate at speeds very close to the speed of light. This is simply because though the primary may have traveled slowly, the particles created in the decay need to be very energetic in order to cause an observable particle cascade. This, in truth, applies to any EAS caused by any primary. Causing an observable event through the production of an EAS demands a high kinetic energy for every particle participating in the shower and therefore an EAS will never be seen to evolve slowly. This means for a slow event to trigger the FD it must generate light through a mechanism other than those available to the particle cascades in an EAS.

These arguments forbid any already observed cosmic ray primary within the Standard Model from being the source of a measurable subluminal shower. This simple fact forms the underlying motivation for a velocity based search in the Pierre Auger Observatory's cosmic ray data set. Essentially, because all known or expected cosmic ray primaries can be neglected outright, any accurately detected and reconstructed subluminal cosmic ray event would strongly point toward new physics. This begs the question: What qualities must an

---

[4]80 km is much smaller than the actual minimum distance to the event as HEAT's field of view does not reach vertical but only 60° above the horizon. A perpendicular trajectory maximizes the angular velocity across the camera.

object possess to create a slow evolving event to which the Pierre Auger Observatory's FD would be sensitive to?

4.1 Candidate Particle Characteristics

In order for a theoretical object or particle to be considered a candidate for a velocity based search in the FD data, it must meet the following criteria:

1. It must either deposit significant amounts of energy in the atmosphere without relying on it's kinetic energy to drive the creation of a hadronic particle cascade, emit a large amount of its internal rest mass energy as it traverses the atmosphere through slow decay, or somehow derive significant amounts of energy from the atmosphere itself.

   This is absolutely necessary as otherwise there is no means to create UV light needed for FD observation.

2. It must have an interaction mechanism that preserves the structure of the particle and its ability to interact throughout the event.

   This is required as the exotic primary must interact multiple times in order to have an event that develops at net subluminal velocity. This is mainly due to the fact that all secondary particles and their offspring will likely travel at speeds very near to the speed of light. This, in turn, means that if the subluminal primary is destroyed or becomes inert early in the event, the secondary particles will only be able to create a particle shower that will evolve indistinguishably close to the speed of light.

3. It must interact in a way that either directly emits photons or diverts a significant portion of the energy released in the event into the electromagnetic cascade.

   Only the FD is able to directly observe the event's evolution velocity, meaning that without direct photonic emission or an abundant electromagnetic shower producing UV light, the FD will be blind to the event. The larger the percentage being directed

into the electromagnetic cascade the better, as that means more of the energy released in the shower will be detectable by the FD, increasing the chances of observation.

4. It must be able to interact at a high rate as it traverses the atmosphere.

   The interactions caused by the primary need to dominate the energy release in the shower as the FD will only be able to measure the net velocity of the shower. This is again because the secondary particles and their offspring will travel at speeds very close to the speed of light, which in turn means that unless the exotic primary causes the bulk of the interactions in the shower, the event's measured evolution velocity will be much closer to the speed of light then the speed of the exotic primary.

5. It must have a cross section large enough to create an event with brightness at least equal to that of a $10^{18}eV$ SM comic ray.

   Without satisfying this requirement, it is likely that the event will not be recorded by the FD.

6. It must have a plausible mechanism for acceleration to observable velocities.

   Because of the maximum event duration limit on FD observations, candidate particles must be accelerated to at least a few % of the speed of light in order to have a chance of being measured by the FD. This rules out the extremely heavy side of this spectrum as there is no expectation of these objects reaching these speeds.

7. Finally, there must be a reasonable theoretical expectation of a meaningful local flux.

   Simply, if there is no reason to expect a measurable flux on the earth then there is little reason to expect to see it.

These requirements severely reduce both the available interaction mechanisms and the list of possible particles, but literature does present some viable candidates. These include

high mass Strangelets[58][5], macroscopic dark matter [61][6], Magnetic Monopoles and finally Q-Balls [62]. The theory supporting slow, detectable Strangelets appeared too late for full consideration here. Macroscopic dark matter does not have a clear acceleration mechanism to reach the velocities necessary to clear the FD T2 trigger. Monopoles were originally considered as a strong candidate, however, the specific types necessary to trigger a detectable slow event are quite speculative and relatively unsupported in literature. For these reasons they are no longer considered a serious candidate, but are still covered in Appendix B. Q-Balls, however, have been established for some time and well fit all the criteria listed above and are therefore given a general overview below.

4.1.1 Q-Balls

Though the LHC has begun to significantly constrain the available versions of the minimally super-symmetric standard model (MSSM), it will not be able to rule definitively on it due to the mass scale limitations of its accelerators and the diversity of super-symmetric (SUSY) theories [63]. It is therefore important to attempt to search for phenomena predicted by super-symmetry in order to limit regimes that are unavailable to current accelerators. To this end, one of the most promising candidates for observation within the cosmic ray spectrum is the Q-Ball.

Super-symmetric extensions of the standard model, especially MSSM, predict the existence of a non-topological soliton with an unconstrained baryon number, which has been dubbed a Q-Ball [64], [65]. "(A) Q-ball is a coherent state of a complex scalar field, whose

---

[5]Strangelets are well supported by theory and expected from the current understanding of QCD, however their ability to cause low velocity showers as described in [58] is difficult to judge as solid energy deposit models are not provided. Inferring from [59] and [60] the deposit mechanism would likely be a combination of fusion, fission and friction effects. Strangelets are a viable candidate, but [58] appeared too late for in depth treatment here.

[6]Macroscopic dark matter is a catch-all for heavy and, therefore, low number density dark matter candidates that would likely deposit energy through a friction mechanism. Unfortunately, many macroscopic dark matter candidates lack a strong acceleration mechanism and are expected to propagate at galactic velocities ($\sim 10^{-3}c$). This largely rules out this thesis as a means for search as these events will be vetoed by the FD T2 trigger. However, one could envision some possibly reaching higher velocities and therefore appearing in the Observatory's data. Alternatively, these could be looked for, using the FD, by monitoring the count rate of each PMT string of each telescope before T2 veto to look for events that 'march' across the Eye.

existence and stability are due to the conservation of some global U(1) quantum number"[66], and they should become absolutely stable when a certain baryon count threshold is reached. Additionally, according to most super-symmetric theories, Q-balls should be produced in large numbers during baryogenesis and, due to their inherent stability, should survive to this day. These factors make Q-Balls an attractive candidate for cold dark matter, and lead to expectations of a non-trivial local flux [66], [67].

Unlike most dark matter candidates, Q-Balls are able to interact strongly with matter, but are still able to fit the qualifier 'Dark'. For any dark matter candidate, integrated over any given path through a region populated with baryonic matter, the net interaction rate of that dark matter candidate (r_b) and therefore its astrophysical brightness goes as $r_b \approx n_{dm}\sigma_{dm}$, where n_{dm} is the number density and σ_{dm} is the cross section. For any single variety dark matter theory in general, $n_{dm} = \rho_{dm}/M_{dm}$ where (ρ_{dm}) is the mass density of dark matter which is constrained by astrophysical observation and M_{dm} is the mass of the chosen candidate particle. This means that $r_b \propto \sigma_{dm}/M_{dm}$, leading to two possibilities for a very low interaction rate and therefore a high 'darkness' in astrophysical data:

- Like WIMPs, σ_{dm} can be very low, meaning M_{dm} can be low and n_{dm} can be high.

- For a constant r_b, σ_{dm} can be large as long as M_{dm} grows at an equal or greater pace forcing down n_{dm}.

It is probable that upon creation during baryogenesis, most Q-balls were initially highly positively charged. These Super-symmetric Electrically Charged Solitons (SECS) would be accelerated in this very energetic epoch to high velocities. During this time, Q-Balls would have high cross sections and energies meaning at high densities they would be quite bright. However Q-Balls have the interesting property of absorbing particles of the opposite charge and therefore, over time, will tend toward neutrality [67]. This is a relatively slow process in interstellar media as the matter density is very low, and while the cross section for absorption is proportional to the object's mass and initial charge, it is still quite small. This cross section

shrinks as the Q-Ball absorbs particles of opposite charge as the volumetric gains due to the increased mass are outpaced by loss of net charge. These objects would continue to accelerate stochastically, over time, at a rate dictated by their charge to mass ratio and the rate at which they absorb either anti-protons or electrons until they either impede on the earth's atmosphere or become charge neutral.

Once neutrality is reached, these Super-symmetric Electrically Neutral Solitons (SENS), would travel in a straight line, slowly losing their kinetic energy to the effects of red-shifting due to cosmic expansion. Upon becoming [68] SENS (this would happen quickly if a SECS entered the atmosphere), there is no longer a Coulomb barrier preventing protons from accessing the internal structure of the Q-ball and its ability to violate both baryon number (B) and lepton number (L) conservation at low energies, instead preserving the quantity $B - L$[7]. This leads to a Kusenko-Kuzmin-Shaposhnikov-Tinyakov (KKST) proton decay of the form $Q + p \rightarrow Q + e^+ + \pi^0$, with a cross-section proportional to the object's mass [69]. This is the primary process allowing for slow Q-Balls to generate measurable events at the Pierre Auger Observatory.

There are two possible mechanisms for a Q-Ball to create an event large enough to allow for Auger FD observation. In the first speculated mechanism, a lighter mass Q-Ball could have a large enough initial velocity for the very small kinetic energy transferred to the secondary particles to be sufficient to cause an EAS capable of passing the energy threshold of the FD [70]. The second possible pathway for achieving detectability, is for the Q-Ball mass, and therefore its KKST cross-section, to be big enough to cause such a large number of decays that the FD energy threshold is passed at any initial velocity [62]. The first mechanism requires extremely high velocities and therefore is not applicable to this work, but is explored through simulation and applied to the Pierre Auger FD dataset by Schuster

---

[7]Both baryon number and lepton number conservation are understood to be possible under the Standard Model in the form of sphalerons, but only at the near impossibly high temperatures reached immediately after the big bang [68], and have never been observed. The difference between the baryon number and lepton number, $B - L$, is an alternative conserved quantity that appears in many grand unified theories (Guts).

in [70]. The second mechanism, however, would result in exactly the type of signal this search would be capable of isolating.

The flux limits set on the existence of Q-balls are so far mainly limited to regions of low mass and high number density, or low mass and high velocity and are often carried out simultaneously with monopole searches or are a byproduct of proton decay signature experiments [71]. The most stringent limits for SENS are AMANDA's limit of $\Theta_{90\%C.L.} \sim 5 \times 10^{-16} cm^{-2} sr^{-1} s^{-1}$ for $M \geq 10^{11} GeV/c^2$ and BAIKAL at comparable flux of $\Theta_{90\%C.L.} \sim 4 \times 10^{-16} cm^{-2} sr^{-1} s^{-1}$ for $M \geq 5 \times 10^{13} GeV/c^2$ [62]. These masses are far below where the FD will become fully efficient. If the full FD aperture can be used, much lower limits can be placed although at much higher masses. The top end of the mass spectrum is constrained to very low fluxes according to the relationship $n_{dm} = \rho_{dm}/M_{dm}$, as ρ is set by astrophysical data.

4.1.2 CORSIKA Simulation of Q-Ball Showers

Q-Balls derive the high energies and interaction rate needed for a measurable shower from proton decay catalyzation. There are two questions of high relevance to this work:

- Given the relatively low energy of each proton decay and the relatively short attenuation length of the emitted e^+s and π^0s, can a proton decay event trigger the Pierre Auger Observatories detectors at all?

- If it is possible, what Q-Ball cross sections and masses are needed to satisfy the FD's and SD's triggering threshold?

To answer these questions simulation is necessary.

For high energy astroparticle physics 3D EAS simulation, especially within the Pierre Auger collaboration, CORSIKA (COsmic Ray SImulations for KAscade) is used [72]. CORSIKA is a high energy EAS simulation software package that was originally developed to

interpret the results of KASCADE[8], but is now used for simulation extensively in nearly all high energy astroparticle physics projects. CORSIKA uses a large number of particle interaction simulators[9] and has been shown, based on which sub-simulators are chosen, to well predict interactions at an impressively wide range of energies, reaching down to the energy range of the LHC and up to and exceeding UHECR energies. CORSIKA has become a standard tool in high energy particle physics, being used in cosmic ray observatories, high energy collider experiments, as well as neutrino and dark matter observatories. As of 2014, it was currently being used to further physics in over 40 experiments world wide [73].

CORSIKA comes with a large and ever-expanding set of primary particles and interaction types which span a wide range of traditional and exotic particles. The strongest subluminal candidate, super-symmetric Q-Balls, did appear in this list thanks to the combined efforts of Dr. Schuster and Dr. Pierog in [70] and were used as the basis for simulation. Unfortunately, the Q-Ball description was for a speculated light, high velocity Q-Ball with a heavy reliance on large momentum transfer and, therefore, needed to be adapted to fit the interaction models described in [62]. This was done by removing momentum transfer in Q-Ball/proton interactions and adjusting the mass (M_Q) as well as the cross section (σ_Q) to reflect the predicted values. For all simulations, the symmetry breaking parameter was set to $1 TeV$, the value specified in [62]. The result was a Q-Ball shower simulation with no dependence on initial energy or velocity. The resulting showers, an example of which can be seen in Figure 4.1, grow in intensity as they push deeper in the atmosphere, but shrink in radius. Both of these features are well in-line with expectations[10].

---

[8]KASCADE was a high precision detector made to simultaneously measure the hadronic, muonic and electromagnetic components of showers in the $10^{16} - 10^{18} eV$ range

[9]For very high energy interactions Corsika uses VENUS, QGSJET, DPMJET and SIBYLL which use either Gribov-Regge theory or a minijet model. Hadronic interactions at lower energies are described either by the GHEISHA module, by FLUKA, or by the UrQMD model. For a more thorough overview see [72].

[10]The intensity should grow proportionally with atmospheric depth as rate of proton decays depends only on the rate at which the Q-Ball is presented with protons and therefore grows with atmospheric density. The shower radius decreases with atmospheric depth because each proton decay releases an identical amount of energy meaning the attenuation length of the product particles is the same in terms of g/cm^2 statistically. This, in turn, means the distance each daughter travels is inversely proportional to atmospheric density.
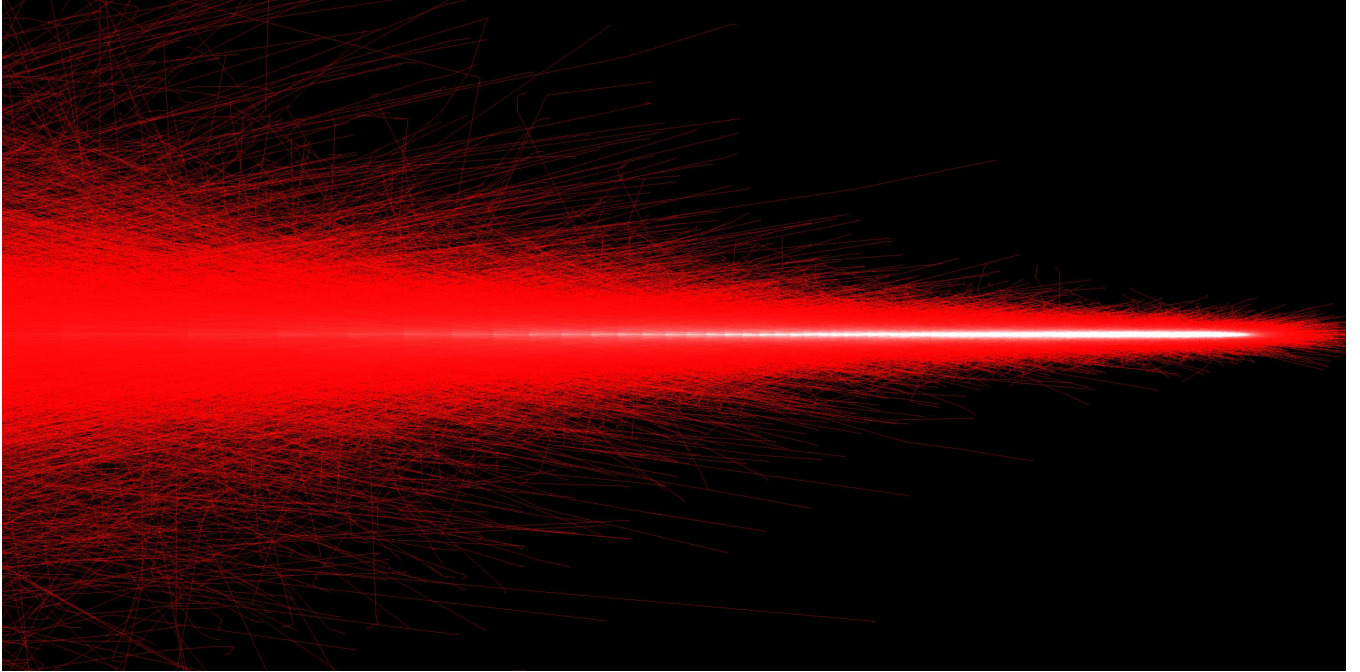
Figure 4.1: Corsika Simulation of Proton Decay Shower. The Electromagnetic shower caused by a 5 kB proton decay catalyzing Q-Ball with atmospheric depth increasing from $0g\ cm^{-2}$ on left to $900g\ cm^{-2}$ on the right.

Because this type of shower consists of a very large number of unique cascades at low energies, the techniques and tools usually employed to speed up the simulation process could not be used. As a result of this, the computation time necessary for each individual simulation grew proportionally with cross section and zenith angle. This motivated a choice to simulate only vertical events as they represent shortest possible path length to the ground. Even with this choice, the simulations for a single shower at the higher σ_Q values took well over a month of real world time to complete. Additionally, due to the huge number of interactions and particles that needed to be traced as the shower moved deeper into the atmosphere, the simulations were very CPU and memory intensive, limiting the number of simulations possible at a time, to one. This made it difficult to simulate more than a few events. However, because each proton decay and its products do not effect the interactions of later decays, each decay can be treated as an independent event. This, combined with the more than 10^9 separate decay events in each simulated shower, means that the law of

74

large numbers applies well to each individual simulation. This results in almost no shower to shower fluctuations, meaning that simulations performed with the same parameters will be statistically identical to each other, which greatly limits the need for multiple simulations with the same parameters.

In order to study at what cross section the FD and SD begin to respond to a proton decay shower, eight full simulations with cross sections varying from 1000 $barn$ (1kb) to 41.7×10^6 $barn$ (41.7mb) were run, taking a total of 167 days. The upper limit of this simulation range represents a theoretical energy deposit of $10^{19}eV$. These simulations were then imported into the $\overline{\text{Off}}\underline{\text{line}}$ detector simulations and thrown with random core locations in front of Coihueco. The parameters of each simulation and whether they were detected by the FD and SD can be seen in Table 4.1. The calculations to derive these values were obtained following the perscription laid out in [62]. The values predicted in Table 4.1 do differ by about half an order of magnitude from those predicted in [62]. This is because [62] allows for the decay of both neutrons and protons, while the CORSIKA simulations were constrained to only proton decay and simulated the energy released per nucleon. The differences, however, can be completely accounted for in calculation and important results for both proton only and proton/neutron decay are presented.

Table 4.1: Q-Ball Simulation Parameters and Detectability.

| σ_Q ($barn$)	M_Q ($GeV\ c^{-2}$)	Theoretical Energy Loss	FD Triggered?	SD Triggered?
100kb	1.21×10^{24}	$2.4 \times 10^{16}eV$	No	No
500kb	1.35×10^{25}	$1.2 \times 10^{17}eV$	No	No
1Mb	3.82×10^{26}	$2.4 \times 10^{17}eV$	No	Not Fully. Rarely 1
5Mb	4.27×10^{27}	$1.2 \times 10^{18}eV$	Rarely	3
10Mb	1.21×10^{28}	$2.4 \times 10^{18}eV$	Yes	3 to 4
20Mb	3.42×10^{28}	$4.8 \times 10^{18}eV$	Yes	4
41.7Mb	1.027×10^{29}	$10^{19}eV$	Yes, Reliably	6 Tanks

From Table 4.1 it is clear that the simulations confirm that Q-Balls are able to trigger both the FD and SD once their cross section exceeds a few million $barns$. This means that as long as a sufficiently large Q-Ball enters the atmosphere within the Observatory's field of

view with a high enough velocity to pass the T2 trigger, they will be observed. According to calculation, Q-Balls begin to successfully trigger the FD around $E_{deposit} \approx 2EeV$ which agrees well with the cosmic ray trigger threshold of $1EeV$. The FD reliably triggers at $E_{deposit} >\sim 5EeV$. With M_s set to $1TeV$, this gives the FD a minimum Q-Balls mass sensitivity of $M_Q > 9.19 \times 10^{27} GeV\ c^{-2}$. If one allows Q-Balls to catalyze the decay of both protons and neutrons, the minimum mass sensitivity lowers to $M_Q > 3.25 \times 10^{27} GeV\ c^{-2}$[11].

In Figure 4.2 and Figure 4.3, an example $41.7Mb$ event reconstructed by both the FD and SD is shown. First, as seen in Figure 4.2(b) the event strongly and cleanly triggered the FD, and looks strikingly similar to a laser event. The timing signature, Figure 4.2(c), was also clean and well fit by the standard hybrid timing equations represented by the red line. As expected, the light profile of the shower, Figure 4.2(d), departs from the Gaisser-Hillas shape expected in cosmic rays showers, shown for a real FD event in Figure 3.10. This large difference in profile provides a means of potentially identifying Q-Balls in slow candidate events, or possibly another avenue to search for these particles all together.

From Table 4.1 and Figure 4.3(a) it is obvious that Q-Balls seem to have an easier time fully triggering the SD than the FD and will do so at lower cross sections and masses. Figure 4.3(b) shows Q-Balls have LDFs not dissimilar from those expected from cosmic rays. This is important for this work, as it means that Hybrid detections are a possible search avenue for Q-Balls. Also, very interestingly, as can be seen in Figure 4.3(c), by the a disagreement between the green line and the data, Q-Ball showers do not trigger stations with a timing structure that matches what is predicted from a cosmic ray event. The shape of the SD timing, where the far tanks are triggered much later than is expected, can be understood through the fact that the proton decay products all have the same energy and, therefore, will have very similar attenuation lengths at some atmospheric density. This has the effect of creating a sphere with a small fixed radius, meaning the farthest tanks only
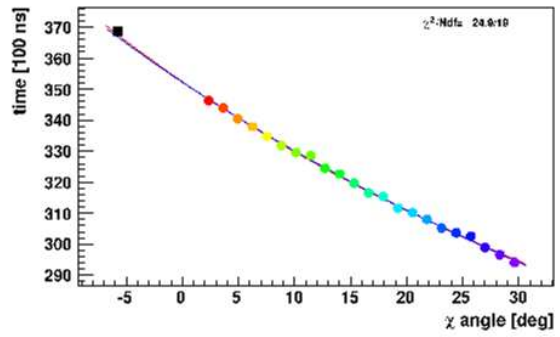
---

[11]This is only at the lowest measurable cross section. Sensitivity at the $5EeV$ range, corresponding to $M_Q > 3.63 \times 10^{28} GeV\ c^{-2}$ for proton only and $M_Q > 1.28 \times 10^{28} GeV\ c^{-2}$ for both proton and neutron decay, is more realistic.
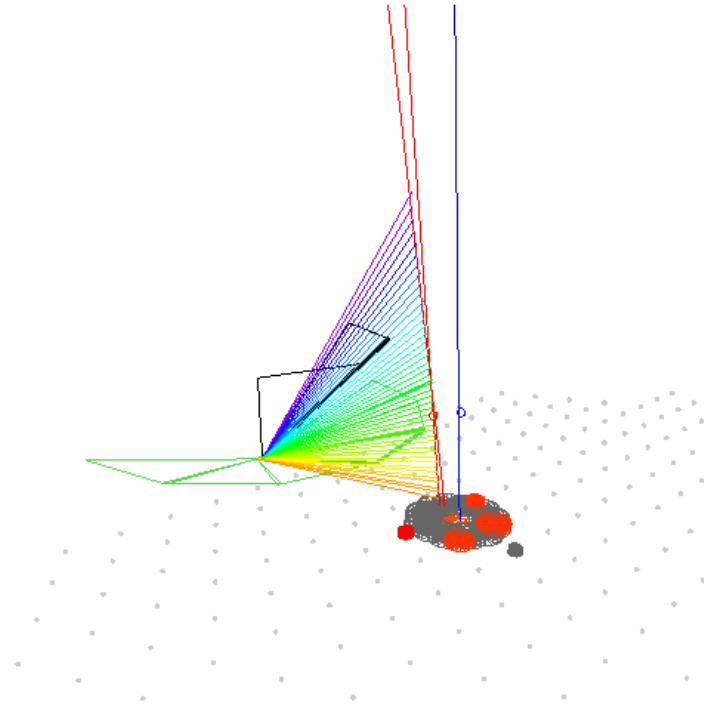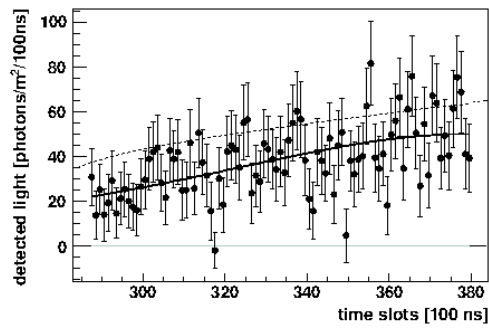
(a) Simulated Q-Ball Event
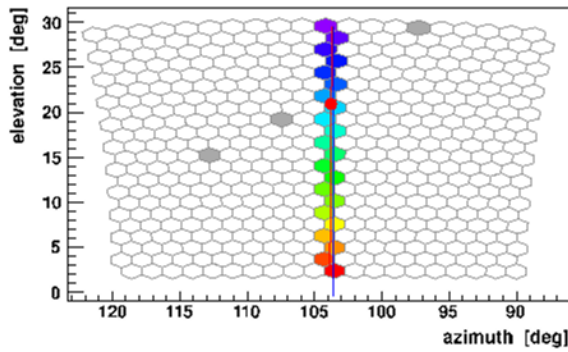
(b) Simulated FD Pixel Trace

(c) Simulated FD Timing

(d) Reconstructed Light Profile

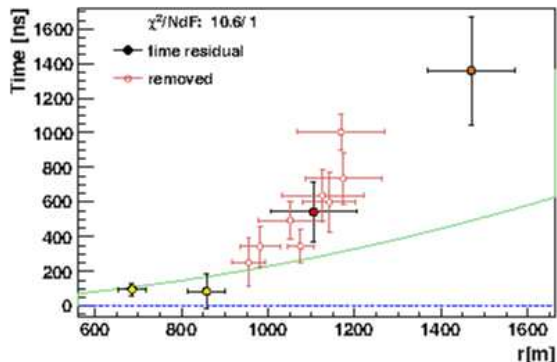Figure 4.2: Simulated FD Response to a $20MB$ Q-Ball.

trigger from the decays occurring as the Q-Ball approaches the level of the tanks. The size of this effect will grow more pronounced as the Q-Ball slows, further differentiating them from the background of cosmic ray events. The velocity dependent timing signature of Q-Ball is explored more fully in Section 7.1.
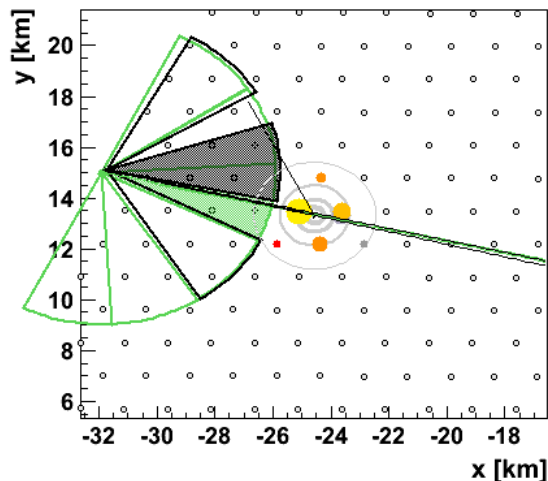
(a) Simulated SD Response
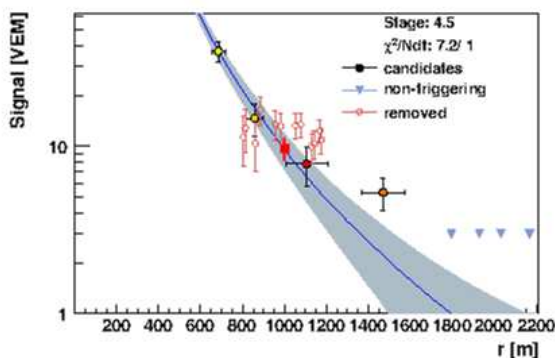
(b) Simulated SD LDF

(c) Simulated SD Timing

Figure 4.3: Simulated SD Response to a $20Mb$ Q-Ball.

If the strong differences between the SD timing profile of cosmic rays and Q-Balls can be confirmed by a dedicated study with more in-depth simulation, these drastic differences in SD timing open up the possibility of systematically searching for Q-Balls and like candidates in the SD. These differences should be even clearer if discrimination between electromagnetic and hadronic components becomes possible. Because Q-Balls trigger the SD fully at smaller

values of σ_Q and therefore have sensitivity to lighter masses, they are sensitive to a wider parameter space than the FD. Additionally, slow events will not be rejected due to the T2 trigger, meaning that the search could potentially extend down to the galactic velocity range of $\sim 1 \times 10^{-3}$ c. However the effect of the SD's T4 physics trigger needs to be investigated to verify that slow events will not be cut by the timing restrictions.

According to the simulation results, when the Q-Ball's energy deposit reaches $1EeV$ the SD will almost certainly reliably trigger anywhere in the array. For Q-Balls that trigger only proton decay, $1EeV$ corresponds to $M_Q > 4 \times 10^{27} GeV\ c^{-2}$, if both proton and neutron decay is allowed that mass lowers to $M_Q > 1.15 \times 10^{27} GeV\ c^{-2}$. Because at these masses the full SD is available to observe Q-Balls, a search looking for a Q-Ball in the SD would have a huge exposure. This, in turn, means very stringent limits could be placed on their flux. Because of these factors, further Q-Ball simulations should be performed and the SD should be used to search for these objects in the future.

CHAPTER 5

THE VELOCITY SENSITIVITY OF THE PIERRE AUGER OBSERVATORY

Of central importance to the search for slow events at the Pierre Auger Observatory is the verification that the FD instrumentation is capable of making this measurement. As shown in Section 3.5, the reconstruction techniques employed by the Observatory all rely on the assumption that showers travel imperceptibly close to the speed of light in one way or another. This is mainly because it very much simplifies the process of reconstructing the trajectory of a fast moving, dim and distant object by removing a parameter from the propagation equations. By introducing the event velocity (V), the number of independent parameters that need to be calculated to describe the event is raised from five to six, greatly increasing the burden on the data. Of these six parameters, the geometric parameters (θ_{axis}, ϕ_{axis}, x_{core} and y_{core}) and timing parameter (T_0) are already reconstructed, as explained in Section 3.5. A reconstruction of the velocity requires high resolution measurements of the location and timing of several points during an event's evolution in the atmosphere. In order to ascertain whether the FD is capable of these measurements two questions must be answered:

1. How does the FD T2 minimum timing trigger affect the sensitivity of the Observatory as the velocity decreases?

2. Given the 100 ns time resolution and 1.5° angular resolution of the FD's cameras, with what accuracy and precision can the FD reconstruct the Velocity?

5.1 Simple Velocity Dependent Propagation Model with a Known Geometry

In order to test the velocity resolution of the Pierre Auger FD, the geometric and velocity reconstructions must be separated. This can be done if the geometric shower parameters are fixed to their correct values in order to dedicate all of an event's timing information to

the reconstruction of the velocity. For this to be done, a sample of events whose geometry and location are well known are needed. This need could be satisfied through simulations, however they would be unable to say anything about the real world performance of the FD. Furthermore, because the alignment and response of each Eye can change over time, the sample of events should ideally cover all Eyes and periods of FD operation. As explained in Section 3.4.4, the atmospheric laser facilities provide just such a sample.
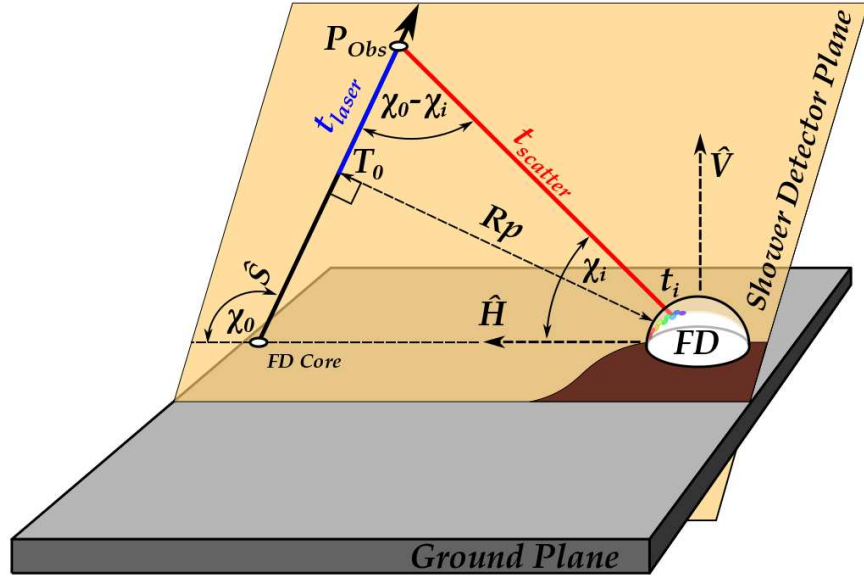

Figure 5.1: The Geometry of a Monocular Event.

To reconstruct the velocity, the same methods that were outlined in Section 3.5 are used. The shower propagation equations, however, need to be altered in order to reflect the variable event velocity. The first step to doing this is to separate out the timing of the laser's movement (t_{laser}), blue in Figure 5.1, from the timing of the scattered light ($t_{scatter}$), red in Figure 5.1. Using Figure 5.1, the distance the laser travels (D_{laser}) from the point of Rp to the point of observation (P_{Obs}) is

$$D_{Laser} = \frac{Rp}{\tan{(\chi_0 - \chi_i)}},$$

(5.1)

while the distance the scattered laser light travels ($D_{scatter}$) from P_{Obs} to the Eye is clearly

$$D_{Scatter} = \frac{Rp}{\sin(\chi_0 - \chi_i)}.$$ (5.2)

By dividing (5.1) and (5.2) by their propagation velocities, a free velocity, V, for D_{Laser} and the speed of light in air, c_{air}, for $D_{Scatter}$, we get a close approximation of the expected time each segment will take to travel resulting in

$$t_{Laser} = \frac{Rp}{V \tan(\chi_0 - \chi_i)},$$ (5.3)

and

$$t_{Scatter} = \frac{Rp}{c_{air} \sin(\chi_0 - \chi_i)}.$$ (5.4)

These two equations now generally describe the expected timing of an up-going event in an observing Eye, but in the Laser's time-frame. In order to translate the timing to the Eye's time-frame, these equations need to include a reference point and time on the shower axis, T_0. Since the laser propagates upward, it reaches P_{Obs} after T_0. Therefore, t_{Laser} needs to be added to T_0. From the point P_{Obs} the scattered laser light now propagates to the detector, so $t_{Scatter}$ also needs to be added. So t_i^{exp} for a laser event with a free velocity is defined as

$$t_i^{exp} = T_0 + t_i^{Scatter} + t_i^{Laser} = T_0 + \frac{Rp}{c_{air} \sin(\chi_0 - \chi_i)} + \frac{Rp}{v \tan(\chi_0 - \chi_i)}.$$ (5.5)

5.2 Velocity Sensitivity Range

The velocity sensitivity range is limited only at low velocities by the T2 condition of triggering at least 4 pixels in one of the required geometries in a time window of $20\mu s$. As can be seen in Figure 5.2, because the shower's light only needs to trigger a portion of the first and last of the four pixel group, conservatively the minimum angle that one of these geometries can have is $\sim 5.7°$ which in turn translates to a minimum detectable angular velocity of $\dot{\chi}_i \simeq 0.285°\mu s^{-1}$.

Figure 5.3(a) and Figure 5.3(b) show the sensitivity of the FD for a wide range of velocities and geometries. The observed angular range is always assumed to be the $5.7°$ window
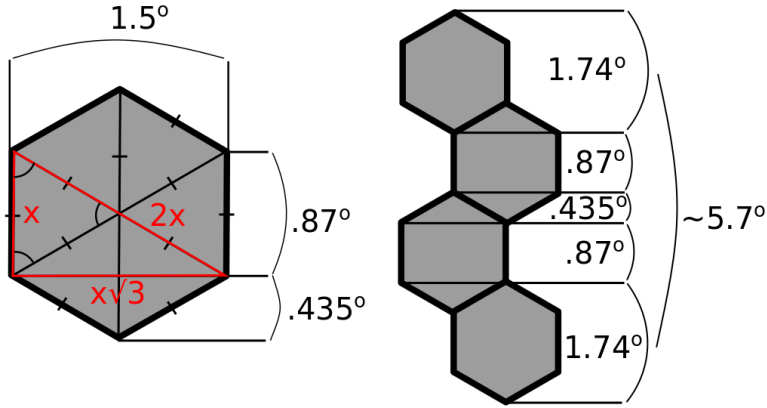
Figure 5.2: The Minimum Detectable Angle due to the T2 FD Trigger. This is the most compact T2 geometry and therefore this represents the minimum angular length an event needs to pass in the required $20\mu s$ window.

surrounding the region of maximum sensitivity and (5.5) is used to calculate the angular velocity across the Eye.

Figure 5.3(a) and Figure 5.3(b) show that Auger should have sensitivity to a wide range of event velocities. The fact that the sensitivity seems to extend all the way down to 1% of c is quite promising. As expected, the velocity sensitivity roughly follows the form of (5.5), being approximately proportional to the velocity (V) and inversely proportional to the distance to the event, which means that as the velocity of an event drops so too does the effective aperture of the Observatory. Both Figure 5.3(a) and Figure 5.3(b), however, display some interesting behavior with respect to χ_0.

Clearly something is going on at very high values of χ_0. This feature of the velocity sensitivity can be pretty easily understood geometrically. Looking at Figure 5.4, it is clear $l_1 < l_2 < l_3$ meaning the observed track lengths for each axis get smaller as χ_0 increases. Because the angular velocity at the Eye is roughly proportional to the observed track length, this means the FD has an enhanced velocity sensitivity as χ_0 climbs. Theoretically as χ_0 nears 180° the FD becomes sensitive to events at almost any Velocity, however, the effective aperture at this extreme limit quickly approaches zero. As χ_0 decrease and events become more vertical, this enhanced sensitivity vanishes.
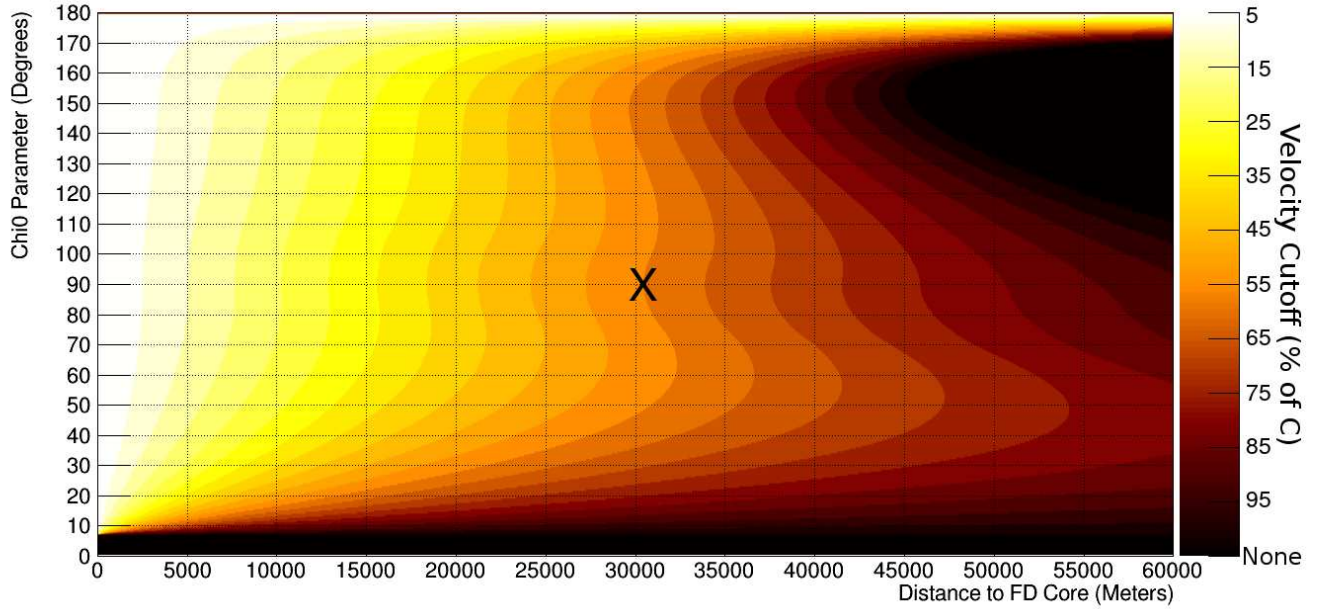
(a) Pierre Auger Velocity Sensitivity 100% to 5% of C
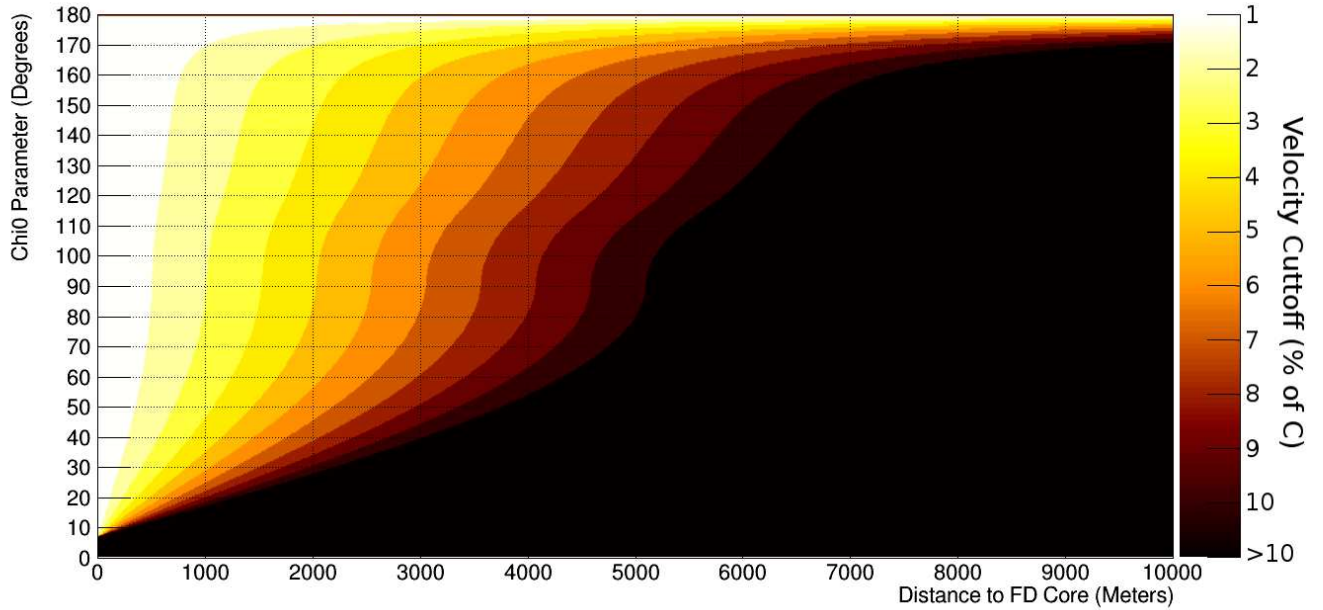
(b) Pierre Auger Velocity Sensitivity 10% to 1% of C

Figure 5.3: Pierre Auger Velocity Sensitivity due to the T2 FD Trigger: the shower geometries and velocities that are capable of passing the timing requirement set by the FD T2 $\sim 5.7°$ in $20\mu s$ window. The large **X** in (a) denotes the geometry of the simulations in Figure 5.6.
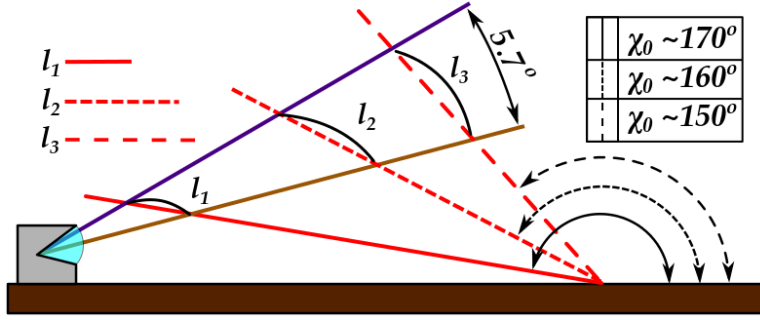
Figure 5.4: Velocity Sensitivity for Events with $\chi_0 > 90°$. The purple and orange lines indicate the top and bottom of the 5.7° viewing window. $l_{(1-3)}$ are the projected length of the viewing window of each shower axis.

For events with $\chi_0 < 90°$, calculating the angular velocity at the Eye is somewhat more complicated. Clearly, according to Figure 5.4, as the axis is inclined away from the detector the observed track length is increased, meaning the observed angular velocity at the Eye should decrease as χ_0 decreases. However, because an event can travel at speeds similar to the light emitted from its interactions in the atmosphere, for certain geometries the light emitted at each point on the event's axis can arrive at the Eye at similar times. Figure 5.5, illustrates this clearly using an event with a low χ_0 traveling at c. As the event moves down the red axis it crosses the purple line at time T_1 where it emits light that will follow the purple line to the Eye. The event continues moving down the red line at a speed of c and eventually crosses the orange line at a time T_2 where it emits light that will follow the orange line to the Eye. At this time the light emitted at T_1 has traveled down the purple line to the point indicated as T_2. From here, both the light following the purple line and the light following the orange line travel to the detector at c. As shown in the enlarged square in Figure 5.5, after time T_2 the path length for the light following the purple line and the light following the orange line differ only by the length Δ_{path} which is quite small. This means that though the event traveled a long time between observations at the purple line and the orange line, the light emitted at T_1 and T_2 will arrive at the Eye within Δ_{path}/c of each other, greatly increasing the apparent angular velocity at the Eye, which in turn, greatly enhances
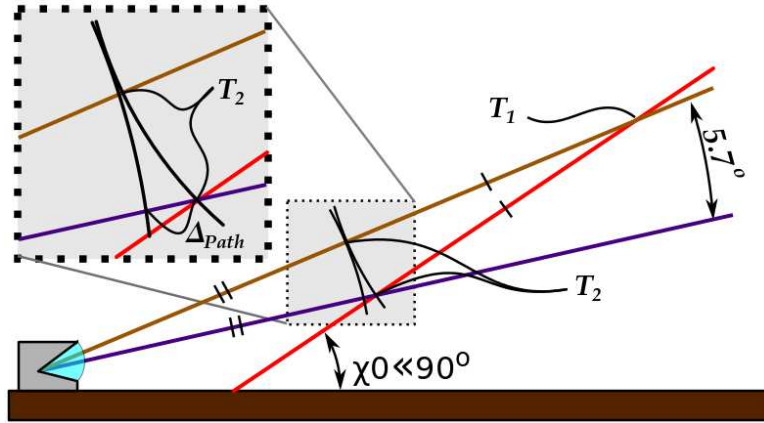
85

Figure 5.5: Velocity Sensitivity for Events with $\chi_0 < 90°$. For this illustration the event following the red line is moving at c. The purple and orange lines indicate the top and bottom of the 5.7° viewing window. Where indicated, T_1 and T_2 are the emission times at the top and bottom of the viewing window. Δ_{path} represents the difference in path length between the observations at the top and bottom of the viewing window.

the velocity sensitivity of the FD.

As velocity drops the ability for events to keep up with the emitted light decreases, gradually weakening the strength of the effect. Because of this, sensitivity is maximized for the widest range of velocities around a χ_0 of 45° as this represents balance a point between minimizing the observed axis length and still taking advantage of the catch up effect. Eventually as the speed the decreases, the increase in the observed axis length of any geometry inclined away from the Eye outweighs any benefit gained by the event moving toward the Eye. This means the increase in velocity sensitivity seen around 45° should vanish at low velocities. Additionally, because it is impossible to observe an event at a χ_i angle greater than the event's χ_0 no event with a $\chi_0 < 5.7°$ can ever be observed.

In order to quickly investigate how well the actual velocity sensitivity range of the FD matches the predictions of Figure 5.3(a) and Figure 5.3(b), toy slow event simulations were created using the $\overline{\text{Off}\underline{\text{line}}}$ standard laser simulation modules. To do this, throughout these modules the propagation speed of the laser was changed from c to a velocity ranging from 95% of c to 45% of c. Using these altered modules, a simulated sample of 700 slow laser events fired vertically from the CLF with varying energies was generated at each velocity. The detector

response of the Coihueco detector was then simulated and the event was reconstructed using (5.5) and the FixedGeometryVelocityFinder module described in the next section. The results of these toy simulations and reconstructions are shown in Figure 5.6.
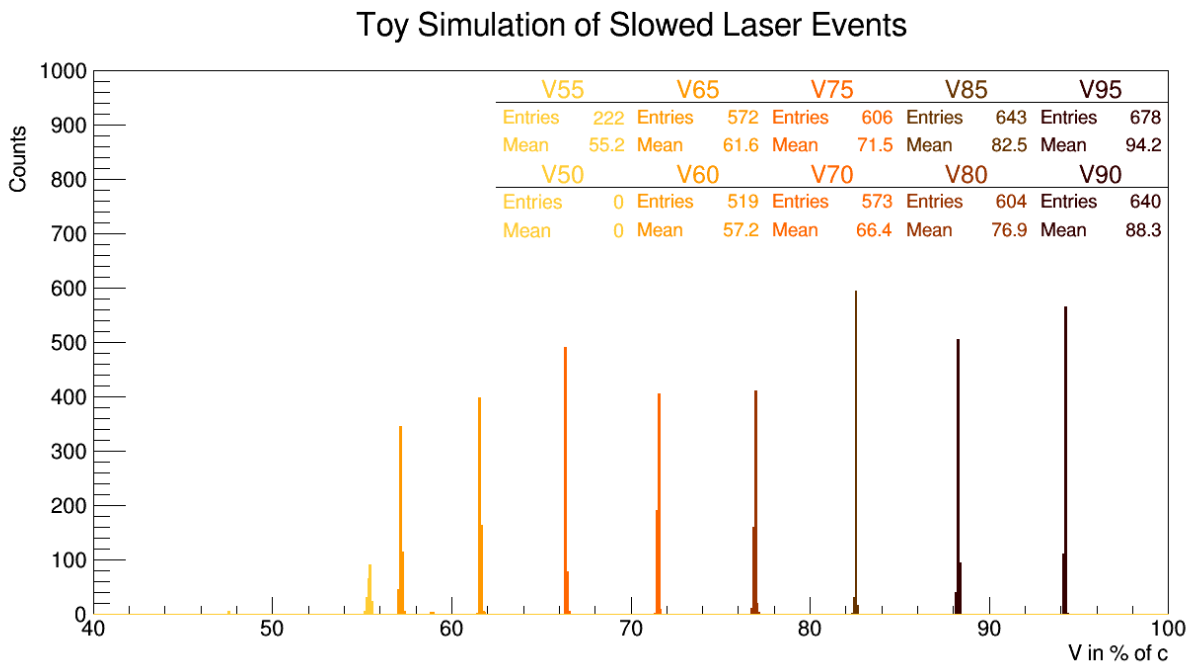

Figure 5.6: Simulated Speeds at ~30,000 Meters. Simulated slow laser events every 5% of c. The simulations start at 95% of c and decrease to 45% of c. As expected from Figure 5.3(a), the events at 45% of c and 50% of c failed FD detection as they were too slow to trigger enough pixels. Events at 55% of c often passed the T2 selection criteria due to triggering just over the required number of pixels.

There are a few interesting things that present themselves in Figure 5.6. First, the sensitivity predicted in Figure 5.3(a) seems to be accurate. The simulations at 45% and 50% of c failed to be detected by the observatory due to the T2 trigger. The simulations at 55% of c were often detected, but only 222 out of 700 events were successfully reconstructed. Investigation of this revealed that the majority of the missing events were simulated with low energy and failed reconstruction due to weak signals in the top and bottom pixels. This lead to large errors in the SDP reconstruction which caused the later reconstruction steps to fail entirely. The short tracks and weak signals in the top and bottom pixels continued to be a problem in the higher velocity samples and occasionally caused SDP errors large enough

to cause the event to fail in either the geometry or velocity reconstructions, though with decreasing regularity.

There also seems to be a small problem with reconstruction accuracy at slow velocities. It is unclear if this is the fault of the short and weak tracks, the errors in SDP reconstruction, the toy simulations or the method. If this effect is real and carries to the reconstruction of real events it shouldn't pose a large problem simply because the reconstruction seems to err toward slower rather than faster speeds. This would have the effect of pushing truly slow events further from c increasing their isolation from the normal cosmic ray events. Clearly, this would complicate any energy or mass calculations for observed exotic events, but these calculations are beyond the intent of simply identifying possible candidates. It is therefore clear that in the event of a positive identification of a strong candidate, further study would be required. In any case, the Observatory and the core of the method are capable of detecting, reconstructing and identifying events down to a few % of c with a reasonable degree of confidence.

5.3 Atmospheric Corrections to the Velocity Dependent Propagation Model

Equation (5.5) represents a relatively simple and general free velocity propagation model for the FD laser events in an atmosphere with a constant index of refraction n_{air} and speed c_{air}. However, the optical properties of the earth's atmosphere, while fairly uniform horizontally, vary widely over large distances especially as altitude increases. As the height above the ground increases there is a significant change in air density which directly affects the atmosphere's index of refraction. To accurately predict the timing and trajectory of light traveling through this atmospheric gradient, the density profile needs to be tracked and its effects accounted for. Luckily, this work has already been done by Daniel Kümpel in [51]. The index of refraction (n) as a function of the height (h), the air density at the Eye (ρ_0) and the air density at altitude ($\rho(h)$) is given by (2.4) in [74] as

$$n(h) = 1 + 0.000283\frac{\rho(h)}{\rho_0}. \tag{5.6}$$

The height dependent density profile of the atmosphere is well approximated by an exponential of the form

$$\rho(h) = \frac{b_j}{c_j} e^{-h/c_j}, \tag{5.7}$$

where b_j and c_j are values given by one of four regions: 0 to 4 km, 4 to 10 km, 10 to 40 km and 40 to 100 km. The U.S. standard atmosphere values for b_j and c_j can be found in Table 5.1. For the reconstructions of real events, the GDAS databases are used to provide the actual values measured at the time and location of the event.

Table 5.1: The Parameters of the U.S. Standard Atmosphere

Layer (j)	Altitude (h)	b_j $[g/cm^2]$	c_j $[cm]$
1	0 to 4 km	1222.6562	994186.38
2	4 to 10 km	1144.9069	878153.55
3	10 to 40 km	1305.5948	636143.04
4	40 to 100 km	540.1778	772170.16

By combining (5.6) and (5.7) the height dependent index of refraction $n(h)$ can be calculated as

$$n(h) = 1 + \frac{0.000283 b_j}{\rho_0 c_j} e^{-h/c_j}, \tag{5.8}$$

the form of which, by region, can be seen in Figure 5.7.

This varying index of refraction effects the propagation and timing of light as it travels through the atmosphere and can change the observations of an event in two ways:

1. **Decreasing the propagation velocity of scattered light**

   This effect is fairly straightforward to understand. Basically, the light given off at any point of observation on the shower axis will travel a different path to the detector. Because of this, as the light travels to the detector it will experience a unique profile of indices of refraction giving each path a unique average index of refraction and therefore, effective speed. Since each observed point on the shower travels to the detector with a different speed, the timing of the event subtly changes as the signal moves across the
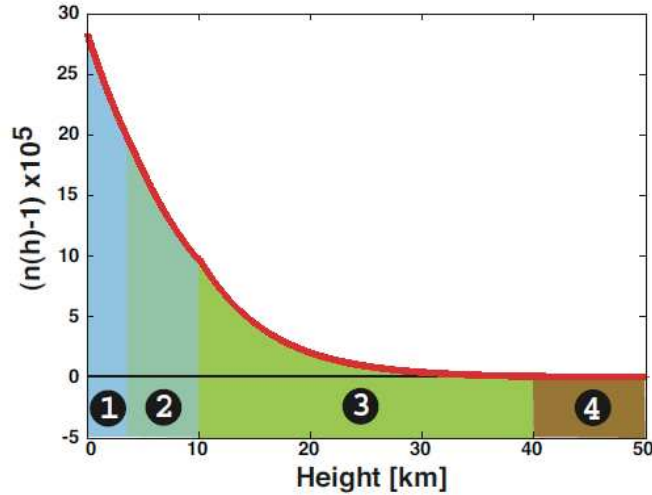
89

Figure 5.7: Index of refraction as a function of altitude. The four atmosphere layers are shown. The U.S. standard atmosphere was used [51].

Eye. Because of this, at the lowest observed angles in the FD, light traveling to the detector arrives $\sim 20 ns$ later than it would have had it traveled the same distance on a path observed at higher angles.

2. **Bending the path of scattered light**

This effect is due to Fermat's principle which states that when light moves from a region with a low index of refraction to a region with a higher one, it is refracted to a steeper angle. As seen in Figure 5.8, because the index of refraction increases as light propagates downward through the atmosphere it continuously bends to steeper and steeper angles. The difference in path length due to the increased length of this curved trajectory is negligible, only amounting to a worse case timing difference across the Eye of $< 0.03 ns$. However, because the light arrives at the detector at an inclination greater than it would had it traveled a straight line, this effect can cause χ_i to be overestimated by up to $0.05°$. This is considerable as at high observation angles a difference of $0.05°$ at a distance of $30 \ km$ results in the telescope observing the axis almost 35 meters lower than the light's arrival direction would suggest, meaning light

90

reaches the detector $\sim 100ns$ faster than it should. As Keri Kuhn showed in [75], this effect can increase the observed velocity up to $\sim 0.4\%$ of c at large distances.
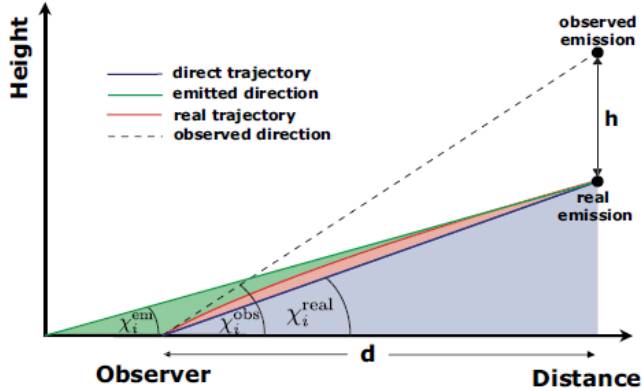

Figure 5.8: Bending of observed light on path to Eye[51].

To accurately reconstruct the velocity, the effects of a height dependent index of refraction, $n(h)$, need to be accounted for. Unfortunately, the bending effect is extremely difficult to correct as it affects the fit of both the SDP and geometry. In order to account for it, the geometry would have to be reconstructed so that the SDP can be fixed, which would require the geometry to be refit again, requiring the SDP to be tweaked resulting in a recursive process. Because of this, corrections were never implemented into $\overline{\text{Off}\underline{\text{line}}}$. Attempting to work in a correction for this effect, while also fitting the shower velocity, was deemed impractical, but should be addressed at some point by the collaboration.

Because this phenomena is unaccounted for, a noticeable effect should be expected in both the laser and shower distributions. First, because laser events in this section have nearly the same geometry, the bending effect should affect them very similarly. This in turn could lead to a systematic shift in the mean reconstructed velocity of laser shots of up to $\sim 0.4\%$ of c at distance. Shower events, however, have a widely varying set of geometries meaning the effect should also vary. The effect should drive the reconstruction in the same direction leading to a smaller increase in the mean reconstructed velocity. More importantly, because different geometries will result in different offsets, up to a $\sim 0.4\%$ increase in the

91

RMS values of shower distributions should also be expected.

The correction to the light propagation velocity is also complicated, but correctable by simply changing the t_i^{exp} calculations. The full correction is thoroughly outlined in [51] and will therefore not be covered here. The end result is the replacement of c_{air} in (5.5) with the effective velocity due to the average index of refraction for the path scattered light takes coming from each observed point on the shower, c_i'. These corrections use the regularly updated, location specific atmospheric GDAS profiles made available in $\overline{\text{Off}}\underline{\text{line}}$. This correction is applied to all real event reconstructions throughout the rest of this thesis. At this point, the propagation equation takes the form

$$t_i^{exp} = T_0 + \frac{Rp}{c_i' \sin{(\chi_0 - \chi_i)}} + \frac{Rp}{v \tan{(\chi_0 - \chi_i)}}. \tag{5.9}$$

By fitting this equation to the FD data, all of the shower parameters including velocity could be reconstructed. However, because there are more parameters than the data can provide a fit for, this monocular velocity reconstruction would be wildly inaccurate and would say little about the velocity resolution of the FD. To fix this, the geometric reconstruction needs to be separated from the velocity reconstruction. The next step is therefore to define the SDP and geometric parameters, Rp and χ_0, using the known position and firing trajectory of the vertical laser shots.

Because the Pierre Auger Observatory is so large, the laser facilities and the Eye's are separated by distances ranging from 29 to 42 km. At this scale the curvature of the earth has a significant effect on the relative trajectories of events. As illustrated in Figure 5.9, this can be approximately corrected by taking into account the average radius of curvature of the earth at the location array RE_C. Using this correction, χ_0 for a vertical event is

$$\chi_0 = \pi/2 - 2\arcsin{[\frac{D_{UTM}}{2RE_C}]}, \tag{5.10}$$

while Rp is calculated as

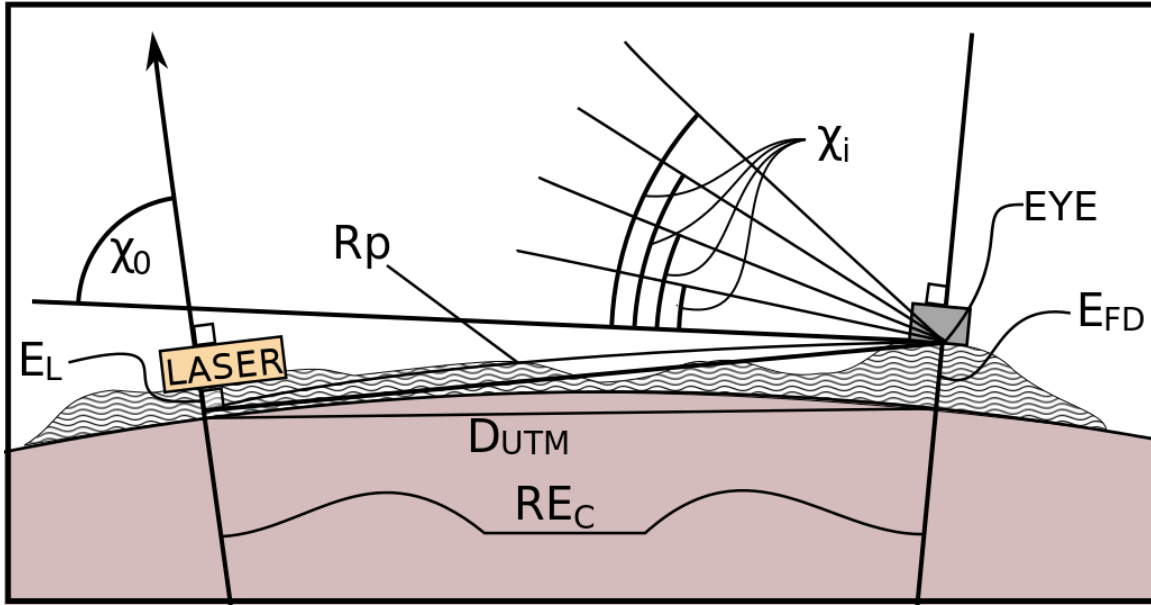$$Rp = (RE_C + Alt_{FD})sin[\chi_0 + \pi/2], \tag{5.11}$$

92

Figure 5.9: The Geometry of a Vertical Laser Event: the difference in vertical due to the curvature of the earth is illustrated by the arrows that lay perpendicular to the ground at both the Eye and laser facility.

where D_{UTM} is the flat UTM distance between the points, and Alt_{FD} is the Altitude of the Eye. The SDP calculation is simple. Each laser facility's vertical beam is known to be aligned to within 0.1° of gravitational vertical as measured at each facility. Therefore, assuming that the vector representing vertical at the Eyes and the laser facilities both point back toward the center of the earth, the vertical vectors at the laser facility and Eye together define a perfectly vertical plane, the SDP. After taking into account all of these corrections the final fixed geometry laser model takes the form

$$
\begin{aligned}
t_i^{exp} = T_0 + & \frac{(RE_C + E_{FD})sin[\pi/2 - 2\arcsin\left[\frac{D_{UTM}}{2RE_C}\right] + \pi/2]}{c_i' \sin\left(\pi/2 - 2\arcsin\left[\frac{D_{UTM}}{2RE_C}\right] - \chi_i\right)} \\
& + \frac{(RE_C + E_{FD})sin[\pi/2 - 2\arcsin\left[\frac{D_{UTM}}{2RE_C}\right] + \pi/2]}{v\tan\left(\pi/2 - 2\arcsin\left[\frac{D_{UTM}}{2RE_C}\right] - \chi_i\right)}
\end{aligned} \quad (5.12)
$$

To be clear, Figure 5.9 and therefore Equations (5.10) and (5.11) are only used for illustration and the SDP is not perfectly vertical. While (5.12) is certainly better than the model with no corrections, it fails to account for the fact that the radius of curvature at

93

any point on the earth has directional dependence. This is because the earth is not a sphere but an ellipsoid. Generally, the curvature in the East West direction is less severe than the North South curvature. Accounting for this directly in the model is impractical as the equations involved are extremely complex and would cause (5.12) to dramatically increase in size. Instead, the effect of earth's true shape is addressed in software by using the coordinate system and geometry packages of $\overline{\text{Off}\underline{\text{line}}}$. Basically, this is done by defining a vector at each laser facility that is aligned with local gravitational vertical and then translating that vector to each observing Eye's coordinate system using the WGS84 gravitational reference ellipsoid. The SDP is then defined as

$$\hat{\mathbf{n}}_{SDP} = \hat{\mathbf{S}} \times \hat{\mathbf{H}}, \tag{5.13}$$

while χ_0 is now

$$\chi_0 = \arccos \hat{\mathbf{S}} \cdot \hat{\mathbf{H}}, \tag{5.14}$$

and finally Rp is

$$Rp = |\vec{H}| \sin \chi_0. \tag{5.15}$$

At this point the only unknown parameters are V and T_0. These are fitted using the χ^2 minimization technique outlined in Section 3.5. Specifically the monocular χ^2 function, (3.5), is used where t_i^{exp} is calculated through Equations (5.9), (5.13), (5.14) and (5.15). During the χ^2 minimization, calculation of the errors on the parameters and their cross correlation are all done using Cern's Root analysis framework, specifically the Minuit fitting packages outlined in [76]. This method, called the fixed geometry velocity reconstruction, was implemented in an $\overline{\text{Off}\underline{\text{line}}}$ reconstruction module, the FixedGeometryVelocityFinder. The FixedGeometryVelocityFinder uses the $\overline{\text{Off}\underline{\text{line}}}$ standard monocular reconstruction module, the FdAxisFinderOG, as a framework, and adheres to $\overline{\text{Off}\underline{\text{line}}}$ and Pierre Auger standard practices. As seen in Figure 5.10, this module was then placed at the end of the standard Observer Monocular reconstruction to make sure the event data was correctly prepared.

```
<moduleControl>
  <loop numTimes="unbounded" save="yes">

    <module> EventFileReaderOG          </module> ⎫
    <module> EventCheckerOG             </module> ⎬
                                                    │
    <module> EventPicker                </module> ⎬ Observer Standard
                                                    │
    <module> FdCalibratorOG             </module> ⎬
    <module> FdPulseFinderOG            </module> │
    <module> PixelSelectorOG            </module> │
    <module> FdSDPFinderOG              </module> │
    <module> FdAxisFinderOG             </module> ⎭

    <module> FixedGeometryVelocityFinder </module> Velocity Reconstructor

  </loop>
</moduleControl>
```

Figure 5.10: The Fixed Geometry Velocity Reconstruction Module Sequence: this is the module sequence used to reconstruct the velocity of vertical laser events. The first part is exactly the Auger standard monocular reconstruction, except for the module EventPicker which selects only vertical laser events using their GPS firing time recorded in the auto-log files produced by both laser facilities. The FixedGeometryVelocityFinder then constrains the geometry to the known values to reconstruct the event velocity.

5.4   Laser Distributions and Interpretation

The FixedGeometryVelocityFinder was used to reconstruct all of FD measured CLF and XLF laser shots fired from January 2007 through December 2013. The GPS firing time recorded in the auto-log files from each laser facility was used to select only vertical laser shots. The atmospheric aerosol database, the IR camera and GOES cloud databases were used to select only events measured during clear, cloudless periods. The results of this analysis are the distributions shown in Figure 5.11(a) for the CLF and Figure 5.11(b) for the XLF.

Because each distribution represents a sample of measurements of essentially the same event over and over again, they are all fairly normal. Surprisingly, however, each Eye seems to have a similar yet different response. First, and most noticeably, the centroid of each distribution does not lay at the expected value of c_{air}. This shows that the method is either misrepresenting the geometry of the laser events or does not account for some effect inherent

95
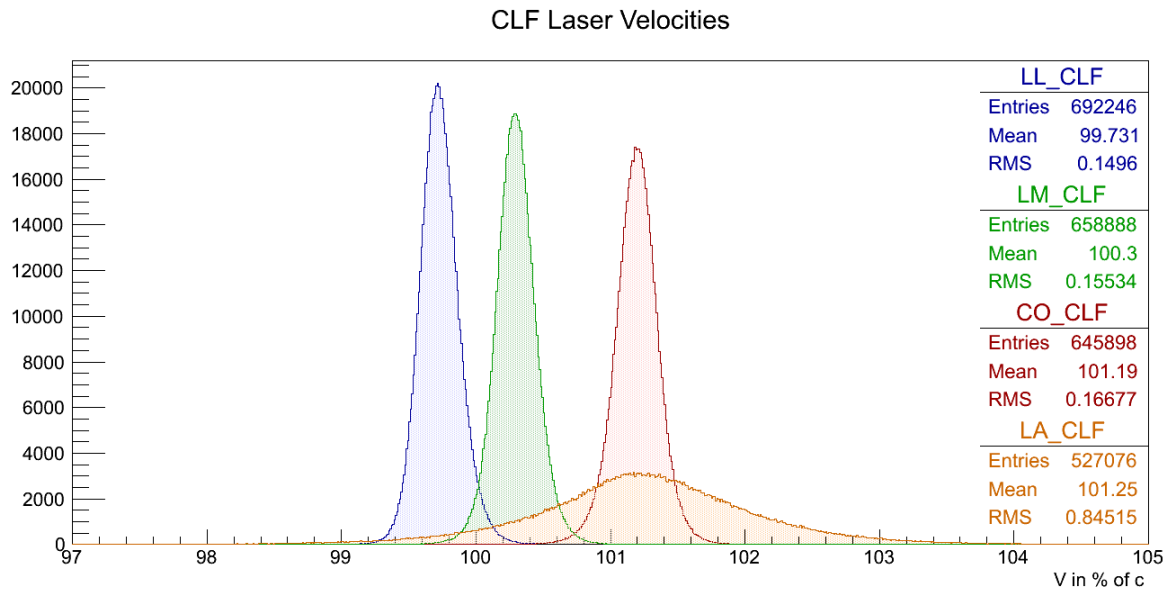
(a) CLF
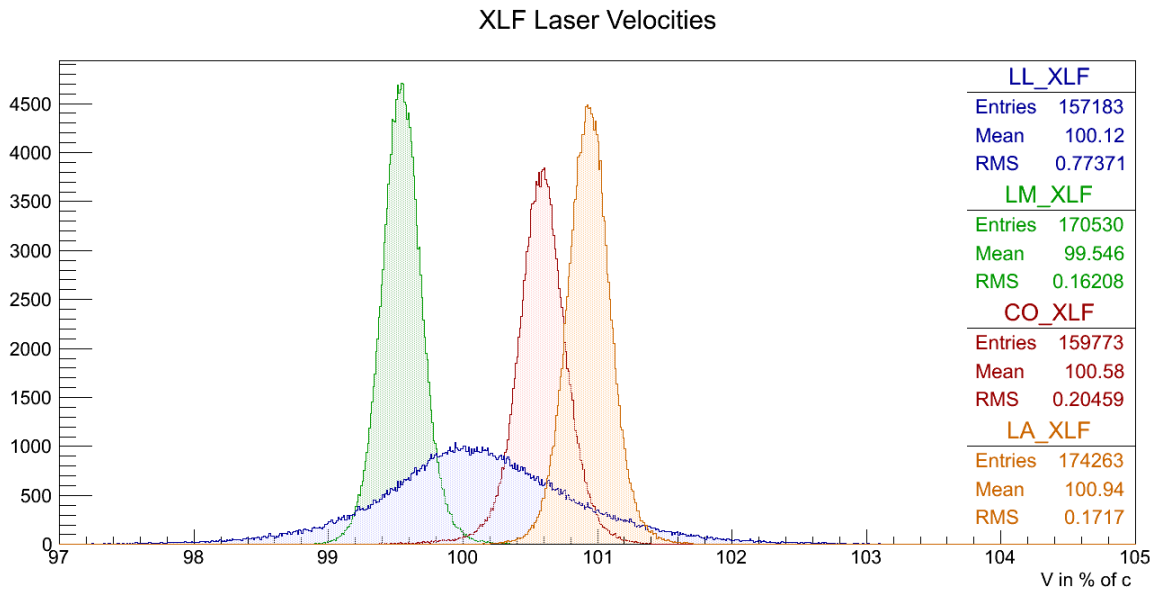
(b) XLF

Figure 5.11: Reconstructed Real Laser Velocities: the reconstructed velocity of vertical laser shots recorded from the CLF and XLF from 2007 through 2013. Only laser shots fired during non-hazy and cloudless periods are used. For all plots in this section, Blue is Los Leones, Green is Los Morados, Orange is Loma Amarilla and Red is Coihueco.

to either the Eyes themselves and/or the atmosphere, or possible there are unknown problems with the standard $\overline{\text{Off}\underline{\text{line}}}$ modules upstream of the FixedGeometryVelocityFinder or in the $\overline{\text{Off}\underline{\text{line}}}$ detector description.

For the CLF, both Coihueco and Loma Amarilla are particularly interesting as their offsets are substantially larger than those of Los Leones and Los Morados. Additionally, Loma Amarilla's distribution is much wider than that of the other Eyes, though this is to be expected as it is much farther from the CLF and therefore the laser light will be much dimmer and noisier in the camera. For the XLF, both Loma Amarilla and Coihueco again have a large offset, but both are less severe than they were for the CLF. Now Los Leones, as is expected due to its distance from the XLF, has a distribution width similar to that seen for Loma Amarilla in the CLF plots. It is interesting to note that, as predicted by the light bending effect, Loma Amarilla sees the $10km$ closer XLF to be $\sim 0.3\%$ of c slower than the CLF, while Los Leones sees the $10km$ closer CLF to be the same $\sim 0.3\%$ of c slower than the XLF. As can been seen in Figure 3.1, the CLF and XLF are aligned from the point of view of both Los Leones and Loma Amarilla, so closely so that the same pixel track is triggered in Los Leones. This isolates the increased distance as a likely cause for the $\sim 0.3\%$ of c shift between both laser facilities.

By far, the most worrying possible cause for the offsets to be ruled out is problems with the velocity reconstruction method. The easiest way to deconvolve the real world effects of the atmosphere and detector from errors in the software is to simulate a sample of events with an ideal atmosphere and detector response. This was accomplished through the use of the laser simulation software already built into $\overline{\text{Off}\underline{\text{line}}}$. These simulations are widely trusted by the collaboration and have been used to carry out multiple studies on the FDs over the years. The simulation sample generated for this research used a simple atmosphere with no clouds, areosols and constant index of refraction of 1. 8000 laser shots were simulated with a perfectly vertical trajectory for both the CLF and XLF and were reconstructed using the vacuum propagation model (5.5). The resulting velocity distribution for the CLF can be

seen in Figure 5.12(a) and the XLF in Figure 5.12(b).

Clearly, many of the effects seen in Figure 5.11(a) and Figure 5.11(b) are no longer present. Additionally, with an overall maximum spread of the simulated CLF centroids of only $\sim 0.1\%$ compared to $\sim 1.5\%$ for real data and $\sim 0.03\%$ as compared to $\sim 1.4\%$ for the XLF, the agreement between Eyes is an order of magnitude better. However, there is still a $\sim 0.4\%$ from c offset seen by all Eyes for both laser facilities. This agreement in velocity for all Eyes, for both laser facilities, rules out geometric effects in the velocity reconstruction method as a probable cause for the offsets seen in Figure 5.11 and strongly indicates that these offsets are due to the atmosphere and unaccounted for detector effects or misalignments.

The geometry used in the FixedGeometryVelocityFinder reconstructions has been verified by checking the simulation datafiles to ensure that the geometry used by the FixedGeometryVelocityFinder and the simulations are in agreement. With the geometry ruled out, there is still the possibility of errors in the velocity dependent propagation model, the FixedGeometryVelocityFinder data preparation and fitting algorithms, or that $\overline{\text{Off}\underline{\text{line}}}$ itself has a problem either in the simulations, detector description or reconstruction modules. Errors in any of these places would likely create similar offsets in the mean reconstructed velocity for all Eyes. This is because the velocity is the only free parameter in the FixedGeometryVelocityFinder reconstruction, meaning the χ^2 fit process must try to account for any errors in the data or propagation model by changing the velocity away from the expected answer of c.

One way to check to see whether the FixedGeometryVelocityFinder or $\overline{\text{Off}\underline{\text{line}}}$ itself is responsible for the offsets in the mean reconstructed velocity, is to remove the FixedGeometryVelocityFinder from the equation entirely and instead look at how well the $\overline{\text{Off}}$ $\underline{\text{line}}$ standard Observer reconstruction reproduces the simulated geometry. If the geometric reconstructions for all of the Eyes agree with each other within reasonable expectations for each of the two laser facilities, then the FixedGeometryVelocityFinder and not the $\overline{\text{Off}}$
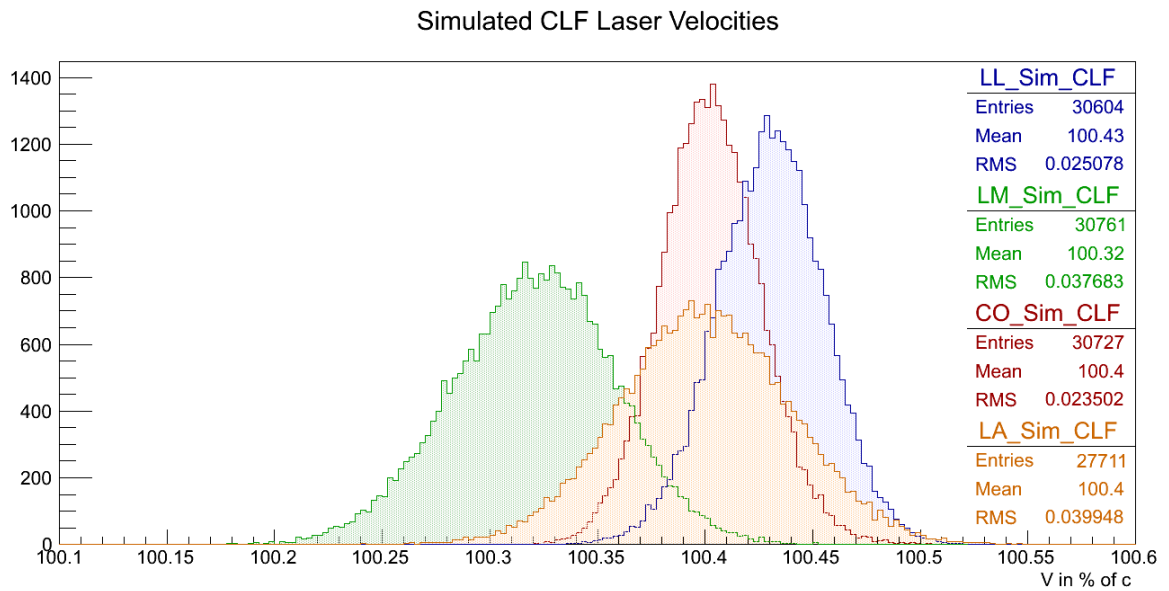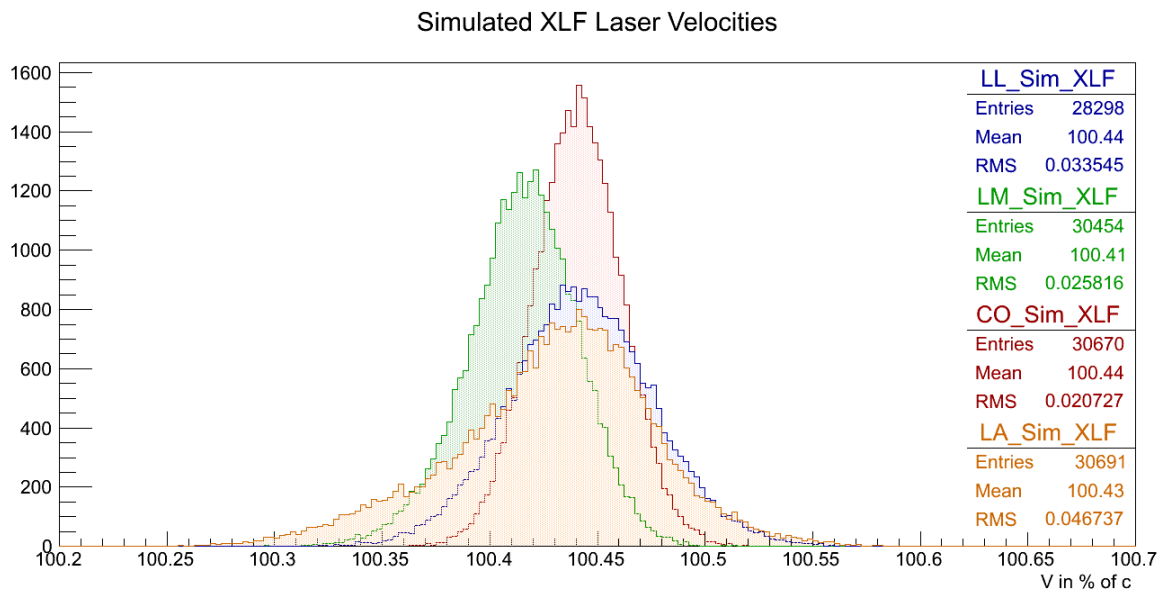
(a) Simulated CLF

(b) Simulated XLF

Figure 5.12: Reconstructed Simulated Laser Velocities: the reconstructed velocity of roughly 32,000 simulated laser vertical shots. An ideal atmosphere and detector were used for both simulation and reconstruction.

<u>line</u> software is responsible for the offsets. To this end, the standard Observer geometric reconstruction was performed on the simulation sample. The resulting distributions for the geometry produced by each of the Eyes are shown in Figure 5.13. The average values for the reconstructed core locations and axis geometries are shown in Table 5.2.

Table 5.2: The Average Observer Reconstructed Simulated CLF and XLF Geometries.

Laser/Eye	Zenith (deg)	Azimuth (deg)	UTM N Error (m)	UTM E Error (m)
CLF LL	0.194 ± 0.069	-61.7 ± 66.2	6.3 ± 54.8	-10.7 ± 23.4
CLF LM	0.473 ± 0.083	37.4 ± 8.75	-49.9 ± 4.3	120.5 ± 92.0
CLF LA	0.612 ± 0.170	-119 ± 72.1	248.3 ± 210.4	-7.6 ± 62.6
CLF CO	0.398 ± 0.048	164 ± 37.9	39.6 ± 49.9	32.0 ± 65.0
XLF LL	0.551 ± 0.087	-139 ± 63.5	295.3 ± 155.6	-0.90 ± 67.3
XLF LM	0.191 ± 0.049	0.67 ± 25.3	-3.5 ± 28.1	-47.7 ± 60.7
XLF LA	0.454 ± 0.16	102 ± 74.9	6.0 ± 217.7	93.4 ± 54.3
XLF CO	0.503 ± 0.10	-152 ± 17	110.0 ± 19.0	$-201.6 \pm 67.1 S$

The values in Figure 5.13 and Table 5.2 are presented in the same, universal reference frame, and clearly show that each Eye's reconstructions systematically do not agree with each other. To be certain, error is expected in these reconstructions, because they were carried out monocularly without any SD information to supplement the FD data. However, these are simulations and therefore represent an ideal case. Furthermore, the angular uncertainty which is reserved to account for various atmospheric effects and timing uncertainties should not really apply here. Even if these errors did apply, they should contribute randomly and therefore increase the width of distributions but not significantly shift the mean. The offsets seen in Figure 5.13(a), Figure 5.13(b), Figure 5.13(c) and Figure 5.13(d) are systematic, which points to a consistent problem either in the simulations or the $\overline{\text{Off}\underline{\text{line}}}$ detector description.

The disagreement between the geometric reconstructions of the Eyes shows that it is likely that there are problems in $\overline{\text{Off}\underline{\text{line}}}$ upstream of the FixedGeometryVelocityFinder. This doesn't mean that there are not still errors in the velocity dependent propagation model or fitting procedure. Testing for these possibilities is still achievable with this simu-
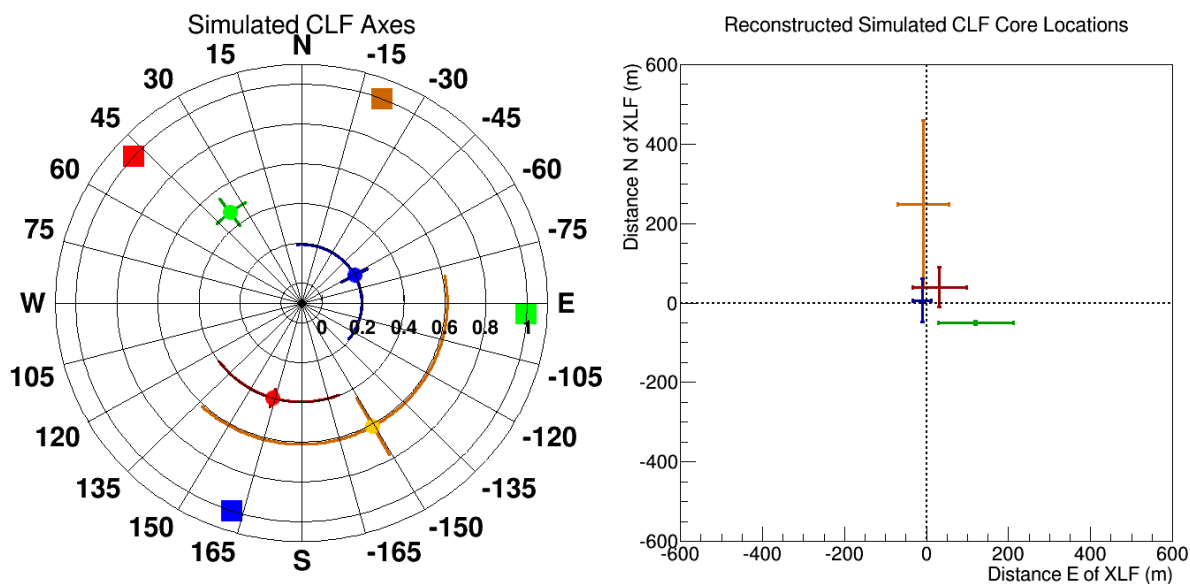
(a) Average Axis Reconstructions for Simulated CLF (b) Average Core Reconstructions for Simulated CLF
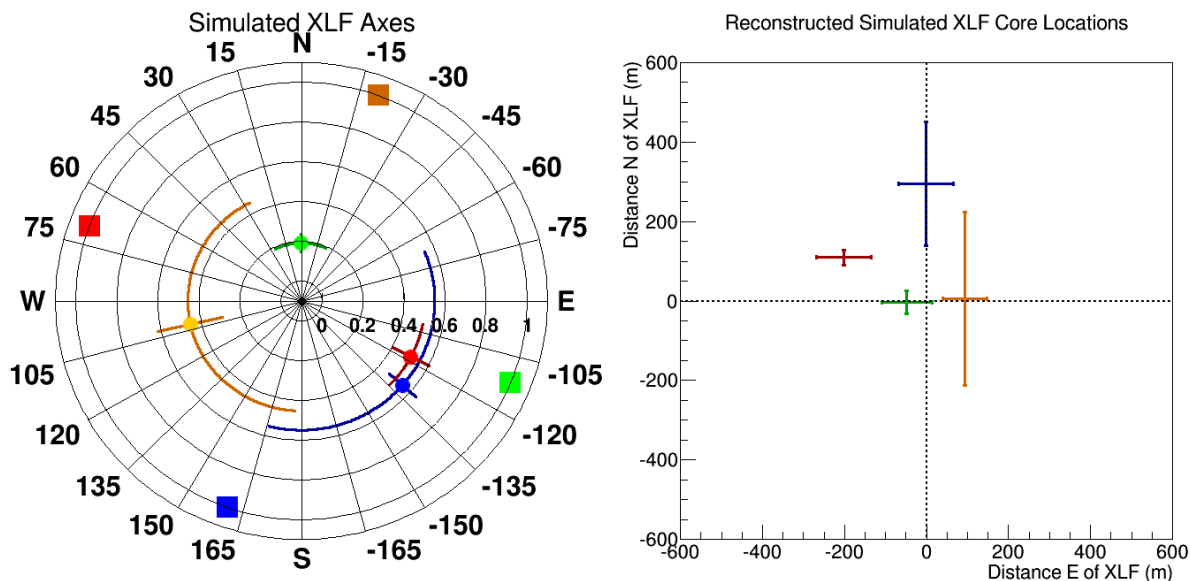
(c) Average Axis Reconstructions for Simulated XLF (d) Average Core Reconstructions for Simulated XLF
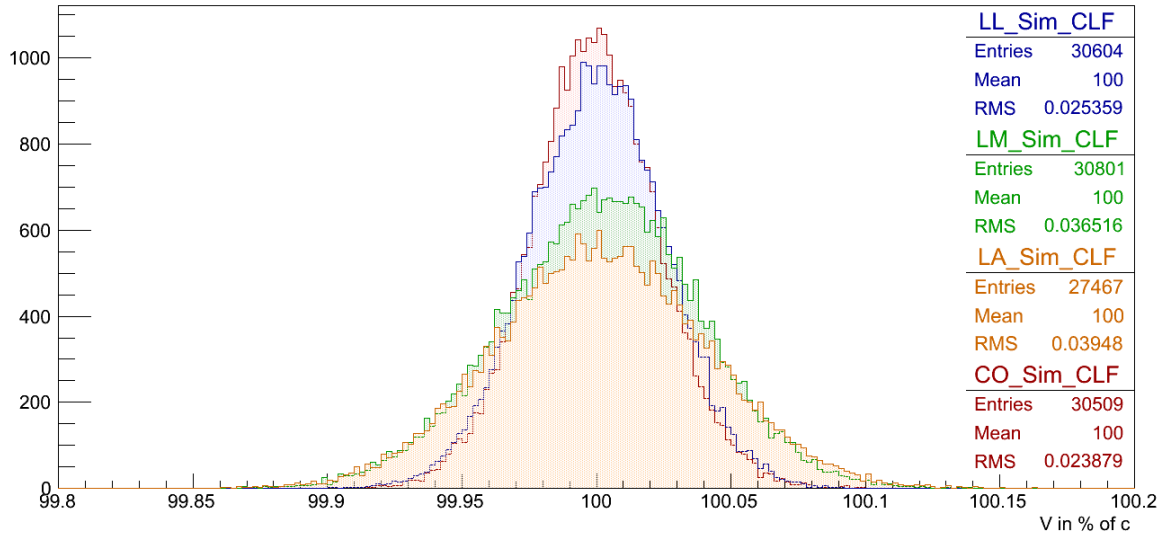
Figure 5.13: Observer Reconstructed Simulated Laser Geometries: the Auger Standard reconstruction for simulated perfectly vertical laser shots from both facilities. In (a) and (c) the average reconstructed axis from each Eye is displayed with errors. The radial coordinate represents the Zenith angle and the polar coordinate is the Azimuth, as indexed from north. The squares represent the angular location of each Eye. Both (b) and (d) show the average reconstructed UTM core locations from each Eye. The center of the plot represents the actual location of each laser facility as measured in a GPS survey

lation sample in spite of the possible $\overline{\text{Off}\underline{\text{line}}}$ problems. Because the error, whatever it may be, has the effect of shifting the geometry of the simulated events for each Eye, if that shift is accounted for in the FixedGeometryVelocityFinder, then, if both propagation model and fitting procedure are sound, the reconstructed velocity distribution for the simulated lasers should now be centered at c. This in turn, would show that the error is indeed upstream from the FixedGeometryVelocityFinder. To do this, the correct CLF and XLF location and firing geometries were replaced with the average values shown in Table 5.2 in the FixedGeometryVelocityFinder. The module was then run again to reconstruct the simulated laser velocities at these new geometries resulting in the distributions for the CLF shown in Figure 5.14(a) and the XLF in Figure 5.14(b).

The velocity distributions in Figure 5.14(a) and Figure 5.14(b) very clearly sit at the expected value of c. Furthermore, and importantly so, the RMS for all Eyes for both lasers are nearly identical to the RMSs produced for the unchanged geometries. This means that though the mean shifts, the precision of the velocity reconstruction is unchanged and trustable in spite of the problem detected with $\overline{\text{Off}\underline{\text{line}}}$. Hence, though the FixedGeometryVelocityFinder is affected by the apparent $\overline{\text{Off}\underline{\text{line}}}$ problem, the important result quantifying the resolution of the method with simulations remains valid. Now in order to see if the FixedGeometryVelocityFinder is likewise stable and sound for real atmospheres and the actual detectors, the geometry offset study should be carried out on the real data.

As expected, the results are substantially more noisy for real data as compared to the simulated data set. Both Figure 5.15(b) and Figure 5.15(d) show systematic offsets from the CLF location, but to what degree they are meaningful is difficult to tell. Loma Amarilla misreconstructs the CLF location by 1.4 km and Los Leones misses the XLF by a full kilometer, but with a mean error of 4.6 km and 3.8 km its hard to trust those numbers. All other Eyes, excluding Los Morados' reconstruction of the CLF, do see larger core position errors than in the simulations, but again have error bars that make interpretation difficult. The angular axis reconstruction offsets seen in Figure 5.15(a) and Figure 5.15(c) are a little easier to

Simulated CLF Laser Velocities With Geometry Change

(a) Simulated CLF

Simulated XLF Laser Velocities With Geometry Change
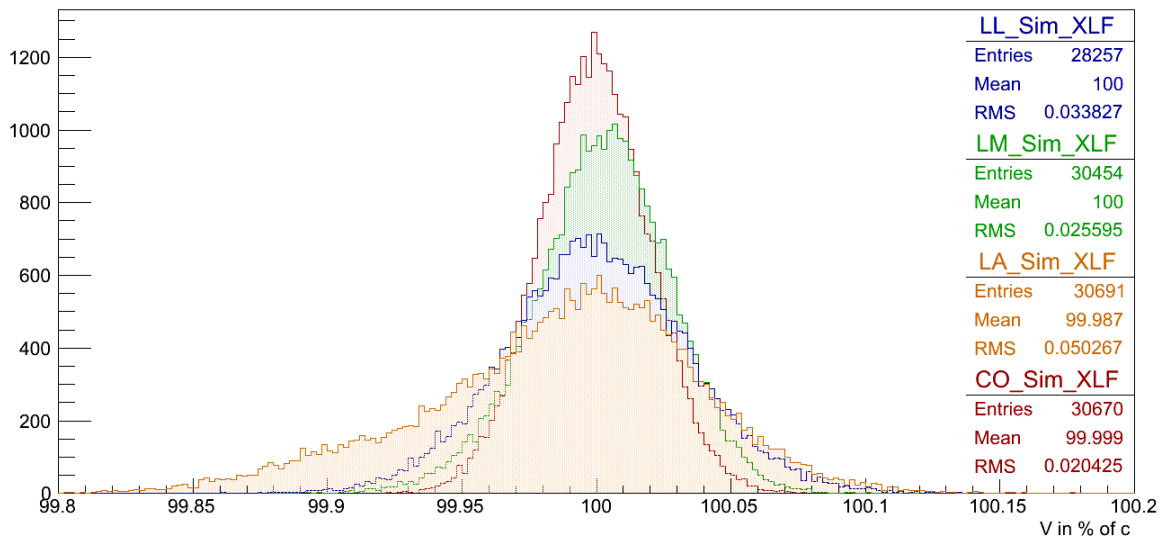
(b) Simulated XLF

Figure 5.14: Simulated Laser Velocities Reconstructed at Observer Geometries: the reconstructed velocities for simulated laser shots when the geometry for each Eye is changed in the reconstruction to mirror the geometry reconstructed by Observer.
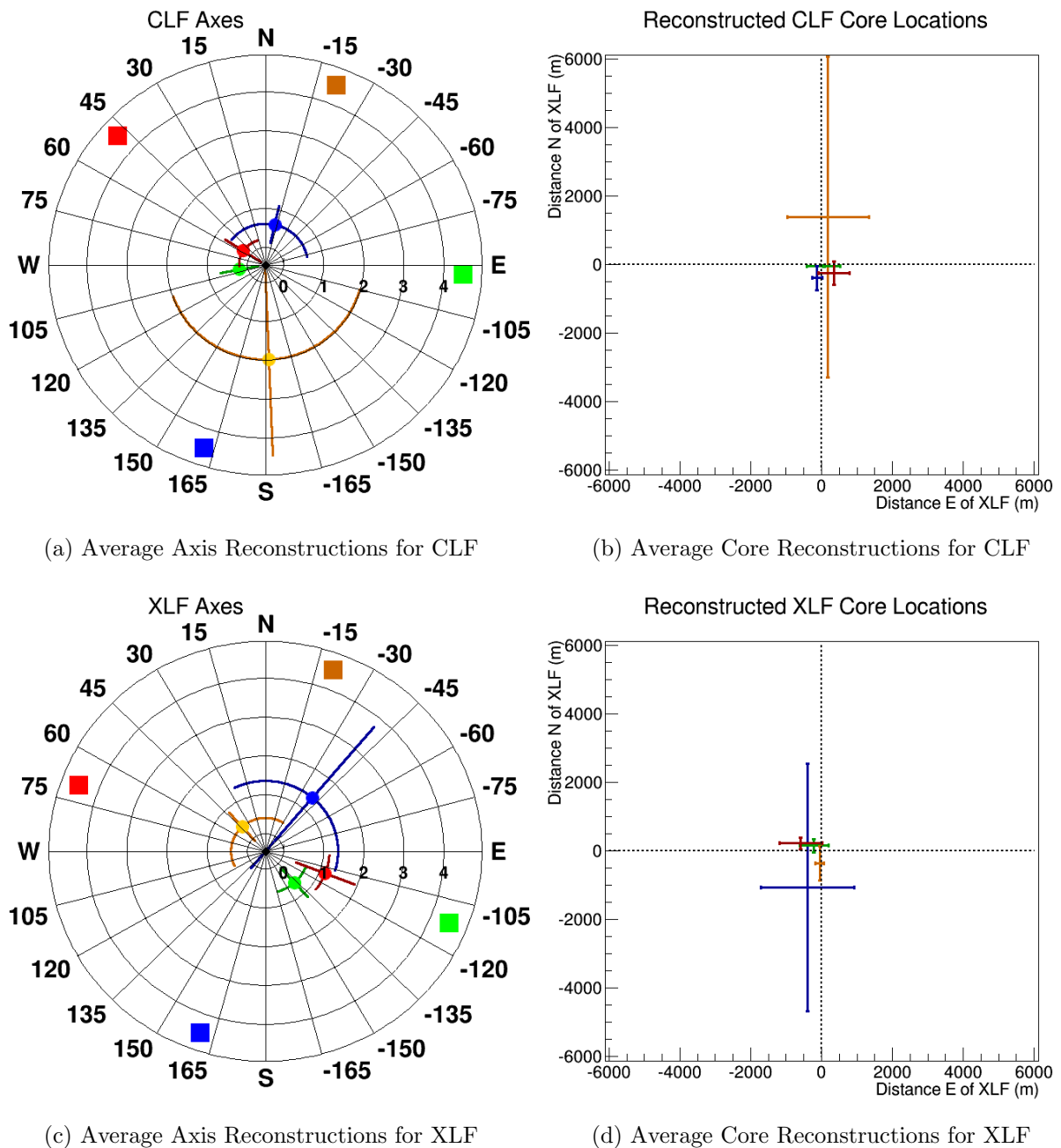
103

(a) Average Axis Reconstructions for CLF

(b) Average Core Reconstructions for CLF

(c) Average Axis Reconstructions for XLF

(d) Average Core Reconstructions for XLF

Figure 5.15: Observer Reconstructed Laser Geometries: the Auger Standard reconstruction for all vertical laser shots fired from both facilities from January 2007 through December 2013 during clear cloudless nights. In (a) and (c) the average reconstructed axis from each Eye is displayed with errors. The radial coordinate represents the Zenith angle and the polar coordinate is the Azimuth, as indexed from north. In (b) and (d) the average reconstructed UTM core locations from each Eye are seen. The center of (b) and (d) represents the actual location of each laser facility as measured in a GPS survey.

judge. Each Eye has an offset from vertical exceeding its error bars with the exception of Loma Amarilla for the CLF and Los Leones for the XLF, which have huge error bars and miss vertical by 1.46° and 1.99° respectively.

Table 5.3: The Average Observer Reconstructed Real CLF and XLF Geometries.

Laser/Eye	Zenith (deg)	Azimuth (deg)	UTM N Error (m)	UTM E Error (m)
CLF LL	0.610 ± 0.482	-13.0 ± 66.4	-393.0 ± 346.51	-121.1 ± 146.76
CLF LM	0.207 ± 0.473	100 ± 7.72	-47.2 ± 23.646	57.3 ± 477.75
CLF LA	1.985 ± 2.47	-177.9 ± 73.3	1389.7 ± 4682	181.3 ± 1153.2
CLF CO	0.208 ± 0.528	56.5 ± 38	-251.3 ± 333.12	346.2 ± 434.77
XLF LL	1.360 ± 2.38	-40.4 ± 66.3	-1072.2 ± 3616.6	-394.2 ± 1320.8
XLF LM	0.632 ± 0.5	-132 ± 25.5	154.7 ± 190.13	-211.2 ± 412.47
XLF LA	0.407 ± 0.481	42.3 ± 74	-360.6 ± 502.94	-49.9 ± 126.4
XLF CO	1.145 ± 0.775	-111.9 ± 17.4	218.9 ± 169.48	-582.7 ± 594.37

Table 5.3 contains the exact values for the geometric reconstruction errors. It shows that there are large geometric offsets, but these are definitely muddled by the greatly increased uncertainties. These uncertainties show the effects of a real variable atmosphere, changes in the alignment and strength of the laser facilities and the complexity and uncertainty involved in correctly quantifying the real detector response, and are therefore more in line with what the quoted uncertainties are meant to deal with. Even with these uncertainties, the geometric offsets greatly exceed those seen in the simulations suggesting that there may be more than just the possible $\overline{\text{Off}\underline{\text{line}}}$ issues amiss in these real world Observer reconstructions. To investigate whether or not these average values can be trusted, and to see if the FixedGeometryVelocityFinder is handling the data correctly, again the FixedGeometryVelocityFinder was altered to replace correct CLF and XLF location and firing geometries with the average values shown in Table 5.3. If the velocity reconstruction returns a mean value of c then the FixedGeometryVelocityFinder is not the source of the issues and the geometric offsets seen in Table 5.3 can be trusted to be representative of the data in spite of their large error bars.

Again with the exception of LA for the CLF and LL for the XLF, the two farthest measurements, overall the geometry change worked on the real data as well as it did in
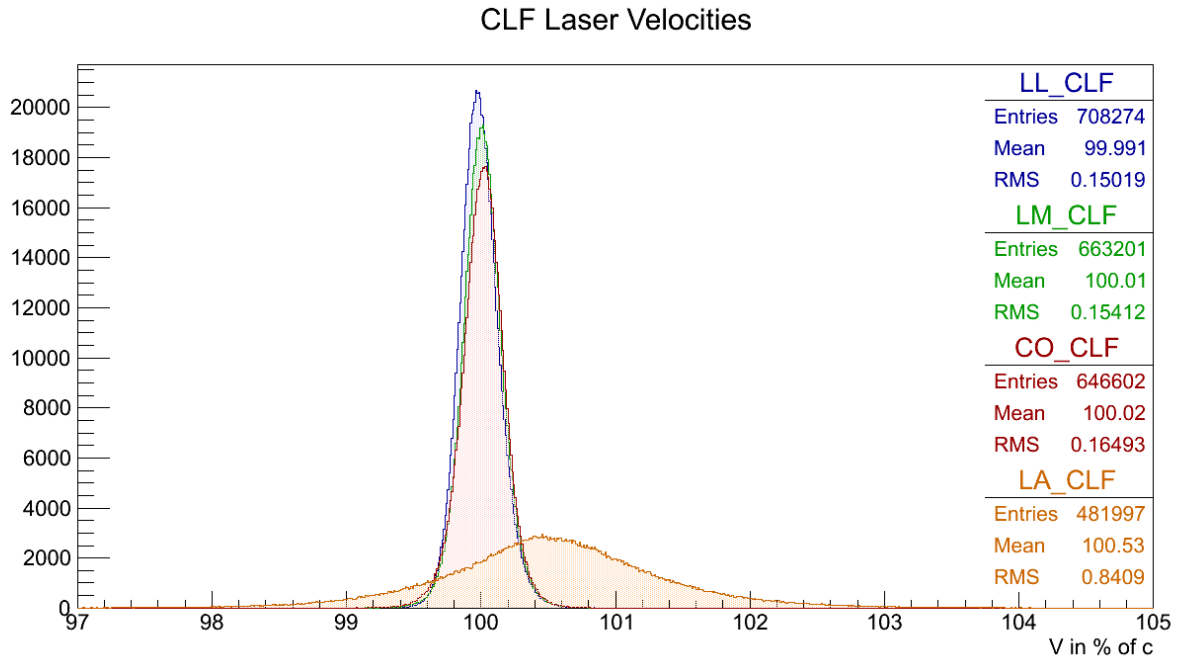
(a) CLF
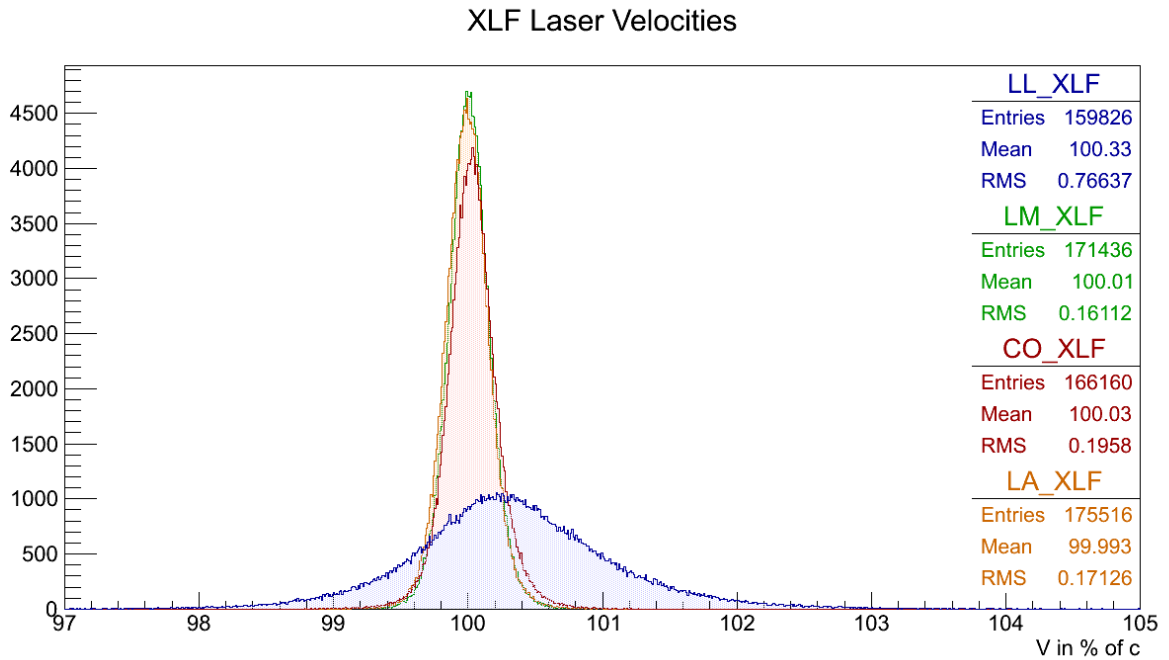
(b) XLF

Figure 5.16: Real Laser Velocities Reconstructed at Observer Geometries: the reconstructed velocities for real laser shots fired from 2007 through 2013 when the geometry for each Eye is changed in the reconstruction to mirror the geometry produced by Observer.

simulations. This strongly suggests that $\overline{\text{Off}\underline{\text{line}}}$ and detector effects are mostly responsible for the offsets observed in the original laser velocity plots. The remaining offset of $\sim 0.5\%$ of C seen for Loma Amarilla in Figure 5.16(a) and $\sim 0.3\%$ of C seen for Los Leones in Figure 5.16(b) are probably due a combination of effects. Obviously the large uncertainties in their geometric reconstruction values make it unlikely that the absolutely correct values for the geometric offset were used in this geometry change. Second, given the size of the increase and the fact that Los Leones' average moved from c to 100.3% of c when the geometry was changed suggests that the unaccounted for light bending effect described in, Figure 5.8 is largely responsible for the remaining offsets.

Due to the shear size and complexity of the array and the code used to interpret the data from it, it is extremely difficult to discern the exact causes of the offsets. This study, does however, provide good hints that the following may be what is going on:

- The Eye's mirrors or cameras or the laser facilities may be misaligned, or there is an Eye dependent timing issue that is specific to the pixel geometries triggered by vertical events.

  The fact that the reconstructions of simulations did not display the offsets seen in the real data suggests that the real world instrumentation is not quite accurately represented in the $\overline{\text{Off}\underline{\text{line}}}$ detector description. This could be in the form of laser facility, camera or mirror misalignments, or by a mishandling of the pixel geometries and responses in vertical events. This idea is reinforced by studies done later on stereo and hybrid lasers in 6.4 and 7.4.

- Somewhere in the core of $\overline{\text{Off}\underline{\text{line}}}$ (probably the detector description) or the simulations, there is a problem that causes the event timing to be miscalculated by up to 0.4%.

  This is evident given the fact that all Eyes saw nearly the same velocity of 100.4% of c while duplicating the exact geometry thrown by the simulations. This is further reinforced by the widely varying results of the observer geometric reconstruction of

simulated data as well as the results of the stereo reconstructions of lasers done in Section 6.4

- The light bending effect described in [51] causes the apparent event velocity to increase by 0.3% to 0.5% of c when distances increase from 30 to 40 km.

  This is strongly supported given that in Los Leones and Loma Amarilla the CLF and XLF trigger nearly identical lines of pixels, yet in Figure 5.11(a) and Figure 5.11(b) both Eyes see a common increase in velocity when the reconstructions of the closer laser facilities are compared to those that are farther away. The residual offsets seen in Figure 5.16(a) and Figure 5.16(b) seem to confirm this. It is possible that this is instead due to the CLF pointing toward Los Leones, and the XLF pointing toward Loma Amarilla, but this is unlikely given the frequent recalibration of the laser facilities.

5.5 The FD Velocity Sensitivity and Resolution

This chapter was intended to simply examine the maximum velocity sensitivity and accuracy of the FD in order to set expectations for, and motivate, the more complex shower sensitive methods to come. Clearly the process of setting realistic expectations for these aspects of a velocity based exotics search are more complex than originally anticipated. However because the basis of the velocity method requires extraordinary accuracy and provides a clear indication of divergence from the correct result, potential problems within the Observatories instrumentation and the analysis software that sat unrecognized for years were highlighted. This alone is a significant result of the method and shows that the fixed geometry velocity reconstruction holds promise as a means of testing the behavior and stability of the instrumentation as well as the accuracy of $\overline{\text{Off}\underline{\text{line}}}$'s data preparation and reconstruction. It is unfortunate that due to the complexity of the problem, the exact causes for the observed offsets could not be found. It is important to remember that this laser study is not the primary focus of the research and should not be advanced at the expense of the original goal of searching for evidence of exotic phenomena in the cosmic ray spectrum.

By developing a simple propagation model in Section 5.1 and using it to test the T2 acceptance at the full range of event geometries in Section 5.2 it was definitively shown that the FD is capable of measuring showers at a wide range of velocities. The results of the slowed laser simulations in Figure 5.6 show that the predicted velocity sensitivity does accurately reflect what the simulated detector is capable of seeing, and that the FD and the velocity dependent propagation model is capable of correctly recognizing and reconstructing the evolution velocity of slow-moving events. This clearly states that the foundation of the velocity based search is sound.

Section 5.3 took the simple velocity dependent model from Section 5.1 and added in the corrections for the atmosphere and the earth's curvature that will be necessary later in the exotic candidate searches. This more complete model was then applied to vertical laser data in order to ascertain the resolution and accuracy of the velocity reconstruction method for real world events traveling at the speed of light, as this information is critical to setting quality cuts and search criteria in later studies. Things this point on became somewhat less straight forward as offsets from the correct result were observed and the velocity dependent propagation model needed to be ruled out as a cause. By investigating the response of the FixedGeometryVelocityFinder to both simulations and real data and verifying that the method correctly reproduces the speed of light when the effect is accounted for prior to the velocity reconstruction, the general integrity of the method was validated.

In the end, the important questions to be answered are: on average, with what accuracy and resolution can the FDs and the velocity reconstruction methods measure the speed of an observed event; and is it sufficient to carry out a search for exotic slow moving events? Indeed, each Eye showed a distinctly different response to the laser light and this effect could potentially carry forward to the reconstruction of showers. However, when this offset was corrected, the form of the distributions remained stable on an Eye by Eye basis. This means that as long as candidate selection is based off the form of the parent distribution and is carried out on an Eye by Eye basis whenever possible, then the offsets will have no effect

on the viability of a search. Likewise, with distribution uncertainties of less than $\sim \pm 0.84\%$ of c and maximum centroid offsets no larger than $\sim 1.25\%$ of c it is clear that the FDs are sensitive to velocity and can reliably produce stable self-consistent distributions with low error. Furthermore, it is not clear that these offsets will carry to non-vertical geometries and may only apply to the very small portion of showers that are nearly vertical. These possibilities are investigated using lasers fired at varied geometries further on with methods capable of handling non-vertical events and the effects are shown to vanish. Regardless, the laser studies show that selection of outlying events based on their relative position in the distribution as a whole is valid within a conservative velocity resolution of $\sqrt{0.84^2 + 1.25^2} \approx 1.5\%$ of c.

VELOCITY RECONSTRUCTION: STEREO OBSERVATIONS

It is clear that in order to accurately reconstruct the velocity of a cosmic ray event, the location and geometry of the event's shower axis needs to be very well constrained by the data. As explained in 3.5.4, stereo observations provide the most data on a single event out of all observation types possible at the Observatory. Because any stereo observation includes data from multiple angles, simply by cross correlating the SDPs the event geometry is already constrained to a very narrow region. Adding the timing information from each Eye constrains the possible event geometry even further. This makes stereo observations and the stereo event dataset, a very natural place to begin reconstructing the velocity of cosmic ray events.

6.1   The Stereo Velocity Reconstruction

Out of design, the stereo velocity reconstruction adheres as closely as possible to the Pierre Auger Observatory standard stereo reconstruction explained in 3.5.4. The principal changes to the overall method come in the form of altering the standard stereo propagation model, (3.15), to include a free velocity parameter, the atmospheric corrections outlined in Section 5.1 and a minor correction aimed at accounting for the fluorescence emission time.

First, the geometric timing model needs to be changed in two places. Primarily, like the model developed in Section 5.1, the shower timing needs to be separated into the component that describes the evolution of the shower (t_{shower}) and that which describes the propagation of the fluoresced light to the detector ($t_{fluoresce}$). However, because we are now looking at showers that propagate downward, t_{shower} is subtracted from T_0 as, using the geometry shown in Figure 6.1, the observed point on the shower occurred before the shower passed P_{Rp} and therefore occurred, earlier than T_0. With these changes to (3.15) the velocity dependent
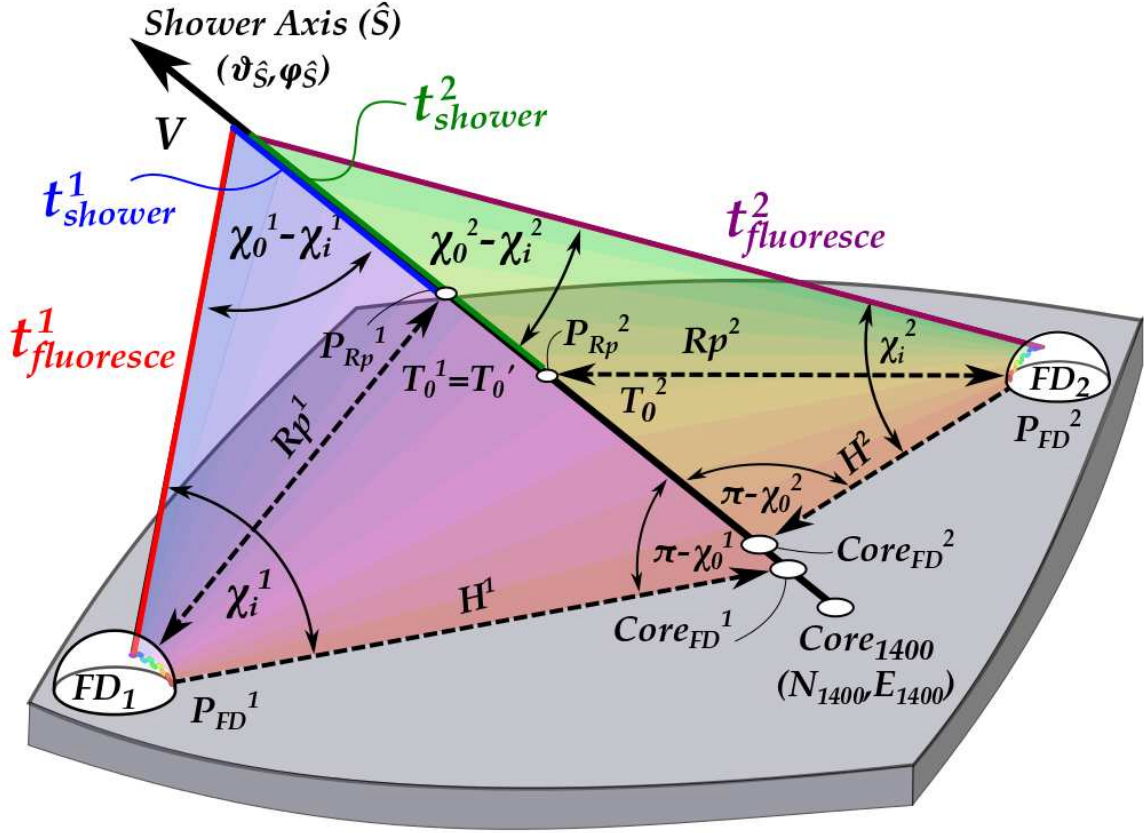
Figure 6.1: The Geometry of the Stereo Method with Free Velocity: Like the standard case, FD_1 is the lowest indexed observing Eye so it is regarded as Eye'. The SDP of each Eye is represented by the colored portion. The white dots represent important geometric points. The blue and dark green lines represent the shower propagation time for Eyes 1 and 2. The red and purple lines represent the fluoresced light propagation time.

equation takes the form

$$t_i^{Eye} exp = T_0 + t_{fluoresce} - t_{Shower} = T_0 + \frac{Rp}{c_{air} \sin(\chi_0 - \chi_i)} - \frac{Rp}{V \tan(\chi_0 - \chi_i)}. \qquad (6.1)$$

Using Figure 6.1 and placing this new separated model in to (3.15) the stereo propagation model takes the form,

$$t_i^{Eye} exp = T_0^{Eye} + \frac{Rp^{Eye}}{c_{air} \sin(\chi_0^{Eye} - \chi_i^{Eye})} + \frac{Rp^{Eye}}{v \tan(\chi_0^{Eye} - \chi_i^{Eye})}, \qquad (6.2)$$

where again equations (3.16) to (3.24) are used to find R_p, χ_0 and T_0 for each Eye using only the shower parameters, but now with V added ($\theta_{\hat{\mathbf{S}}}$, $\phi_{\hat{\mathbf{S}}}$, N_{1400}, E_{1400}, T_0' and V). Because the

shower now travels at a speed V instead of a set c, (3.22) needs to be changed to the form

$$T_0^{Eye} = T_0' + \frac{P_{Rp}^{Eye} - (P_{Rp}^{Eye'})}{V}.$$ (6.3)

Next, the effects of the atmosphere need to be added to the model. Again the bending effects outlined in Section 5.1 will not be accounted for due to the shear difficulty of the corrections, however, the altitude dependent slowing effects of $n(h)$ will again be added to (6.2) by including the effective speed of light for each pixel $(c_i'^{Eye})$. The expression for $t_i^{Eye}exp$ now has the form

$$t_i^{Eye}exp = T_0^{Eye} + \frac{Rp^{Eye}}{c_i'^{Eye} \sin{(\chi_0^{Eye} - \chi_i^{Eye})}} + \frac{Rp^{Eye}}{v \tan{(\chi_0^{Eye} - \chi_i^{Eye})}}.$$ (6.4)
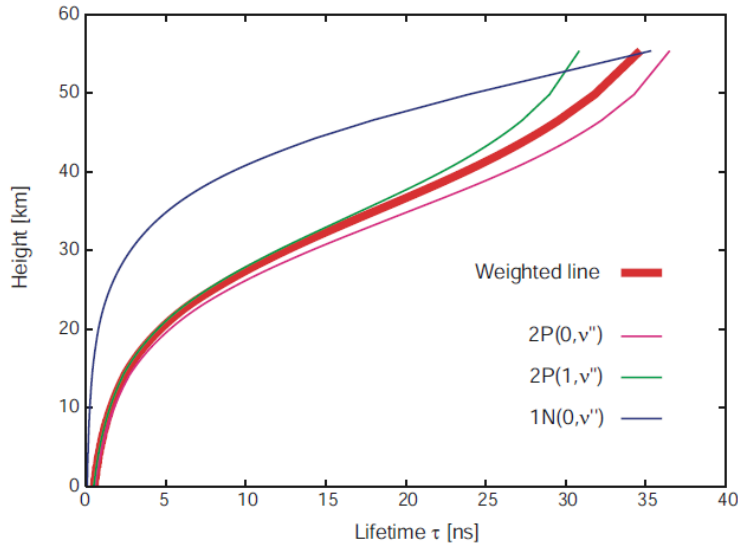
Figure 6.2: The Height Dependence of Nitrogen Emission Lifetimes: the emission lifetime of atmospheric Nitrogen has dependences on temperature and pressure which vary strongly with height. The thin lines represent the calculated height dependent lifetimes $(\tau(h))$ of the major spectral components of Nitrogen fluorescence. The bold red line shows the spectrally weighted average [51].

The last correction to the model stems from the fact that the excitation and de-excitation of Nitrogen in the atmosphere by charged particles is non-instantaneous. As shown by Kümpel in [51], typical Nitrogen emission lifetimes $(\tau(h))$ are small, $\sim 40ns$, but as can be seen in Figure 6.2, drop significantly as the altitude decreases due to quenching effects. This

speed-up in the emission time as the events move to lower altitude increases the angular velocity of the event across the camera meaning the event appears to move faster than it does. To account for the emission lifetime and its variation, the lifetime at the observed point on the shower for each pixel (τ_i) needs to be added to (6.4), altering its form to

$$t_i^{Eye} exp = T_0^{Eye} + \frac{Rp^{Eye}}{c_i'^{Eye} \sin{(\chi_0^{Eye} - \chi_i^{Eye})}} - \frac{Rp^{Eye}}{v \tan{(\chi_0^{Eye} - \chi_i^{Eye})}} + \tau_i, \qquad (6.5)$$

where τ_i is calculated using the height of the ith pixel's observation on the shower axis, the atmospheric profile provided by GDAS and models predicting the emission time and quenching effect at different temperatures and pressures. This lifetime calculation is performed by an $\overline{\text{Offline}}$ function using the test geometry of the event, the time it occurred and the location of each observing Eye.

At this point (6.5) is fit to the t_i^{Eye} and χ_i^{Eye} values recorded by the event using a χ^2 minimization. The addition of the velocity to the stereo model does not change the χ_{Stereo}^2 functions and therefore they are used unaltered in the stereo velocity reconstruction. To refresh, by combining (3.12), (3.13) and (3.14) we get the full general stereo χ^2 fit equation which takes the form

$$\chi_{Stereo}^2 = \sum_{Eyes} \sum_i \left(\frac{(T_i^{Eye} - Texp_i^{Eye})^2}{(Terr_i^{Eye})^2} \right) + 4 \sum_{Eyes} \sum_i \left(\frac{(\pi/2 - \arccos{(\hat{\mathbf{r}}_i^{Eye} \bullet \hat{\mathbf{n}}_{SDP}^{Eye}))^2}}{(\hat{\mathbf{r}}_i^{Eye} err)^2} \right) \qquad (6.6)$$

6.2   StereoVelocityFinder Module

As shown in Section 5.1, when performing a velocity reconstruction it is difficult to account for the intricacies of the detector and the data it collects. Because of this, it is difficult to know whether the results of a velocity reconstruction are truly representative of the data or are tainted by the implementation of the reconstruction itself. It is therefore important to build the software in a way that lends as much credibility to it as possible. It was therefore decided that the $\overline{\text{Offline}}$ standard stereo reconstruction would be adhered to as closely as possible to ensure that the velocity reconstruction reproduces the results of the

standard module when the velocity is reconstructed to be c.

```
<moduleControl>
  <loop numTimes="unbounded" pushEventToStack="yes">

    <module> EventFileReaderOG        </module>
    <module> FdEventSelectorKG        </module>
    <module> EventCheckerOG           </module>

    <module> FdCalibratorOG           </module>
    <module> FdPulseFinderOG          </module>    Observer Standard
    <module> PixelSelectorOG          </module>
    <module> FdSDPFinderOG            </module>
    <module> FdAxisFinderOG           </module>
    <module> StereoGeometryFinderOG   </module>

    <module> StereoVelocityFinder     </module>   Velocity Reconstructor

  </loop>
</moduleControl>
```

Figure 6.3: The Stereo Velocity Reconstruction Module Sequence: The module sequence used to reconstruct the velocity of stereo measured events. The first part is exactly the Auger standard stereo geometry reconstruction. The StereoVelocityFinder performs the velocity reconstruction using the results of the preceding modules.

In Auger $\overline{\text{Off}\underline{\text{line}}}$, the standard stereo reconstruction is carried out by a module called the StereoGeometryFinderOG, which sits toward the end of the Observer stereo reconstruction module sequence just before the light profile reconstruction and data writing modules. Figure 6.3 shows the Observer standard module sequence minus any profile reconstruction modules as they are unneeded for this analysis. After this standard stereo reconstruction, the velocity reconstruction module is run so that it can use the standard reconstruction results as a first guess. Neglecting the stereo hybrid functions which are unused in this research, the StereoGeometryFinderOG module can be considered to consist of two parts:

Data Collection

In data collection the event data and parameters needed for the stereo reconstruction are grabbed from the event data structure. The data used is not the raw event data, but the data that has been prepared by the modules that come before it in the module sequence. The main purposes of this part of the module is to verify that the event

115

meets the minimum requirements necessary for stereo reconstruction, to grab the event data to be fit and to give the geometric reconstruction values for an initial guess.

Geometric Reconstruction

The geometric reconstruction is the portion of the module that fits the stereo propagation module to the event data being handed to it by data collection. This part of the module is split into two sub functions: one that sets up the χ^2 fit method, tolerances and parameters called FindAxis, and one that calculates the χ^2 value of each iteration of the fit called the MinuitFitFunction.

To build the stereo velocity reconstruction module, here on referred to as the StereoVelocityFinder, the StereoGeometryFinderOG module was used as a starting point. Much of the data loading, preparation and fitting procedures were used verbatim, but in order to accurately fit the shower velocity, changes to both the MinuitFitFunction and FindAxis functions were needed. The MinuitFitFunction was altered to incorporate the changes outlined in Section 6.1. The FindAxis function was changed to add the velocity as a free parameter and to tweak the χ^2 fit setup to address the possibility of runaway fits due to the destabilization caused by adding velocity as a parameter. At the end of the module, a new function was added to calculate and externally store a wide range of variables in a ROOT TTree structure for subsequent analysis.

6.3 Velocity Sensitivity Range

As seen in Figure 6.4(a) and Figure 6.4(b), by geometric necessity, at least one Eye must have an Eye to core distance ($D_{Eye2CoreFD}$) greater than or equal to half the distance between it and the other triggered Eye ($D_{Eye2Eye}$). This means that at absolute minimum, in stereo events, one Eye must be have $D_{Eye2CoreFD} \geq 20.3km$, or half the distance between CO and LA, the two closest Eyes. Because an event can only be measured in stereo if both Eyes are capable of observing it, the geometry of both observing Eyes needs to be weighed simultaneously while calculating the stereo velocity sensitivity. Since it is impossible for
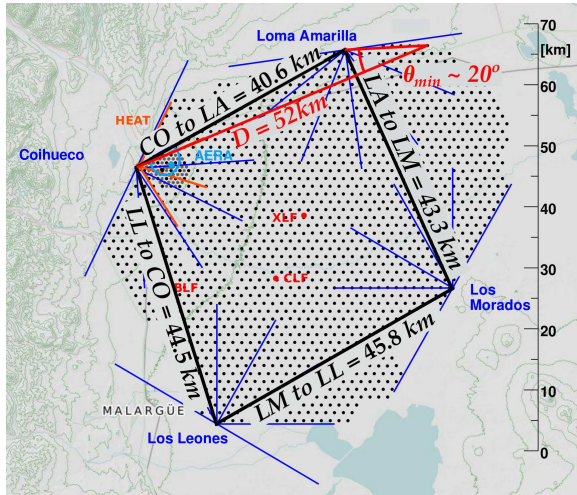
(a) The Distance Between Eyes
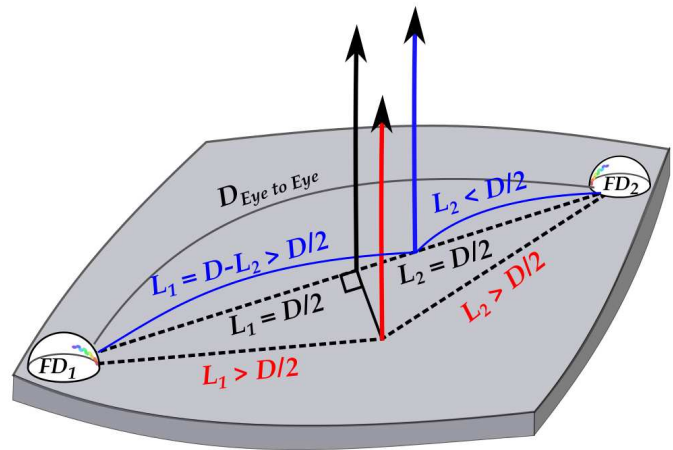
(b) The Minimum Stereo Event Geometries
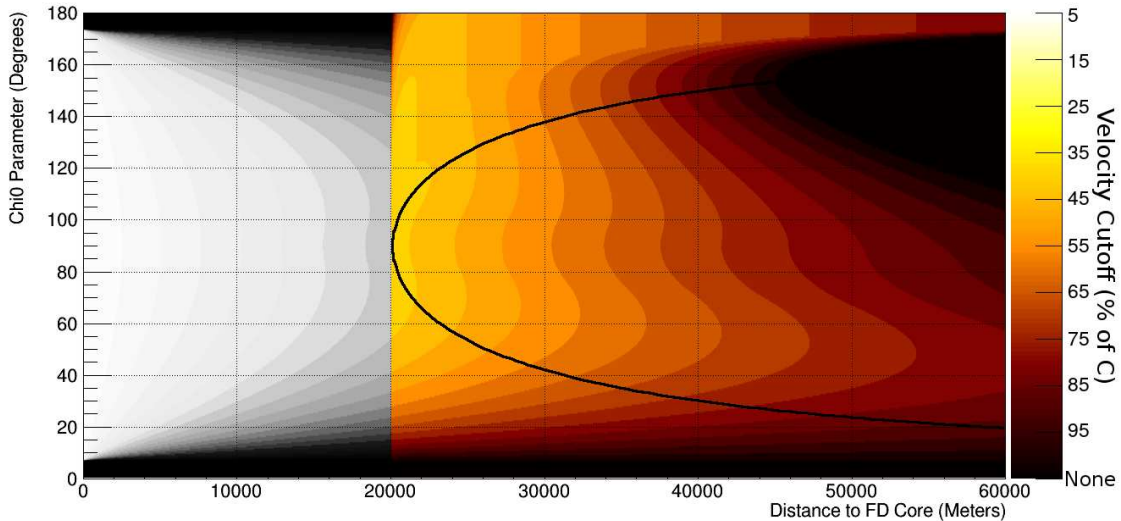
(c) The Maximum Velocity Sensitivity for Stereo Events

Figure 6.4: Stereo Velocity Sensitivity: the minimum distance and geometry a stereo event can have to maximize velocity sensitivity occurs for a vertical event with origin halfway between the two observing Eyes. The gray portion in (c) is less than half the distance between CO to LA, the minimum Eye to FD core distance for a stereo event and therefore is forbidden. The area inside the curve in (c) represents the region where the χ_0 of both Eyes can be the same due to the FD core not laying directly between the observing Eyes. Outside this curve, $\chi_{01} + \chi_{02} + \chi_{0curve} \leq 360°$ due to the requirements of tetrahedral geometries resulting in the features seen.

117

both Eyes to have $D_{Eye2CoreFD} < 20.3$, stereo is simply not sensitive to events with these geometries giving rise to the grayed-out portion of Figure 6.4(c).
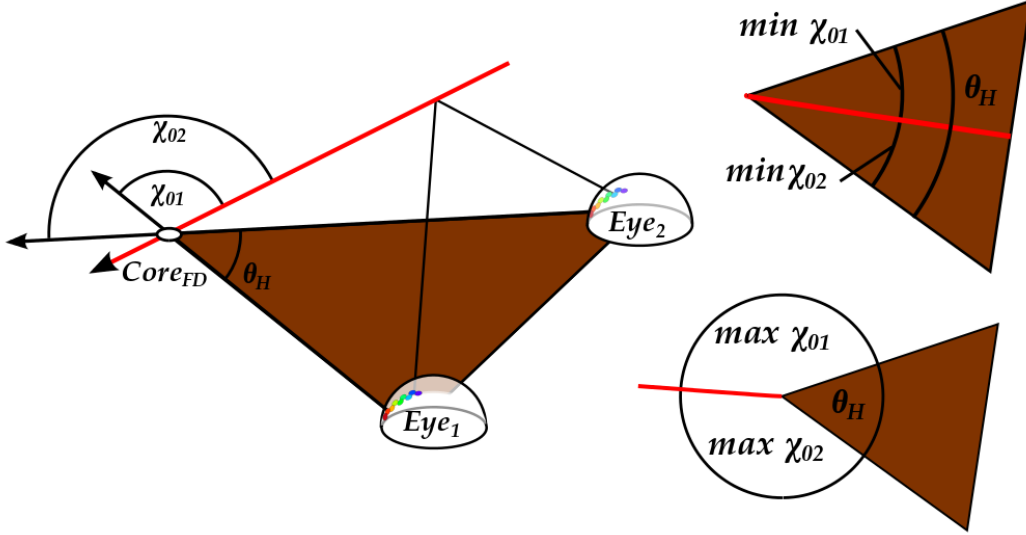
Figure 6.5: Intersection Angles of a Stereo Event.

The velocity sensitivity with respect to χ_0 is more complicated. When two Eyes observe the same axis, each Eye's SDP and the plane on the ground can be approximated to form the corner of a tetrahedron, as shown in Figure 6.5. By geometric necessity, the sum of the interior angles of a tetrahedron must be less than or equal to 360°. This requirement restricts the possible χ_0 angles of the two observing Eyes based on the angle at which their horizontal vectors intersect (θ_H). As seen in Figure 6.5, in order for both Eyes to share the same χ_0, each Eye's χ_0 can not exceed $180 - \theta_H/2$ or be smaller than $\theta_H/2$. For any triangle with $\theta_H \leq 60°$, the smallest possible θ_H for the shortest leg lengths occurs in isosceles triangles. For an isosceles triangle with a base of length $D_{Eye2Eye}$, the angle of the point (θ_H) in terms of leg length ($D_{Eye2CoreFD}$) is

$$\theta_H = 2\arcsin\left(\frac{D_{Eye2Eye}}{2D_{Eye2CoreFD}}\right). \tag{6.7}$$

Therefore, the maximum flexibility in χ_0 for the minimum $D_{Eye2CoreFD}$ occurs when the $core_{FD}$ sits equidistant from the two observing Eyes. Outside of this curve any gains in χ_0

flexibility are greatly offset by the larger distance to the $core_{FD}$. Therefore, the maximum shared χ_0 value ($\chi_{0shared}^{max}$) is restricted to

$$\arcsin\left(\frac{D_{Eye2Eye}}{2D_{Eye2CoreFD}}\right) \leq \chi_{0shared}^{max} \leq 180 - \arcsin\left(\frac{D_{Eye2Eye}}{2D_{Eye2CoreFD}}\right), \qquad (6.8)$$

giving rise to the black curve seen in Figure 6.4(c). Inside this curve both Eyes can share the same χ_0 and $D_{Eye2CoreFD}$ values. Therefore, because the velocity sensitivity is maximized when both Eyes have a common geometry, the velocity sensitivity within this curve is identical to that seen in Section 5.2. Outside this curve, geometries must still obey the relationship $\theta_H \leq \chi_{01} + \chi_{02} \leq 360°$, meaning that as one Eye's χ_0 value (χ_0^{ex}) becomes larger or smaller than the limits of $\chi_{0shared}^{max}$, the χ_0 range available to the other Eye is limited to

$$chi_0 \leq 2\chi_{0shared}^{max} - \chi_0^{ex} \qquad (6.9)$$

for $\chi_0^{ex} > \chi_{0shared}^{max}$ and

$$chi_0 \geq 2\chi_{0shared}^{max} - \chi_0^{ex} \qquad (6.10)$$

for $\chi_0^{ex} < \chi_{0shared}^{max}$. This means that in these geometries, stereo is only sensitive to velocities that are simultaneously measurable on both sides of this curve, giving rise to the odd structure seen at large χ_0 values in Figure 6.4(c). With these effects taken into account, the stereo method is found to be sensitive to events with velocities no slower than $\sim 40\%$ of c.

6.4 Laser Distributions and Interpretation

In order to briefly see how the effects observed in Section 5.4 apply to stereo velocity reconstructions, the sample of laser events that are included in the Observatory's stereo event data stream were reconstructed. These laser shots are fired at a specific GPSns that is different from the calibration shots analyzed in Section 5.4 and are measured like cosmic ray events, allowing for CDAS to cross correlate the observations from many Eyes. This in turn allows them to be measured and reconstructed as stereo events. Additionally, as seen in Figure 6.6(a), this laser event set includes both vertical and inclined events, providing a means to investigate whether the errors of Section 5.4 are restricted to just vertical events or

could possibly extend to every measured event. Applying the stereo reconstruction technique, as well as the quality cuts described in the next section, results in the distributions seen in Figure 6.6(b).

The distributions in Figure 6.6(b) show two behaviors worth commenting on:

- Stereo reconstructions of vertical laser events fired from both the CLF and XLF see a centroid offset that is similar to the offset seen for the simulated laser events in Section 5.4. This confirms that there are problems somewhere in the chain of $\overline{\text{Off}\underline{\text{line}}}$ event reconstructions or in the detector description. The fact that the offset of the vertical events resembles the results of the simulations more closely than the distributions of real laser events, suggests that the individual issues with the Eyes canceled out while the problems in $\overline{\text{Off}\underline{\text{line}}}$ did not.

- Stereo reconstructions of inclined events do not display this offset.

This shows that the problem in the earlier laser studies are confined only to vertical events. This is good news for a velocity-based search as, by solid angle, vertical events represent a very small portion of the FD's exposure. This in turn means that the vast majority of reconstructed shower events will not be strongly affected by the offsets.

6.5 Data, Cuts and Final Distributions

At this point, the stereo method was used to reconstruct every stereo event measured at the Observatory from January 2007 through December 2013 resulting in the distribution seen in Figure 6.7. The full 2007-2013 reconstructed stereo event set consists of 42043 events out of which a full 38882 are GPSns verified laser shots like those that were analyzed in the preceding section. 1275 of the remaining 3161 events were seen to have started at the ground and propagated upward into the atmosphere. The vast majority of these 'up-going' events have a FD core co-located with a laser facility pointing to laser events that were fired outside their proper GPSns time window. The rest of these events are strongly bunched in time and are the result of one of the many FD calibration studies done at the Observatory

Stereo Reconstructed CLF Trajectories

(a) Laser trajectories
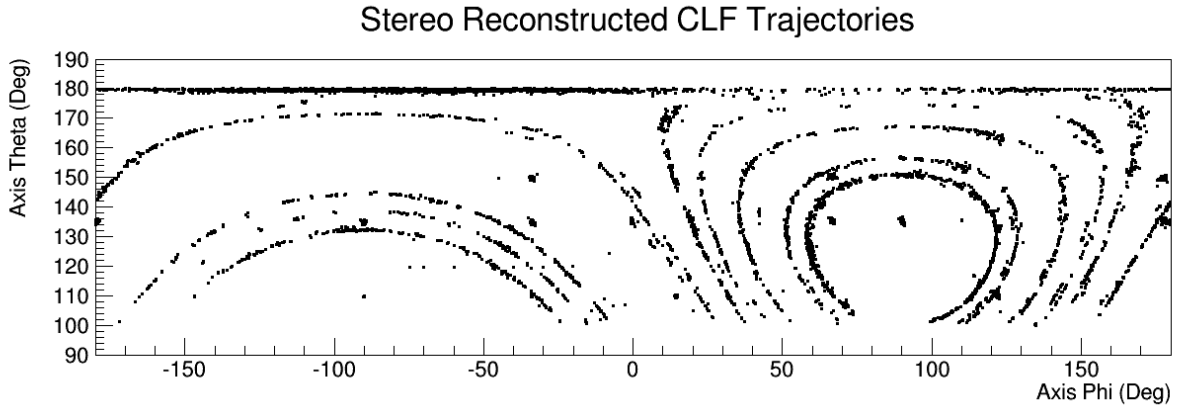
Stereo Reconstructed Velocity of Vertical and Inclined CLF Shots
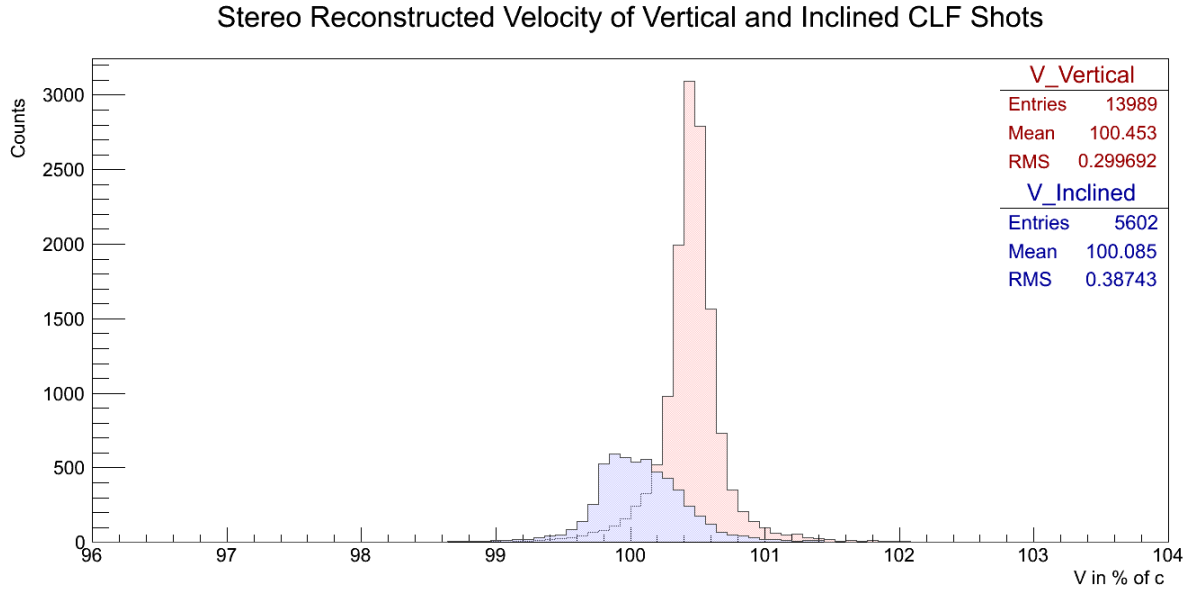
(b) Vertical and inclined laser velocities

Figure 6.6: Stereo Velocity Reconstructions of Vertical and Inclined Lasers: (a) shows the trajectories of laser events fired from January 2007 through December 2013. The events at $\theta_{axis} = 180°$ with the widespread in ϕ_{axis} are the vertical events fired at the array. The curved set of events are fired at various astronomic objects at specific times each night and therefore show the paths these object trace around the sky over the course of many years. The clumps of events are fired at specific geometries that have been requested for calibration studies. (b) shows the velocity reconstruction of these laser events split into vertical (red) and inclined (green).
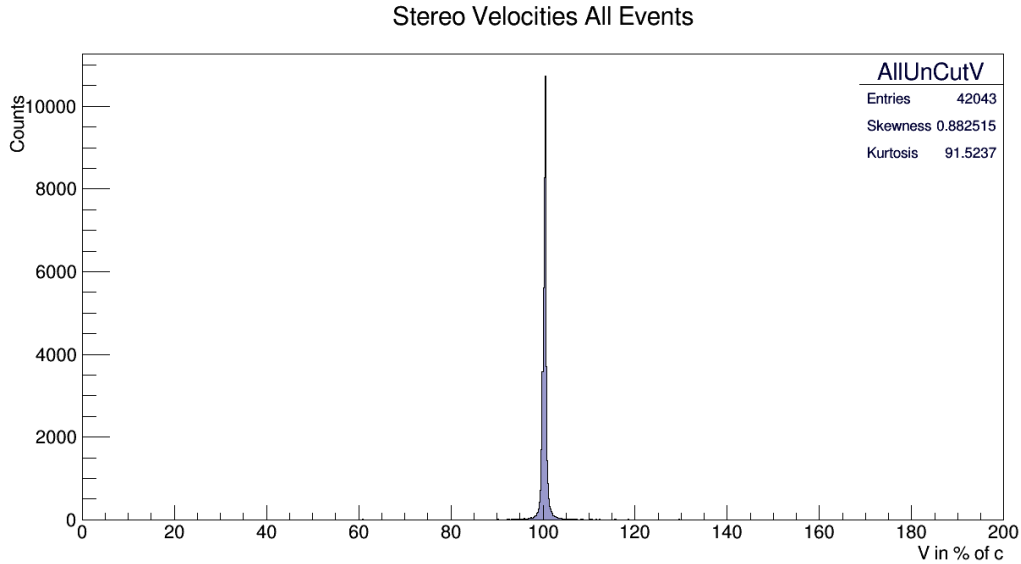
Figure 6.7: All Reconstructed Stereo Event Velocities: The velocity of the 42043 reconstructed stereo events measured between January 2007 and the end of December 2013.

using a mobile laser. Once these are removed, only 1886 stereo events remain representing the reconstructed sample of shower events. This low number is expected due to the stringent requirements needed to trigger more than one Eye. The reconstructed velocity distribution of these 1886 events can be seen in Figure 6.8.

Clearly, given the extremely strong peak at the expected value of c, the stereo method is capable of accurately reconstructing the velocity for a wide range of cosmic event strengths and geometries. The skewness of ~ -1.5 seems promising as it indicates that the slow tail is significantly larger than the fast tail, however with a kurtosis of ~ 104 the tails are far too strong to simply pull slow events as candidates. Furthermore, there are events that were reconstructed well below the theoretical minimum detectable velocity of 36% of c and many events with velocities far above c, indicating that something may be amiss. These features of the distribution suggest the need for strong and targeted quality cuts.
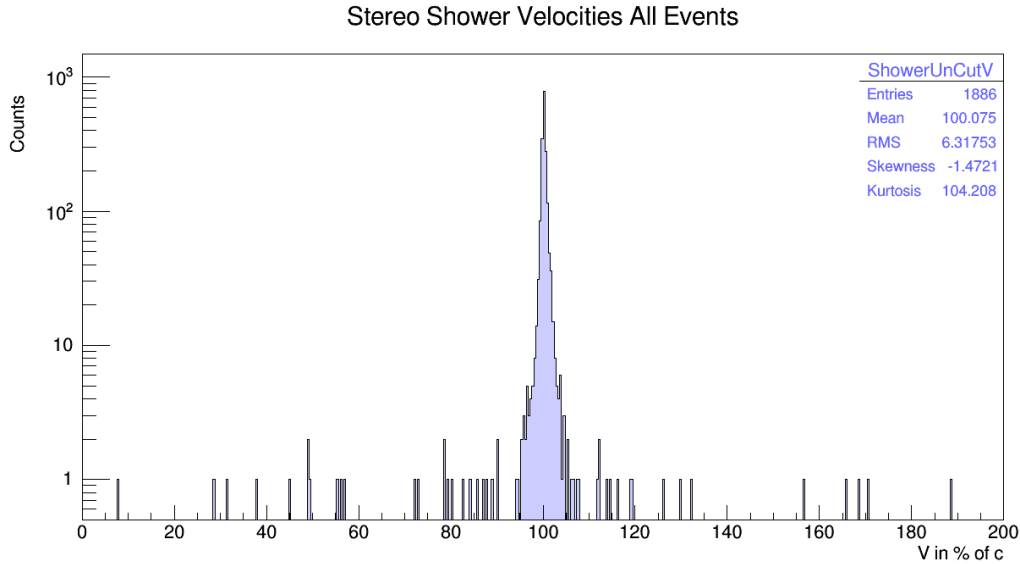
Figure 6.8: All Reconstructed Stereo Shower Velocities: The log plot of the velocities of the 1886 reconstructed down going events measured between January 2007 and the end of December 2013.

6.5.1 Quality Cuts

The already delicate process of choosing and implementing quality cuts for events measured at the Pierre Auger Observatory is made quite a bit more difficult in the case of an exotics search. This is mainly because few of the Collaboration's standard quality cuts can be used without potentially cutting out the very same exotic events we are searching for. Specifically, the following types of cuts can not be implemented without biasing the end result:

Direct or indirect cuts on velocity

Obviously by directly cutting on velocity the distribution is being tailored to some desired result. As tempting as it is, the faster-than-light events can not be thrown out simply due to the fact that they are non-physical. Nothing about the model or method breaks down at these velocities, so even though they may be non-valid physically they are still perfectly allowed in the reconstruction. This restriction also extends to removing events based on the theoretical maximum sensitivity as compared

123

to the reconstructed geometry. The fact that it was observed does call into question the accuracy of the velocity reconstruction, however the event may still have propagated slowly, just not as slowly as measured.

Direct or indirect cuts on the events light profile

Because, at its core, the search is looking for events that would be dissimilar from standard cosmic ray events, any requirement that uses the measured profile risks removing the exotic events we are looking for. This forbids the use of any shower parameters calculated from the profile in cuts. Energy cuts are disallowed, as the only requirement that can be set on the energy of a potentially exotic event is the already stringent requirement that it be energetic enough to trigger the array. X_{max} cuts, $\langle X_{max} \rangle$ and X_{max} field of view cuts of course can not be used as it is unclear whether an exotic shower would have peak deposit at all. Certainly in the case of Q-Balls there would be no X_{max}. Cuts based on undesirable features of the profile, such as large gaps or peaks, are also disallowed as we can not be sure that these features are not simply due to an exotic event's interactions.

Cuts using the standard Observer reconstruction

In the event of a slow exotic event, any reconstruction done assuming the event moved at c would produce incorrect results. This means comparing the standard reconstructed FD or SD geometry to the velocity reconstruction is forbidden. However, because a real slow event would be badly reconstructed by Observer, comparing the quality of the velocity reconstruction to the standard one would potentially indicate whether an event's exotic velocity is reliable.

In addition to these restrictions on what cuts can be used, it is obvious that given the relatively low number of stereo events available the efficacy of the cut must by weighed against the number of events removed from the data set. With these requirements in mind the following cuts were selected:

Table 6.1: Stereo Quality Cuts.

Quality Cut	Showers After Cut	% Showers Cut
All Stereo Shower Events	1886	
IR Camera Cloudy Pixels $= 0$	1675	11.2%
GOES on Axis Cloud Probability $\leq 20\%$	1298	22.5%
$V_{err} \leq 0.675\%$ of c	1226	5.6%
$\eta\chi_t^2 \leq 3$	1125	8.2%
All Cuts	1125	40.3%

Cloud Cuts

For velocity measurements, out of all possible atmospheric conditions, clouds above the Observatory represent the largest threat to the data quality and therefore reconstruction accuracy. If an event strikes a cloud then a large degree of multiple scattering occurs rendering the validity of any light propagation model described in this work invalid. Because the light can, and will, take a meandering path through the cloud, and will only begin traveling toward the Eye uninterrupted when it exits the cloud, the timing structure of the light arriving at the camera is no longer representative of the event's progress through the atmosphere. Because the timing of the event is now dependent on the shape of the cloud, it can trick the velocity reconstruction into reporting the event to either travel faster or slower than the actual event's speed. If the light reaches the face of the cloud at distant locations at similar times, the event will appear to be moving very fast. Conversely, if the light takes more time to reach the cloud face as altitude increases, the apparent event velocity will be slowed. Because of this, any event whose measurement may have been interfered with by a cloud must be cut from the dataset. To insure these events have been removed, the following requirements have been imposed on the data.

- IR Camera data must show there are no clouds either on or obscuring the reconstructed axis for any of the FD pixels that observe the event.

- GOES cloud measurements must exist and indicate that the probability of the event's axis intersecting a cloud is 20% or less.

As can be seen in Table 6.1 and Figure 6.9 the IR cut reduced the shower event set to 1675 events representing a 11.2% cull of the data, while the GOES cut reduced it to 1298 events, removing an additional 22.5% of the data. The GOES cut could have been more stringent by demanding a probability of 0% at the cost of an additional 25% of the data. However because the more accurate IR camera must already show that there are no clouds in the field of view of the camera, placing a lower cut on the less reliable satellite measurements was deemed not worth the data loss.

Velocity Error Cut The minuit minimizer used to fit the model to the data calculates the optimum values of the fit parameters by comparing how the χ^2 value changes as each parameter is varied. This means that the maximum accuracy of a fit parameter determined by how strongly the χ^2 value depends on that parameter. This maximum accuracy is reported for each parameter through its reconstruction error. By cutting on this error value the theoretical accuracy of velocity reconstruction can be effectively set. To cut events with high velocity error (V_{err}) while minimizing the loss of data, the location of the velocity error cut is set at the 95th percentile removing approximately the worst 5% of events.

- $V_{err} \leq 0.675\%$ of c

This V_{err} cut demands a resolution less than half the stated 1.5% of c accuracy found in Chapter 5, and for most datasets would be far too stringent. However, because stereo reconstruction very strongly constrains the geometry of the event, V is also highly constrained in the reconstruction process leading to very low estimates of V_{err} by minuit. If the cut was placed at 1.5% of c as the laser studies suggest it should be, the cut would be completely ineffective. Because of these factors, the cut position was

selected statistically. As can be seen in Table 6.1 and Figure 6.9, the velocity error cut reduced the shower event set to 1226 events representing a 5.6% cull of the data.

Reduced Timefit χ^2 Cut The timefit χ^2 value is representative of how well the propagation model matches the data with the minimized parameters. The reduced timefit χ^2 value ($\eta\chi_t^2$) is $\chi_t^2/NDoF$ where $NDoF$ is the number of degrees of freedom and is equal to the number of data points minus the number of fit parameters. Therefore, a demand placed on $\eta\chi_t^2$ is a demand on how well the model matches each data point on average, normalized by the strength of the measurement. This of course is an important quantity to limit as a reconstruction can not be trusted if it results in parameters that fail to match the observed data. The upper bound on the allowed $\eta\chi_t^2$ is difficult to set non-arbitrarily, however, by following the guidelines laid out in [77], a cut of $\eta\chi_t^2 \leq 3$ was used as it theoretically corresponds to a good fit, yet in our case minimizes the number of events removed from the final dataset.

- $\eta\chi_t^2 \leq 3$

Theoretically, if the data has been fit perfectly, the average offset of the model from each data point should be equal to the average error of the data, resulting in an $\eta\chi^2$ close to 1. Of course the $NDoF$ is smaller than the number of data points, the error is never perfectly estimated and a model is, in all but a small number of cases, a best approximation. This means that $\eta\chi^2$ is very seldom close to 1. As can be seen in Table 6.1 and Figure 6.9 the reduced timefit χ^2 cut removed 8.2% of the data, lowering the stereo shower event count to 1125.

The above cuts represent the minimum requirements a stereo event must satisfy for confidence in the velocity reconstruction. As Table 6.1 states, combined, these cuts remove 40.3% of the stereo shower events. This is, of course, a large percentage when the data set is as small as this one is at the beginning, however any events that do not meet the above selection criteria simply could not be trusted. Figure 6.9 clearly shows that as each
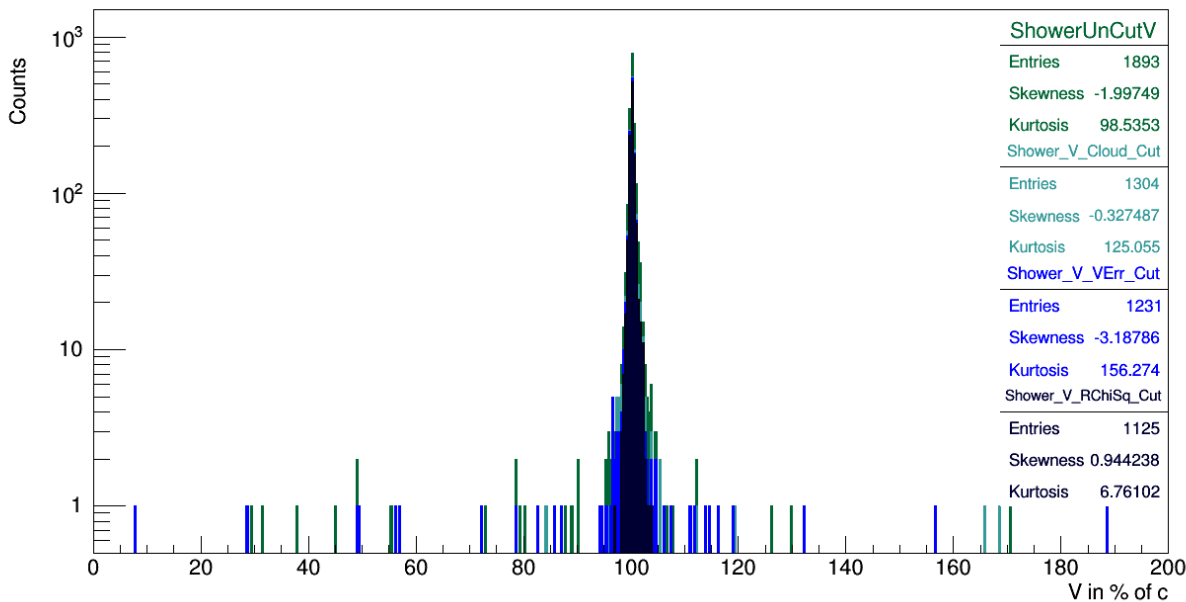
Figure 6.9: Stereo Quality Cut Velocities: A log plot showing the effect of each of the stereo quality cuts. Each colored event either shows that the event was removed in the next applied quality cut, or in the case of the dark blue final event set, which events survived all quality cuts.

of these cuts are imposed on the data, the tail events are quickly removed while the core of the distribution remains intact. This is ideal and speaks to the quality of the stereo reconstruction.

6.5.2 Final Stereo Distribution

Shown in Figure 6.10, after the quality cuts are applied, the final velocity distribution for stereo shower events is quite narrow. So narrow in fact, that it has no events that are either slower than $\sim 97\%$ of c or faster than 104% of c, largely ruling out the possibility of slow exotic showers, at least in the stereo data set. The distribution however does have at least one slow event that is distinct from the parent distribution that may be a potential candidate. Surprisingly, it also seems to have two or three fast outliers that may qualify as candidate events of interest. However, clearly the distribution, while more normal than the uncut distributions, is still very tail heavy calling into question the significance of these events.
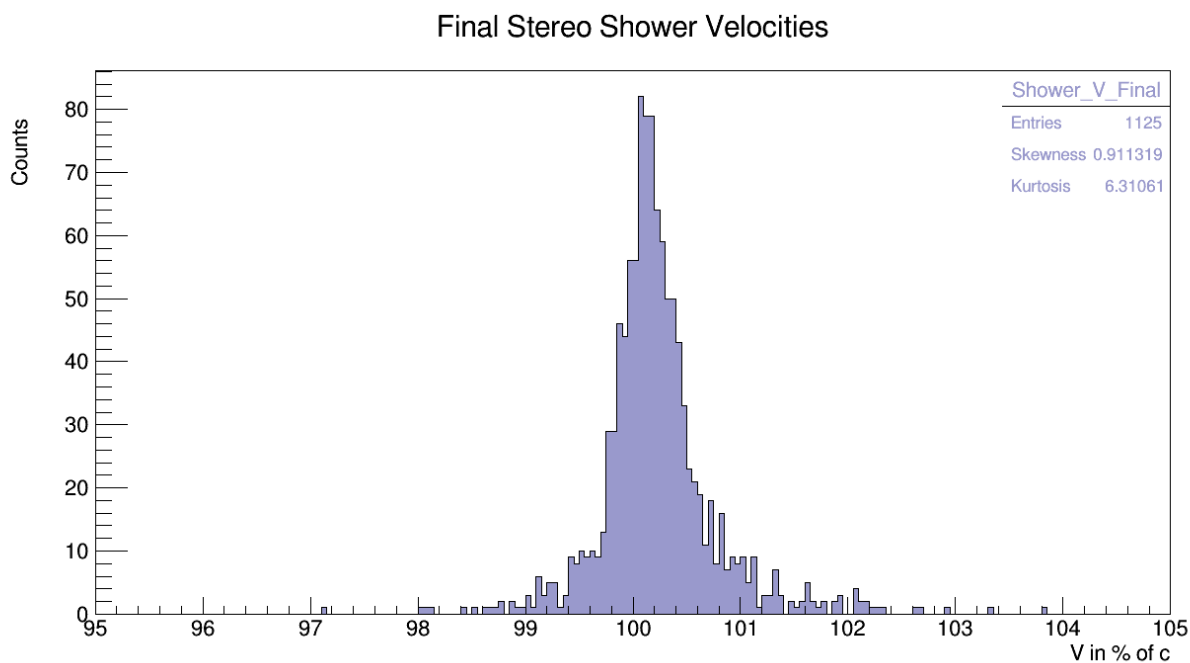
Figure 6.10: Final Stereo Shower Velocities: The final velocity distribution of all stereo shower events that passed the quality cuts. No surviving events appeared with a velocity less than $\sim 97\%$ of c or faster than 104% of c. This largely rules out the existence of slow events in the stereo data set.

Also, curiously, with a skewness of ~ 0.94, the distribution is decidedly asymmetric with the faster-than-light side showing an excess. These factors point to a small but meaningful inherent error rate in the reconstruction that may be different for the left and right sides of the distribution. This possibility will be examined and accounted for in Chapter 8, Candidate Selection and Analysis.

CHAPTER 7

VELOCITY RECONSTRUCTION: HYBRID OBSERVATIONS

While the stereo measurement and reconstruction leverages the most constraining set of observations available at the array, the dataset is somewhat sparsely populated due to the very specific conditions that a shower must meet in order to be recorded in stereo. Furthermore, as explained in Section 6.3, because each shower is observed by two eyes, it has a reduced velocity sensitivity range. Hybrid events however, are plentiful. Additionally, because the SD covers the entire land mass under the FD's aperture, there is no minimum distance at which the events may occur and therefore no cutoff in the velocity sensitivity.

This gain in event count and sensitivity, however, comes at a loss in the constraints on the event geometry. With the addition of the tank position and timing to the FD data there is exactly enough constraints to fit the 6 shower parameters $(\theta_{\hat{\mathbf{S}}}, \phi_{\hat{\mathbf{S}}}, x_{core}, y_{core}, T_0$ and $V)$ in any geometry. However, this relies on the pixel timing having good curvature, which means that the Hybrid fit can be sensitive to small sources of uncertainty in observation. This is especially true for events that arrive at geometries tilted away from the detector, as these geometries minimize the curvature available to the fit. With these factors in mind, the velocity dependent hybrid model was developed as follows.

7.1   Velocity Dependent Hybrid Reconstruction

Like Stereo, the design of the hybrid velocity reconstruction closely follows the design and implementation of the $\overline{\mathrm{Off}\underline{\mathrm{line}}}$ standard reconstruction outlined in Section 3.5.3. The principal changes to the overall method are the alteration of the FD propagation model, (3.4) to add in the velocity as a free parameter and account for the atmospheric effects outlined in Section 5.3 resulting in (5.9). Then, like the stereo case, the fluorescence emission time shown in Figure 6.2 needed to be accounted for. With these changes, t_i^{exp}, the expected time

of observation for a pixel with observation angle χ_i, becomes,

$$t_i^{exp} = T_0 + \frac{Rp}{c_i' \sin(\chi_0 - \chi_i)} - \frac{Rp}{v \tan(\chi_0 - \chi_i)} + \tau_i. \tag{7.1}$$

Where c_i' is the speed of light corrected by the effective index of refraction for the light observed by the ith pixel and τ_i is the average fluorescence emission time for Nitrogen at the height of the ith pixel's observation on the shower axis in the conditions reported by GDAS.
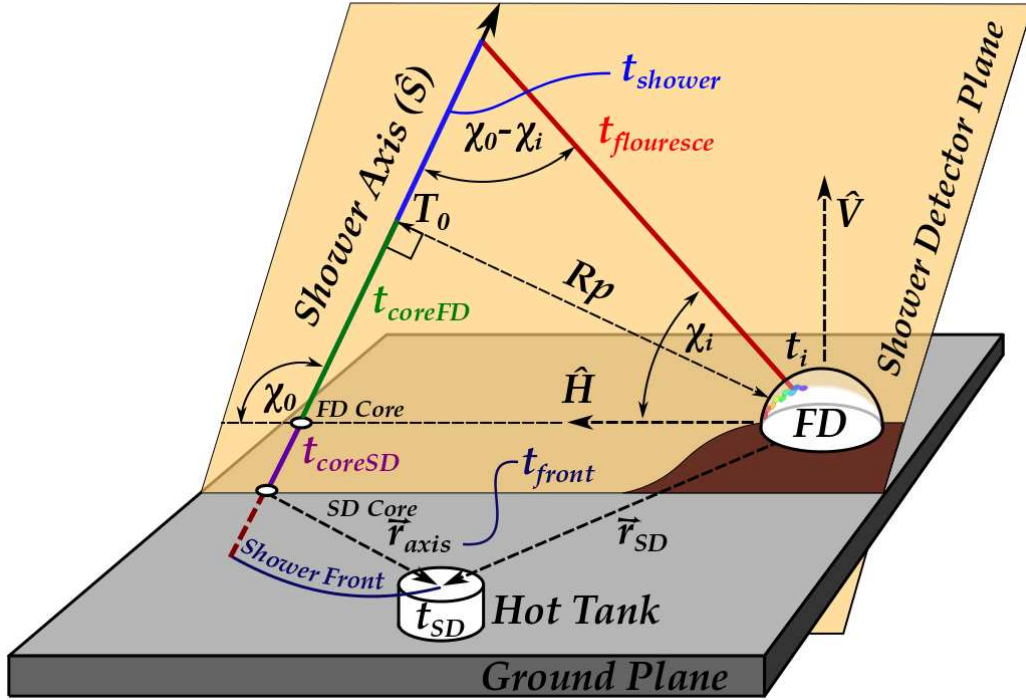
Figure 7.1: The Geometry of a Hybrid Event: The propagation of the event core is shown in bright blue. The propagation of fluorescence light is shown in red. Green indicates the propagation of the event from the point of closest approach to the FD core. Purple indicates the event moving from the FD core to the SD core which sits level with the Pampas. The curved dark blue line is representative of the shower front and the dark red line extending from the end of shower axis to the shower front curve is proportional to the time the event's shower front would take to reach the tank.

In addition to the changes that had to be made to the FD model, the SD timing model, (3.11) also needs to be changed to include a free velocity. Clearly, as seen in Figure 7.1, both t_{coreFD} and t_{coreSD} represent the propagation of the event's core and therefore need to have a free velocity assigned to them. The time it takes the event to move from the the point of

closest approach to the FD core, t_{coreFD} is now

$$t_{coreFD} = T_0 + \frac{Rp}{V} \cot(\pi - \chi_0),$$ (7.2)

while the time difference between the FD and SD core, t_{coreSD}, is now

$$t_{coreSD} = -\frac{\vec{r}_{SD} \cdot \hat{\mathbf{S}}}{V}.$$ (7.3)

Again t_{coreSD} is negative because the shower axis $(\hat{\mathbf{S}})$ always points up by collaboration convention, while Eye is always above the Hot Tank so the z component of $(\vec{r}_{SD})$ is always negative, this results in the dot product returning a negative length which needs to be corrected.

(a) EAS Shower Front   (b) Proton Decay Shower Front

(c) Variable Velocity Shower Front
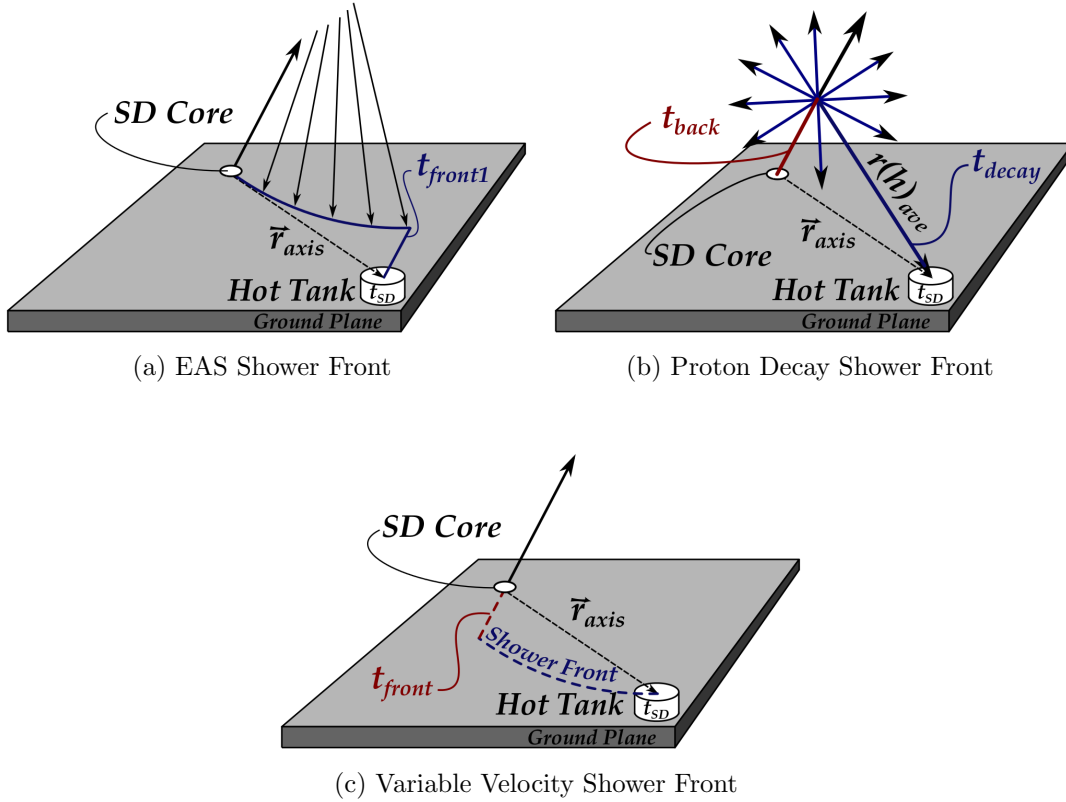
Figure 7.2: Shower Front Possibilities.

The question of what if any changes the showerfront time (t_{front}) needs is a somewhat more difficult question. There are three possibilities:

EAS Shower Front

Figure 7.2(a) shows the shower front for a cosmic ray shower. In this case the front is physically represented by particles propagating at c sourced from interactions farther up the shower axis earlier in the shower. The equation for the time lag due to the shower front of this type is

$$t_{frontCR} = \frac{a_1 |\overrightarrow{r}_{axis}| + a_2 |\overrightarrow{r}_{axis}|^2}{c},$$

(7.4)

where a_1 and a_2 are empirically defined constants that describe the shape of the shower front.

Proton Decay Shower Front

Figure 7.2(b) shows an approximation of the shower front delay that would be caused by a proton decay shower. In this case, the particles that make up the shower front would be directly sourced from the exotic parent particle. As explained in Section 4.1.2, all of the decay product particles produced in this type of event have the same relatively low energy and therefore, a very similar short attenuation length. This results in the event being well described by a sphere, with a radius equal to the average attenuation length of the decay products at that height's atmospheric density $r(h)_{ave}$, of energetic particles traveling radially outwards at the speed of light, represented by the dark blue vectors in Figure 7.2(b). This results in a travel time from the decay point (t_{Pdecay}) of

$$t_{Pdecay} = \frac{r(h)_{ave}}{c}.$$

(7.5)

Since the proton decay that created the particles that first reached the Hot Tank occurred above the SD core, the time back to that point (t_{back}) needs to be subtracted from t_{coreSD}. This time, represented by the dark red line in Figure 7.2(b) is described by

$$t_{back} = \frac{r(h)_{ave}}{V} \left(\frac{\vec{r} \cdot \hat{\mathbf{S}}}{r(h)_{ave}} + \sqrt{1 - \frac{|\vec{r}|^2 + (\vec{r} \cdot \hat{\mathbf{S}})^2}{r(h)_{ave}^2}} \right).$$

(7.6)

133

By subtracting t_{back} from t_{Pdecay} we find the total time the proton decay shower front takes to travel from the SD core to the triggered tank, $t_{frontDecay}$, to be

$$t_{frontDecay} = \frac{r(h)_{ave}}{c} - \frac{r(h)_{ave}}{V} \left(\frac{\vec{r} \cdot \hat{\mathbf{S}}}{r(h)_{ave}} - \sqrt{1 - \frac{|\vec{r}|^2 + (\vec{r} \cdot \hat{\mathbf{S}})^2}{r(h)_{ave}^2}} \right). \qquad (7.7)$$

As expected, this function essentially describes a tight spherical wave front which, depending on velocity and geometry, may arrive at the triggered tank before the event reaches the SD core.

Variable Velocity Shower Front

Figure 7.2(c) shows the third option of having a traditional shower front of the form described in (7.4), but with a net subluminal travel velocity. Basically, instead of invoking a realistic picture of a front caused by a build up of particles traveling at light speed sourced from earlier interactions in the shower, it is simply assumed that the whole shower front holds a traditional form but travels at the event velocity V. This front would therefore arrive at the triggered tank at a time $t_{frontSlow}$, predicted by

$$t_{frontSlow} = \frac{a_1 |\vec{r}_{axis}| + a_2 |\vec{r}_{axis}|^2}{V}, \qquad (7.8)$$

again where a_1 and a_2 are empirically defined constants that describe the shape of the shower front. To be clear, this is an approximation only and does not accurately represent shower physics at velocities far from c.

Certainly, the EAS shower front shown in Figure 7.2(a) with the timing predicted by (7.4) is the correct model for the vast majority of cosmic ray events. This model however, will fail badly when confronted with an exotic shower as there is no flexibility to fit slow events. The proton decay model shown in Figure 7.2(b) with the timing predicted by (7.7), seems to be the logical choice given that proton decay is the strongest candidate interaction for observable slow events. This is certainly true, however, as highlighted in Figure 4.3(c), this model's timing structure represents a strict departure from the expected timing signature of

an EAS even when the event velocity is equal to c. This means that while it may do a good job of describing any true candidate events, it will badly represent the timing of the vast majority of the events in the sample.

The variable velocity shower front model, shown in Figure 7.2(c), however, attempts to strike a balance between the EAS and proton decay model. First, the predicted tank timing described by (7.8), scales well with velocity, clearly reducing to (7.4), the EAS model, at the speed of light. This means that the vast majority of events, which indeed are cosmic ray events and therefore do travel at c and generate EAS, will be accurately represented by this model. Second, as the velocity slows, the (7.8) predicts that the arrival time at the tank will grow, leading to much later than expected arrival times at the triggered tanks. While this doesn't exactly match the simulations of Section 4.1.2 and (7.7), it doesn't completely miss them either. Because the variable velocity shower front model accurately describes cosmic ray events at c and does a decent job on slow events, this model is on average the best choice overall for the hybrid velocity reconstruction.

Adding (7.8) to (7.2) and (7.3) we find the velocity dependent expected event time at the hot tank, (t_{SD}^{exp}) to be

$$t_{SD}^{exp} = T_0 + \frac{Rp}{V} \cot{(\pi - \chi_0)} - \frac{\overrightarrow{r}_{SD} \cdot \hat{\mathbf{S}}}{V} + \frac{a_1 |\overrightarrow{r}_{axis}| + a_2 |\overrightarrow{r}_{axis}|^2}{V}. \tag{7.9}$$

(7.9) and (7.1) are then fit to the FD and SD data using the hybrid χ^2 fit equation (3.7), derived in Section 3.5.3. To refresh, the hybrid χ^2 fit equation simultaneously compares the times predicted by both the FD and SD models using a set of shower parameters, to the observed time in instrumentation and takes the form

$$\chi_{hy}^2 = \chi_{FD}^2 + \chi_{SD}^2 = \sum_i \frac{(t_i - t_i^{exp})^2}{(t_i^{err})^2} + \frac{(t_{SD} - t_{SD}^{exp})^2}{\left(t_{SD/FD}^{err}\right)^2}.$$

The velocity, event time and geometry that minimize the χ_{hy}^2 value represent the best set of reconstructed parameters possible with this method.

7.2 HybridVelocityFinder Module

Like the stereo velocity reconstruction module, the StereoVelocityFinder, the hybrid velocity reconstruction module, the HybridVelocityFinder, is strongly based off of the $\overline{\text{Off}}$ $\underline{\text{line}}$ standard hybrid geometry reconstruction module, the HybridGeometryFinderWG. The HybridGeometryFinderWG module, like the StereoGeometryFinderOG, uses the reconstructions performed by earlier modules as a first guess to its own reconstruction. It then improves upon these fits by adding the SD information to the event data to provide additional constraints to the system. This means SD data preparation modules need to be run before the hybrid reconstruction in addition to the FD modules that were used in the Stereo and Fixed geometry cases. Figure 7.3 shows the Observer standard hybrid shower reconstruction up to the profile reconstruction which is unneeded for this analysis.

Figure 7.3: The Hybrid Velocity Reconstruction Module Sequence: The module sequence used to reconstruct the velocity of hybrid events. The first part is exactly the Auger standard stereo geometry reconstruction. The HybridVelocityFinder performs the velocity reconstruction using the results of the preceding modules.

Most of the HybridGeometryFinderWG data loading, handling and processing was used unchanged in the HybridVelocityFinder, while major changes were made to the functions that calculate the geometric first guess, prepare the Minuit minimization, and the form of the Minuit fit function itself. The functions used to make a first guess for the fit were replaced with a function that loads the standard hybrid reconstruction performed by earlier modules. The function that prepares and runs the Minuit minimization was rewritten to accommodate an additional variable, have increased sensitivity and to carefully check that the reconstruction was successful. The Minuit fit function, the function that calculates the expected times and the χ^2 values to be minimized, was rewritten to incorporate the model changes described in Section 7.1 and given the capability of reconstructing in an ideal or real atmosphere. At the end of the module, a new function was added to pull and store all of the results and Observatory data needed for later in-depth analysis.

7.3 Velocity Sensitivity Range

The calculation of velocity sensitivity for the hybrid method is substantially easier than it is for the stereo case. This is mainly because only one Eye is used at a time and therefore the geometry of each event, in terms of the velocity sensitivity, is simply the reconstructed geometry itself. This means the results of Section 5.2 can be used almost unchanged. The only differences are the loss of sensitivity to events closer than $3km$ to the Eye due to a cut that removes very close events, and the removal of any events with $\chi_0 \leq 15°$, due to the combined requirements of each event having a minimum angular length in the camera $(\chi_i^{top} - \chi_i^{bottom})$ of at least $15°$ and the removal of any events with a χ_0 less than highest observation angle (χ_i^{top}). The purpose of these cuts will be explained below in Section 7.5.

As can be seen in Figure 7.4(a), these changes to the allowed geometries do very little to limit the overall hybrid velocity sensitivity. Furthermore, as can be seen in Figure 7.4(b), because hybrid events can be as close as $3km$, the hybrid method has good sensitivity to very low velocity events. Disregarding geometries with a $\chi_0 \geq 170°$ which have a vanishing exposure, the hybrid method has sensitivity to events moving at $\sim 4.5\%$ of c and above.
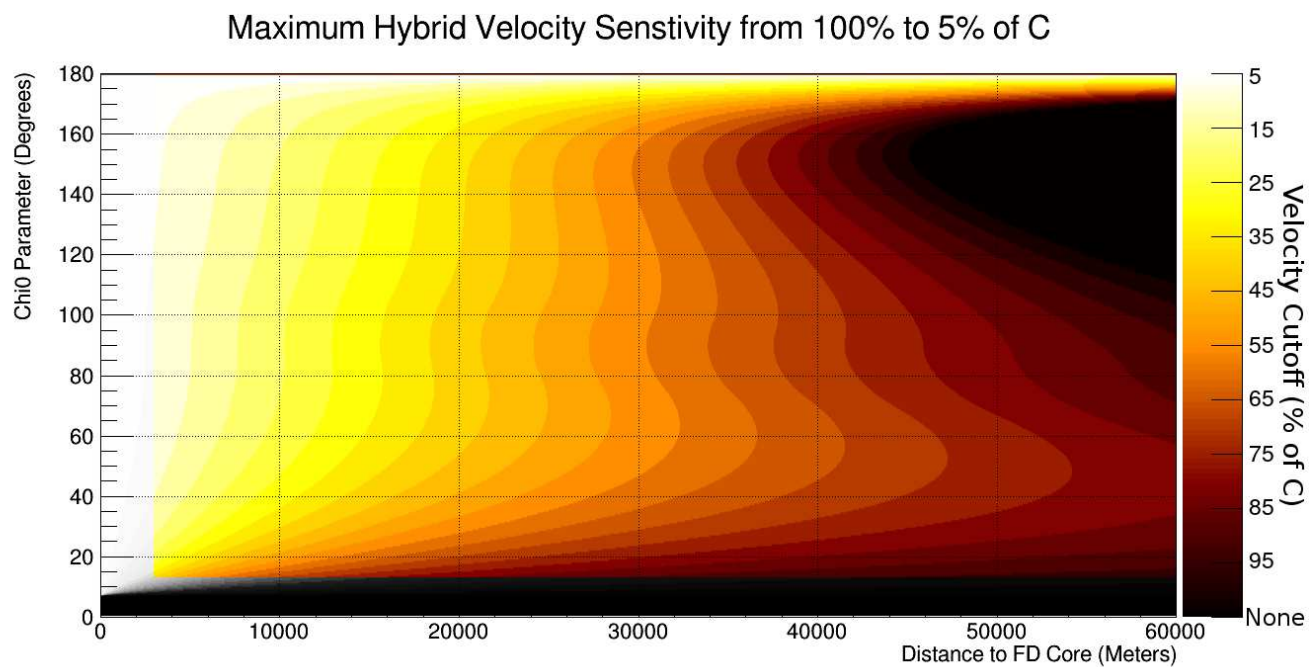
(a) Hybrid Velocity Sensitivity 100% to 5% of C
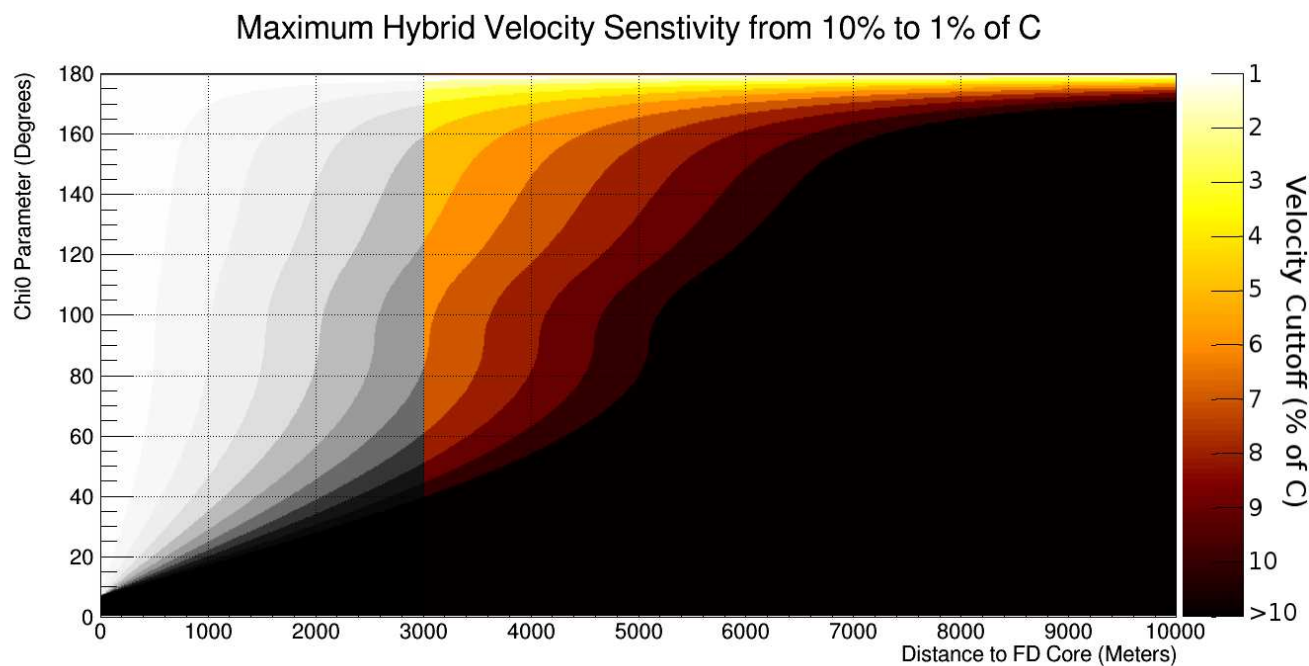
(b) Hybrid Velocity Sensitivity 10% to 1% of C

Figure 7.4: Hybrid Velocity Sensitivity due to the T2 FD Trigger: the shower geometries and velocities that are capable of passing the timing requirement set by the FD T2 $\sim 6.75°$ in $20\mu s$ window. The gray regions represent areas forbidden by quality cuts.

7.4 Laser Distributions and Interpretation

Like in the stereo case, in order to briefly see how the effects observed in Section 5.4 apply to hybrid velocity reconstructions, the sample of laser events that are included in the Observatory's hybrid data stream were reconstructed. Again, these laser shots are fired at a specific GPSns that is different from the calibration shots analyzed in Section 5.4 and are measured like cosmic ray events, allowing for CDAS to cross correlate the observations from the FD and SD. For these shots, a portion of the laser light of each shot is sent to the SD station that is co-located with each laser facility so that it is triggered in conjunction with the FD. This triggered station then acts as the hot tank in a hybrid reconstruction. As shown in Figure 7.6(a), just as in the stereo case, this laser event set includes both vertical and inclined events. These events therefore provide a means to investigate how the errors seen in Section 5.4 affect hybrid reconstruction and whether or not these effects are restricted to just vertical events or extend to every measured event. Applying the hybrid reconstruction technique, as well as the quality cuts described in the next section, results in the distributions seen in Figure 7.5 and Figure 7.6(b).

Clearly, Figure 7.5(a) and Figure 7.5(b) show that many of the effects seen in Section 5.4 carry through to hybrid reconstructions. LA for the CLF and LL for the XLF have too few events to comment on. However, the other Eyes match up very well with the offsets seen in Section 5.4, at least for the CLF. The fact that hybrid reconstruction sees these offsets and stereo reconstruction does not is because hybrid reconstruction only uses one eye at a time while stereo reconstruction uses several. This suggests that the common velocity that both stereo reconstruction and the laser simulation reconstructions of Section 5.4 see is an average offset that is inherent to $\overline{\text{Off}\underline{\text{line}}}$ and not to the method or to the detectors. The offsets seen in both hybrid and the fixed geometry analysis of real lasers must then be due to the addition of the individual Eye effects to the $\overline{\text{Off}\underline{\text{line}}}$ errors. What causes these errors is still uncertain. From the stereo reconstruction of inclined lasers, it is clear that the $\overline{\text{Off}}$ $\underline{\text{line}}$ problem is restricted to only vertical events. A similar study should be done to see if
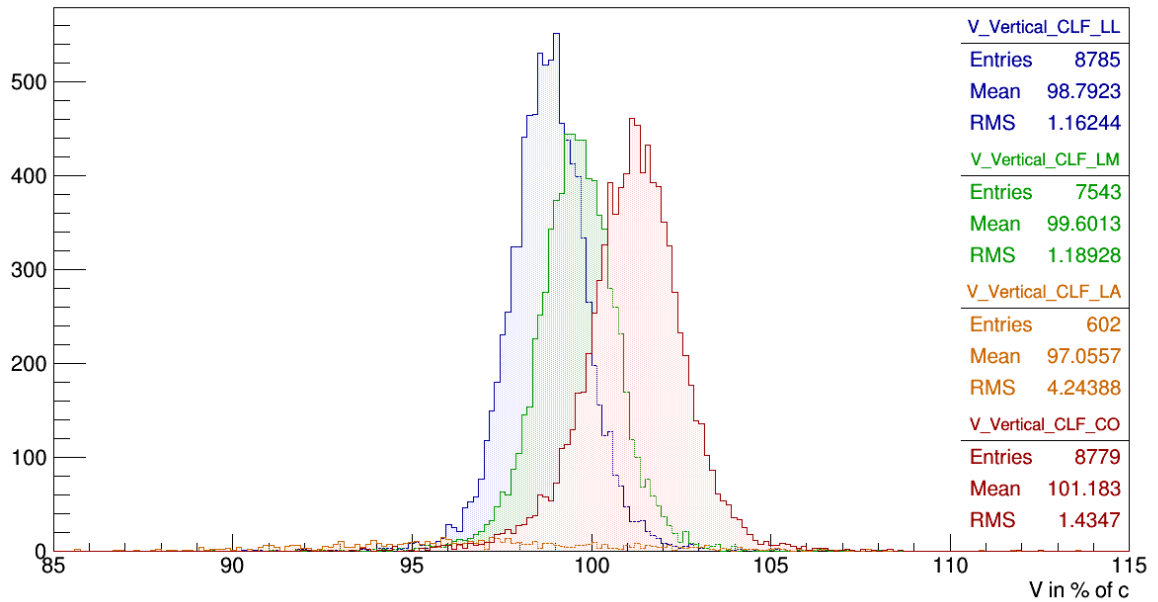
(a) Hybrid Velocity of Vertical CLF Shots
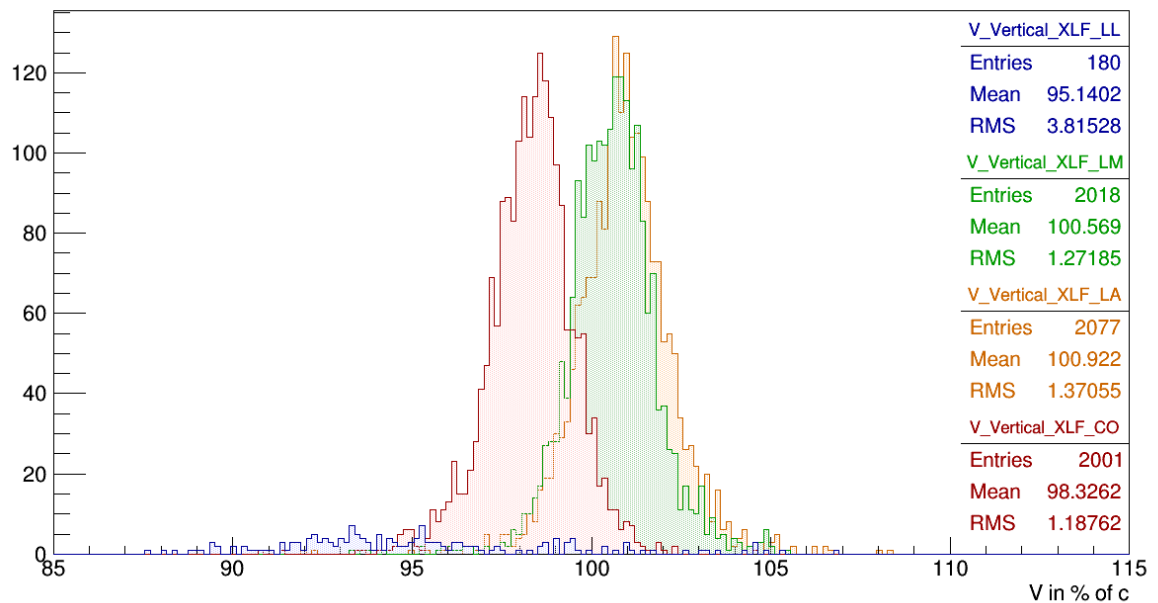
(b) Hybrid Velocity of Vertical XLF Shots

Figure 7.5: Hybrid Velocity of Vertical Laser Events: (a) shows the reconstructed velocities of all vertical hybrid CLF laser events fired from January 2007 through December 2013 after quality cuts by Eye. (b) shows the reconstructed velocities of all vertical hybrid XLF laser events fired from January 2007 through December 2013 after quality cuts by Eye.

the individual Eye offsets carry to inclined events or are restricted to vertical only.

Figure 7.6(b) shows that each of the Eyes behave similarly when inclined shots are recon-structed. Additionally, the strongly peaked distribution does not look like a sum of similar Gaussians suggesting that the offsets aren't simply being averaged out. This indicates that, like the $\overline{\text{Off}\underline{\text{line}}}$ errors for the stereo case, the individual Eye offsets vanish when the velocity reconstruction is applied to events with widely varying geometries. This again means that because vertical geometries represent a tiny fraction of overall FD exposure by solid angle, the vast majority of shower events will be unaffected by these systematic offsets. Because of this, as long as events closer than a few percent of c are not considered as potential candidates, a hybrid based velocity search of shower events can be carried forward with confidence.

7.5   Data, Cuts and Final Distributions

The Hybrid method was used to reconstruct every hybrid event measured at the Obser-vatory from January 2007 through December 2013, resulting in the decidedly non-normal distribution shown in Figure 7.7. Out of the full 2007-2013 hybrid event set, 691019 events were successfully reconstructed. Of these 691019 events, 132954 are verified laser shots that were analyzed in the preceding section. 1368 of the remaining 558065 events were also seen as upgoing but were outside the laser time windows. Unsurprisingly, all of these events were collocated with a laser facility, struck clouds or were at very extreme geometries. Once these upgoing events are removed, there are a full 556697 hybrid events remaining which represent the sample of hybrid shower events that were successfully reconstructed. The fact that this number greatly exceeds the stereo event count is unsurprising as the full FD aperture is available and the energy required to trigger a hybrid event is an order of magnitude lower than what is needed to trigger a stereo event. The reconstructed velocity distribution of these 556697 events can be seen in Figure 7.8.

The distribution of velocities seen in Figure 7.8, with its very strong peak centered at c and massive tails, is quite interesting. One troublesome feature is the large and unphysical

Hybrid Reconstructed Laser Trajectories
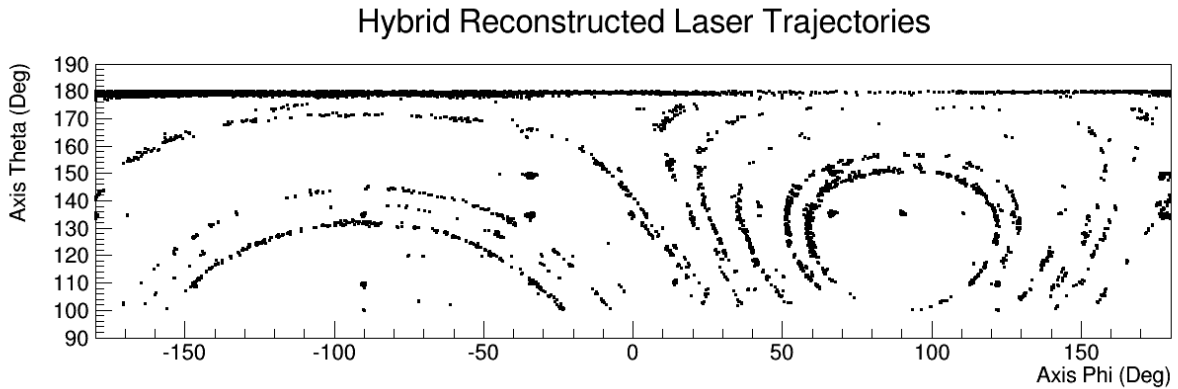
(a) Hybrid laser trajectories

Inclined Laser Velocities
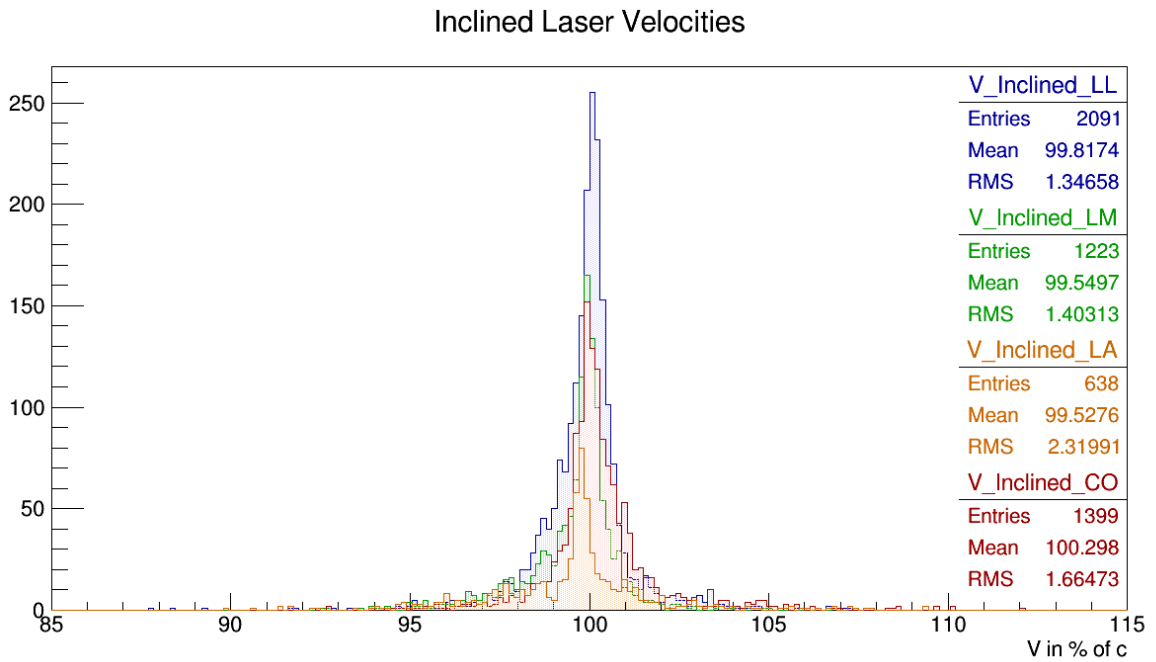
(b) Inclined hybrid laser velocities

Figure 7.6: Stereo Velocity Reconstructions of Vertical and Inclined Lasers: (a) shows the trajectories of laser events fired from January 2007 through December 2013. The events at $\theta_{axis} = 180°$ with the wide spread in ϕ_{axis} are the vertical events fired at the array. The curved set of events are fired at various astronomic objects at specific times each night and therefore show the paths these object trace around the sky over the course of many years. The clumps of events are fired at specific geometries that have been requested for calibration studies. (b) shows the hybrid velocity reconstruction of the inclined laser events by Eye.
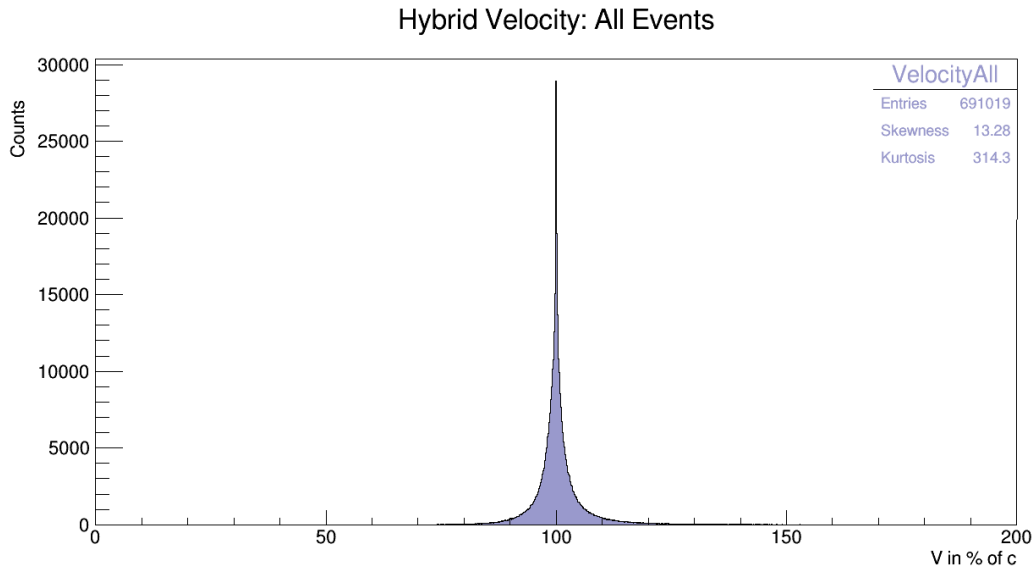
Figure 7.7: All Reconstructed Hybrid Event Velocities: The velocity of the 691019 reconstructed hybrid events measured between January 2007 and the end of December 2013.

faster-than-light tail. While the count of events in this tail is surprising, the extent of it is less so, simply because by definition, the velocity is unable to be slower than not moving, but there is no such, non-relativistic constraint on the upper end of velocities. Perhaps in the future the propagation models could somehow be changed to protect Lorentz invariance, however this was not attempted in this work. These large tails, especially the faster than light tail, indicate that there is an instability in the reconstruction for some event type or condition at the array. This is not unexpected, as the hybrid event set varies wildly in data quality and signal strength, especially compared to stereo, leaving no choice but to employ stringent quality cuts aimed at limiting the hybrid data set to only events whose velocity reconstruction can be trusted as accurate.

7.5.1 Quality Cuts

Again, because of the exotic nature of the targeted phenomena, the restrictions on what cuts could be used with the stereo data also apply to hybrid. Namely the inability to cut on velocity, energy, profile and the theoretical sensitivity of the FD. Now that the SD response

143
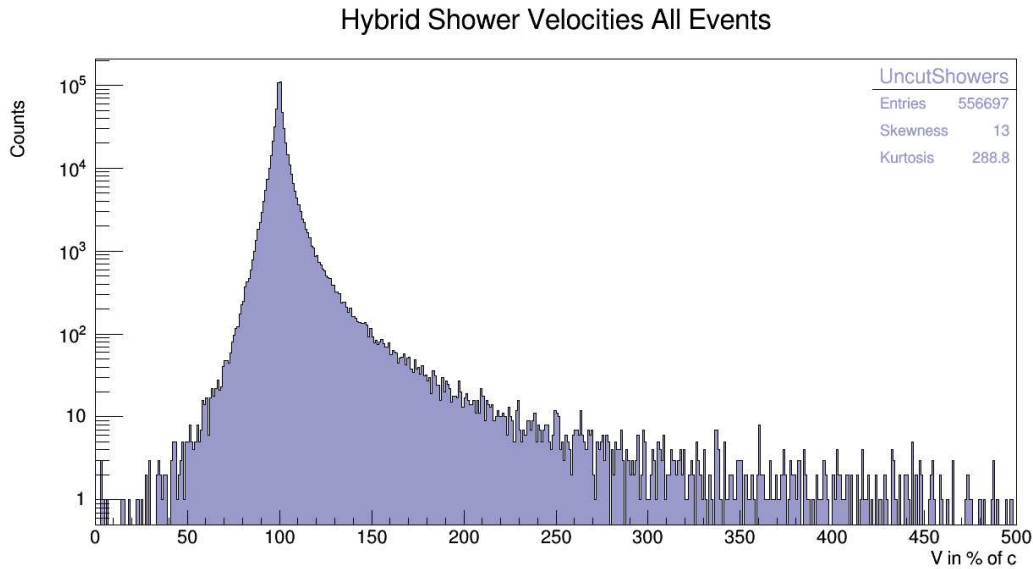
Figure 7.8: All Reconstructed Hybrid Shower Velocities: The log plot of the velocities of the 556697 reconstructed hybrid shower events measured between January 2007 and the end of December 2013.

is a factor in the reconstruction, additional restrictions on what SD specific cuts can be used come into play. The following list contains the SD cuts that are specifically forbidden.

Cuts on the strength of the SD response

Though Q-Balls were shown in Section 4.1.2 to reliably trigger several stations at the energy range the FD is sensitive to, the search is not limited to only these potential candidates. Because of this, we can not demand a minimum SD response or number of triggered tanks without potentially eliminating exotic events. Therefore, cuts on triggered station count, LDF, energy or hot tank signal strength can not be used directly.

Cuts on the timing of the SD response

In Section 4.1.2 the SD timing profile of Q-Balls was clearly shown to strongly depart from the standard SD timing profile. This alone forbids the use of the SD timing signature from multiple tanks in cuts.

144

Cuts using the SD geometry reconstruction

When available, it would be tempting to use the SD calculated geometry to judge whether the geometric reconstruction from the hybrid method, and therefore the measured velocity, make sense. This however would rely on the LDF and timing profile to calculate the SD core and event arrival direction. As both of these are already forbidden above, using the geometry reconstruction is also explicitly forbidden.

These rules combine to restrict the SD information available to use in both the reconstruction and the quality cuts to simply the hot tank location, timing and status.

Unlike the stereo case, the hybrid shower data does not suffer from low statistics. This is indeed fortunate, as Figure 7.8 definitely illustrates the need for extensive cuts if candidates are going to be selected with any confidence. To this end, three different sets of cuts are applied to the data, each focused on different areas of event quality and designed to guarantee that only trustworthy events make it to the final data set. However, some cuts were far too strict at their theoretically defined location and were tuned to minimize the number of events removed from data set while maintaining the intent of the cut. The first set of cuts, data quality cuts, is directed at ensuring that the data recorded from each event can be trusted to be accurate and representative of the measured event.

Table 7.1: Hybrid Data Quality Cuts

Quality Cut	Showers After Cut	% Showers Cut
All Hybrid Shower Events	556697	-na-
$VAOD(3km) \leq 0.03$	405683	27.1%
Has IR Data or GOES Cloud Probability $= 0\%$	384414	5.2%
GOES on Axis Cloud Probability $\leq 40\%$	306359	20.2%
IR Camera Cloudy Pixels $= 0$	287443	6.1%
Hot Tank Crown Count $= 6$	214459	25.4%
$|\vec{r}_{SD}| \geq 3km$	187585	12.5%
Events With Good Data	187585	66.3%

Aerosol Cuts

High aerosol content in the atmosphere significantly increases scattering of the light

propagating from the event. This leads to increased multiple scattering and decreased light intensity at the camera. These factors directly decrease the signal to noise ratio and significantly increases the timing uncertainty of each pixel. Additionally, the aerosol profile is not uniform across altitudes leading to an effect that varies strongly with altitude, which can be particularly problematic for a velocity reconstruction. Due to these factors, events measured during atmospherically hazy periods should not be used in a velocity-based search. According to [78], atmospheres are considered to have above average levels of aerosols if the VAOD at $3km$ exceeds ~ 0.03.

- $VAOD(3km) \leq 0.03$

As seen in Table 7.1 and Figure 7.9, this cut is fairly stringent, reducing the event count from 556697 to 405807- a 27.1% reduction of the data.

Cloud Cuts

Like in the stereo case, clouds can easily trick the velocity reconstruction into falsely reconstructing slow or fast events. Therefore, any event whose measurement may have been interfered with by a cloud must be cut from the dataset. Additionally, because the hybrid dataset is well populated, stricter requirements than those leveled against the stereo data can be used here. Events are required to have IR camera and lidar or GOES data, and when the IR camera data is not present GOES must report a zero probability of the event having a cloud on the events axis. If there is IR data, GOES must report a 40% or less probability of clouds and the IR camera must show that none of the event's pixels observe a cloud up to or on the event's axis.

- Has IR Data or GOES Cloud Probability = 0%

- GOES on Axis Cloud Probability $\leq 40\%$

- IR Camera Cloudy Pixels = 0

146

The GOES probability could be set to a lower value, however, this deeply cuts into the data. This is not an issue, as this high probability is only allowed when the more reliable IR camera sees no clouds that could interfere with the event observation. As it stands these cuts reduce the event count from 405683 to 287443- representing a 29.1% reduction of the data

SD Functionality Cuts

The hybrid reconstruction depends strongly on the fact that the tank with the hot tank is in fact the closest tank to where the event struck the ground. This can only be assured when the hot tank is fully surrounded by functioning SD stations. If this is not the case, one of the absent tanks could in fact be closer to the event core than the reported hot tank. Due to the SD geometry, every station that does not lay on the edge of the array has six stations surrounding it. These six stations are called the station's crown and the number of these stations that are reported to be fully functioning at the time of the event observation is the station's crown count. For an event to be trusted, its crown must be full, giving it a crown count equal to six.

- Hot Tank Crown Count = 6

This cut is again fairly stringent. It removes all events with a hot tank on the edge of the array or near gaps in the array. Additionally SD stations do occasionally go offline for extended periods of time mostly due to hardware failure. As can be seen in Table 7.1 and Figure 7.9 this cut reduces the event count from 287443 to 214459- a 25.4% reduction of the data.

Random Hybrid Trigger Cut As explained in Section 3.1 the SD passes the T2 trigger at a rate greater than $20Hz$. The FD has a slower trigger rate, however, as the distance between the event and the observing Eye decreases, the FD becomes much easier to trigger. Hence, the majority of FD events are triggered by low energy showers very close to the Eye. Occasionally one of these low energy showers will occur when the

SD randomly triggers, leading to a false hybrid event. Of course these erroneously detected events can not be trusted to be reconstructed with an accurate velocity and should be removed from the event set. The only way to do this without risk of letting one of these events through is to simply cut all events that occur very close to the Eye. To this end, any event whose hot tank is closer than $3km$ from the Eye is removed from the dataset.

- $|\overrightarrow{r}_{SD}| \geq 3km$

$3km$ was chosen, as it roughly corresponds to the first two lines of stations in front of the Eye. The first line of stations is already cut by the crown count cut, meaning this cut removes few additional tanks. It is true that this cut will remove a number of viable and real low energy hybrid events, however, because the area immediately around the each Eye represents a tiny fraction of the Observatory's aperture, the removal of these events is far outweighed by the removal of random coincidence events. As seen in Table 7.1 and Figure 7.9, this cut reduces the event count from 214459 to 187585- representing a 12.5% reduction of the data.

After data quality cuts, the observations of each event can be considered trustworthy and representative of the witnessed event, this however comes at a cost of 66.3% of the hybrid shower data. Furthermore, as can be seen in the dark blue distribution of Figure 7.9, though the tails are reduced, there is still far too much noise for candidate selection to be possible. This is because, though the data can now be trusted, the full event measurement may not be sufficient to accurately reconstruct the velocity. To address this, a second round of cuts aimed at ensuring that the full event measurement is of high enough quality to enable velocity reconstruction is implemented. These measurement quality cuts are defined as follows.

Angular Length of Observation Cut

In order to accurately measure the velocity, enough of the evolution of event needs to be seen in the detector to reduce the uncertainty in the fit. This is because as
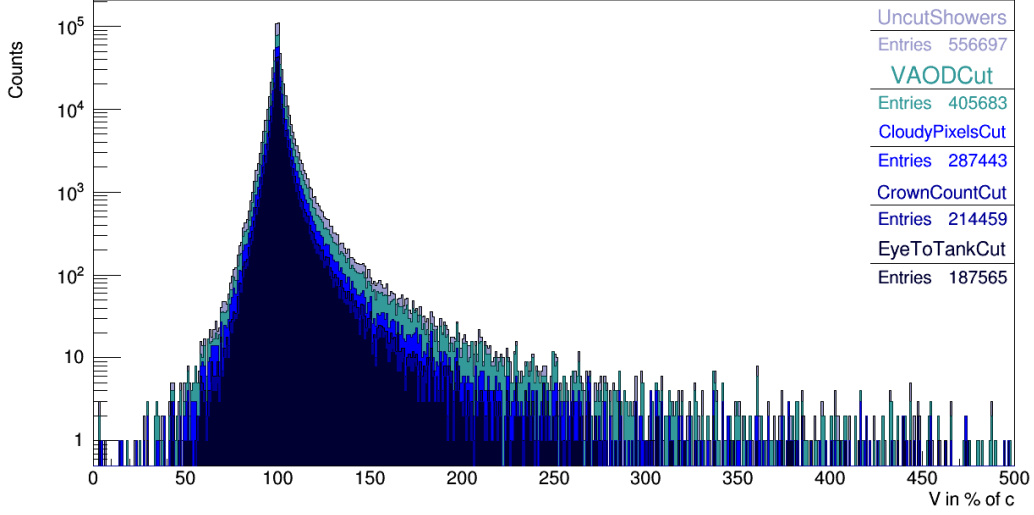
Figure 7.9: The Effects of the Hybrid Data Specific Quality Cuts as described in the text.

Table 7.2: Hybrid Measurement Quality Cuts

Quality Cut	Showers After Cut	% Showers Cut
Events With Good Data	187565	-na-
$\chi_i^{top} - \chi_i^{bottom} \geq 15°$	166139	11.4%
$0.5 \leq (\chi_i^{top} - \chi_i^{bottom})/N_{pix} \leq 1.25$	91565	44.9%
If $N_{telescopes} = 2$ then $\theta_{SDP} \leq 80°$ or $\theta_{SDP} \geq 100°$	85238	6.9%
Well Measured Events	85238	54.6%

the length of the track shortens, the constraint on the fit far away from the data is reduced. This is seen frequently in physics and is given large amounts of attention in the context of determining the spectral content of oscillating data. This quality of the data was not a concern in stereo due to the simple fact that each stereo event was observed multiple times by spatially separated detectors. With stereo, the geometry is almost completely determined by the pixel geometries; leaving nearly all of the timing information for the velocity fit. This luxury is not available to hybrid data as the SD signal only constrains the geometry and timing at a single point, making both the angular and velocity reconstructions the responsibility of the pixel timing data. This is only possible if the event observation has enough angular length to provide a good

measure of the timing profile's curvature.

Setting a theoretically determined minimum length is difficult due to a strong reliance on the event's location and geometry. Because of this, several different cuts were tried looking for a balance between the efficacy of the cut and how deeply it cut the data. Of the cuts tried, events seemed to be well constrained when at least half the camera, or 15°, observed the event. Results did improve at high arc lengths, however, above this limit data began to be cut very deeply.

- $\chi_i^{top} - \chi_i^{bottom} \geq 15°$

This cut is fairly relaxed and could be much tighter, however, as will be seen later, the sum total of the quality cuts leveled against the hybrid data do remove a large percentage of events. Additionally, other later cuts on reconstruction quality directly mitigate the effects of any events that pass this cut and still have too short of tracks to sufficiently constrain the data. As can be seen in Table 7.2 and Figure 7.10 this cut reduces the event count from 187565 to 166139 a 11.4% reduction of the data[12].

Shower Track Density Cut

Occasionally, recorded events can have gaps in their pixel track. These gaps are usually due to a weak event or the presence of a cloud between the event and the Eye. Gaps in the data increase uncertainty in the velocity reconstruction and should be removed. The angular pixel density of the shower track (ρ_{track}) is calculated as $\rho_{track} = (\chi_i^{top} - \chi_i^{bottom})/N_{pix}$. For an unbroken shower track, the minimum possible ρ_{track} is 1.5° per pixel, occurring when the event has an SDP inclined at 60° or 120° and is therefore aligned with camera's pixel arrangement. In this geometry the uncertainty in the

---

[12]In conjunction with the angular length cut an additional requirement was leveled against the data that demanded that the reconstructed χ_0 was less than the highest angular observation χ_i^{top}. This cut was made because it is physically impossible to observe an event at an angle higher than its inclination angle. This is simply because at this point the vector representing the view of the pixel is parallel to the shower axis and therefore they never intersect. This cut only removed one event that appeared to be a 'cluster event' that made it past the TLT FD trigger. The fact that no quality events had impossible χ_0 values lends confidence to the accuracy of the geometric reconstruction of the velocity dependent hybrid method.

SDP is maximized, which in turn increases the uncertainty in both the geometric and velocity reconstructions. Ideally for velocity reconstruction the pixel track should be 2 pixels wide leading to a ρ_{track} of 1° per pixel. This cut is too stringent, however, so the cut was placed at 1.25° per pixel, half way between minimum and ideal value.

Though the cloud cuts are stringent, they can not possibly remove all cloudy events from the data set. Also, as explained in Section 3.2, the FD occasionally records direct hits to the camera, instrumentation noise or bright background fluctuations that cause large events with random time ordering. These 'cluster events' can last for extended periods of time and do sometimes occur in conjunction with a legitimate hybrid event. Because of their large and temporally unordered signals, these events, like cloud events, can cause erroneous velocity measurements and also need to be removed. Both the cluster and cloud events appear as groups of pixels that are triggered in track geometries, and therefore have a large number of triggered pixels as compared to the events angular length. Due to these characteristics, both cluster and cloud events can be removed by cutting on the bottom end of the angular pixel density. By requiring a ρ_{track} of at least 0.5° per pixel, most clouds and clusters can be removed while still allowing events that are three pixels wide to be passed.

- $0.5 \leq (\chi_i^{top} - \chi_i^{bottom})/N_{pix} \leq 1.25$

As seen in Table 7.2 and Figure 7.10, this cut, while less stringent than the ideal placement, still represents a significant cut on the data reducing the event count from 166139 to 91565, a 44.9% reduction of the data.

Telescope Interface Cut

If an event travels along the interface between two adjacent telescopes in an Eye, the signal will jump back and forth between the two. Because the telescopes are not perfectly synchronized with each other this can lead to the timing profile spreading out. This in turn will increase the uncertainty of the velocity reconstruction requiring

151

the removal of these events. For the purposes of this cut, these events are identified by having nearly vertical SDPs (within $10°$) while appearing in two telescopes.

- If $N_{telescopes} = 2$ then $\theta_{SDP} \leq 80°$ or $\theta_{SDP} \geq 100°$

This cut reduces the event count from 91565 to 85238- cutting 6.9% of the data.
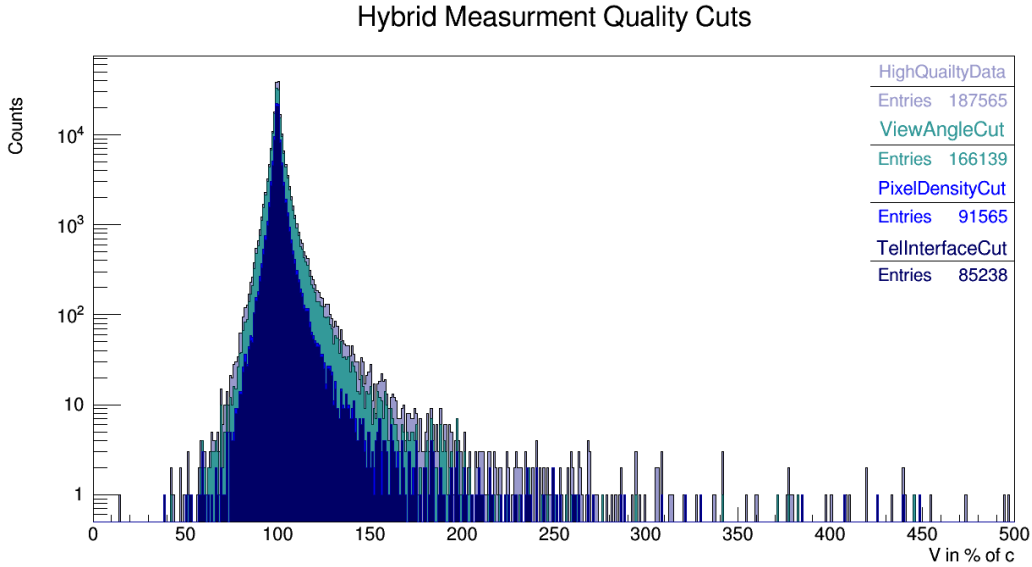
Figure 7.10: The Effects of the Hybrid Measurement Specific Quality Cuts as described in the text.

Figure 7.10 shows that the tails have been significantly reduced by the measurement quality cuts, however though a further 54.6% of the data has been removed, the tails still remain far too large for candidate selection. With the data and measurement quality cuts already applied, the only set of cuts left are those that directly weigh how well the fitted parameters match the data. These reconstruction quality cuts are defined as follows:

Fit Quality Cuts

As was stated in the description of the stereo cuts, one of the best metrics for how well the fitted parameters match the data is the reduced χ^2 value. The cut on the reduced hybrid timefit χ^2 ($\eta\chi^2_{hy} = \chi^2_{hy}/NDoF_{hy}$) will ensure that the reconstructed

Table 7.3: Reconstruction Quality Cuts

Quality Cut	Showers After Cut	% Showers Cut
Well Measured Events	85251	-na-
$\eta\chi^2_{hy} \leq 3$	84925	0.38%
$.75 < \eta\chi^2_{SDP} \leq 3$	77282	9.0%
$Core_{FDerr}/D_{EyeToCore} \leq 10\%$	76959	0.42%
$\phi_{\hat{\mathbf{S}}err}sin\theta_{\hat{\mathbf{S}}} \leq 4°$	71241	7.4%
$\theta_{\hat{\mathbf{S}}err} \leq 3.6°$	67404	5.4%
$|\vec{r}_{axis}| \leq 1km$	63744	5.4%
$V_{err} \leq 1.5\%$ of c	30404	52.3%
Well Reconstructed Events	30404	64.3%

parameters match the event data. As in the stereo case, the upper limit for $\eta\chi^2_{hy}$ is set at 3 following the guidelines laid out in [77].

- $\eta\chi^2_{hy} \leq 3$

From the data shown in Table 7.3, it is clear that the preceding cuts did prepare the data well for reconstruction as the $\eta\chi^2_{hy}$ cut only removed 0.38% of the data lowering the event count from 85251 to 84925.

For hybrid reconstruction, a cut on the reduced SDP χ^2 value ($\eta\chi^2_{SDP} = \chi^2_{SDP}/NDoF_{SDP}$) is also needed as the quality of the SDP fit largely dictates the quality of the velocity fit. This is because any error in the SDP plane would serve to increase the track length while having little effect on the event timing. This would lead to an increase in the event's reconstructed velocity. However, a cut on $\eta\chi^2_{SDP}$ is not as simple as a cut on $\eta\chi^2_{hy}$. Depending on the width of the shower in the Eye, the optimal value of $\eta\chi^2_{SDP}$ will change. This is because the pointing directions of the pixels are static and can never perfectly match the fitted SDP. As an event track gets wider, the average distance of each pixel from the SDP increases, therefore $\eta\chi^2_{SDP}$ is dependent not only on the final value of the SDP, but also on the width of the event track. Following this logic, if the $\eta\chi^2_{SDP}$ is too low, then it is likely that there was an error as only an event consisting of a single pixel track can have a very small $\eta\chi^2_{SDP}$. Though these events

153

do minimize $\eta\chi^2_{SDP}$ quite well, they also maximize the SDP uncertainty so these must be cut as well. To address both these concerns, $\eta\chi^2_{SDP}$ is constrained on both sides. The low end cut is placed at 0.8° which is slightly more than half the width of a single pixel, while the high end cut is placed at three allowing 3-pixel-wide showers through, but removes bad fits as well as any clusters or cloudy events that survived the previous cuts.

- $\eta\chi^2_{hy} \leq 3$

The majority of the data cut was removed by the top end of the cut, suggesting that the pixel density cut did its job well. The application of these cuts removed 9% of the remaining data taking the event count from 84925 to 77282.

Geometric Reconstruction Error Cuts

One of the key determinates of how well the reconstruction of the propagation speed can be trusted, is the level to which the geometric reconstruction can be trusted. Like the velocity error in stereo, each reconstructed geometric parameter is reported with an associated error. This error is a measure of how strongly the χ^2 function varied with regard to that parameter near its minimized values. If the χ^2 function does not vary strongly with changes in a variable, then the level of certainty in the end value of the variable is greatly reduced. So, because changes in geometry directly change the velocity, it is important to only look at events whose geometric reconstruction can be trusted. Essentially, the geometric reconstruction error is broken into two components: the error in the core location, and the error in the axis trajectory.

The first cut applied restricts the maximum allowable error in the core position as a percentage of the event's distance from the detector. It is cut as a percentage because if the event is very close to the Eye, small changes in the location of the core can have a huge impact on the velocity, meaning that lower errors have larger effects on the velocity. The converse of this is true for distant events. The specific applied cut is

fairly liberal allowing an error of up to 10% of distance from the event.

- $Core_{FDerr}/D_{EyeToCore} \leq 10\%$

This demand on the data removes only 323 of the worst events, lowering the event count from 77282 to 76959.

The second cut applied restricts the angular error on the axis reconstruction. When cutting on polar angles it is important to remember that if the zenith angle is near vertical then very large changes in azimuthal angle will only have a small effect on the overall direction of the vector. This means that a cut on the azimuthal error should have zenith angle dependence. This was done by multiplying the azimuthal error by the sine of the zenith angle which is a good metric of how strongly the azimuthal error can effect the overall direction of the axis. The specific location of both of these cuts was made by looking at the distribution of the angular error and then cutting where the main body of the histogram gave out to the tails. The azimuthal error was very tightly bunched up to a value of 4° with a large tail after, while the zenith error had a smaller tails starting around 3.6°.

- $\phi_{\hat{\mathbf{S}}err} sin\theta_{\hat{\mathbf{S}}} \leq 4°$

- $\theta_{\hat{\mathbf{S}}err} \leq 3.6°$

These cuts removed 7.4% and 5.4% of the data respectively, reducing the dataset from 76959 to 67404 events. As can be seen in Figure 7.11, after these geometric cuts the tails are greatly reduced, with the furthest out event appearing at 160% of c as compared to almost 430% before the cuts.

FD Core Hot Tank Agreement Cuts

Between the crown cut and the $Core_{FDerr}$ the closest tank to the event core should be the selected hot tank. Because the SD array is arranged in a $1.5km$ triangular grid, the furthest any point in the SD array can be from a tank is $\sim 866m$. This leads to

an expectation of the FD core always being within $866m$ of the triggered hot tank. In reality, it is not quite so simple as this as the hot tank is, with some complicated exceptions, the tank that is closest to the axis at any point in the shower. This leads to Hot Tanks that are a little more distant than the maximum $866m$ distance from a tank when the event is severely inclined and lands just right in the array. To allow for these rare special cases, while still assuring that only reconstructions with decent FD and SD agreement are allowed into the final data set, any events with the FD core further away than $1km$ from the hot tank are removed from the data set. Recalling that $|\vec{r}_{axis}|$ is the vector pointing from the core on the ground to the hot tank, the cut is:

- $|\vec{r}_{axis}| \leq 1km$

This cut removes 3660 events from the data set, lowering the event count from 67404 to 63744 events, a 5.4% reduction.

Velocity Error Cut

The last cut on the data is the cut that sets the maximum allowed reconstruction error on the velocity. With this cut, assuming that the data presented to the reconstruction is of a high quality and suitable for a velocity measurement, the velocity resolution of the hybrid method is set. Choosing the location of the cut needs to be done with external consideration as it, to a large degree, determines the width of the cosmic ray parent distribution against which any potential candidates will be weighed. Because the hybrid distribution still contains a good number of events as compared to the stereo distribution, the cut location of 1.5% of c suggested by the laser studies was used.

- $V_{err} \leq 1.5\%$ of c

This limit does cut deeply into the remaining event set, removing 52.3% of the data, however, as seen by the dark blue distribution with the white outline in Figure 7.11 the

156

effect of this cut is impressive. After application of this cut the core of the distribution remains intact, however the tails and shoulders of the distribution are largely removed leaving a small number of distinct outliers. The cut does come at a considerable price, however, as event count now stands at 30404 events as compared to 63744 before the cut. In the future, perhaps this cut can be relaxed to search for events farther and farther from c.
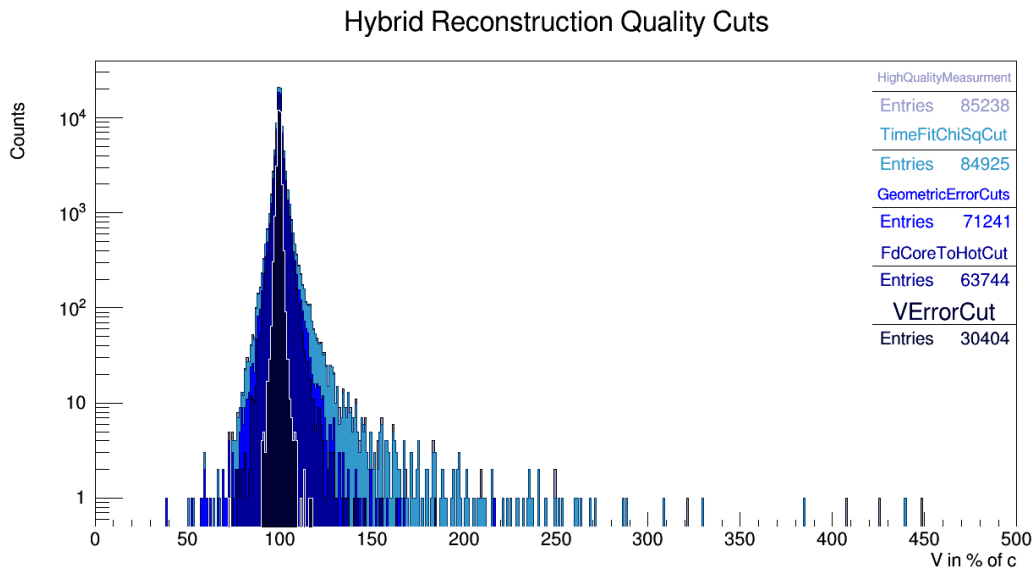
Figure 7.11: The Effects of the Hybrid Reconstruction Specific Quality Cuts: .

Comparing the before and after effects of the cut set in Figure 7.12, the result is striking. The distribution has narrowed to a massive degree, lowering the skew and kurtosis by an order of magnitude. This, unfortunately, comes at an order of magnitude loss of data. Most of this data was removed due to atmospheric conditions, however it is still a considerable amount of data loss. In the future these cuts should be readdressed to see if an equally effective but more forgiving set can be implemented.

7.5.2 Final Hybrid Distributions

Shown in Figure 7.13, after the quality cuts are applied, the final velocity distribution for hybrid shower events is quite narrow for each Eye. Each Eye also displays a strikingly similar
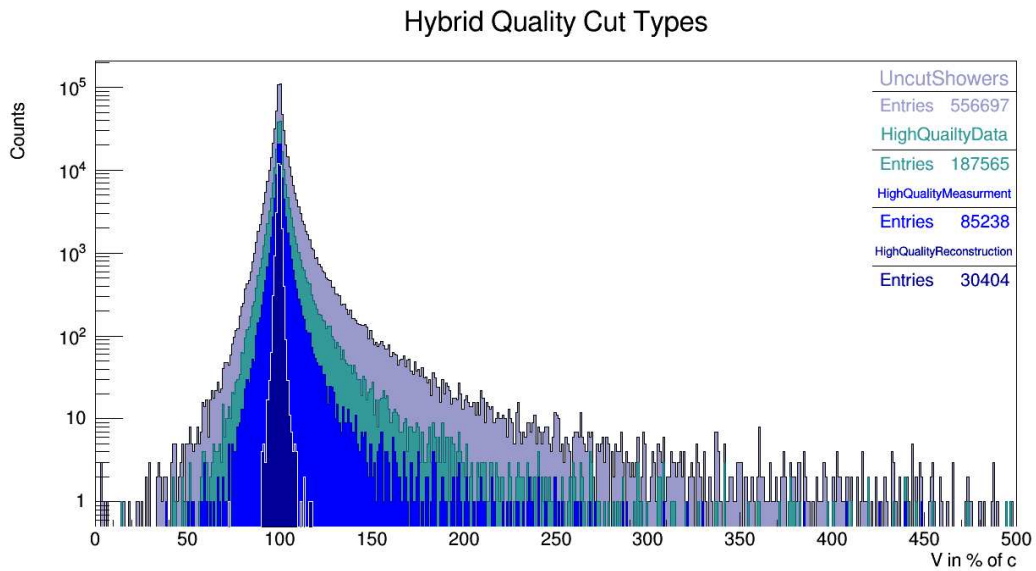
Figure 7.12: The Effects of the Hybrid Quality Cut Sets: The results of each set of quality cuts.

distribution with some definite left-right asymmetry. This suggests that there is indeed an underlying parent distribution and that different errors push the velocity slower or faster. These factors point to a small inherent error rate in the reconstruction that is different for the left and right sides of the distribution. By using this error rate to quantify the rarity of any outlier events, it should be possible to statistically decide which, if any, outliers are promising as candidates. Exactly this will be done in Chapter 8, Candidate Selection and Analysis.
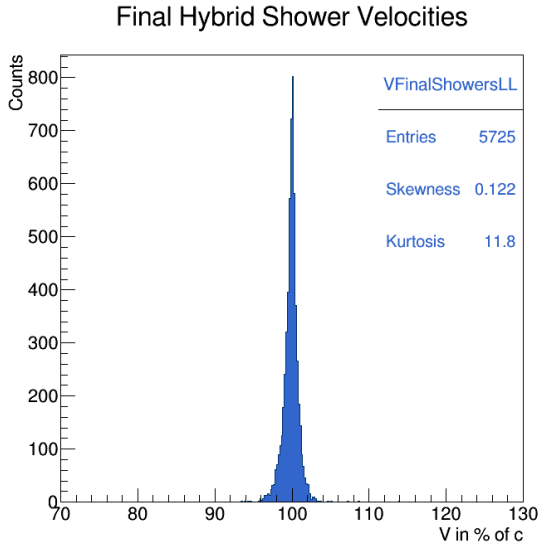
(a) Los Leones
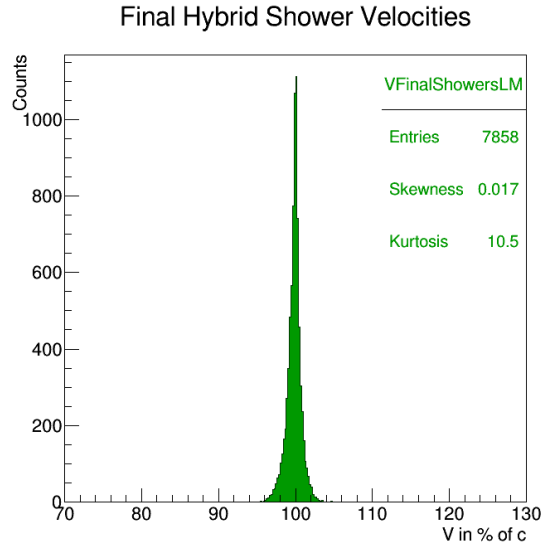
(b) Los Morados
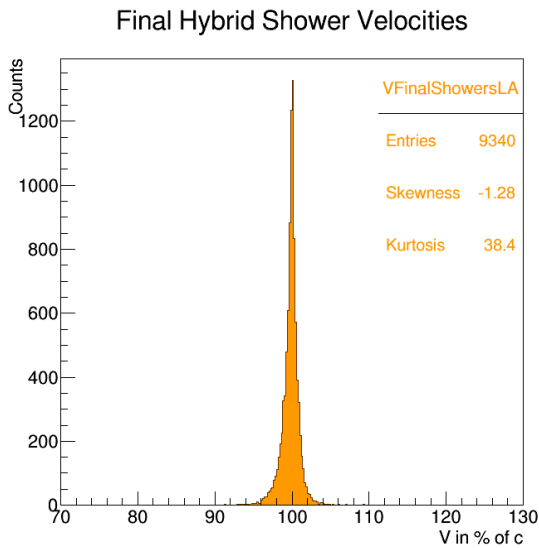
(c) Loma Amarilla
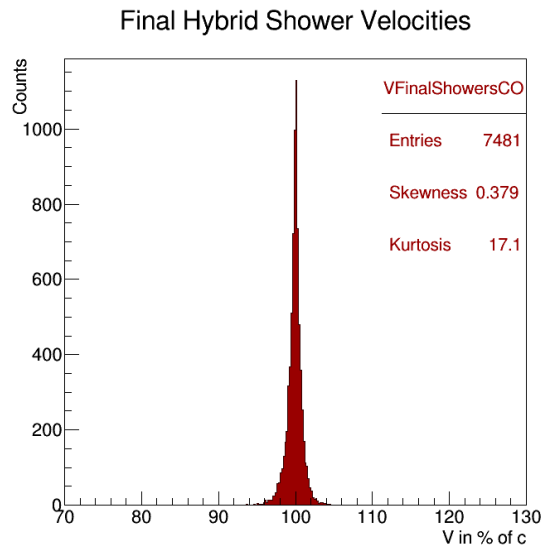
(d) Coihueco

Figure 7.13: Final Hybrid Shower Velocities.

159

CHAPTER 8

CANDIDATE SELECTION AND ANALYSIS

The purpose of candidate selection is to determine which, if any, of the velocity outliers present in the final stereo or hybrid distributions are significant and can be considered potential candidates. Given the sizable tails in the uncut stereo and hybrid shower distributions shown in Figure 6.8 and Figure 7.8, both methods are capable of producing false positives. The quality cuts imposed on both datasets are aimed at eliminating all possible false positives, however they will not do so perfectly. The fact that the velocity reconstruction and quality cuts are imperfect is clear in both Figure 6.10 and Figure 7.13. Given that the vast majority of the events in both the stereo and hybrid samples are assuredly cosmic rays and therefore do propagate at c, if the reconstruction method was perfect, the distributions shown in Figure 6.10 and Figure 7.13 should be delta functions. However, clearly this is not the case as both stereo and hybrid instead display parent distributions with a substantial width. Because of this, the possiblity of false positives is present and a selection criteria in addition to the velocity, needs to be employed; the fit improvement ratio.

The fit improvement ratio is a measure that compares how well the data from each even was represented by the reconstruction with a free velocity as compared to the standard reconstruction performed at c and is defined as $\eta\chi_c^2/\eta\chi_v^2$. The basic idea for using this as a means of validating candidates is that if an event truly propagated at a velocity faster or slower than the speed of light then the data from that event should be much better represented by a model using that velocity than the standard propagation model with the event velocity fixed to c. This has to be done carefully, simply due to the fact that the velocity dependent model has one more parameter than the standard version. This means that the model is more flexible and can therefore always represent the data better. This is somewhat compensated for by using the reduced χ^2 values instead of the raw χ^2 values. Because the

reduced χ^2 value is defined as $\eta\chi^2 = \chi^2/NDoF$ where $NDoF$, the number of degrees of freedom, is equal to the number of data points minus the number of fit parameters, meaning that for a reconstruction at c, $\eta\chi^2_V$ should always be slightly larger than $\eta\chi^2_c$ as in nearly every case $NDoF_v = NDoF_c - 1$. This however, is not enough to completely compensate for the increase in the flexibility of the model, meaning that a parent improvement ratio distribution consisting only of cosmic ray events should be expected to have a tail extending to high values.

In order for an event to be considered as an exotic candidate it needs to have both an outlying velocity **and** be fit significantly better with the reconstructed velocity. However, simply cross referencing outliers in both distributions would not provide fair selection. If an event is a very significant velocity outlier, but is not among the furthest outliers in the fit improvement distribution, it should still be able to be selected if the combination of its velocity offset and improvement ratio is far above what is expected. To do this, the metric against which an event will be judged as a candidate is chosen to be its velocity offset times its improvement ratio to produce a value here on called the event "exoticness".

The basic method to be employed in this section is as follows: First, because both Figure 6.10 and Figure 7.13 show that the left and right sides of the distributions reliably display different behaviors, the left and right sides of the distributions need to be treated separately. To do this, the final velocity distributions are split at their mode. The mode is used instead of c, or the centroid, as the distributions are asymmetric and not centered exactly at c. Each side's parent distribution will be fit with a normalizable function with the goal of accurately describing the error rate. The same process will be carried out on the improvement ratio to find a normalizable function that closely describes its behavior as well. These fitted functions will not be used directly, but will instead be used to build a function to describe the exoticness of each event set.

From here, the left and right sides of the velocity distribution will be combined with the fit improvement values on an event-by-event basis to calculate the exoticness of each

event. This combined distribution will then be fit using the combination of the velocity and improvement functions. This function is then normalized to form a probability density function (PDF) that estimates the chance of finding some level of exoticness given the error rate of parent distribution. From here, the exoticness value of each event will be compared to the probability of that value being due to random chance given the number of independent events in the dataset. If an event is found to display an exoticness value with a less than 3×10^{-7} (5σ) probability of occurring in a dataset of size N_{Events}, then it will be selected as an exotic candidate.

This method relies on the assumption that if candidates are present in the dataset, they are small in number compared to the number of cosmic ray events and therefore fits to the parent distributions are representative of the error rate of the method and are not significantly affected by the presence of any exotic candidates. This is not, however, true for stereo given that the stereo dataset only contains 1125 events. Once split, each side of the distribution will have around 600 or less events, meaning a fit to the distribution could easily be changed by outliers. Therefore, in stereo, 5% of the most outlying events, roughly corresponding to 2σ, will be excluded from the fit. Given the number of events in the hybrid distribution, the fits to the split datasets should be swayed little by the presence of outliers. To be safe, the outliers will be removed before fitting, however removing 5% of the data cuts quite deeply into the distributions. Therefore, the cut on the hybrid data is placed a 3σ, keeping 99.7% of events.

8.1 Stereo Event Selection and Candidates

The first step is to split the velocity at the mode and fit both sides. Because these velocity distributions are strongly peaked near the mode, small changes in the mode's location can cause the number of events on either side of it to vary to a large degree. Additionally, because with binned data the location of the mode is dependent on the binning, calculating its position in a velocity distribution takes a little forethought. To combat these effects, the mode of the velocity distribution was found with histograms split into 1000, 2000, 4000 and
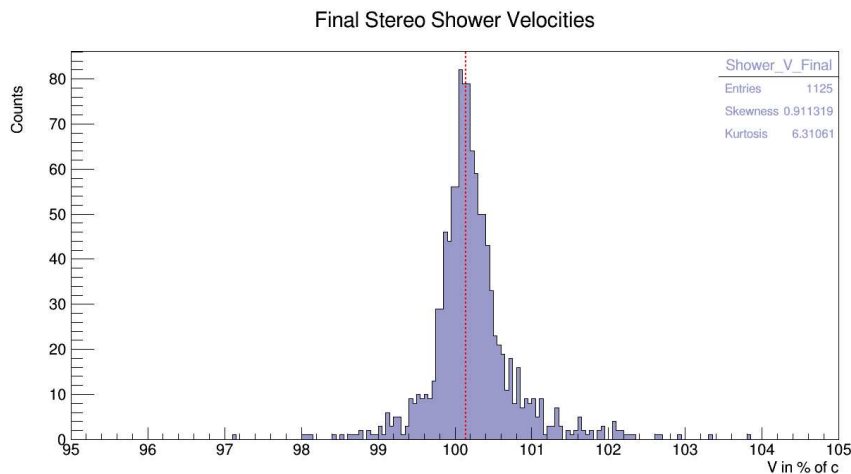
Figure 8.1: Stereo Final Distribution with Mode.

6000 bins. These mode values were then averaged to get a stable value. The placement of this calculated mode can be seen superimposed on the velocity in Figure 8.1.

The data was then split at this value resulting in a slow ($V < mode$) and fast ($V > mode$) data set. The absolute value of the velocity offset from the mode was then placed into histograms, $Offset = mode - V$ in Figure 8.2(a) and $Offset = V - mode$ in Figure 8.2(b). These histograms were then fit with a variety of normalizable functions until a good match was found. In the end an exponential function of the form

$$y = Exp[Constant + Slope * x] \tag{8.1}$$

was shown to describe both sides of the data well. This function was then fit to the distribution using Root's standard χ^2 fitting routine. The resulting fits were shown to very well match the offset data returning $\eta\chi^2 = 1.1$ for the slow side and $\eta\chi^2 = 1.0$ for the fast side. The fitted curves and fit values can be seen in Figure 8.2(a) and Figure 8.2(b).

The next step was to quantify the behavior of the improvement ratio for values above 1. This was somewhat more difficult as the log plot of the distribution is concave up. First, fitting with an exponential was attempted, but was found to severely underestimate the tails. Then ChiSq distributions with 1 or 2 degrees of freedom, ($\chi^2(k = 1)$ and $\chi^2(k = 2)$) were tried, only to have both underestimate the peak and overestimate the tails. Then, because

163

(a) Stereo Velocity: Slow Side

(b) Stereo Velocity: Fast Side
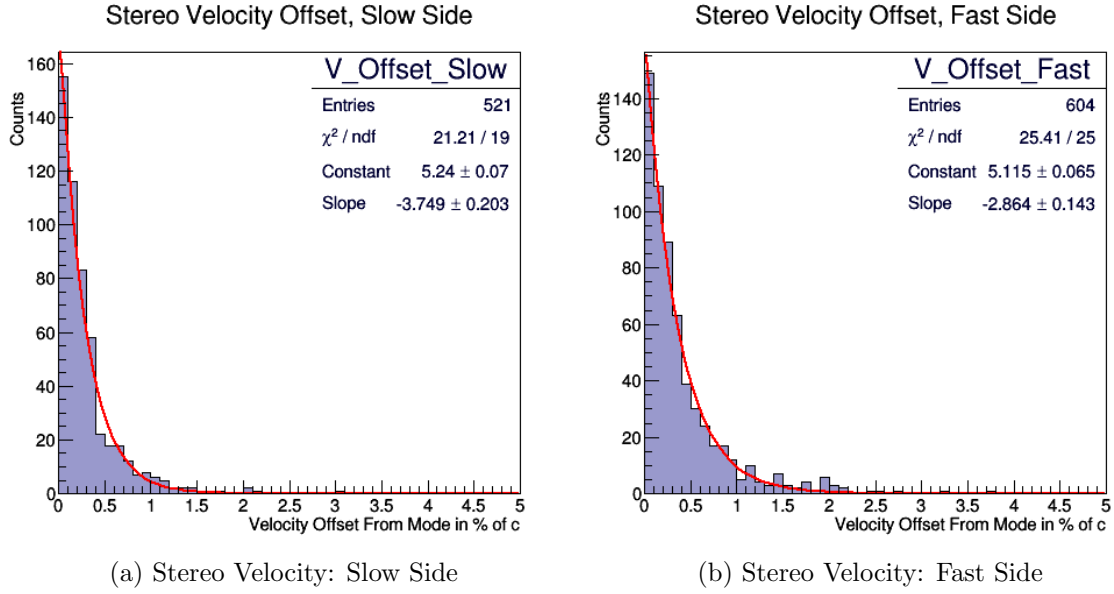
Figure 8.2: Stereo Slow and Fast Velocities.

the improvement ratio is the ratio of a 5 parameter ChiSq population over a 6 parameter ChiSq population, a fit was attempted with the function $\chi^2(k = 5)/\chi^2(k = 6)$ which failed describe the body of the distribution and overestimated its tails [79]. Eventually, the Pareto distribution which has found use describing forest fires, Bose-Einstein condensates and the distribution of wealth in America was tried as it splits the behavior of the exponential and ChiSq functions and was found to work well. The scalable Pareto distribution has the form

$$p = \begin{cases} \frac{[0]x_m^{[1]}}{x^{([1]+1)}} & x \geq x_m \\ 0 & x \leq x_m \end{cases} \tag{8.2}$$

where [0] is a scaling factor to fit a non-normalized distribution, x_m is the value below which the distribution drops off (1 in our case) and [1] a curvature parameter. Because Root had difficulty fitting this distribution when it was offset from 0, one was subtracted from the improvement value to bring the left side of the distribution to zero, to compensate in the Pareto distribution $x \rightarrow x + 1$. In the end the Pareto described the improvement ratio distributions well, with the fit returning $\eta\chi^2 = 1.25$. The fitted curve and values can be seen in Figure 8.3.
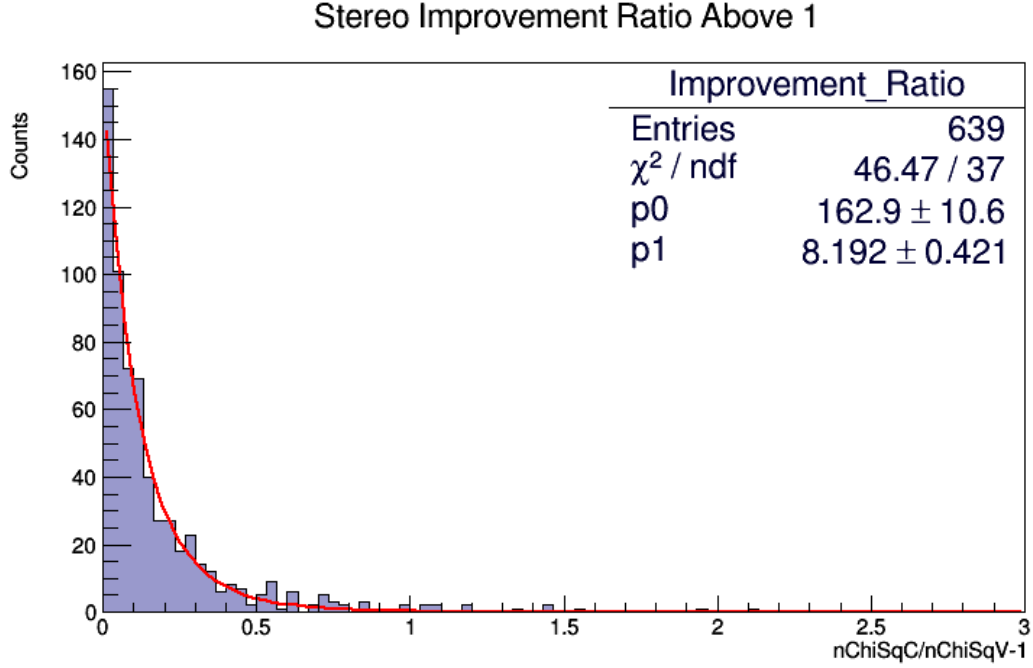
Figure 8.3: Stereo Fit Improvement Ratio.

With the form of both the split velocity and the improvement ratio understood, fitting on the exoticness of the slow and fast event sets can begin. The first step is to combine the velocity offset with the improvement ratio on an event by event basis. For slow events

$$Exoticness_{Slow} = (mode - V) \times \eta\chi_c^2/\eta\chi_v^2, \tag{8.3}$$

while for fast events

$$Exoticness_{Fast} = (V - mode) \times \eta\chi_c^2/\eta\chi_v^2. \tag{8.4}$$

Next, the exponential function was combined with Pareto distribution. After the constant in the exponential was combined with the scaling factor of the Pareto, the resulting function took the form

$$y = [0]\frac{e^{[2]x}}{(x+1)^{[1]+1}}. \tag{8.5}$$

Because of the relatively small sample size of the stereo data, any outliers in the exoticness distribution could easily affect the fit and pull the selection limits farther out. To address
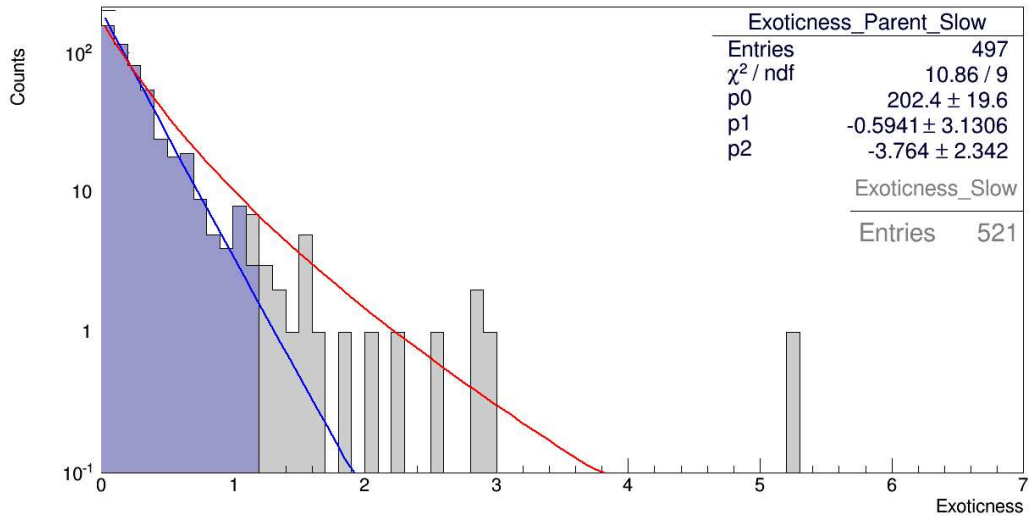
(a) Stereo Exoticness: Slow Side
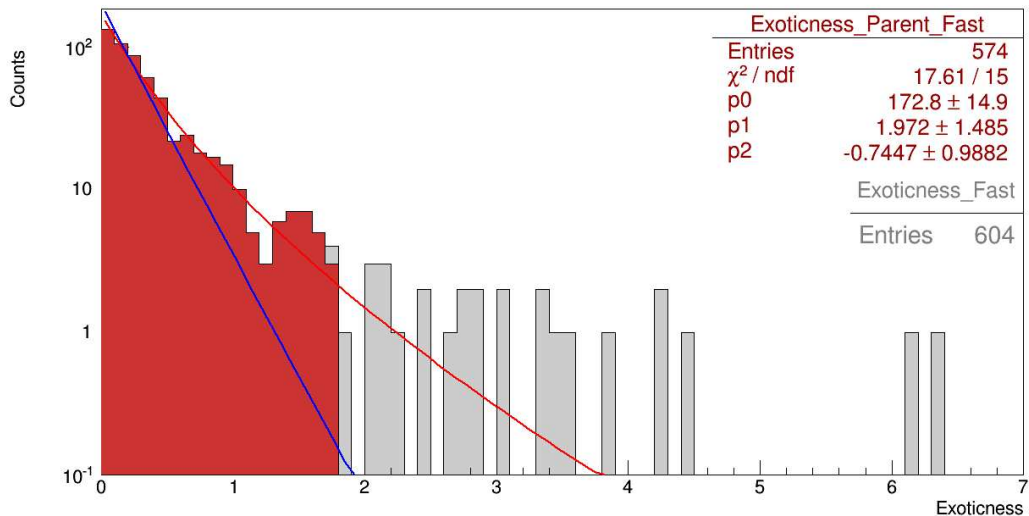
(b) Stereo Exoticness: Fast Side

Figure 8.4: Stereo Exoticness: (a) shows the histogram and fit for events with a reconstructed velocity below the mode. The full event set is shown in grey, while the blue histogram shows events within 2σ of the mode. (b) is for events with a reconstructed velocity above the mode. In this case the red histogram shows events within 2σ of the mode. In both figures the red and blue curves are the same. The blue corresponds to the best fit of the blue histogram while the red corresponds to the best fit of the red histogram.

this possibility, only the closest 95% of the data, representing the events within 2σ of the null result were considered as part of the parent distribution of cosmic rays. The idea being that since all of these events are cosmic rays that propagated at c, then the form of the distribution is directly indicative of the stereo method's error rate. Following this logic, the furthest 5% of events were removed and (8.5) was fit to the exoticness data. The resulting fit described the data well on both sides returning $\eta\chi^2 = 1.20$ on the slow side and $\eta\chi^2 = 1.17$ on the fast side. Neither an exponential or Pareto alone faired nearly as well with the exponential ignoring the tails and the Pareto hugely overestimating them. The fitted curves and values can be seen in Figure 8.4(a) and Figure 8.4(b) along with the parent distributions (the colored histogram) and the close outliers.
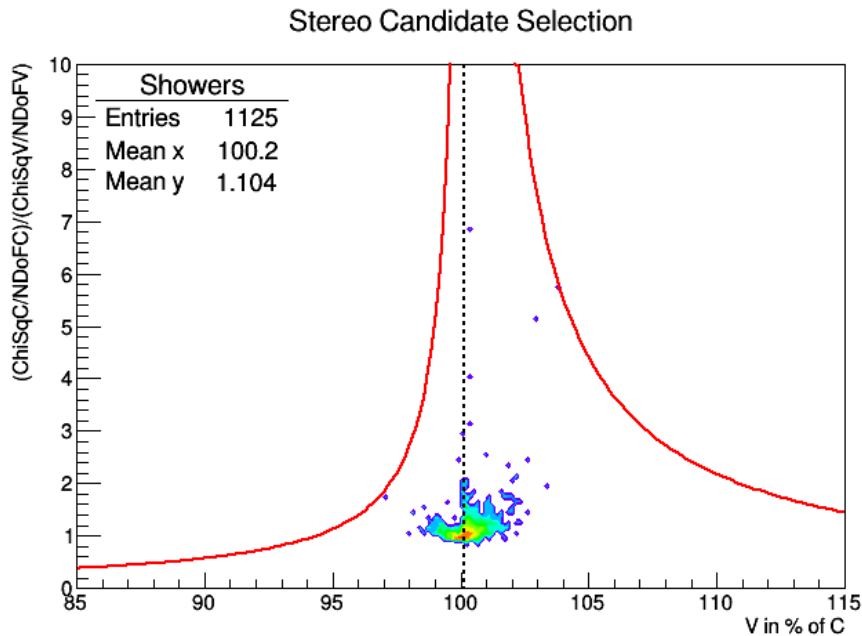
Figure 8.5: Stereo Candidate Selection.

By comparing the fitted curves for the slow side (blue) to the fast side (red) in Figure 8.4(a) and Figure 8.4(b), the asymmetry of the parent distributions becomes clear. The stereo method does seem to have a significantly higher error rate for the unphysical speeds above c than below it. This means that for a faster than light candidate to be considered

167

that it will need to surpass a proportionally higher exoticness limit. To set this limit, first the combined function was numerically normalized to form a probability density function. Then the 5σ exoticness limit which corresponded to $3 \times 10^{-7}/N_{event}$ was calculated via numerical integration, finding that an event with an exoticness exceeding 5.75 for slow events and 21.44 for fast events would be considered a statistically meaningful candidate. Setting (8.3) and (8.4) equal to the limit value resulted in the red hyperbolic curves seen superimposed on the 2D density plot of each event's reconstructed velocity and improvement ratio in Figure 8.5. Any event in the region outside of these curves would be a 5σ exotic candidate.

It is clearly visible in Figure 8.5 that no stereo event exceeded the candidate selection criteria, meaning no stereo events are considered confidently exotic. There are however the two events circled in Figure 8.6 which are rather close. Because a small future change in the fit of the distribution or quality cuts very well may push these events into the selected region, some highlights and interpretation of these events will be given here. Their full standard and velocity based reconstructions, as well as plots of their Observer reconstruction can be found in Appendix D.
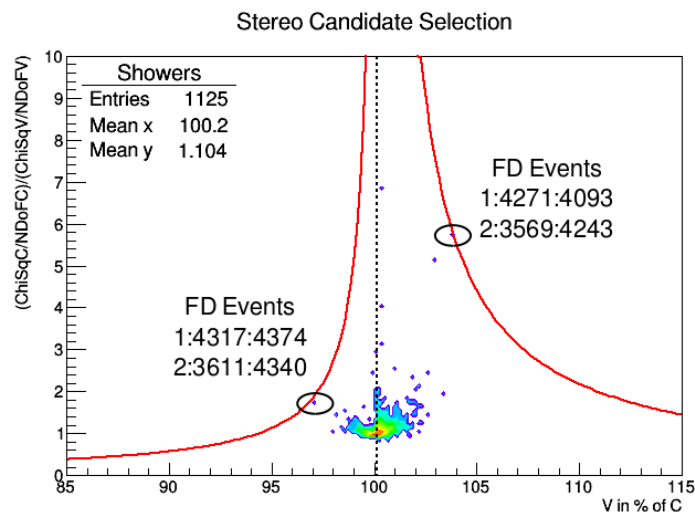
Figure 8.6: Stereo Candidate Selection: the listed FD Events are identified by Eye Number : Run Number : Event Number.

The more extreme outlier, event 1:4271:4093-2:3569:4243 (Eye#:Run#:Event#), shown in Figure 8.7(a), was reconstructed 5.75 times better with a velocity of 103.849% of c than it was at c. This event displays a few qualities that may be responsible for its odd velocity reconstruction. First, as seen in Figure 8.7(b), which shows the intersection of the Los Leones' SDP (blue lines) with Los Morados' SDP (pink lines), the event landed directly in between Los Leones and Los Morados with a nearly vertical trace in each Eye, meaning that the SDPs from each Eye are almost coplanar. Because any axis within this shared plane will fit the pixel geometry of both Eyes, this event geometry effectively nullifies the ability for the stereo method to leverage the SDP information to constrain the axis.

(a) Event Overview   (b) Top Down Core View

(c) Pixel Track Los Morados   (d) Pixel Track Los Leones
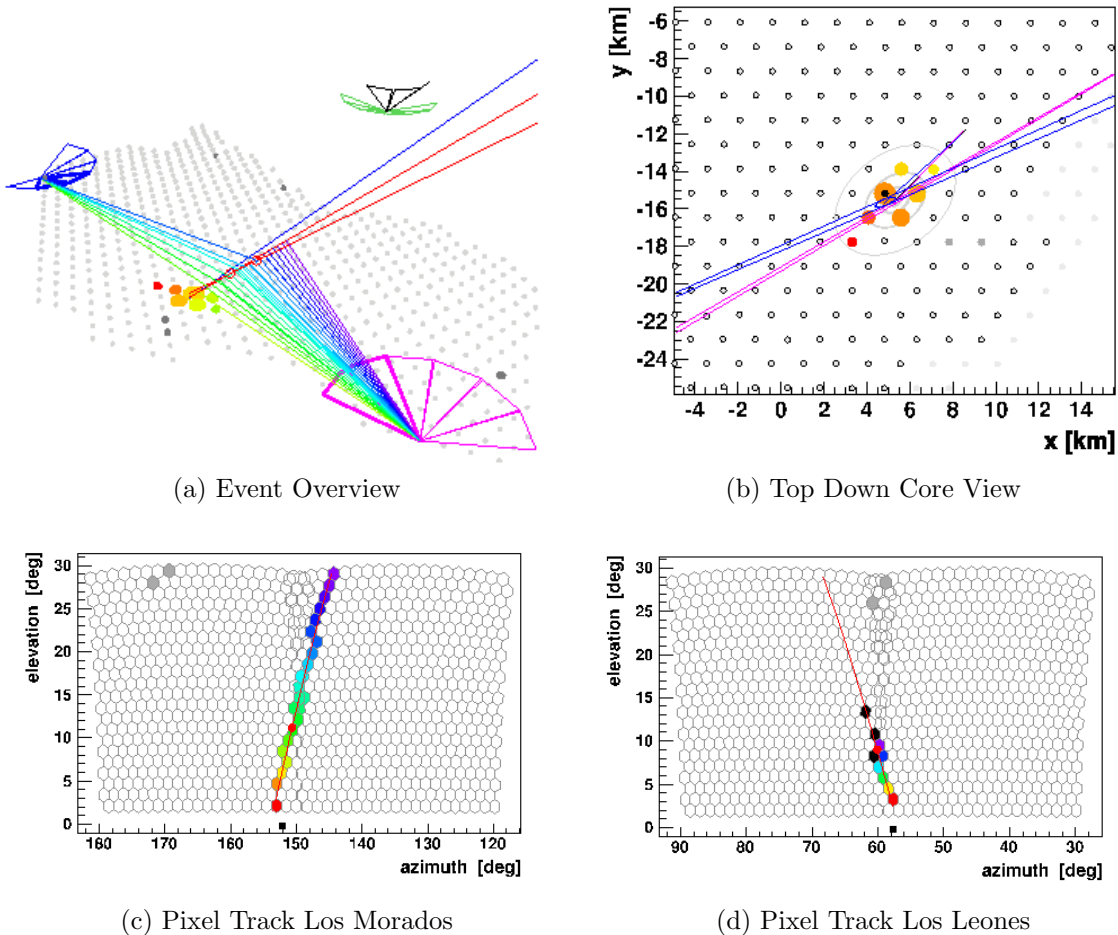
Figure 8.7: Stereo Near Candidate Event 1:4271:4093-2:3569:4243.

Because crossing the SDPs is of no help in this event, the pixel timing from the two Eyes is all that is available to reconstruct both the event geometry and the velocity. This is a significant problem because while the observation from Los Morados, seen in Figure 8.7(c) is quite strong, the observation from Los Leones, seen in Figure 8.7(d), is not. In a stereo event with two distinct and widely separated vantages, this would be less of an issue as long as both Eye's were able to constrain their SDPs. In this case however, the weakness of the Los Leones measurement does little to supplement the measurement from Los Morados and this event practically becomes a monocular reconstruction. Lastly, both pixel traces occupy a telescope to telescope interface further increasing uncertainty in the event timing. To check the validity of the stereo velocity reconstruction, the Hybrid method was applied to the Los Morados data, which disagreed with the stereo result finding an event velocity of 97.4% of c. Because of weakness of the stereo measurement and the strong disagreement between the stereo and hybrid methods, no confidence can be lent to the reconstruction of event 1:4271:4093-2:3569:4243's velocity.

The slow outlier, event 1:4317:4374-2:3611:4340, shown in Figure 8.8(a), was reconstructed 1.75 times better with a velocity of 97.15% of c than it was at c. First, looking at Figure 8.8(b), we can see that in this case the event occurred well off axis and that the SDPs from each Eye are distinct. Given that the SDPs from both Eyes are reliable, the event axis should be fairly well constrained. Neither of the observations from the Eyes are particularly strong however. The observation from Los Morados, seen in Figure 8.8(c) is spread out and weak, but has good length. The observation from Los Leones, seen in Figure 8.8(d), is a bit stronger perhaps, but is short and in a geometry that makes SDP fitting difficult. Because the quality of the individual Eye observations is pretty poor, the minimum number of pixels required for hybrid reconstruction had to be lowered for either Eye to reconstruct this event. When this was done Los Morados returned a hybrid velocity of 98.26% of c and Los Leones found an obviously erroneous velocity of 197.58% of c. These reconstructions are very spread out and really aren't much help. Additionally, due to the low quality of the two individual
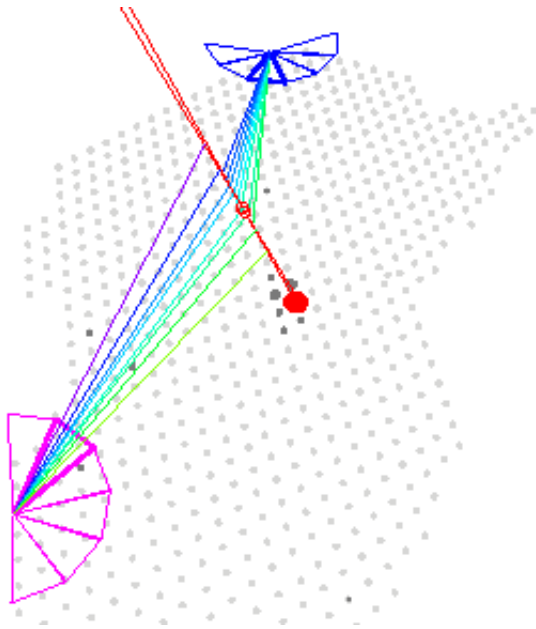
(a) Event Overview
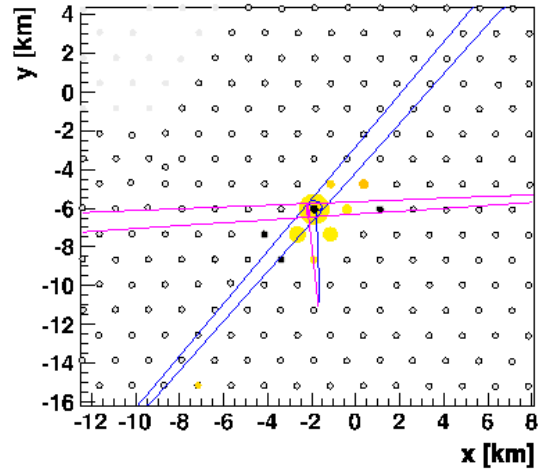
(b) Top Down Core View
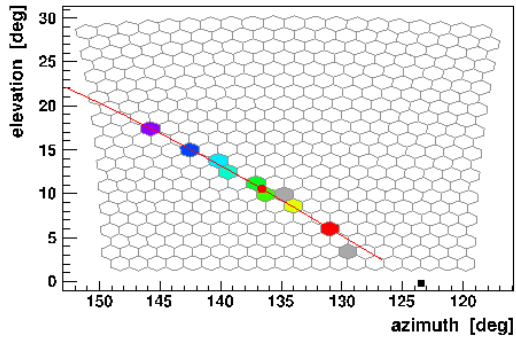
(c) Pixel Track Los Morados
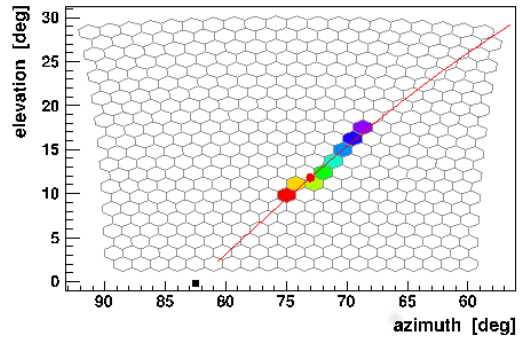
(d) Pixel Track Los Leones

Figure 8.8: Stereo Near Candidate Event 1:4317:4374-2:3611:4340.

events, the results of these hybrid velocity reconstructions can't be lent much confidence anyway. Nothing about this event specifically invalidates the reconstruction, but there is nothing to indicate it is trustworthy either. In any case, the event 1:4271:4093-2:3569:4243 was not selected as an candidate and given its nature, there is no visible reason to elevate it to that status.

8.2 Hybrid Event Selection and Candidates
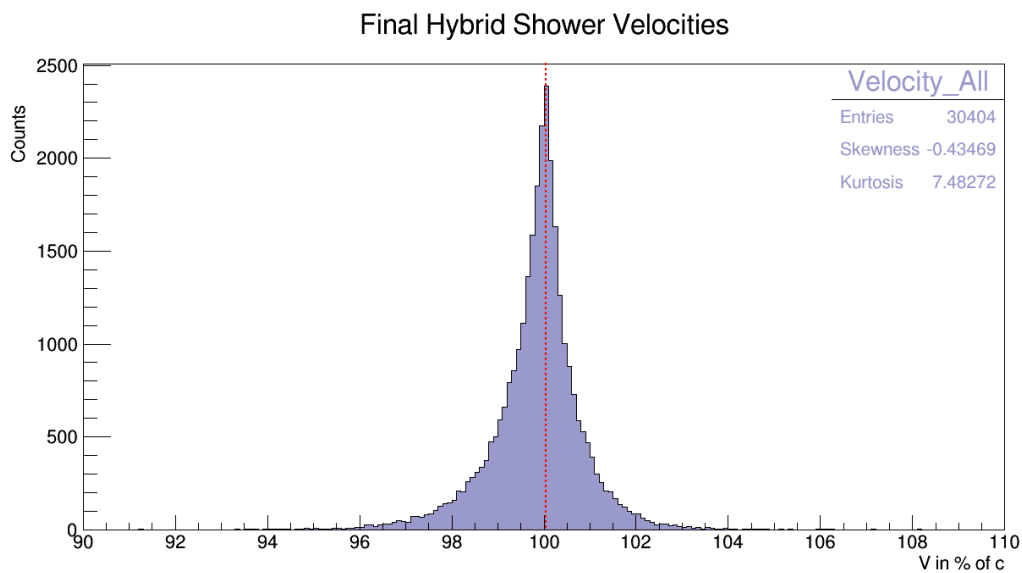
Figure 8.9: Hybrid Final Distribution with Mode.

Hybrid candidate selection follows the same course as stereo candidate selection. Though candidate selection was performed independently for each Eye, because of the sheer number of plots presenting each separately would involve, the process is demonstrated and illustrated with the data from all Eyes simultaneously. For the individual plots, fits and selection criteria, see Appendix C. Like stereo, the first step of hybrid candidate selection is to split the velocity at the mode. This, again, is done by finding the mode for velocity histograms with 1000, 2000, 4000 and 6000 bins and then averaging each result to get a stable value for the mode. The placement of this calculated mode can be seen superimposed on the full hybrid velocity distribution in Figure 8.9.

172

(a) Hybrid Velocity: Slow Side   (b) Hybrid Velocity: Fast Side
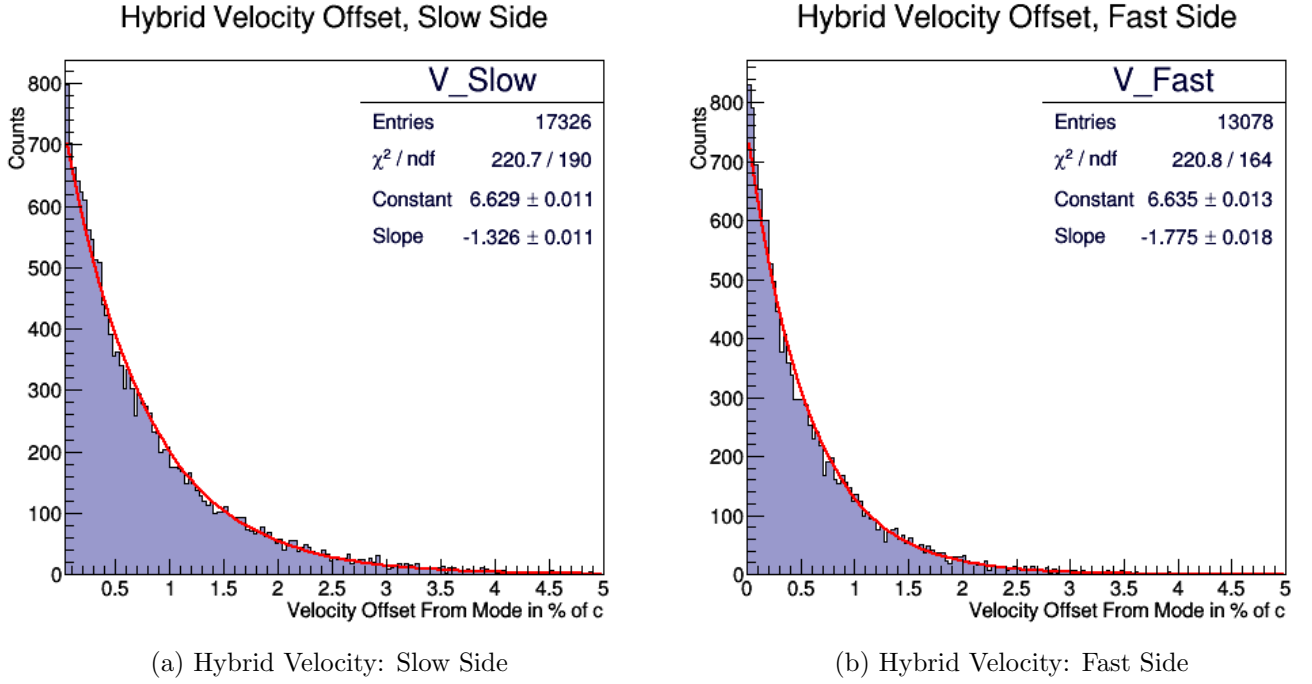
Figure 8.10: Hybrid Slow and Fast Velocities.

The hybrid data was then split at this value resulting in a slow and fast data set. The velocity offset from the mode was then placed into histograms, $Offset = mode - V$ in Figure 8.10(a) and $Offset = V - mode$ in Figure 8.10(b) and fit with (8.1), the same exponential function used in stereo. Root was again used to fit the data to the distributions via its standard χ^2 fitting routine. The resulting fits returned $\eta\chi^2 = 1.16$ for the slow side and $\eta\chi^2 = 1.34$ for the fast side of the full distribution, and can be seen in Figure 8.10(a) and Figure 8.10(b). The fit and $\eta\chi^2$ values for the individual Eyes can be found in Table 8.1. Both the fits for the whole dataset and the individual Eyes show that an exponential describes the velocity data rather well, though perhaps not quite as well as in the stereo case.

The next step was to check that the improvement ratio was still well described by (8.2), the Pareto function. A Root fit was performed on the improvement ratio histogram for all hybrid data resulting in the curve and values seen in Figure 8.11. Clearly with $\eta\chi^2 = 3.7$, the Pareto distribution does not describe the hybrid improvement ratio as well as it did for the stereo data. It did however continue to perform better than both a standard exponential
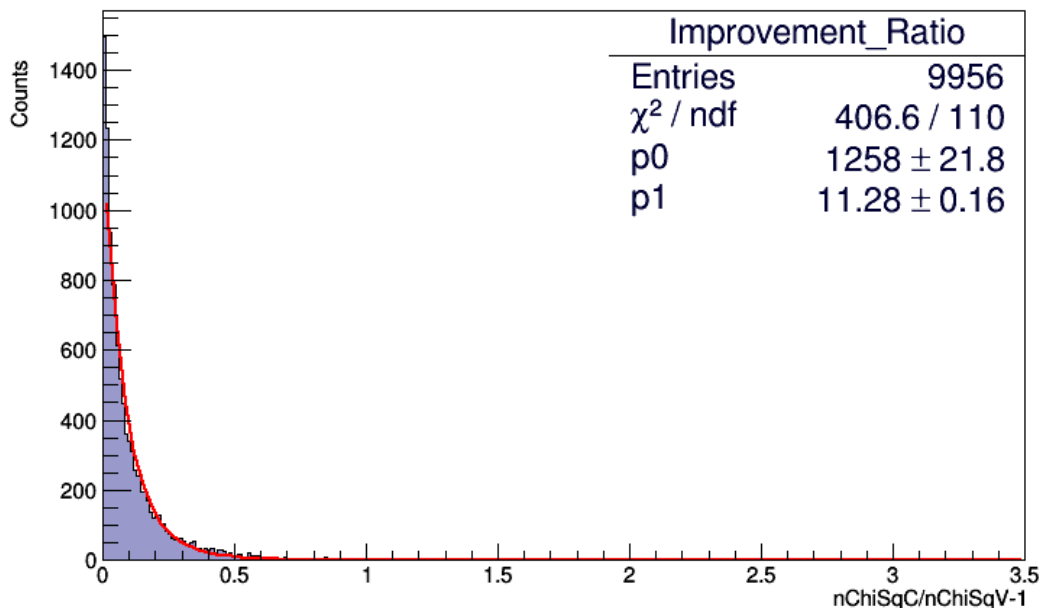
Figure 8.11: Hybrid Fit Improvement Ratio.

and any combination of ChiSq distributions and was therefore still chosen as the function that best represents the data. The fit and $\eta\chi^2$ values for the individual Eyes can be found in Table 8.1[13] and generally show that the Pareto works better on the individual Eyes than it does for the distribution of all events.

Because the functions used in the stereo candidate selection generally still work well for the hybrid data, the same combined function (8.5), was again used on the hybrid data. The notable difference between the two selections is that in the hybrid case 99.7% of the data, or 3σ, was kept and only 0.3% of the data was cut out of the fit as outliers. This change from 2σ to 3σ is due to the large increase in the event count and the fact that selecting only events within 2σ, deeply cut the parent distribution. The results of fitting (8.5) to the slow exoticness distribution are shown in Figure 8.12(a), while the fast fit, curves and values can be seen in Figure 8.12(b).

---

[13]The parameters [0], [1] and [2] are those that appear in (8.5).
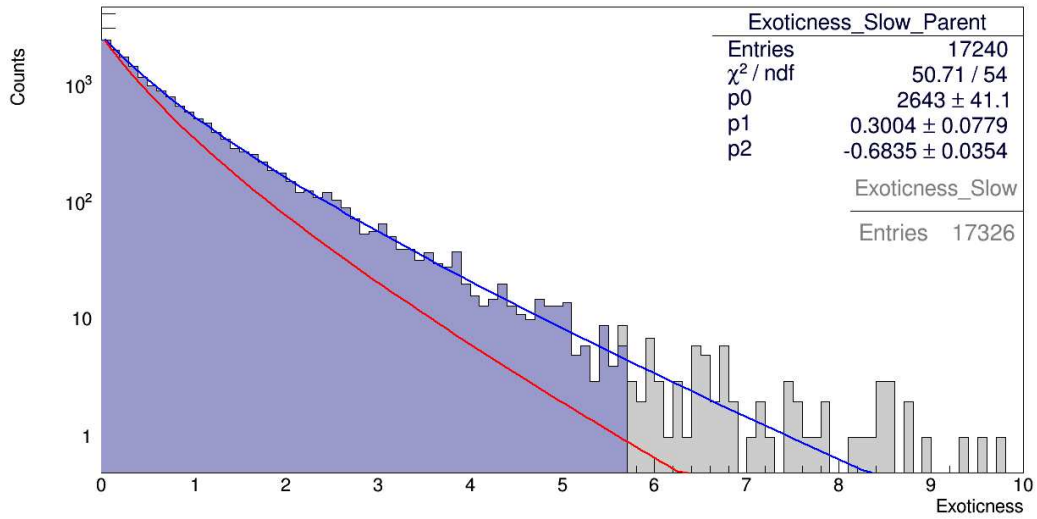
(a) Hybrid Exoticness: Slow Side
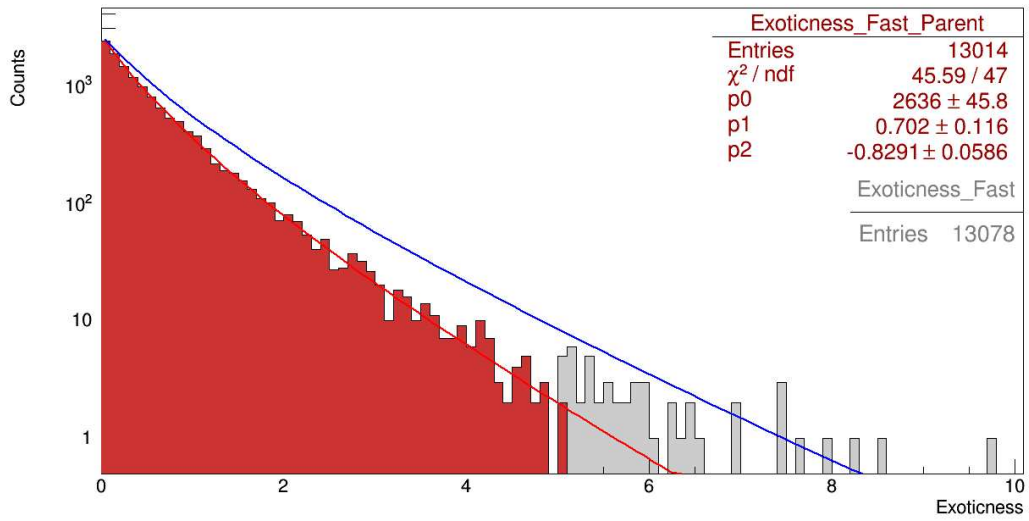
(b) Hybrid Exoticness: Fast Side

Figure 8.12: Hybrid Exoticness.

Table 8.1: Hybrid Distribution Fits

Distribution	$\eta\chi^2$	[0]	[1]	[2]	Selection Limit
Los Leones					
Velocity Slow	0.88	5.97	-1.332		
Velocity Fast	1.38	6.194	-1.806		
Improvement Ratio	1.83	740.6	11.71		
Exoticness Slow	0.85	436.7	-0.1676	-0.907	22.76
Exoticness Fast	1.08	524.9	-0.1364	-1.324	15.75
Los Morados					
Velocity Slow	0.80	6.467	-1.328		
Velocity Fast	0.94	6.281	-1.805		
Improvement Ratio	3.07	1064	12.38		
Exoticness Slow	1.136	715.6	-0.166	-0.939	22.68
Exoticness Fast	1.00	665.6	0.430	-1.033	18.75
Loma Amarilla					
Velocity Slow	1.83	6.461	-1.246		
Velocity Fast	1.42	6.535	-1.724		
Improvement Ratio	3.19	1125	10.28		
Exoticness Slow	1.54	788.9	0.519	-0.547	34.9
Exoticness Fast	1.24	818.2	0.898	-0.710	25.5
Coihueco					
Velocity Slow	1.09	6.345	-1.398		
Velocity Fast	1.08	6.367	-1.76		
Improvement Ratio	3.50	881.4	11.11		
Exoticness Slow	1.152	672.9	0.359	0.748	26.17
Exoticness Fast	0.944	665.9	0.532	-0.932	20.53

Again by comparing the fitted curves for the slow side (blue) to the fast side (red) in Figure 8.12(a) and Figure 8.12(b) an asymmetry in the distributions, most notably a preference for slow events, becomes clear. Following the same procedure as in the stereo case, the fitted functions were normalized forming a probability density function. This full procedure was carried out separately for each Eye and the fit quality, values, and the final selection criteria for each are listed in Table 8.1, while the related plots can be seen in Appendix D. The differences between the Eyes are clearly visible in Table 8.1. Most obvious is Loma Amarilla's continued poor performance as compared to the other Eyes, meaning only very exotic events can be considered as candidates in that detector. Los Leones and

Los Morados have the most stable results, with fairly narrow distributions and solid fits, while Coihueco has a somewhat extended slow tail.

Again, from here, if an event was found to display an exoticness value with a less than 3×10^{-7} probability of occurring in a dataset of size N_{Events}, then it is selected as an exotic candidate. The location of each selection limit was found through the numerical integration of each distribution looking for the exoticness value where the area at and beyond that point was less than or equal to $3 \times 10^{-7}/N_{events}$. The position of this selection limit, as compared to the value of an event's velocity and improvement ratio, is illustrated by the red hyperbolic curves seen in Figure 8.13 and Figure 8.14. Each red curve represents (8.3) or (8.4) set equal to the appropriate limit value.

Figure 8.13(a), Figure 8.13(b) and Figure 8.14(b) show that no hybrid event observed by Los Leones, Los Morados or Coihueco during the analyzed data period can be confidently selected as a candidate. Furthermore, there are no events for these Eyes that were nearly selected as there where in the stereo distributions. This, however, is not the case for Loma Amarilla. In the top left corner of Figure 8.14(a) the very exotic event 3:1015:3694 is visible. This event, with a reconstructed speed of 72.83% of c was reconstructed 3.19 times better at 72.83% of c than it was at c leading to an exoticness value of 86.74. For the slow side of Loma Amarilla, the probability of an event like this being due to random error in a sample of 5234 events is 2.12×10^{-18} or approximately 1 in 472000000000000000.

An observation like that of event 3:1015:3694 is exactly what this research was designed to find and separate from the cosmic ray data. Though a velocity, of 72.83% of c is much larger than the expected velocity range for Q-Balls and other similar candidates, this reconstruction is clearly well outside what is currently describable in particle astrophysics. Figure 8.15(a) clearly shows that the FD data quality of this event should be more than sufficient. Figure 8.15(b), a plot comparing the hot tank distance to event duration, clearly shows that this event took much longer to evolve than any other event with a hot tank at a similar distance. This is significant, as both the Hot tank to Eye distance and event du-

177
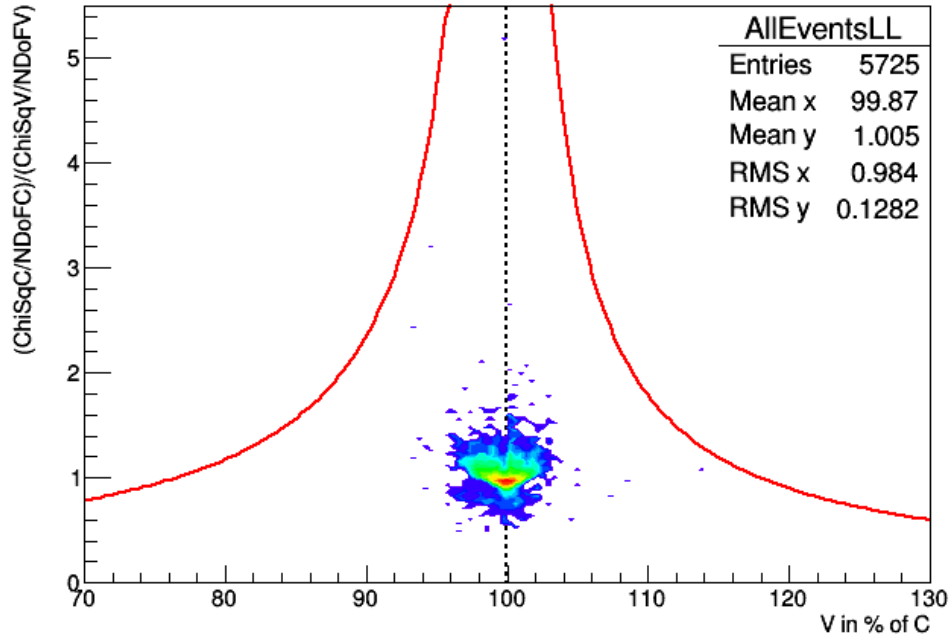
(a) Los Leones
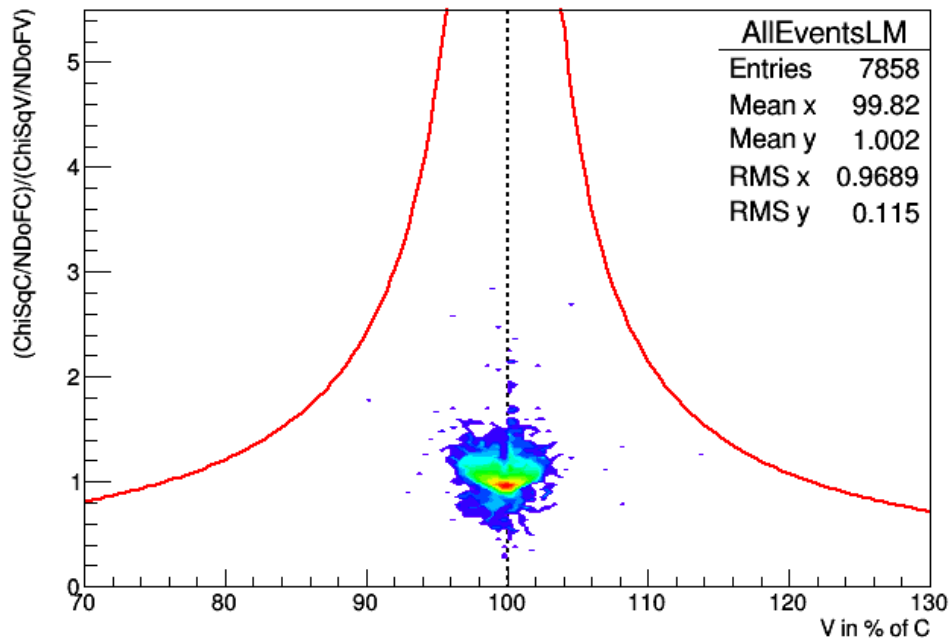
(b) Los Morados

Figure 8.13: Hybrid Candidate Selection LL and LM: The colored portion shows the density of the events. The red hyperbolic curves show the exotic selection limits. No exotic events were found in either LL or LM data.
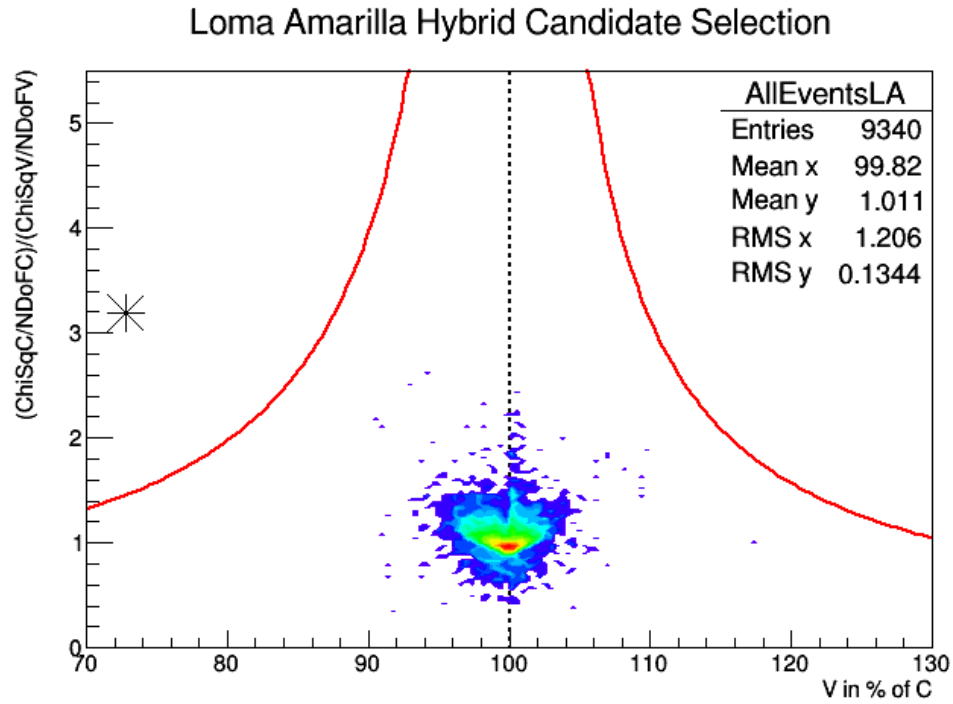
(a) Loma Amarilla
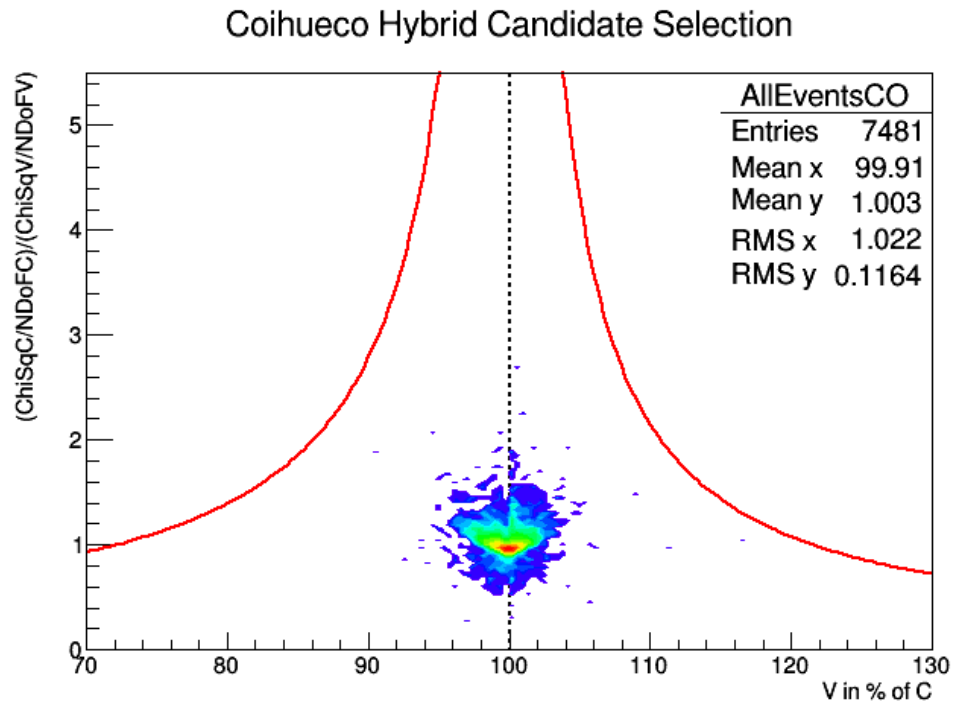
(b) Coihueco

Figure 8.14: Hybrid Candidate Selection LA and CO: The colored portion shows the density of the events. The red hyperbolic curves show the exotic selection limits. The black star in (a) shows a selected LA exotic event. No exotics were found in the CO data.
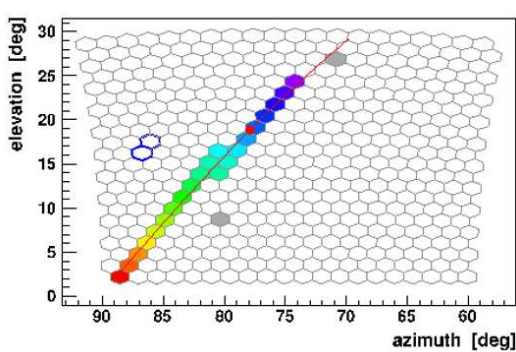
(a) Exotic Event 3:1015:3694 Pixel Trace   (b) Eye to Hot Tank Distance
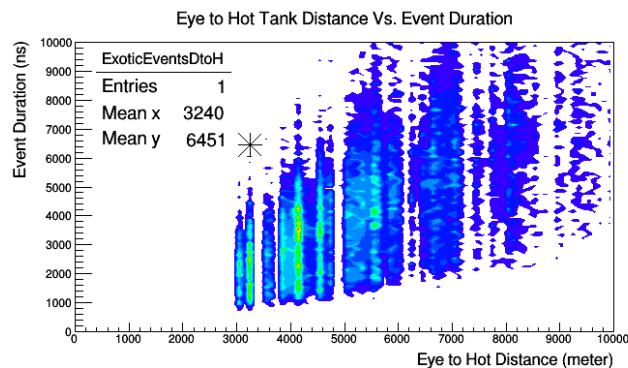
Figure 8.15: Hybrid Exotic Trace and Timing: (a) shows that the event 3:1015:3694 was well measured by the FD. (b) shows a density plot of the event duration (the time difference between when the first and last event pixels were triggered) as compared to the distance between the event's hot tank and the triggered Eye. The black star indicates event 3:1015:3694.

ration are measured directly by the detector and not reconstructed. Since these metrics are independent from the velocity reconstruction, they reinforce confidence of the exotic event speed.

Though this event 3:1015:3694 looks singularly exotic from the perspective of the hybrid data stream, as Figure 8.16 shows, there is a simple reason for the reconstructed exotic velocity if the full response of the SD is considered. Figure 8.16(a) shows the geometric result of the velocity reconstruction of event 3:1015:3694 if the SD station that recorded the highest signal during the event is used as the hot tank. Using this station for the reconstruction resulted in the event being measured to have a speed of 72.83% of c. Figure 8.16(b) shows the geometric result of the velocity reconstruction of event 3:1015:3694 if the SD station with the highest signal within the independently triggered SD event is used instead as the hot tank. By moving the hot tank to this location the velocity reconstruction returned a speed of 99.9006% of c.

Basically, during event 3:1015:3694 a tank that was geometrically disassociated with the shower core had the highest signal and therefore, the assumption of the hot tank being the station nearest to the core was not valid. This was not accounted for in cuts or during the

180

(a) 3:1015:3694 Hot Tank Reconstruction

(b) Event 3:1015:3694 Reconstruction with Hottest Tank in SD Event
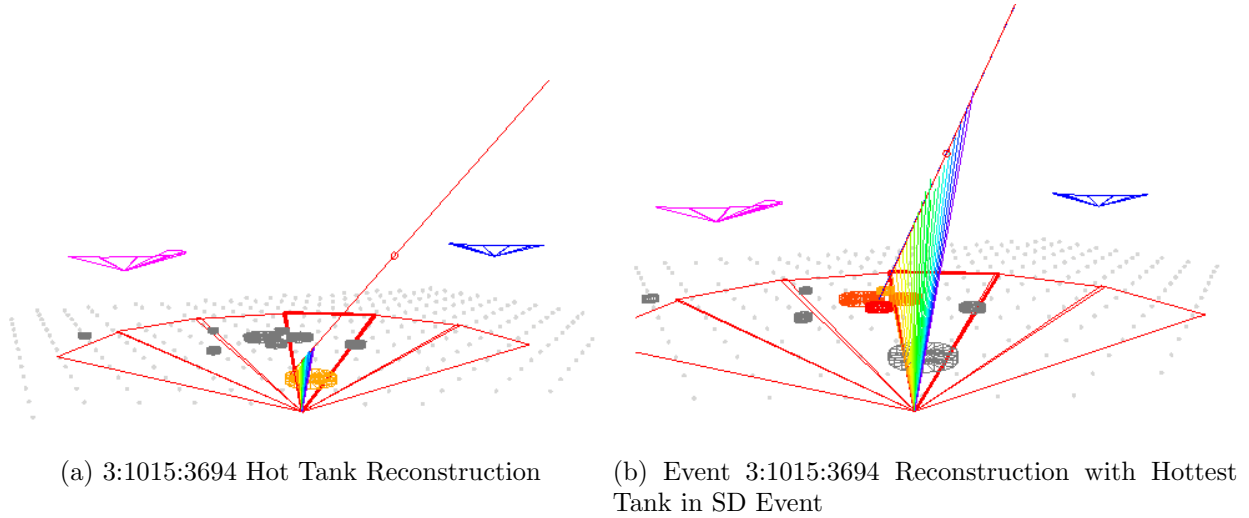
Figure 8.16: Hybrid Exotic Cause: (a) shows the event reconstruction using SD station 1108, the station with the highest signal during the event, as the hot tank. (b) shows the event reconstruction using SD station 1360, the station with the highest signal within the independently triggered SD event, as the hot tank.

reconstruction simply because an event of this type should be impossibly rare. In this case station 1108 had a signal of 34.7 VEM, which is roughly equivalent to the signal that would be produced when 35 vertically inclined muons passed directly through the center of the tank. A signal of this size is more than an order of magnitude above what is expected due to random fluctuations or low energy showers and can not be easily explained. Furthermore, this large signal occurred within a few $100ns$ of the FD measurement, in line with the SDP and was able to be fit with a high degree of confidence. These factors allowed tank 1108 to be chosen as the hot tank and used in the hybrid fit. The probability of something like this occurring is truly staggeringly low. However, the probability of the same thing happening, but with four tanks triggering simultaneously, is even lower. The fact that the velocity reconstruction using the group of four tanks returns the speed of light solidifies them as the correct signal at the ground. The erroneous reconstruction was replaced with the corrected one and the exotics search concludes with no candidates found.

CHAPTER 9

CONCLUSIONS AND PERSPECTIVES

The central purpose of this thesis was to develop and test methods to add the event propagation velocity to the list of shower parameters that the Fluorescence Detector of Pierre Auger Observatory is capable of measuring. This new capability was then to be leveraged to differentiate exotic slow propagating shower events from the rest of cosmic ray flux as by relativistic necessity all known cosmic ray primaries can only generate an extensive air shower at propagation velocities indistinguishably close to the speed of light. This means that any accurate observation of an event propagating at a slower than light velocity would provide an unmistakable indicator of new physics. The following section summarizes the results of this search and evaluates the validity of the assumptions made in the introduction. Then, perspectives on future work, suggestions for improvements to the method and promising alternative search methods are presented in hopes that the next researcher to take up this line of inquiry can make progress quickly.

9.1 Research Summary

In Chapter 4 the physical characteristics a particle must possess in order to be considered capable of producing a sub-luminal shower were outlined. With these requirements in mind, high mass Strangelets, macroscopic dark matter, and super-symmetric Q-Balls were identified as strong candidates. The theory supporting high mass Strangelets and macroscopic dark matter as viable candidates appeared too late for their full inclusion in this work, however super-symmetric Q-Balls were given a full theoretical overview. To test the detectability of Q-Ball induced showers at the Pierre Auger Observatory, new CORSIKA simulations of high mass, low velocity Q-Balls were created. The simulated detector response to these showers showed, in good agreement with theoretical predictions, that the

FD has sensitivity to Q-Balls with a mass $M_Q > 3.25 \times 10^{27} GeV \ c^{-2}$ while the SD gains sensitivity at $M_Q > 1.15 \times 10^{27} GeV \ c^{-2}$.

In Chapter 5, the ability for the fluorescence detector to record slow events and measure event evolution velocity was examined. Using a simple model describing the velocity dependent timing signature of FD events, the velocity sensitivity of the Observatory was examined at a wide range of geometries. Velocity reconstructions of simulated slow events were then used to test the accuracy of both the velocity sensitivity study and verify that the FD was capable of correctly identifying slow events. Through this work it was shown that though the aperture shrinks dramatically as the velocity slows, the FD should have sensitivity to showers moving as slow as a few % of c.

From here, a more accurate velocity dependent model, accounting for most atmospheric effects and the elliptical shape of the earth, was developed. This new model was applied to laser shots fired from the laser facilities in order to inspect the velocity resolution of the Observatory. The reconstruction of these laser events exposed a variety of probable systematics in both the Observatory's instrumentation and the analysis software used to reconstruct observations. Due to the scale of the instrumentation, the specific causes of the offsets could not be conclusively identified. Regardless, the Fluorescence Detector was shown to be accurate to $\sim 1.5\%$ of c, and, more importantly, very precise, meaning the method is capable of confidently identifying velocity outliers. Furthermore, in the stereo and hybrid studies of laser events in the following chapters, the offsets were shown to largely vanish in distributions of the non-vertical geometries which dominate in shower events.

Chapters 6 and 7 established the techniques and programs needed to search the stereo and hybrid datasets for exotic events. Two methods were developed each leveraging the observations from multiple detectors to constrain both the event velocity and geometry. Stereo reconstruction is by far the more accurate of the two methods and uses the simultaneous observations of one event from multiple Eyes to strongly constrain an event. This high accuracy means that few quality cuts are needed, but because of the high energy threshold of

stereo measurement, the stereo dataset suffered from both poor statistics and relatively low quality individual FD observations. Furthermore, because any stereo event must take place at a large distance from at least one Eye, the stereo method loses sensitivity to events slower than $\sim 36\%$ of c. Hybrid reconstruction, on the other hand, has great statistics and velocity sensitivity due to its non-geometric and substantially lower, trigger threshold. Hybrid events, however, are less strongly constrained than stereo and therefore much less accurate. This low accuracy needs to be compensated for by constraining the searched dataset to only well measured events. This fact necessitated dramatic quality cuts, which somewhat offset hybrid's statistical advantage over stereo. After quality cuts of 1125 remaining stereo events, none had reconstructed event velocities more distant than 4% away from c. After hybrid quality cuts, 30404 events remained with outliers displaying reconstructed velocities as low as 70% of c.

In Chapter 8, the hybrid and stereo distributions were investigated for statistically meaningful exotic candidates. This was done by building a prediction of the inherent error rate of each method and then using that prediction to evaluate the probability that any observed event occurred simply due to random fluctuation in a sample set containing N_{events}. Any events predicted to have a probability lower than 3×10^{-7} (5σ) of appearing due to a random error were selected as an exotic candidates. This selection resulted in exactly one hybrid event being recognized as confidently exotic. However, after further analysis, this event's exotic reconstruction was found to be due to what appears to be a second, possibly correlated, simultaneous low energy shower which lead to the false identification of the event's hot tank. Once this error was fixed, the event was reconstructed normally. In addition to this hybrid event, two stereo events nearly qualified as candidates. These events did show interesting characteristics. The most distinct of which being their long, flat light profiles, shown in Appendix D, as these resemble the profiles seen in the exotic simulation results of Chapter 4. However, these events also had velocities very near to c and generally poor individual FD measurement quality, meaning these stereo events could not be confidently

kept in defiance of the rigidly defined selection criteria. In the end, this research finds no exotic candidates exist in the 7 years of Observatory FD data analyzed.

With these results in hand the assumptions made during the introduction can now be reexamined.

1. **Within the universe there exist stable particles that will interact energetically with the atmosphere at velocities significantly below the speed of light in a way that allows for the creation of events bright enough to meet the observation criteria of the Pierre Auger Observatory.**

   Chapter 4 did show that these particles are predicted by theory and would be capable of triggering the Pierre Auger Observatory, but the search did not result in the positive identification of an exotic cosmic ray event. However, because of this zero result, this research will be able to provide a limit the flux of these particles. At the time of writing, this work on this limit is currently underway.

2. **That it is possible to reconstruct the speed at which cosmic ray events evolve in the atmosphere using the data already collected by the Pierre Auger Observatory.**

   Chapters 5, 6 and 7 clearly show that the Pierre Auger Observatory is capable of making this measurement using stereo and hybrid detection.

3. **That these exotic particles have already been measured by the Pierre Auger Observatory and can be differentiated from the rest of the cosmic ray flux by their velocity.**

   Because of the zero result of Chapter 8, clearly, either it is true that no exotic particles of this type have been measured by the Observatory's FD from 2007 through 2013, or if they were, they were not measured with sufficient quality and were therefore unable to be distinguished from cosmic ray events. This could change with the addition of more data or if better quality cuts and/or stronger reconstruction methods are developed.

9.2   Perspectives

Though this work approaches and answers a wide set of questions, there are of course things that need to be done to enhance the end result. Primary among these is the calculation of the flux limits to slow showers in general and therefore fast Q-Balls with a mass higher than $M_Q > 3.25 \times 10^{27} GeV\ c^{-2}$. This limit calculation could be extended to cover fast macroscopic dark matter and high mass Strangelets if these can be shown to be capable of triggering the Pierre Auger Observatory in hybrid or stereo. However, without further input from the profile or other identifying metric, any limits would not be object specific, but would instead apply equally to all slow shower candidate phenomena.

There is also potential to improve the aperture and statistics of the hybrid event set by reexamining and improving the quality cuts. In the event of this study being performed again, the following suggestions on the hybrid cuts should be considered:

- The VAOD limit could be relaxed from 0.03 to 0.05 or higher.

  The VAOD cut clearly removes events in the tails, however though it does more strongly affect outlier events than the core of the distribution, it does so only minimally. Because of this, the primary result of limiting the VAOD threshold to 0.03 is simply a significant culling of the data. After consideration, in light of the end results, it is clear that this cut could be significantly relaxed to only remove events in extremely hazy atmospheres without much harm to the confidence in the end result.

- The upper limit on the pixel density cut could be relaxed from 1.25° per pixel to 1.47° per pixel.

  While the pixel density cut does significantly improve the quality of the events in the hybrid data set, the limit of 1.25° per pixel was designed to let through laser-like pixel tracks and may be too stringent for showers, removing many valid pixel geometries. The limit could be increased to 1.47° per pixel in order to allow a wider variety of dense tracks while preserving result confidence.

- The reduced timefit χ^2 cut could be made more restrictive.

  As is evidenced by the tiny fraction of events removed from the sample by this cut, either the cuts preceding it are too stringent and remove events beyond their intended purpose or this cut is too relaxed. The timefit χ^2 is the best metric available for judging how well the result fits the data and should be leveraged more.

Additionally, if the specific cause for the heavy favoring of fast events in the Hybrid dataset can be discovered, many of the imposed quality cuts could be left out entirely.

Simulated cosmic ray datasets should be used to set expectations of how the distributions change with geometry. By selecting all candidates based on the same distribution, vastly different event strengths and geometries are being treated equally. To some degree, the quality cuts assure that the event set is uniform in data quality, however it is reasonable to suspect that different event geometries will have different velocity reconstruction error rates. By using a large set of simulated events as a control, the relationship between geometry and error rate could be understood and used for a far more targeted candidate selection. This was attempted for this thesis, however, the simulated data set failed to match the behavior of the real dataset after quality cuts. This was likely due to the simulations failing to account for some real world phenomena and the fact that the quality cuts were in some regards optimized on the data. If these issues could be addressed, then simulations could be used as a powerful tool to enhance the result.

The SD results of the CORSIKA Q-Ball simulations should be investigated further. If indeed it is shown that Q-Balls reliably differ in SD timing as strongly as is suggested in Section 4.1.2, then they can be looked for using the full aperture of the SD. This would greatly increase statistics and may very well result in a positive observation or, in the case of a zero result, the absolute lowest upper limits to the flux possible through direct detection on current instrumentation. To do this, the exact velocity dependent Q-ball shower front for the altitude of the SD should be calculated using the proton decay shower front equations developed in Section 7.1. Then the timing profiles from every quality event recorded by

the SD would be compared to this shower front to look for events that display timing that matches this profile.

Before carrying out this study, however, a few things would need to be checked. First, how strongly these profiles differ from the timing profiles of any other cosmic ray shower needs to be investigated to make sure this signature would provide good differentiation. Second, more Q-Ball simulations need to be run to investigate reliability of this signature for Q-Balls at a wider variety of zenith angles. Lastly, the SD velocity sensitivity due to the T4 SD trigger needs to be understood, see Section 3.1. The T4 trigger demands that signal start times for all tanks in the event lay within the timing difference defined by the distance between the tanks divided by the speed of light. Clearly (7.7) shows that as the shower velocity drops the tanks that are furthest from the core would trigger outside of this time window. Theoretically this may possibly have one of or all of the following results:

- **The rejection of the event.** Because the full event does not pass T4, the full event would be rejected. This would be the worse case, however any events that triggered in hybrid would be preserved as a T3 event.

- **The removal of the outermost stations.** At all but the lowest velocities, the wavefront near the core of a proton decay or other similar slow event would still be capable of triggering a full SD event fast enough to pass T4. This would result in the center of the event surviving while the outermost tanks would be removed from the event.

- **The splitting the event into a long duration inner event and a ring like outer event.** Though at low velocities the outer stations would not trigger fast enough to be included with the inner stations, they would all trigger at very similar times and could therefore be kept as a separate SD event. This would result in ring-like SD events representing the outermost signals in a decay event appearing in the SD data-stream along with correlated inner events. Furthermore, at very low velocities, it also

is possible that only the outer ring events would trigger at similar enough times to survive, leaving only the ring events.

In any case, save for complete rejection, each of these event types would display the shower front described in (7.7) along with much longer than normal signal durations and would therefore be identifiable.

Finally, like studies could be carried out using the methods and models developed here on other optical cosmic ray observatories like TA and possibly JEM-EUSO. The conversion of the method to TA is obvious and a similar stereo study has already been performed on HighRes data [80], however, it is worth stating that the exact same procedures for hybrid could be followed once the differences in instrumentation and detector geometry were taken into account. The application of this method to JEM-EUSO is a little more complicated and less certain. Because there is no possiblity of hybrid or stereo measurement, the search in JEM-EUSO would have to be done monocularly. This raises the issue of the convolution of the distance to the event with its propagation velocity which made a monocular search at the Pierre Auger Observatory impossible. However, given the huge distance from the detector to the shower and by taking advantage of the knowledge that event must have taken place in the atmosphere this problem is minimized. Instead, the uncertainties in the velocity would be determined not by the uncertainty in the distance to the event, but rather the uncertainty in the angular reconstruction of the axis. There are hints from colleagues that the angular reconstruction accuracy of JEM-EUSO should be on the order of a few degrees, meaning that a velocity based study is a strong possiblity. This however, relies on the end geometric accuracy of the experiment and whether or not a maximum timing trigger, like the SLT for the FD, is imposed on the detector. If it is not, not only could Q-Balls, Strangelets and macroscopic dark matter potentially be searched for, but perhaps meaningful work on micrometeorites could also be carried out.

REFERENCES CITED

[1] Vanessa Cirkel-Bartelt. History of astroparticle physics and its components.

[2] Theodor Wulf. On the radiation of high penetrating power that exists in the atmosphere. *Phys. Zeit*, 1(152-157):124, 1909.

[3] Victor F Hess. Observations in low level radiation during seven free balloon flights. *Phys. Zeit*, 13:1084–1091, 1912.

[4] Jacob Clay. Penetrating radiation. In *Proceedings of the Royal Academy of Sciences Amsterdam*, volume 30, pages 1115–1127, 1927.

[5] Bruno Rossi. On the magnetic deflection of cosmic rays. *Physical Review*, 36(3):606, 1930.

[6] Thomas H. Johnson. The azimuthal asymmetry of the cosmic radiation. *Phys. Rev.*, 43:834–835, May 1933. doi: 10.1103/PhysRev.43.834. URL http://link.aps.org/doi/10.1103/PhysRev.43.834.

[7] Luis Alvarez and Arthur H. Compton. A positively charged component of cosmic rays. *Phys. Rev.*, 43:835–836, May 1933. doi: 10.1103/PhysRev.43.835. URL http://link.aps.org/doi/10.1103/PhysRev.43.835.

[8] Bruno Rossi. Directional measurements on the cosmic rays near the geomagnetic equator. *Phys. Rev.*, 45:212–214, Feb 1934. doi: 10.1103/PhysRev.45.212. URL http://link.aps.org/doi/10.1103/PhysRev.45.212.

[9] Bruno Rossi. Method of registering multiple simultaneous impulses of several geiger's counters. *Nature*, 125:636, 1930.

[10] Pierre Auger, P. Ehrenfest, R. Maze, J. Daudin, and Robley A. Fréon. Extensive cosmic-ray showers. *Rev. Mod. Phys.*, 11:288–291, Jul 1939. doi: 10.1103/RevModPhys.11.288. URL http://link.aps.org/doi/10.1103/RevModPhys.11.288.

[11] CERN Communication Group. Lhc guide and faq. 2009. URL http://multimedia-gallery.web.cern.ch/multimediagallery/Brochures.aspx.

[12] P. Abreu et al. The pierre auger observatory ii: Studies of cosmic ray composition and hadronic interaction models. 2011.

[13] Claudio Di Giulio. "the cosmic rays flux from the pierre auger observatory data". *Gradute Thesis, Universit'a degli Studi di Roma*, 2009.

[14] T K Gaisser. "the cosmic-ray spectrum: from the knee to the ankle". *Journal of Physics*, 47(17), 2006.

[15] S. P. Swordy. "the composition of cosmic rays at the knee". *Astroparticle Physics*, 18 (2):129 –150, 2005.

[16] ENRICO Fermi. On the origin of the cosmic radiation. *Phys. Rev.*, 75(8):1169–1174, Apr 1949. doi: 10.1103/PhysRev.75.1169.

[17] L Cazon and The Pierre Auger Collaboration. Studying the nuclear mass composition of ultra-high energy cosmic rays with the pierre auger observatory. *Journal of Physics: Conference Series*, 375(5):052003, 2012. URL http://stacks.iop.org/1742-6596/375/i= 5/a=052003.

[18] R. U. Abbasi and others. Indications of proton-dominated cosmic-ray composition above 1.6 eev. *Phys. Rev. Lett.*, 104:161101, Apr 2010. doi: 10.1103/PhysRevLett.104. 161101. URL http://link.aps.org/doi/10.1103/PhysRevLett.104.161101.

[19] Kenneth Greisen. End to the cosmic-ray spectrum? *Phys. Rev. Lett.*, 16:748–750, Apr 1966. doi: 10.1103/PhysRevLett.16.748. URL http://link.aps.org/doi/10.1103/ PhysRevLett.16.748.

[20] VA Kuzmin and GT Zatsepin. On cosmic-ray interactions with photons. *Canadian Journal of Physics*, 46(10):S617–S619, 1968.

[21] V. A. Zatsepin, G. T.; Kuz'min. "the composition of cosmic rays at the knee". *Journal of Experimental and Theoretical Physics Letters*, 4:78, 2005.

[22] Gary Taubes. Pattern emerges in cosmic ray mystery. *Science*, 262(5140):1649, 1993. doi: 10.1126/science.262.5140.1649. URL http://www.sciencemag.org/content/262/ 5140/1649.short.

[23] John Linsley. Evidence for a primary cosmic-ray particle with energy 10^{20} ev. *Phys. Rev. Lett.*, 10:146–148, Feb 1963. doi: 10.1103/PhysRevLett.10.146. URL http://link. aps.org/doi/10.1103/PhysRevLett.10.146.

[24] The Hires Collaboration. "observation of the gzk cutoff by the hires experiment". *Nuclear Physics B Proceedings Supplements*, 165, 2006.

[25] Gordon B Thomson. Results from the telescope array experiment. *arXiv preprint arXiv:1010.5528*, 2010.

[26] Observation of the suppression of the flux of cosmic rays above 4×10^{19} *ev*. *Phys. Rev. Lett.*, 101(6):061101, Aug 2008. doi: 10.1103/PhysRevLett.101.061101.

[27] Yoshiyuki Takahashi, JEM-EUSO Collaboration, et al. The jem-euso mission. *New Journal of Physics*, 11(6):065009, 2009.

[28] The Pierre Auger Collaboration. "correlation of the highest-energy cosmic rays with nearby extragalactic objects". *Science*, 318(5852):938–943, November 2007.

[29] J Neto, P Sommers, H Sagawa, P Tinyakov, I Tkachev, L Auger, Telescope Array, Yakutsk Collaborations, et al. Review of the anisotropy working group at uhecr-2012. *arXiv preprint arXiv:1306.4998*, 2013.

[30] Alan Chavez-Meza and Luis VillaSenor. "correlation of ultra high energy cosmic rays with the nearest active galactic nuclei". Technical report, 2013.

[31] Sonali Bhatnagar. "extensive air shower high energy cosmic rays (ii)". *Physics Education*, pages 249 – 256, OCT - DEC, 2009.

[32] Ta colaborator sean stratton's personal page, 2015. URL http://www.physics.rutgers.edu/~seanst/cwork.html.

[33] The Auger Collaboration. Properties and performance of the prototype instrument for the pierre auger observatory. *Nucl. Instrum. Methods Phys. Res. Sect. A-Accel. Spectrom. Dect. Assoc. Equip.*, 2004-05-01.

[34] Darko Veberic. Wikipedia page for the pierre auger observatory, 2015. URL https://en.wikipedia.org/wiki/Pierre_Auger_Observatory.

[35] Pierre Auger Collaboration. "the surface detector system of the pierre auger". *Nucl. Instrum. Methods Phys. Res. Sect. A-Accel. Spectrom. Dect. Assoc. Equip.*, 2008.

[36] J Abraham et al. Trigger and aperture of the surface detector array of the pierre auger observatory. *Nuclear Instruments and Methods in Physics Research Section A: Accelerators, Spectrometers, Detectors and Associated Equipment*, 613(1):29–39, 2010.

[37] The Auger Collaboration. The offical website of the pierre auger observatory, July 2013. URL http://www.auger.org.ar/index2.php.

[38] V Verzi. The fluorescence detector of the pierre auger observatory. *Nuclear Physics B-Proceedings Supplements*, 165:37–44, 2007.

[39] G.Matthiae. "optics and mechanics of the auger fluorescence detector". Technical report, 2001.

[40] H. Gemmeke. "the auger fluorescence detector electronics". Technical report, 2001.

[41] A Schmidt, T Asch, H Gemmeke, M Kleifges, H-J Mathes, A Menchikov, F Schüssler, and D Tcherniakhovski. Third level trigger for the fluorescence telescopes of the pierre auger observatory. *Nuclear Instruments and Methods in Physics Research Section A: Accelerators, Spectrometers, Detectors and Associated Equipment*, 601(3):347–353, 2009.

[42] Roberto Pesce. Energy calibration of data recorded with the surface detectors of the pierre auger observatory: an update.

[43] P Abreu et al. Description of atmospheric conditions at the pierre auger observatory using the global data assimilation system (gdas). *Astroparticle Physics*, 35(9):591–607, 2012.

[44] P Abreu et al. Identifying clouds over the pierre auger observatory using infrared satellite data. *Astroparticle Physics*, 50:92–101, 2013.

[45] Miguel Mostafa et al. Atmospheric monitoring for the pierre auger fluorescence detector. *arXiv preprint astro-ph/0308442*, 2003.

[46] Noaa page on the goes imager instrument, 2015. URL http://noaasis.noaa.gov/NOAASIS/ml/imager.html.

[47] Noaa page on the goes sounder instrument, 2015. URL http://noaasis.noaa.gov/NOAASIS/ml/sounder.html.

[48] BenZvi et al. New method for atmospheric calibration at the pierre auger observatory using fram, a robotic astronomical telescope. *arXiv preprint arXiv:0706.1710*, 2007.

[49] R Abbasi et al. Techniques for measuring atmospheric aerosols at the high resolution flys eye experiment. *Astroparticle Physics*, 25(1):74–83, 2006.

[50] Lawrence R Wiencke et al. Steerable laser system for uv atmospheric monitoring at the high-resolution fly's eye. In *SPIE's International Symposium on Optical Science, Engineering, and Instrumentation*, pages 56–63. International Society for Optics and Photonics, 1999.

[51] Daniel Kmpel. "geometry reconstruction of fluorescence detectors revisited". *PhD Dissertation, Begische Universitat Wuppertal*, 2007.

[52] Eric W. Weisstein. "chi-squared distribution". http://mathworld.wolfram.com/Chi-SquaredDistribution.html.

[53] Miguel Mostaf. Hybrid activities of the pierre auger observatory. *Nuclear Physics B - Proceedings Supplements*, 165:50 – 58, 2007. ISSN 0920-5632. doi: http://dx.doi.org/10.1016/j.nuclphysbps.2006.11.009. URL http://www.sciencedirect.com/science/article/pii/S0920563206008425. Proceedings of the Cosmic Ray International SeminarsProceedings of the Cosmic Ray International Seminars.

[54] Stefano Argiro, SLC Barroso, J Gonzalez, Lukas Nellen, T Paul, TA Porter, L Prado Jr, M Roth, R Ulrich, and Darko Veberič. The offline software framework of the pierre auger observatory. *Nuclear Instruments and Methods in Physics Research Section A: Accelerators, Spectrometers, Detectors and Associated Equipment*, 580(3):1485–1496, 2007.

[55] REne Brun and Fons Rademakers. Root - an object oriented data analysis framework. *Nucl. Inst and Meth. in Phys. Res A*, 389:81–86, 1997.

[56] A Einstein. Does the inertia of a body depend upon its energy-content? 1905.

[57] Diego Janches and Douglas O ReVelle. Initial altitude of the micrometeor phenomenon: Comparison between arecibo radar observations and theory. *Journal of Geophysical Research: Space Physics (1978–2012)*, 110(A8), 2005.

[58] MS Pshirkov. Prospects for strangelet detection with large-scale cosmic ray observatories. *arXiv preprint arXiv:1509.05553*, 2015.

[59] Fei Wu, Ren-Xin Xu, and Bo-Qiang Ma. Propagation of strangelets in the earth's atmosphere. *Journal of Physics G: Nuclear and Particle Physics*, 34(3):597, 2007.

[60] Laura Paulucci and Jorge E Horvath. Interaction of strangelets with ordinary nuclei. *Journal of Physics G: Nuclear and Particle Physics*, 36(9):095202, 2009.

[61] David M Jacobs, Glenn D Starkman, and Bryan W Lynn. Macro dark matter. *Monthly Notices of the Royal Astronomical Society*, 450(4):3418–3430, 2015.

[62] J. Arafune, T. Yoshida, S. Nakamura, and K. Ogure. Experimental bounds on masses and fluxes of nontopological solitons. *Phys. Rev. D*, 62:105013, Oct 2000. doi: 10.1103/PhysRevD.62.105013. URL http://link.aps.org/doi/10.1103/PhysRevD.62.105013.

[63] J. Beringer et al. (Particle Data Group). Chapter 15: Grand unified theories, review of particle physics. *Phys. Rev. D*, 86:010001, Jul 2012. doi: 10.1103/PhysRevD.86.010001. URL http://pdg.lbl.gov/2013/reviews/rpp2012-rev-guts.pdf.

[64] Sidney Coleman. Q-balls. *Nuclear Physics B*, 262(2):263 – 283, 1985. ISSN 0550-3213. doi: http://dx.doi.org/10.1016/0550-3213(85)90286-X. URL http://www.sciencedirect.com/science/article/pii/055032138590286X.

[65] Alexander Kusenko. Solitons in the supersymmetric extensions of the standard model. *Physics Letters B*, 405(12):108 – 113, 1997. ISSN 0370-2693. doi: http://dx.doi.org/10.1016/S0370-2693(97)00584-4. URL http://www.sciencedirect.com/science/article/pii/S0370269397005844.

[66] Alexander Kusenko and Mikhail Shaposhnikov. Supersymmetric q-balls as dark matter. *Physics Letters B*, 418(12):46 – 54, 1998. ISSN 0370-2693. doi: http://dx.doi.org/10.1016/S0370-2693(97)01375-0. URL http://www.sciencedirect.com/science/article/pii/S0370269397013750.

[67] Alexander Kusenko, Vadim Kuzmin, Mikhail Shaposhnikov, and P. G. Tinyakov. Experimental signatures of supersymmetric dark-matter Q-balls. *Phys. Rev. Lett.*, 80:3185–3188, Apr 1998. doi: 10.1103/PhysRevLett.80.3185. URL http://link.aps.org/doi/10.1103/PhysRevLett.80.3185.

[68] Steven D Bass. Electroweak baryon number non-conservation and" topological condensates" in the early universe. *arXiv preprint hep-ph/0407245*, 2004.

[69] Alexander Kusenko, Lee C. Loveridge, and Mikhail Shaposhnikov. Supersymmetric dark-matter q-balls and their interactions in matter. *Phys. Rev. D*, 72:025015, Jul 2005. doi: 10.1103/PhysRevD.72.025015. URL http://link.aps.org/doi/10.1103/PhysRevD.72.025015.

[70] David Schuster. "searching for exotic particles at the pierre auger using bayesian inference". *PhD Dissertation, Colorado School of Mines*, 2011.

[71] G Giacomelli, L Patrizii, and Z Sahnoun. Searches for magnetic monopoles and... beyond. *arXiv preprint arXiv:1105.2724*, 2011.

[72] Dieter Heck, G Schatz, J Knapp, T Thouw, and JN Capdevielle. Corsika: A monte carlo code to simulate extensive air showers. Technical report, 1998.

[73] Wolfgang E Nagel, Dietmar B Kröner, and Michael M Resch. High performance computing in science and engineering'14. *Transactions of the High Performance Computing Center, Stuttgart (HLRS)*, 2014.

[74] R. C. Weast et al. "crc handbook of chemistry and physics, 67th edition". 1986-1987.

[75] Keri Kuhn. "study of the central laser facility and extreme laser facility laser shots using a speed analysis model". *MSc Thesis, Colorado School of Mines*, 2011.

[76] Fed James. "minuit software package". www.cern.ch/minuit.

[77] Rene Andrae, Tim Schulze-Hartung, and Peter Melchior. Dos and don'ts of reduced chi-squared. *arXiv preprint arXiv:1012.3754*, 2010.

[78] Pierre Auger Collaboration et al. Techniques for measuring aerosol attenuation using the central laser facility at the pierre auger observatory. *Journal of instrumentation*, 8(04):P04009, 2013.

[79] Eric W Weisstein. "chi-squared distribution." from mathworld–a wolfram web resource, 2015. URL http://mathworld.wolfram.com/Chi-SquaredDistribution.html.

[80] Samuel Adam Blake. "a search for exotic particles in the hires data set". *PhD Dissertation, The University of Utah*, 2009.

[81] A. Roeck, A. Katre, P. Mermod, D. Milstead, and T. Sloan. Sensitivity of lhc experiments to exotic highly ionising particles. *The European Physical Journal C*, 72(4):1–18, 2012. ISSN 1434-6044. doi: 10.1140/epjc/s10052-012-1985-2. URL http://dx.doi.org/10.1140/epjc/s10052-012-1985-2.

[82] S Balestra, G Giacomelli, M Giorgini, L Patrizii, V Popa, Z Sahnoun, and V Togo. Magnetic monopole bibliography-ii. *arXiv preprint arXiv:1105.5587*, 2011.

[83] Hitoshi Murayama and Jing Shu. Topological dark matter. *Physics Letters B*, 686(23): 162 – 165, 2010. ISSN 0370-2693. doi: http://dx.doi.org/10.1016/j.physletb.2010.02. 037. URL http://www.sciencedirect.com/science/article/pii/S0370269310002248.

[84] Alan H. Guth and S. H. H. Tye. Phase transitions and magnetic monopole production in the very early universe. *Phys. Rev. Lett.*, 44:631–635.

[85] T.W.B. Kibble. Some implications of a cosmological phase transition. *Physics Reports*, 67(1):183 – 199, 1980. ISSN 0370-1573. doi: http://dx.doi.org/10.1016/0370-1573(80) 90091-5. URL http://www.sciencedirect.com/science/article/pii/0370157380900915.

[86] E. N. Parker. The origin of magnetic fields. *Astrophys. J.*, 160, 1970.

[87] G Giacomelli, M Giorgini, T Lari, M Ouchrif, L Patrizii, V Popa, P Spada, and V Togo. Magnetic monopole bibliography. *Arxiv preprint hep-ex/0005041*, 2000.

[88] Steven P. Ahlen. Theoretical and experimental aspects of the energy loss of relativistic heavily ionizing particles. *Rev. Mod. Phys.*, 52:121–173, Jan 1980. doi: 10.1103/ RevModPhys.52.121. URL http://link.aps.org/doi/10.1103/RevModPhys.52.121.

[89] Stuart D Wick, Thomas W Kephart, and Thomas J Weiler. Signature studies of cosmic magnetic monopoles. *arXiv preprint astro-ph/0102002*, 2001.

[90] Toshihiro Fuji. "search for ultra-relativistic monopoles". Collaboration Meeting November 2013.

[91] Alfred Scharff Goldhaber. Dual confinement of grand unified monopoles? *Physics Reports*, 315(13):83 – 94, 1999. ISSN 0370-1573. doi: http://dx.doi.org/10.1016/S0370-1573(99)00014-9. URL http://www.sciencedirect.com/science/article/pii/S0370157399000149.

[92] Stuart D. Wick, Thomas W. Kephart, Thomas J. Weiler, and Peter L. Biermann. Signatures for a cosmic flux of magnetic monopoles. *Astroparticle Physics*, 18(6):663 – 687, 2003. ISSN 0927-6505. doi: http://dx.doi.org/10.1016/S0927-6505(02)00200-1. URL http://www.sciencedirect.com/science/article/pii/S0927650502002001.

[93] Pijushpani Bhattacharjee and Gnter Sigl. Origin and propagation of extremely high-energy cosmic rays. *Physics Reports*, 327(34):109 – 247, 2000. ISSN 0370-1573. doi: http://dx.doi.org/10.1016/S0370-1573(99)00101-5. URL http://www.sciencedirect.com/science/article/pii/S0370157399001015.

[94] Curtis G. Callan Jr. Monopole catalysis of baryon decay. *Nuclear Physics B*, 212(3):391 – 400, 1983. ISSN 0550-3213. doi: http://dx.doi.org/10.1016/0550-3213(83)90677-6. URL http://www.sciencedirect.com/science/article/pii/0550321383906776.

[95] VA Rubakov. Superheavy magnetic monopoles and decay of the proton. *JETP Letters*, 33:644–646, 1981.

[96] S. Dawson and A. N. Schellekens. Monopole catalysis of proton decay in so(10) grand unified models. *Phys. Rev. D*, 27:2119–2128, May 1983. doi: 10.1103/PhysRevD.27.2119. URL http://link.aps.org/doi/10.1103/PhysRevD.27.2119.

[97] M. Ambrosioetal. Final results of magnetic monopole searches with the macro experiment. *The European Physical Journal C - Particles and Fields*, 25(4):511–522, 2002. ISSN 1434-6044. doi: 10.1140/epjc/s2002-01046-9. URL http://dx.doi.org/10.1140/epjc/s2002-01046-9.

[98] IceCube Collaboration. Search for relativistic magnetic monopoles with icecube. *Phys. Rev. D*, 87:022001, Jan 2013. doi: 10.1103/PhysRevD.87.022001. URL http://link.aps.org/doi/10.1103/PhysRevD.87.022001.

[99] The Pierre Auger Collaboration. Measurement of the energy spectrum of cosmic rays above 1018 ev using the pierre auger observatory. *Physics Letters B*, 685(45):239 – 246, 2010. ISSN 0370-2693. doi: http://dx.doi.org/10.1016/j.physletb.2010.02.013. URL http://www.sciencedirect.com/science/article/pii/S0370269310001875.

[100] ANITA Collaboration. Ultrarelativistic magnetic monopole search with the anita-ii balloon-borne radio interferometer. *Phys. Rev. D*, 83:023513, Jan 2011. doi: 10.1103/ PhysRevD.83.023513. URL http://link.aps.org/doi/10.1103/PhysRevD.83.023513.

APPENDIX A - CRLF UPGRADE

The original Central Laser Facility of the Pierre Auger Observatory was built in 2003 and performed reliably until it was retired in early 2013. It was then replaced with a new, larger, cleaner and more reliable facility with the added capability of measuring aerosols via both the bi-static method and with a in-house Raman system. The construction of this new facility, named the Central Raman Laser Facility (CRLF), was a major service component of the first two years of my PhD. This work both rounded out my experience as a researcher by providing valuable hardware design and construction experience well complimenting my mainly analysis focused thesis research, and gave me the detailed knowledge of the laser facilities necessary to interpret the results of the laser studies critical to this thesis. Because of this, this appendix will outline the upgrade to the CLF and highlight my contributions to bringing this important piece of hardware online for the Pierre Auger Observatory.

First off, without Professor Lawrence Wiencke the construction and continued operation of the CRLF as well as the CLF and XLF before it would have been impossible. Dr. Wiencke's excellent direction and insights on the design, logistics, construction and management of this considerable project are entirely responsible for its success. Additionally, without the hard work, dedication and knowledge of my colleague Carlos Medina and the Observatory technician Jorge R. Rodriguez, the task would have been many times more difficult than it was.

My contribution to the construction of the facility, began with helping with its design. As I had helped Dr. Wiencke with the final stages of completing the XLF, I was asked for input on the general layout and functionality of the facility. Primarily, the goal of the upgrade was to build a new facility with the cleanliness, environmental stability and self calibration of the XLF while adding in complete Raman laser system and a higher degree of system monitoring and automation. Dr. Wiencke had a clear vision of what the facility
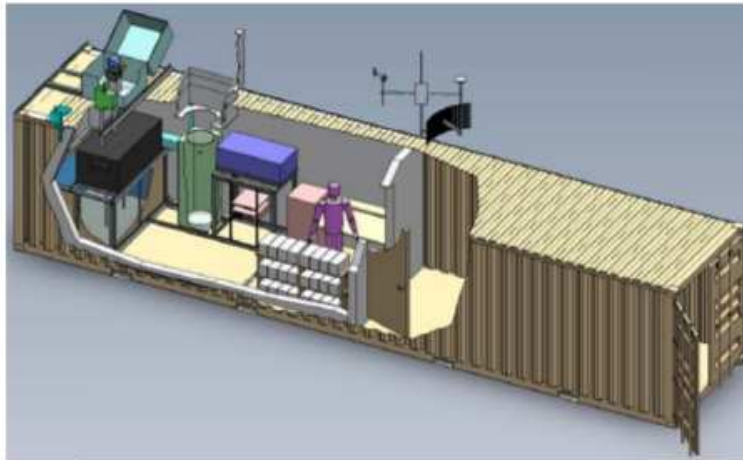
Figure A.1: The Final Design of the CRLF.

should include, but many designs were considered before the final design was settled upon. In the end, as seen in Figure A.1, a 40 foot container, like the container used at the XLF was chosen as the most practical design as it allowed for minimal augmentation to the container itself which would undoubtedly provide a cleaner environment. Replacing the whole facility with a single container added a second benefit of allowing for much of the construction of the facility to be done in Colorado and then shipped, along with nearly all of the equipment necessary to finish the construction, to the observatory to minimize laser down time.
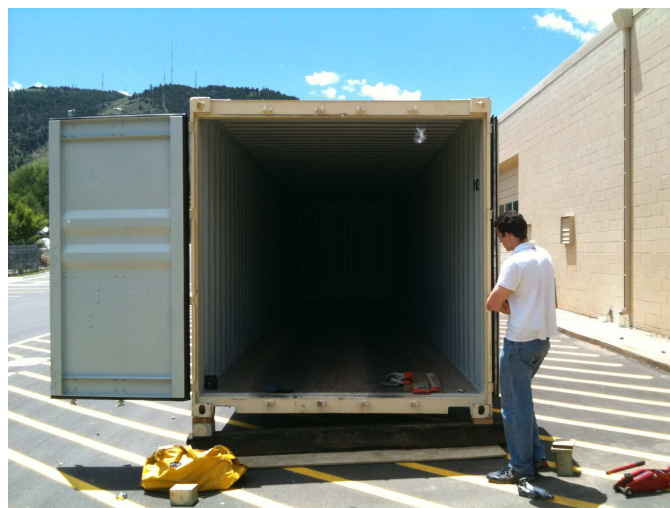
Figure A.2: The Empty, Leveled CRLF Container in Colorado.

The almost new empty 40 foot shipping container, seen after delivery in Colorado in Figure A.2, first had to be finely leveled as the rest of the construction will be carried out with gravitational leveling. Then, the internal steel framing needed to stabilize the laser and Raman systems was welded directly to the structural frame of the shipping container and left floating in order to isolate them from the shipping container floor and therefore the rest of the CRLF construction. The facility was to be split into two rooms. The front third of the container was left bare as a foyer, and storage area in order to minimize contamination in the room housing the laser and Raman system. The back two thirds of the container were to have an insulated floor, walls and ceiling built with low dust materials to provide a clean, thermally stable environment for the facility instrumentation and hardware. The foyer and instrumentation room are separated by a weather and fire proof insulated door set four inches off the ground again to minimize dust contamination. This work, done in Colorado, as well as substantial work on the Raman hatch and Calibration system, was only made possible due to the combined effort of the undergraduates, engineers, grad students, professors shown in Figure A.3(a). The container was then packed with the materials needed to complete construction in Argentina, Figure A.3(b), and shipped to the Observatory.

While the container was in transit, my work pivoted toward building the CRLF control single board computer (SBC) and preparing the facility control software needed to control all of the systems shown in Figure A.4. The first step was to port the Linux OS built for the XLF over to the new CRLF computer. Once this was done two single board serial cards and a custom built GPSY card were stacked on top and brought online. The serial cards were to provide a communication link to all of the hardware shown in Figure A.4, while the GPSY provides a GPS timestamp as well as the highly accurate time pulses needed to trigger and fire the laser system. From here Dr. Wiencke and I ported from the XLF, and where necessary, wrote, the software needed to interface with and control the calibration stages, radiometers, laser, optical switches, steering head, remote power controllers (RPCs), weather system and the vertical and steered beam hatches.

(a) The CRLF Crew in Colorado.

(b) The Packed CRLF Interior Ready For Shpping.

Figure A.3: (a) The Colorado School of Mines CRLF team. Front from the left: Andrew Mahan, Micheal Coco, Levi Patterson, Robert Wright, Nathan Walker, Amy House-Thomas. Back from the left: Eric Mayotte, Dr. Fred Sarazin, Dr. Lawrence Wiencke, Nev DeWitt Pierrat and Chris Runyan. (b) the CRLF packed with the durable instrumentation and construction supplies ready to be shipped to Argentina.
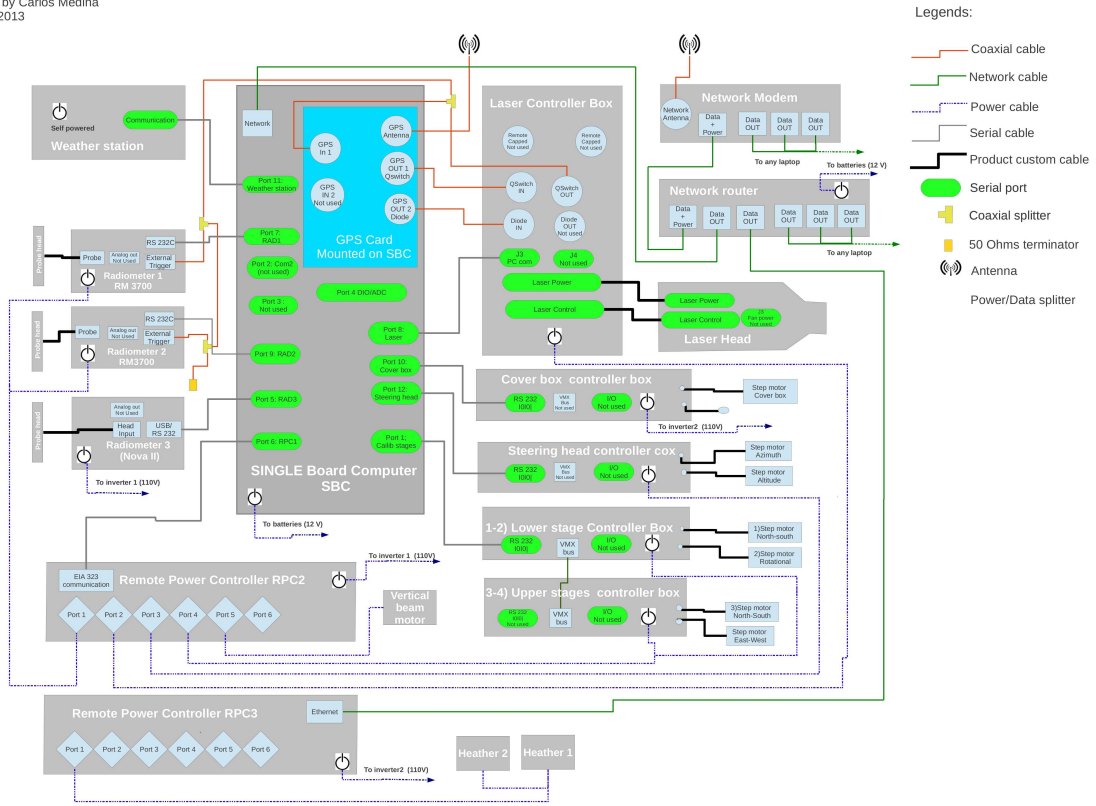
Figure A.4: Full Schematic of the CRLF.

Once the container arrived at the Observatory campus in Malargue, Mendoza, Argentina it was checked for damage and unpacked. Four holes were cut into the top of the container to accommodate the vertical beam pipe, the steered beam pipe, the steering hatch control cables and the Raman telescope aperture. Holes were then drilled into the sides of the containers to serve as cable pass-throughs for the solar array and weather monitoring equipment, as well as gas line ports and vents for the two heaters to be installed later. The floor, walls and ceiling were then insulated, drywalled and painted. A 1.5 m^3 water tank was then built into the steel frame located at the back of the container to serve as a thermal reservoir for the laser system and optics table. The optics tables were then installed and secured to the steel frames. The inside of the container, seen in Figure A.5, was now ready for transport to the CLF location.
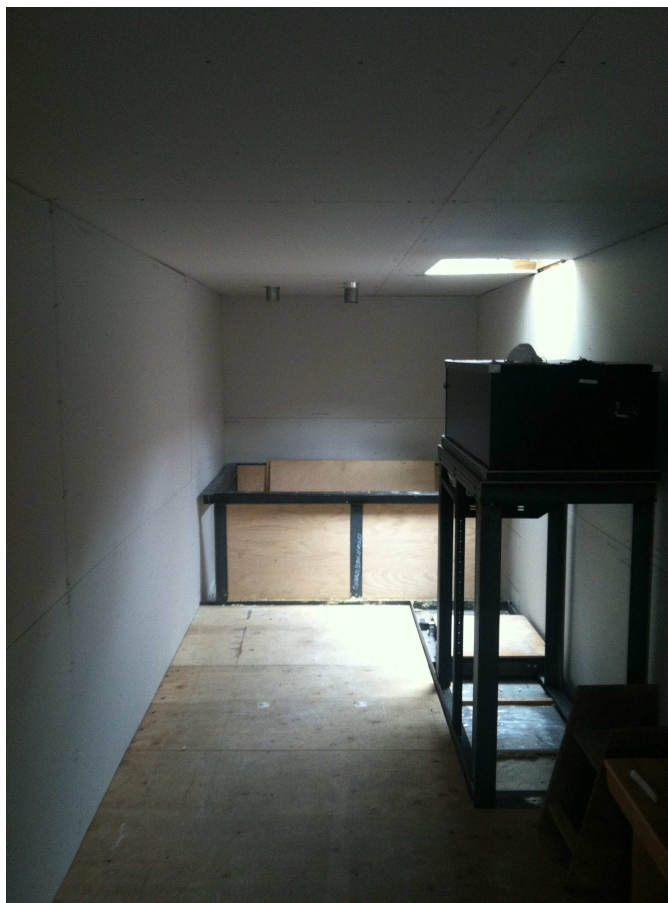
Figure A.5: The CRLF in Malargue Ready For Transport to CLF Site.

Though the XLF is capable of satisfying all of the atmospheric monitoring needs of the Observatory alone, having data from both facilities greatly enhances the quality of the aerosol measurements and provides a layer of redundancy to protect against FD data loss. Because of this, the amount of FD observation time between the decommissioning of the CLF and first light from the CRLF needed to be minimized. To accomplish this, the decommissioning of the CLF started on Sunday March 3rd, the morning after the last night of the preceding dark period. We had expected to have until Friday March 8th to carefully label, document, diagram and disassemble the CLF equipment in preparation for the arrival of the CRLF container. However, on Monday March 4th at around noon we were informed that the crane needed to swap the CRLF and CLF containers had rescheduled the move for the following day. Under this new deadline Carlos, Dr. Wiencke and I managed the impressive feat of

completely labeling, documenting and disassembling the CLF in six hours instead of the four days we had planned on. Then, as Figure A.6(a) shows, the new CRLF container was then swapped out for the old CLF container and quickly filled with the equipment removed from the CLF.

(a) The CRLF Container Being Placed at the CLF Site.   (b) Construction Work at the CRLF

Figure A.6: (a) The CRLF being placed at the CLF site. (b) Construction at the CRLF.

At this point, as shown in Figure A.6(b), the final construction of the CRLF could begin. After quickly weather proofing the container, the first task we undertook was to install the solar panels, hatch covers and instrumentation mounts on container. We then built and installed the work desk, battery bank shelving, laser instrument racks and vertical beam pipes. Once the interior was ready, we connected and tested the power inverters and battery array. Now with power, we connected the power supplies, the SBC, and installed lighting. We then installed and brought online the RPCs, weather monitoring equipment, GPS antenna as well as the network antenna, modem and router to provide an Internet up-link and remote monitoring capabilities via radio communications with Coihueco. The vertical beam hatch, steering head and steering hatch motors and controls were then connected and the control software was tested. The thermal reservoir was then filled using the Observatory's water truck shown in Figure A.7(a). At this point the core of the CRLF's infrastructure was in

place, Figure A.7(b), and Dr. Wiencke returned to Colorado, trusting Carlos, Jorge and I to finish the CRLF.

(a) The Pierre Auger Observatory Water Truck.

(b) CRLF Core Infrastructor Complete

Figure A.7

The CRLF was then made ready for the laser's arrival by mitigating dust contamination from the Pampas and installing the temperature control system. The temperature control system consists of two propane heaters with thermostats, an array of temperature sensors placed around the important temperture sensitive components and a gas detector with an automatic shut off valve all built with redundancy in mind. In order to minimize dust exposure, the floors were finished with low dust tiling, all cable ports were sealed with caulking and the large fused silica Raman window was installed into the Raman hatch. The laser optics and switches were then planned out and placed on the table and the calibration system was installed and tested. The CRLF was now ready for the installation of the UV laser, Figure A.8(a)

The laser was finally delivered, and carefully installed only to find that somehow in transit the controller board was broken and therefore the laser was unable to communicate via its serial port. We carefully and repeatedly tested the laser system and were able to confidently identify the broken component, but also found that there was nothing we could

(a) The CRLF Ready for Laser installation

(b) Carlos' Opinion

Figure A.8

do in Argentina to fix the problem. This put us in an extremely difficult position as we could not possibly get a replacement card in the time left to us in Argentina, nor was the time enough to install the old CLF laser. Our only option was to leave the CRLF as close to completion as possible and make sure the XLF ran robustly and reliably as it would be operating without a failsafe until we could return with the replacement parts. Therefore, during this time Carlos and I stress tested the XLF and fixed the small number of bugs we found, tested and finished the CRLF code, and wrote a simpler more reliable version of cron to replace the standard cron daemon on both the CRLF and XLF OS as it was failing regularly. The XLF performed flawlessly for the three nights before our departure leaving lending us some much needed confidence as returned to Colorado with the broken laser components Figure A.8(b).

It was a full month before we were able to return with a new control board. With the new control board installed the laser fired without issue. Carlos and I then began the tedious process of mounting the laser and aligning the on table optics, shown in Figure A.9. The primary objective of these optics was to deliver a well columnated, randomly polarized, UV laser pulse of a known energy vertically to either the steered or vertical beam paths. The
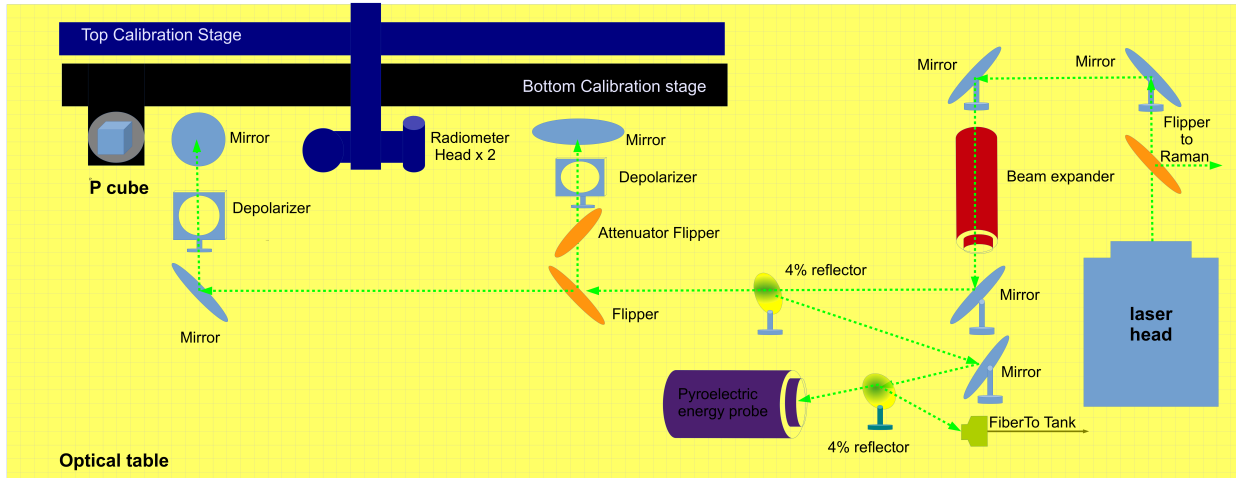
Figure A.9: CRLF on Table Optics.

important on table optical components, listed starting at the laser, are:

Raman Optical Switch : This optical switch sends laser light to the Raman channel which goes through a 3x beam expander before being sent vertically through the Raman hatch for viewing by the Raman telescope.

5x Beam Expander : The beam expander serves to both further columnate the beam and to reduce the on optics light intensity by increasing the beam spot size.

4% Pickoff Mirrors : The pick off mirrors serve two functions. Primarily the pickoff mirrors allow a consistent portion of each shot to be directed to an energy probe for measurement. This in turn, along with the measurements from the calibration system, allow the to-sky energy of each shot to be known. The pickoff mirrors also direct a small portion of the laser light to the adjacent SD tank through a fiber optic cable, allowing for hybrid laser events and SD/FD timing studies.

Steered Beam Optical Switch : This optical switch directs the light to the steered beam channel when up, allowing the laser light to be directed to any above horizon trajectory.

Switchable Attenuator : When activated, the switchable attenuator gives the CRLF the ability to greatly reduce the per shot energy. This is needed to prevent saturating the FD cameras when the laser is fired toward an Eye, a geometry which is needed for alignment and FD/SD timing studies.

Depolarizers : Because the amount of light scattered in the air in any given direction is strongly dependent on beam polarization, in order to ensure that each Eye is seeing a very similar laser source, the beam needs to be randomly polarized so that light is scattered equally in each direction in each shot.

Vertical Steering Mirrors : These mirrors redirect the laser light to trajectory aligned with local gravitational vertical with an error $< 0.1°$.

We then moved to setting up the calibration stages so that the beam energy and polarization could be monitored. The first step in this process was to align the stages with the positions of the vertical and steered beams. The location of the beams then needed to be located and written into the configuration files that controlled the calibration processes. At this point we were able to run the polarization checks on the beams and randomly polarize the laser using the vertical and steered depolarizers. Unfortunately, depolarizing the beam does change the trajectory of the beam after polarization, which in turn meant that the vertical steering mirrors, and therefore also the calibration stages, had to be readjusted.

Once the on table optics were aligned and the calibration system was working, the next stage was to make sure that the azimuthal stage of the steering head shown in Figure A.10, was axially aligned with the steered vertical beam. The azimuthal steering mirror was then adjusted to send the laser down the axial center of the zenith stage also shown in Figure A.10, through the use of a purpose built alignment tool. From here, alignment of the steering head could begin. First the zenith steering mirror was positioned to send the beam out of the steering head at right angle to its axis of rotation. This was necessary as skew in this angle would cause the beam to have rotation dependent alignment and would therefore produce
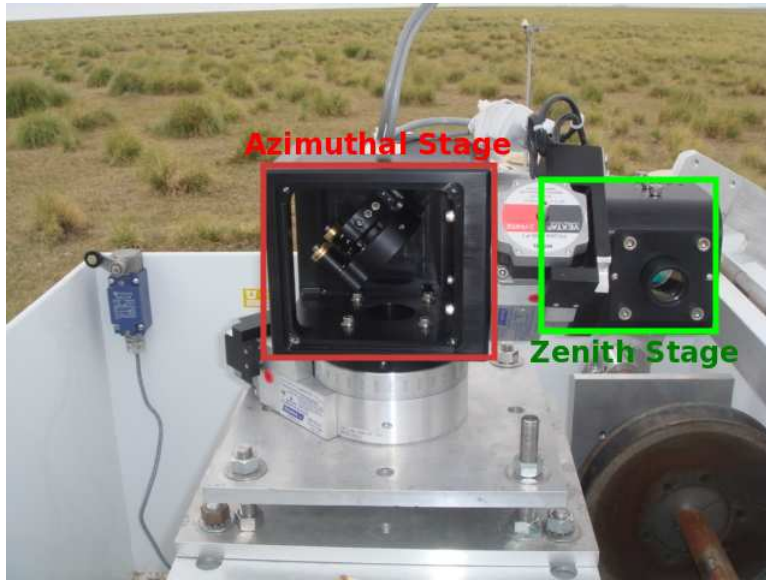
Figure A.10: Laser Facility Steering Head.

a changing and inconsistent trajectory when steered. This was done using a target placed $\sim 10m$ from the steering head output marked with level at the height of the steering head and with two targets placed twice the output width of the steering head. Through surveying with an old US military Theodolite, the steering head was then calibrated so that $0°$ azimuth was North, $90°$ azimuth was West, $0°$ zenith was level and $90°$ zenith was vertical. This alignment was good to estimated error of $0.3°$ but was improved to $< 0.1°$ using the GPS observatory survey and by studying the fired laser trajectories with the observatory FD.

At this point the atmospheric monitoring hardware needed to produce a signal for the bi-static method was installed and ready for operation. The nightly initialization, calibration, and firing routines were automated. The weather, gas and equipment failsafes were implemented and thoroughly tested. The CRLF was now ready to resume the atmospheric monitoring tasks critical to the Observatory. First light from the new CRLF was seen by the FD June 2013 and has continued without gap ever since, Figure A.11(a). At this point, Carlos and I were joined by Dr. Vincenzo Rizi from the Universit Degli Studi dell'Aquila in order to install the Raman Lidar system and prepare the CRLF for long term operation. This work was completed mid June 2013 and the finished CRLF can be seen in Figure A.11.
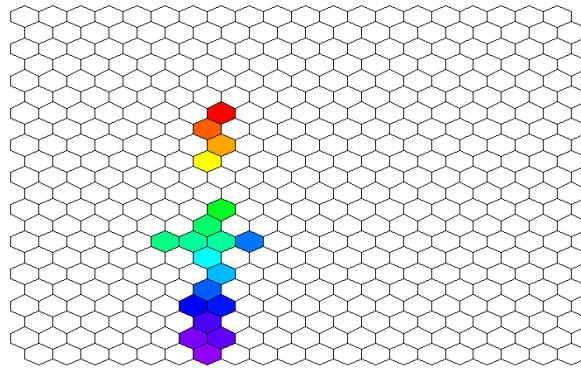
(a) CRLF First Light

(b) The Inside of the Completed CRLF

(c) The Outside of the Completed CRLF

(d) The Completed CRLF

Figure A.11: The Finished CRLF. (b) from the left: Carlos Medina, Eric Mayotte, Vincenzo Rizi.

APPENDIX B - MAGNETIC MONOPOLES

Because of their consistent appearance in a wide range of theories and their expected distinct experimental signatures, magnetic monopoles have been the focus of numerous searches and studies over the last century. There is no consensus on expected monopole mass, however, accelerator experiments of the current generation are expected to rule out masses up to $10^3 GeV/c^2$ [81]. Unfortunately, this only begins to probe the lower-end of masses possible for classical Dirac-Monopoles. GUT monopoles and intermediate mass monopoles have masses likely to be several orders of magnitude beyond the reach of the LHC, therefore it is not possible for accelerator experiments to strongly limit their existence in the near future [82].

Any post inflation, early Universe phase transition can potentially populate the Universe with magnetic monopoles. Due to their inherent stability, this population should survive to the present, meaning one of the best chances for observing monopoles is to search for them within the existing cosmic ray spectrum [83]. The expected current flux of monopoles is calculable, but depending on the type and temperature of the symmetry breaking phase transition assumed in the model, the result is highly variable [84] [85]. However, there is a definite theoretical upper bound to the free monopole flux; the Parker limit of $F_P \sim 10^{-15} cm^{-2} sr^{-1} s^{-1}$, requiring that monopoles must have a density less than that necessary to alter galactic magnetic fields to an observable level [86].

There are four general types of magnetic monopole that each couple with matter differently. Depending on type, a monopole may or may not catalyze the decay of protons it interacts with (catalyzing/non-catalyzing) and it may or may not have internal structure to it (hadron-like/lepton-like) [82] [87]. In the non-catalyzing case, an unstructured lepton-like monopole's ability to directly interact with hadronic matter is limited. This leaves only the standard electromagnetic loss vectors of ionization, pair-production, Bremsstrahlung, and photo-nuclear interactions for monopole energy loss. Fortunately, monopoles have a

much higher electromagnetic coupling then normal ($\alpha_{MM} \approx 34$) [88], greatly improving the strength of showers they can produce. Because the monopole is guaranteed by its topology to survive any interactions and because its energy loss in the atmosphere is a very small portion of its kinetic energy, it will continue to interact and generate sub-showers as it passes through matter. This results in a unique signature. We expect a faint, protracted and consistently luminous profile with no classical X_{max}. However, only ultra monopoles ($\gamma \geq 10^9$) would be bright enough to be visible to Auger meaning these are not a good candidate for subluminal showers [89]. However, because they have a large and easily distinguishable signature, there is work under way to use Auger to search for these events by combining the simulation work of Schuster [70] with traditional search techniques. Early results show that it is quite likely that a new flux limit can be set several orders of magnitude below the current lowest upper limit [90]. A paper on this search is currently under review by the collaboration.

The non-catalyzing case for the more exotic structured baryonic-monopoles described in [91] may be a viable candidate. In addition to the electromagnetic interactions described above, these monopoles may also couple strongly with hadronic matter. Because these structured monopoles consist of very massive components bound through a parallel of the strong force, the energy necessary to break them apart must exceed the energy necessary to create a monopole-antimonopole pair and is therefore extremely high. The reason for this is because, like bound quarks in baryons, the structure of forces involved and the idea of fundamental charge forbid free baryonic-monopoles from existing as the energy of this state exceeds the energy necessary to create and bind additional monopoles to the would-be isolated particle. This means they can absorb a large amount of energy before breaking. Furthermore, since their cross-section with matter is initially near that of a typical hadron and grows at a rate that is roughly proportional to the number of interactions, a structured monopole can absorb, re-emit and deposit most of its kinetic energy very quickly, making them decent candidates for super-GZK primaries if highly boosted [71] [92] [93]. A highly relativistic shower caused by this type of monopole would be similar to that of a high energy

hadronic shower, but would grow very quickly, have a lengthened decay from X_{max} and end with the faint signal of the left-over monopole emitting radiation isotropically [92]. This type of monopole may generate subluminal showers, but only if the rate of energy absorption at low velocities is still higher than the rate of emission. Unfortunately, unless the absorption-rate/emission-rate ratio is still very high at low velocities, a subluminal monopole of this type would probably only cause a strongly muted version of the highly relativistic shower described above, and in turn may not produce enough fluorescent light to allow Auger's FDs to observe the shower.

When proton decay is introduced to the mix there is, in addition to the above interactions, a stream of pion showers that grow more consistent with increased atmospheric density, greatly supplementing the above interactions. This is due to the Callan decay process $M + p \rightarrow M + e^+ + \pi^0$ outlined in [94] [95] [96]. A shower initiated by a catalyzing lepton-like monopole would cause the same prolonged shower as described for the lepton-like case above, but would be supplemented with pion showers caused by proton decay along the shower axis at a rate proportional to the atmospheric density. This would result in a light profile that would grow stronger with increasing atmospheric depth and be more likely to pass the energy threshold of Auger. A subluminal shower is a distinct possibility, but only if the EM + Callan cross-section was very high as a large number of these low energy interactions would be necessary to render the event visible to the FDs. Inferring from [92] and [94], the signature of a highly theoretical, structured, decay catalyzing monopole would be very obvious. The large and potentially increasing cross-section of a structured monopole coupled with the energy release associated with proton decay would result in a very bright shower that in all likelihood would both meet the energy requirements for observation at low velocities and have a light profile strongly dissimilar to anything a conventional primary would produce.

The most stringent measured limits on low velocity monopoles are $\Theta_{90\%C.L.} \sim 1.4 \times 10^{-16} cm^{-2} sr^{-1} s^{-1}$ for $v/c \geq 10^{-4}$ set by MACRO [97], and the pair of limits set by IceCube

of $\Theta_{90\%C.L.} \sim 3 \times 10^{-18} cm^{-2} sr^{-1} s^{-1}$ for $v/c \geq 0.8$ and $\Theta_{90\%C.L.} \sim 5 \times 10^{-17} cm^{-2} sr^{-1} s^{-1}$ for $v/c \geq 0.625$ [98]. These flux limits all improve upon the Parker limit significantly, however Auger still should have enough exposure to comfortably search for monopoles [99]. Though outside the scope of this work, the lowest upper limit on the flux of ultra-relativistic monopoles of $\Theta_{90\%C.L.} \sim 10^{-19} cm^{-2} sr^{-1} s^{-1}$ for $\gamma \geq 10^7$ set by ANITA-II [100] is also beatable by an ongoing search at the Pierre Auger Observatory [90].

APPENDIX C - HYBRID SELECTION PLOTS

Figure C.1, Figure C.2, Figure C.3 and Figure C.4 show the hybrid plots not present in Chapter: 8 for Los Leones, Los Morados, Loma Amarilla and Coihueco in that order.
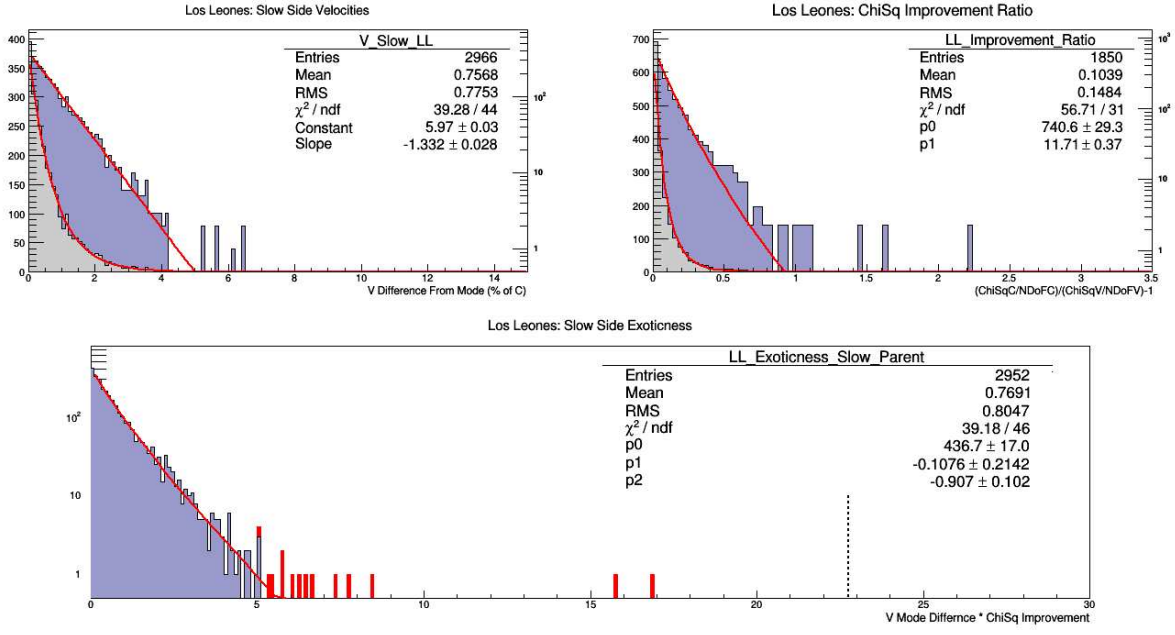
(a) Los Leones Slow Hybrid Fits and Selection
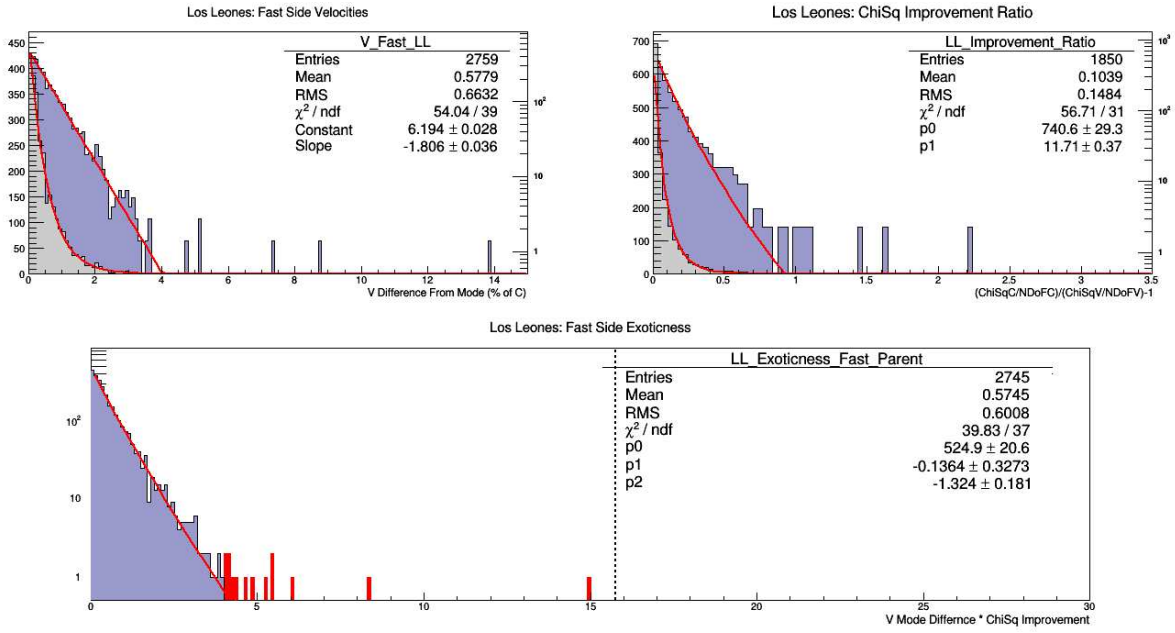
(b) Los Leones Fast Hybrid Fits and Selection

Figure C.1: Los Leones Hybrid Fits and Selection. In these plots the data in the grey and blue histograms are identical. The blue histograms are simply log plots. The red curves are the fits to the functions described in Chapter: 8. The red histogram on the exoticness plots show 3σ outliers while the dotted line shows the 5σ candidate selction limit.
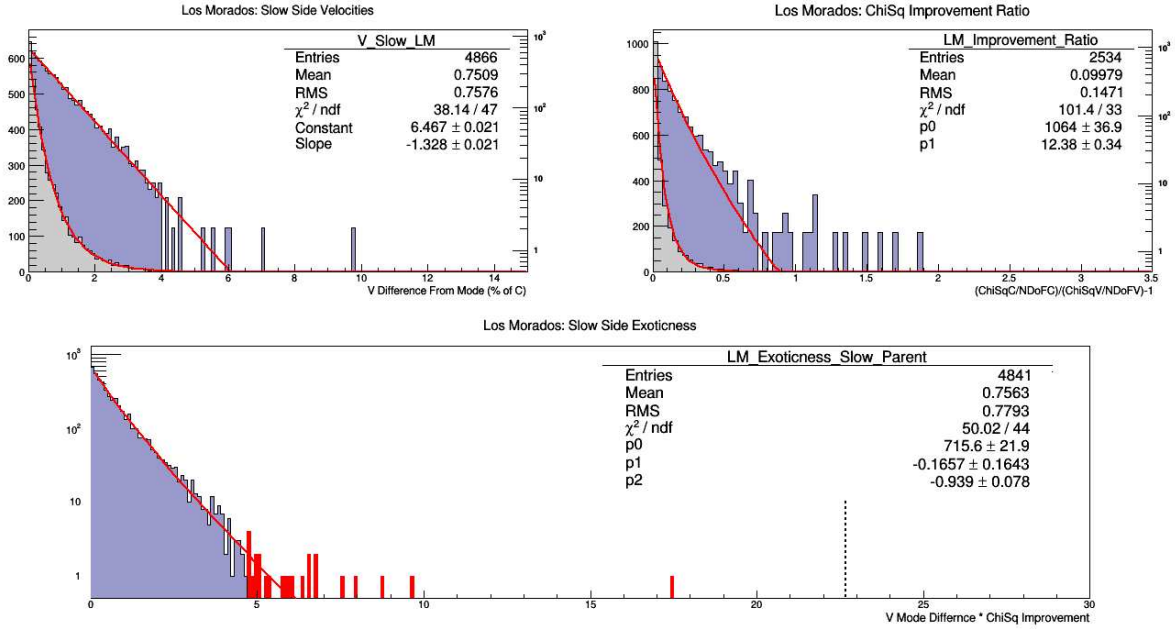
(a) Los Morados Slow Hybrid Fits and Selection
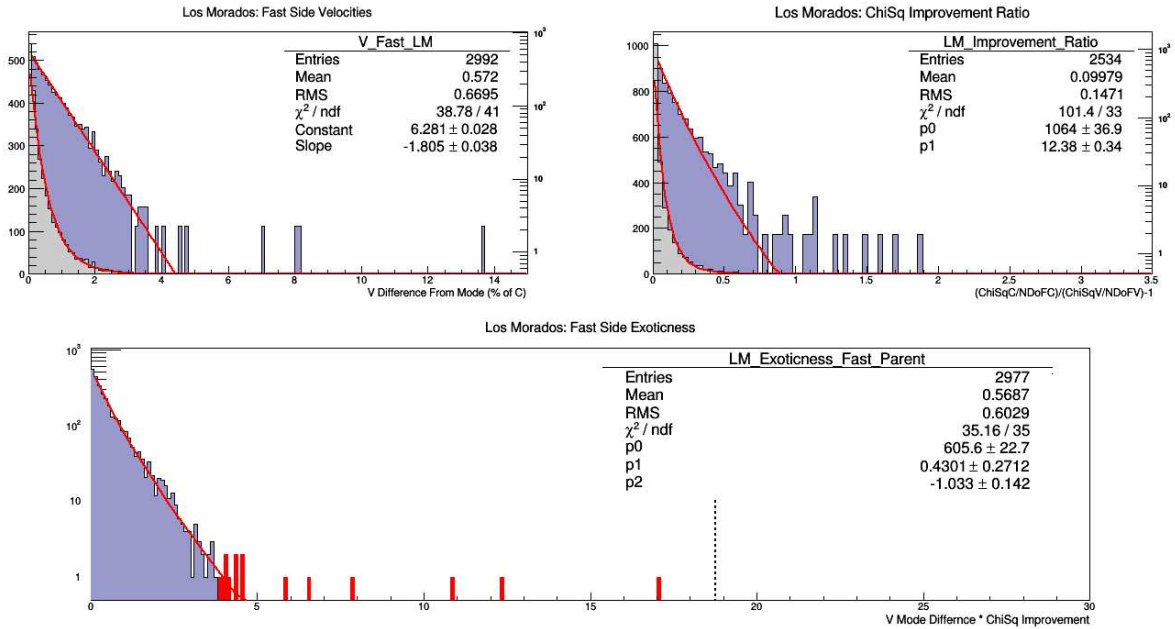
(b) Los Morados Fast Hybrid Fits and Selection

Figure C.2: Los Morados Hybrid Fits and Selection. In these plots the data in the grey and blue histograms are identical. The blue histograms are simply log plots. The red curves are the fits to the functions described in Chapter: 8. The red histogram on the exoticness plots show 3σ outliers while the dotted line shows the 5σ candidate selction limit.
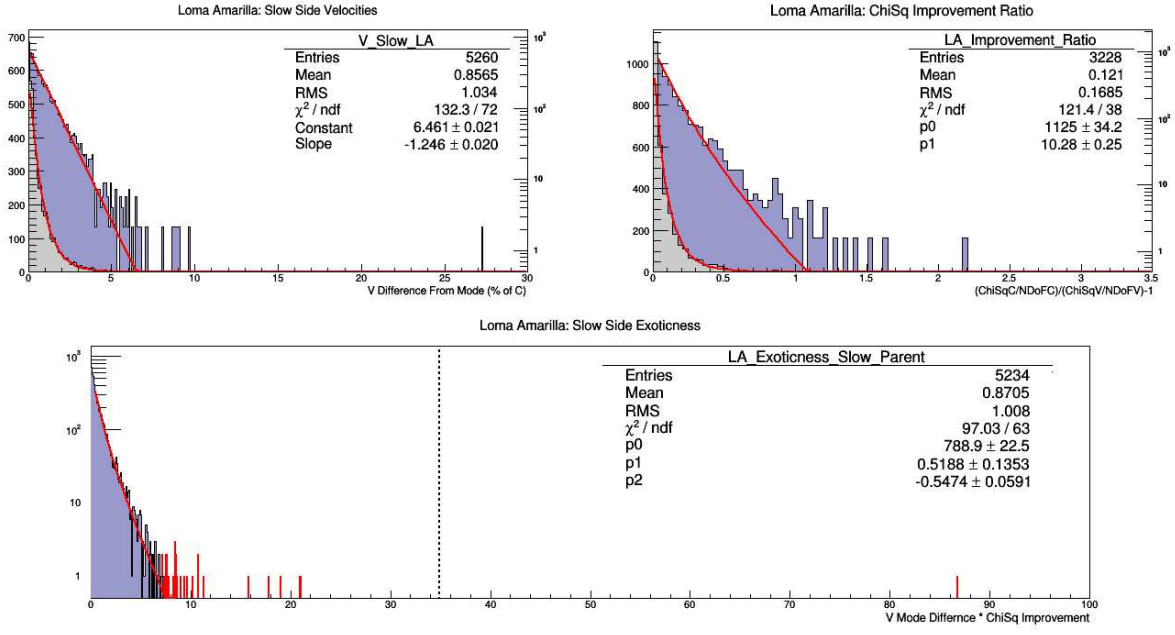
(a) Loma Amarilla Slow Hybrid Fits and Selection
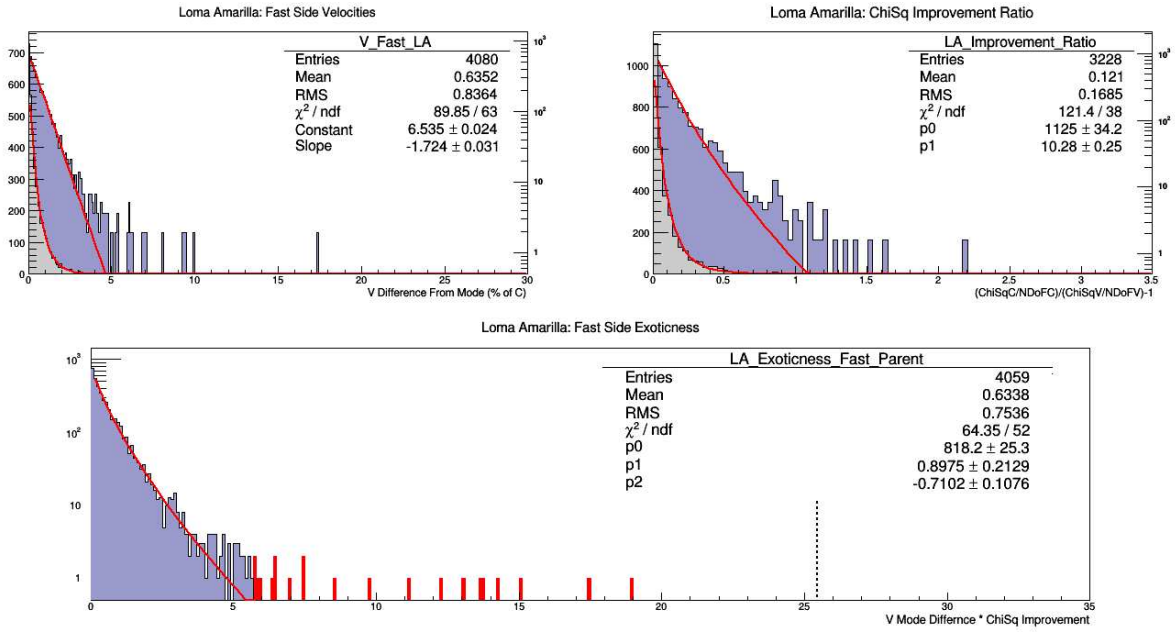
(b) Loma Amarilla Fast Hybrid Fits and Selection

Figure C.3: Loma Amarilla Hybrid Fits and Selection. In these plots the data in the grey and blue histograms are identical. The blue histograms are simply log plots. The red curves are the fits to the functions described in Chapter: 8. The red histogram on the exoticness plots show 3σ outliers while the dotted line shows the 5σ candidate selction limit.
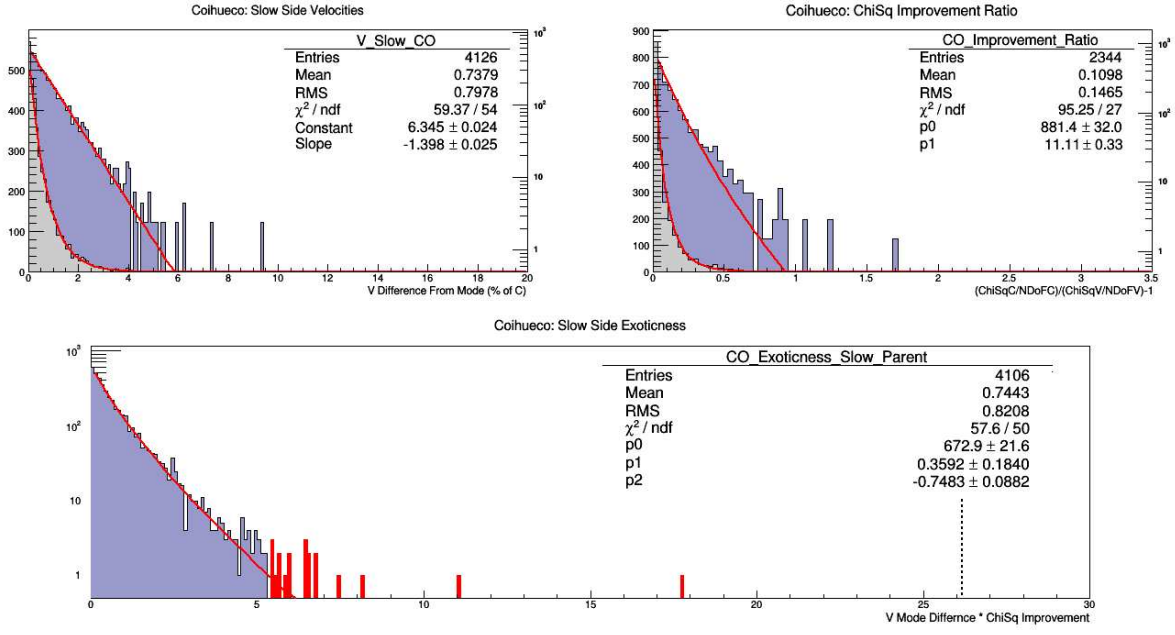
(a) Coihueco Slow Hybrid Fits and Selection
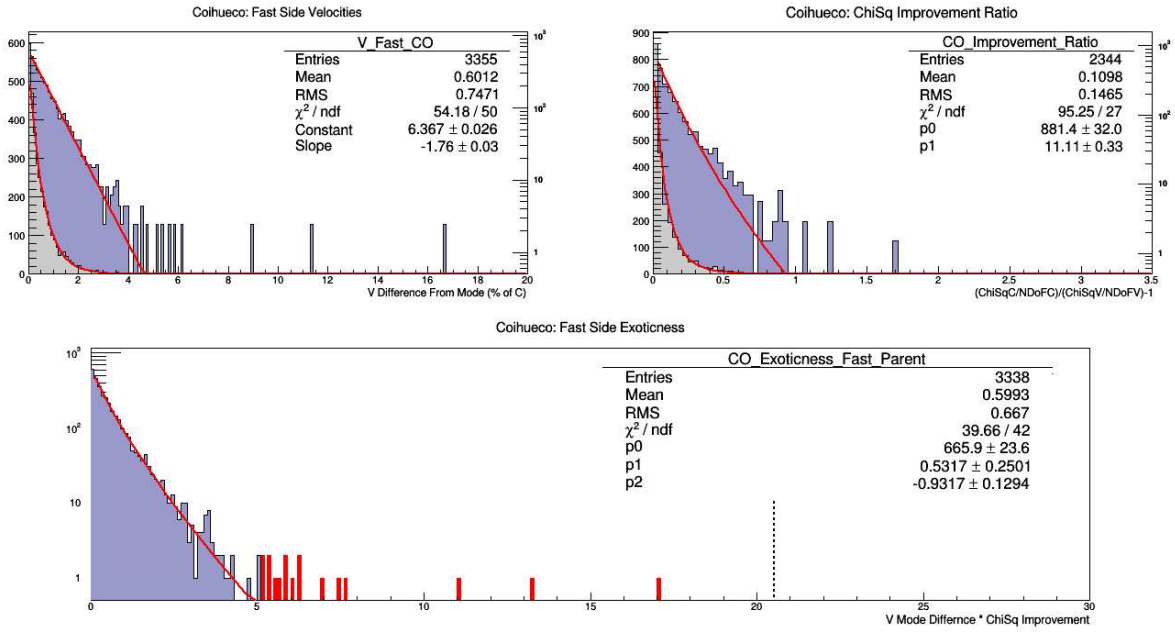
(b) Coihueco Fast Hybrid Fits and Selection

Figure C.4: Coihueco Hybrid Fits and Selection. In these plots the data in the grey and blue histograms are identical. The blue histograms are simply log plots. The red curves are the fits to the functions described in Chapter: 8. The red histogram on the exoticness plots show 3σ outliers while the dotted line shows the 5σ candidate selction limit.

APPENDIX D - SELECTED CANDIDATE EVENTS

Stereo Near Candidate Events 1:4271:4093/2:3569:4243

- Date: 27/6/2012

- Velocity: 103.849% of c

- Improvement Ratio: 5.75

- Hybrid Velocity 97.4% of c

- Hybrid Improvement Ratio 1.2

The overview of the event can be seen in, Figure D.1. Figure D.2 and Figure D.3 show the FD response to the event, while Figure D.4 shows the SD response.
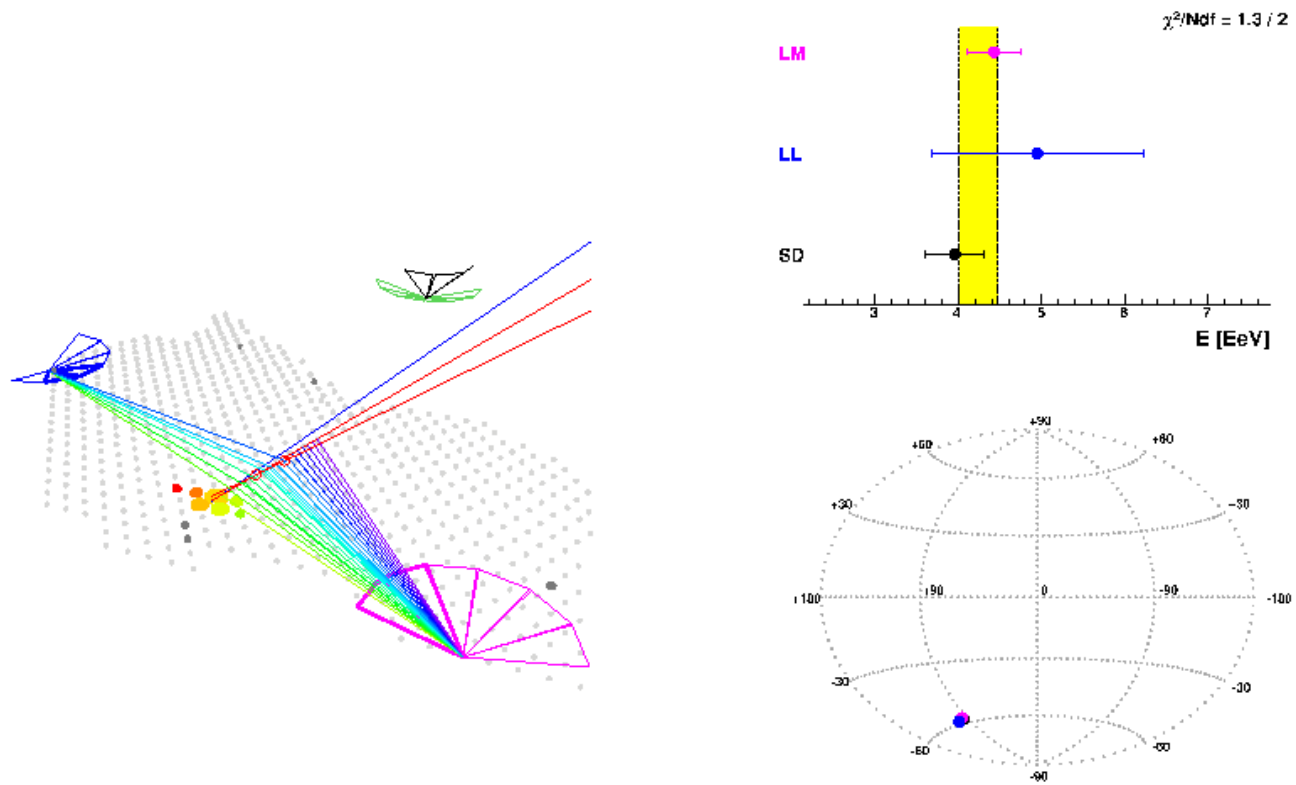
Figure D.1: Candidate Stereo Event 1:4271:4093/2:3569:4243 Overview.
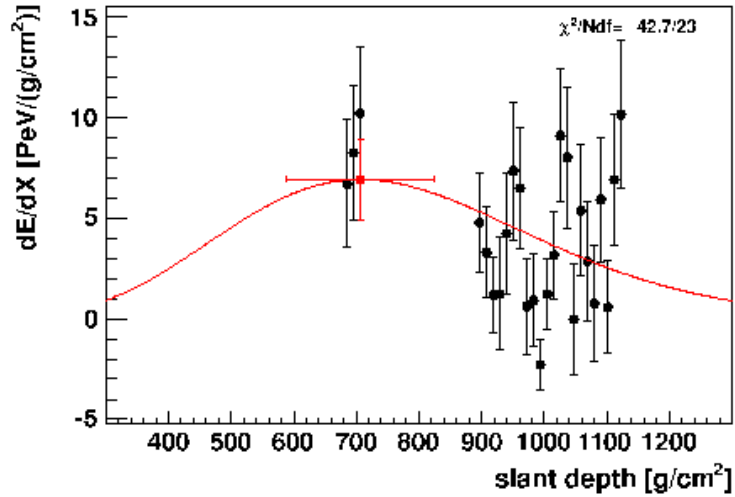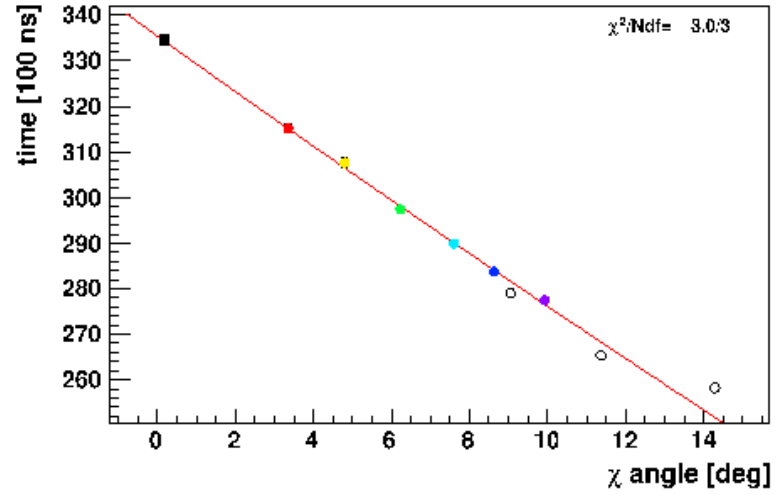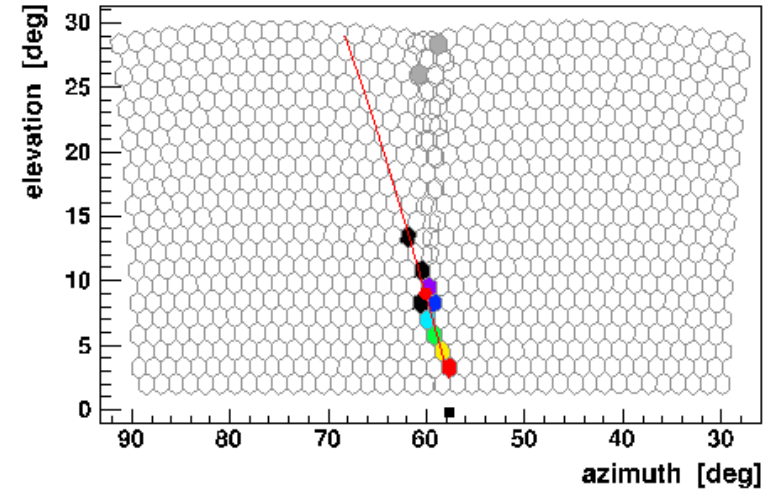
run 4271, event 4093
time stamp: 1024620345 s 499189169 ns
Trigger: 'Physics - Int or L/R trigger', 'Shower Candidate'
In Los Leones mirror 2 3 (in DAQ: 1 2 3 4 5 6)
hybrid geometry, station 250 (unknown), ΛSP = 396 m

(θ,ϕ) = (48.7±1.2, 45.3±1.7) deg
(x,y) = (4.91±0.17, -15.58±0.17) km
dca to Eye = 18.05 + 0.42 km

E = (4.95 ± 1.27) × 10^{18} eV
X_{max} = 707 ± 117 g/cm²
$dEdX_{max}$ = 6.93 _ 1.99 PeV/(g/cm²)
$(\lambda,X0)$ = (68+16,-184-222) g/cm²
Cherenkov-fraction = 19%, mva=34 deg.

Mie attenuation: model
LIDAR: h(cloud)=100.0 km, 0%; CloudCam: no data
molecular profile: GDAS; time correction: good

Figure D.2: Candidate Stereo Event 1:4271:4093/2:3569:4243 Los Leones.
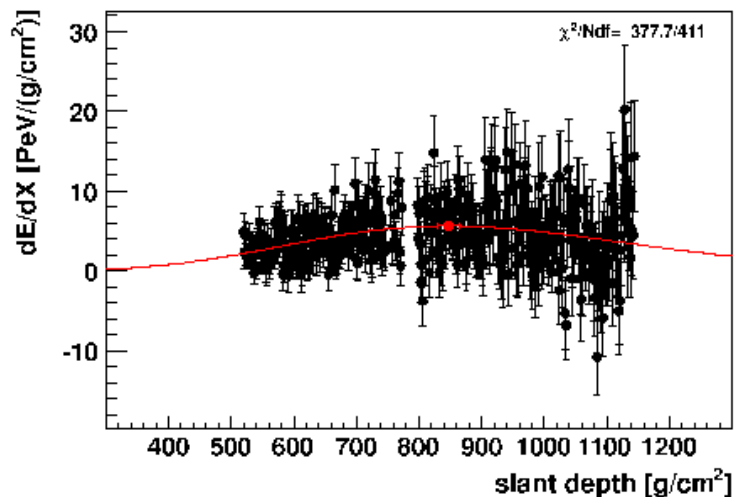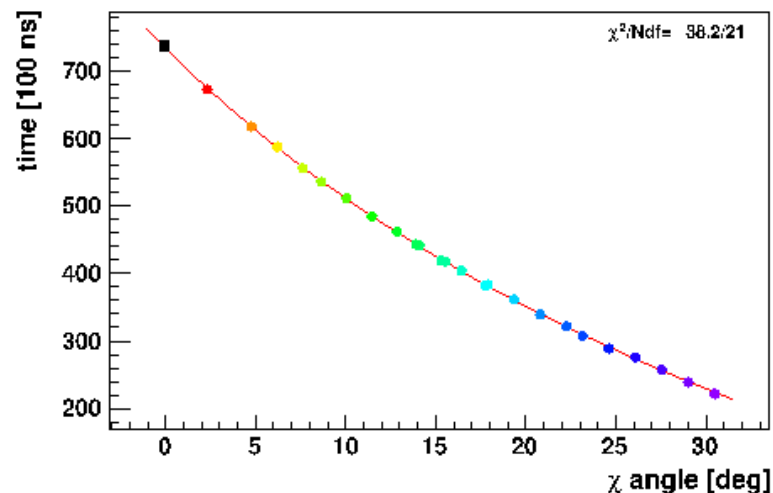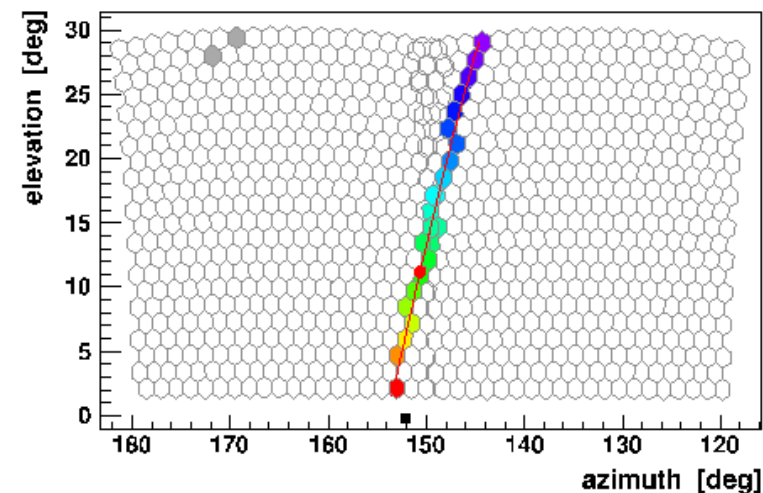
run 3569, event 4243
time stamp: 1024620345 s 499126072 ns
Trigger: 'Physics - Int or L/R trigger', 'Shower Candidate'
In Los Morados mirror 5 6 (In DAQ: 1 2 3 4 5 6)
hybrid geometry, station 250 (unknown), ΛSP = 660 m

(θ,ϕ) = (46.1±0.2, 50.1±0.7) deg
(x,y) = (5.34_0.04, -15.61_0.06) km
dca to Eye = 14.21 + 0.03 km

E = (4.43 ± 0.32) × 10^{18} eV
X_{max} = 847 ± 18 g/cm^2
dEdXmax = 5.66 _ 0.20 PeV/(g/cm^2)
$(\lambda,X0)$ = (68+10,-216-126) g/cm^2
Cherenkov-fraction = 7%, mva=104 deg.

Mie attenuation: model
LIDAR: h(cloud)=100.0 km, 0%; CloudCam: no data
molecular profile: GDAS; time correction: good

Figure D.3: Candidate Stereo Event 1:4271:4093/2:3569:4243 Los Morados.

224
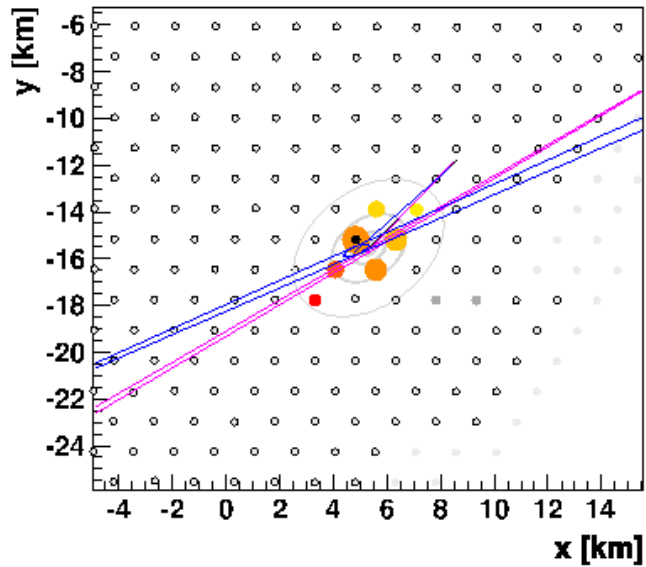
Event 15387666, st. age: 12.5 yr :-)

Time 1024820345 s 499128000 ns

FD & 3TOT & 4C1; 6T5 5T5

Candidates: 7 (Acc: 6, Bad: 11)

$(\theta, \phi) = (45.9 \pm 0.4, 48.9 \pm 0.4)$ deg

$E = (3.96 + 0.35) \times 10^{18}$ eV

$S1000 = 16.3 \perp 1.4 (\perp 0.8)$ VEM

$(x,y) = (5.32 \pm 0.05, -15.54 \pm 0.06)$ km

β (fixed) $= -2.00 (\pm 0.26)$

γ (fixed) $= 0.07$

$R = 8.38 \perp 0.49$ km

$r_{opt} = 882.54$ m
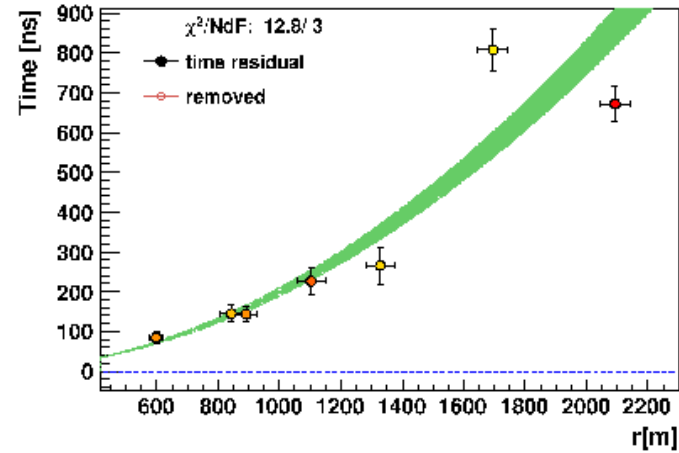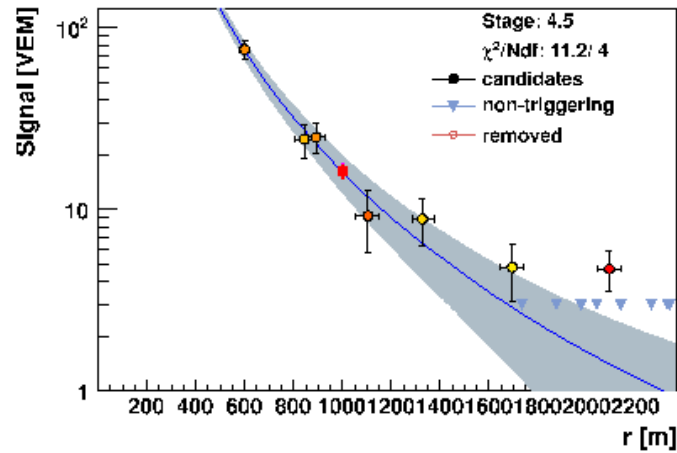
Figure D.4: Candidate Stereo Event 1:4271:4093/2:3569:4243 SD Response.

225

Stereo Near Candidate Events 1:4317:4374/2:3611:4340

- Date: 9/8/2012

- Velocity: 97.1429% of c

- Improvement Ratio: 1.75

- Hybrid Velocity -na-

The overview of the event can be seen in, Figure D.5. Figure D.6 and Figure D.7 show the FD response to the event, while Figure D.8 shows the SD response.
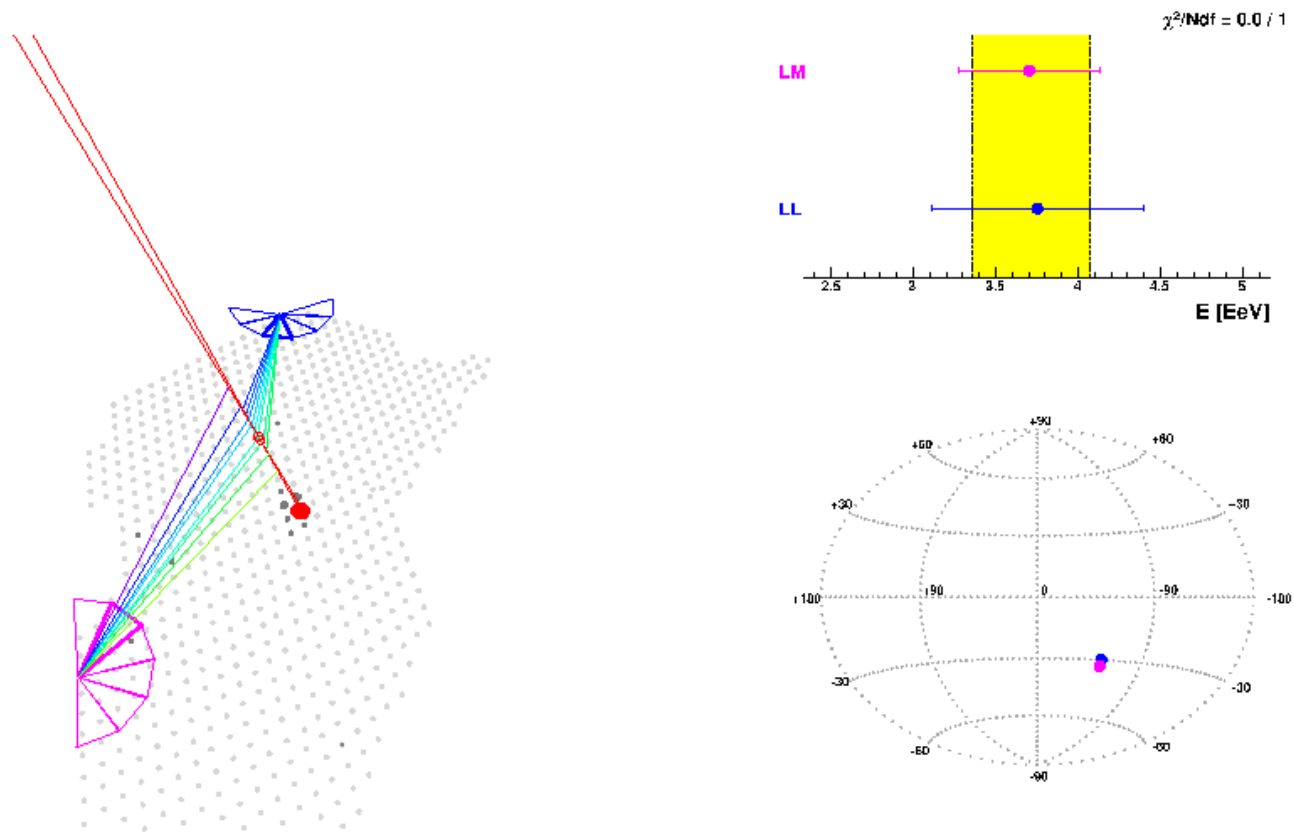
Figure D.5: Candidate Stereo Event 1:4317:4374/2:3611:4340 Overview.

Figure D.6: Candidate Stereo Event 1:4317:4374/2:3611:4340 Los Leones.
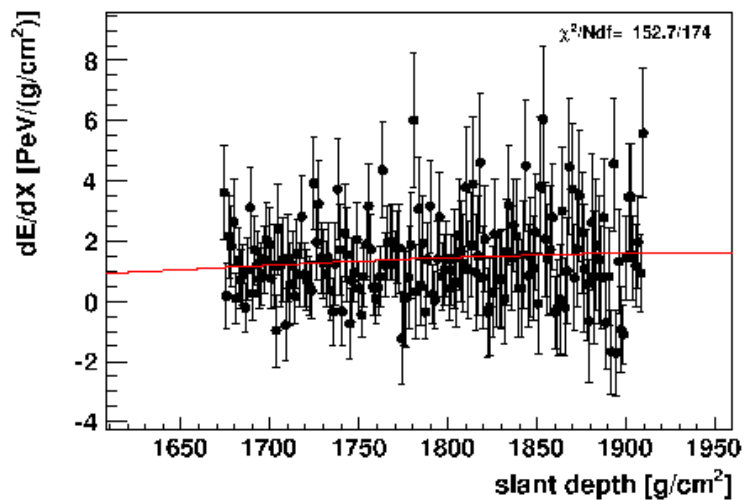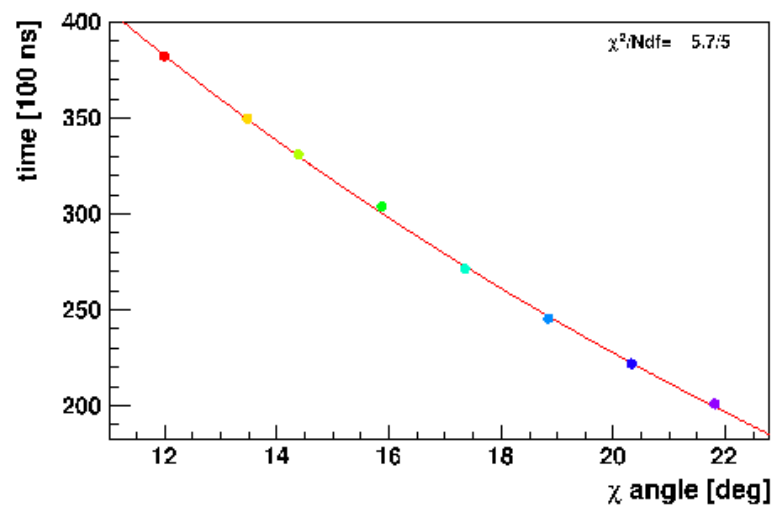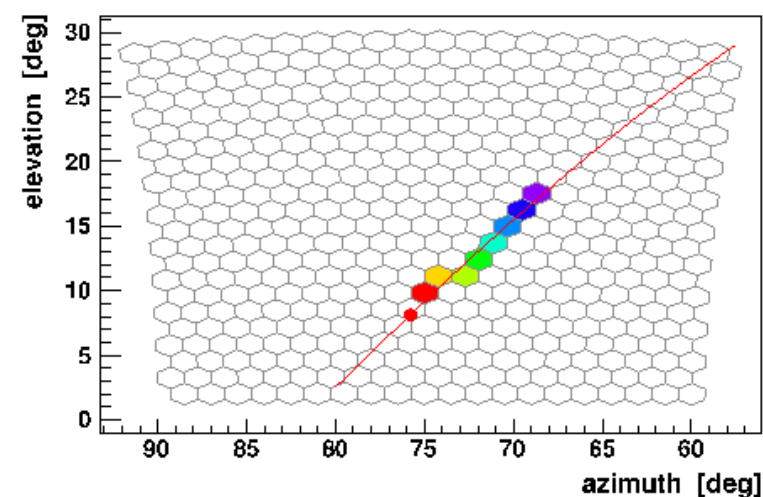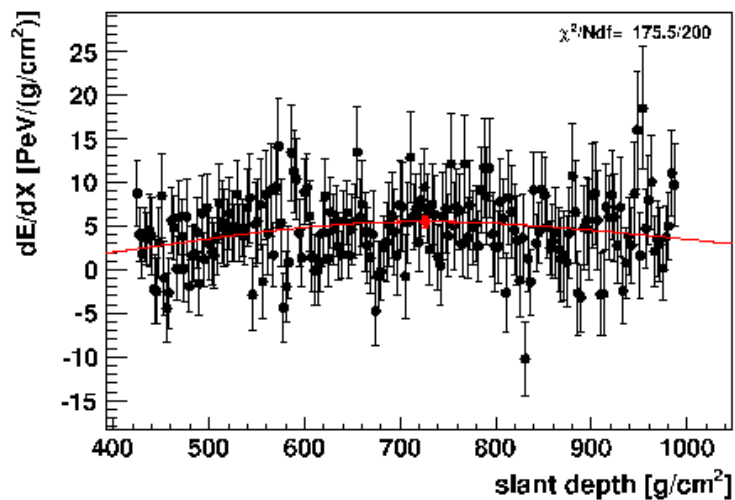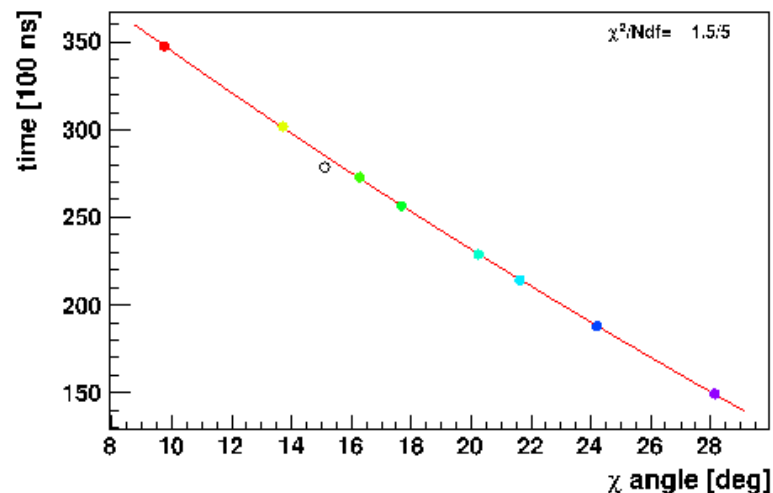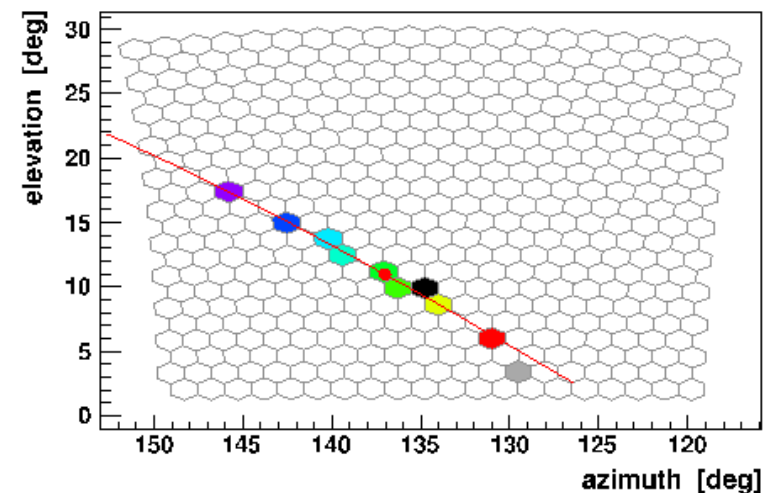
run 3611, event 4340
time stamp: 1028519900 s 624306820 ns
Trigger: 'Physics - Int or L/R trigger', 'Shower Candidate'
In Los Morados mirror 5 (In DAQ: 1 2 3 4 5 6)
hybrid geometry, station -1unknown, ASP = 99 m

(θ,ϕ) = (50.7±1.4, 269.5±9.5) deg
(x,y) = (-3.68±2.39, -6.10±0.37) km
dca to Eye = 25.34 + 2.23 km
E = (4.21± 0.74 = 0.26) × 10^{10} eV
Xmax = 726 ± 30 g/cm^2
dEdXmax = 5.50 ± 0.67 PeV/(g/cm^2)
$(\lambda,X0)$ = (71+11,-249+142) g/cm^2
Cherenkov-fraction = 6%, mva=59 deg.

Mie attenuation: measured (h<11.5 km, VAOD at 3km: 0.01)
LIDAR: no data ; CloudCam: no data
molecular profile: GDAS; time correction: good

Figure D.7: Candidate Stereo Event 1:4317:4374/2:3611:4340 Los Morados.
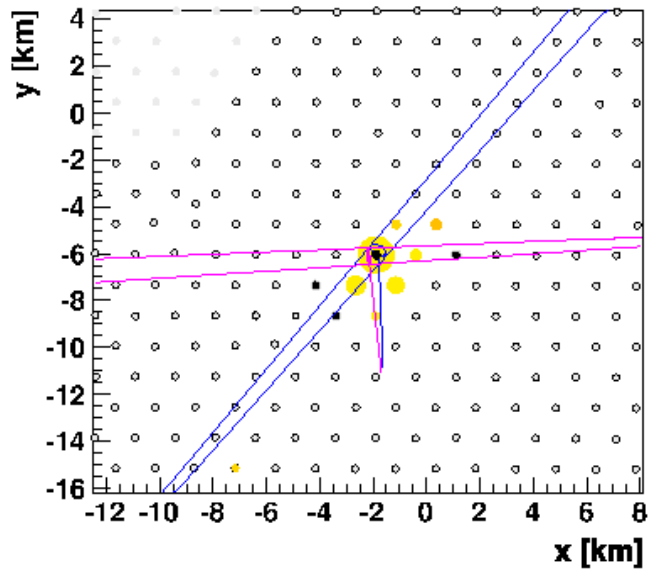
Figure D.8: Candidate Stereo Event 1:4317:4374/2:3611:4340 SD Response.

Hybrid Candidate Event 3:1015:3694

- Date: 23/6/2009

- Velocity: 72.8271% of c

- Improvement Ratio: 3.19

- Velocity After Fix: 99.9006% of c

- Improvement Ratio: 0.9502

The overview of the event using the SD station with the highest signal as the hot tank can be seen in, Figure D.9. The overview and reconstruction of the event using the SD station with the highest signal in the coorelated full SD event as the hot tank can be seen in Figure D.10. The FD response to this event can be seen in Figure D.11, while the SD response can be seen in Figure D.12.
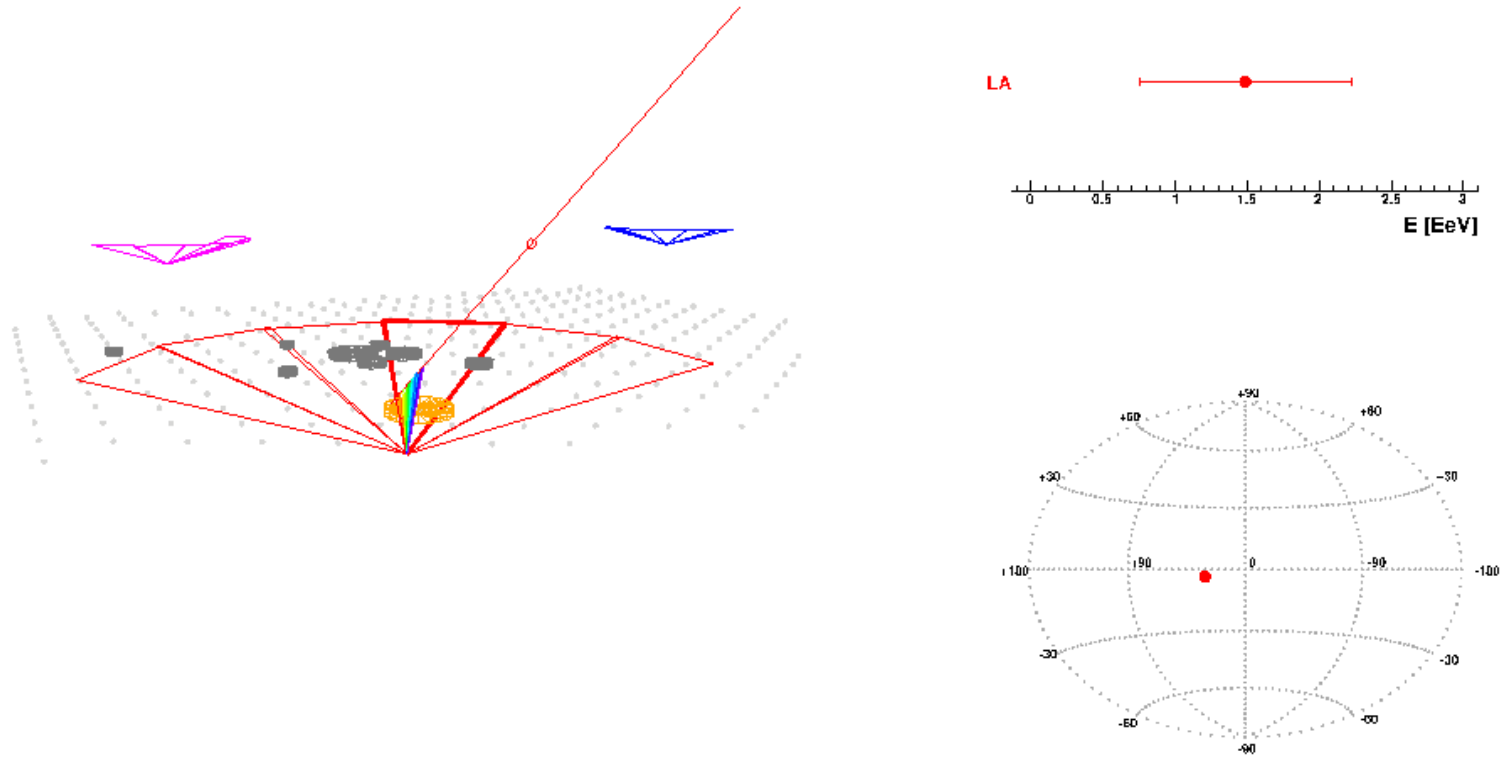
Figure D.9: Hybrid Flagged Exotic: Overview Original.
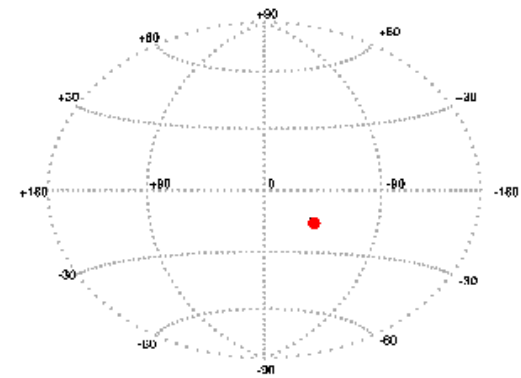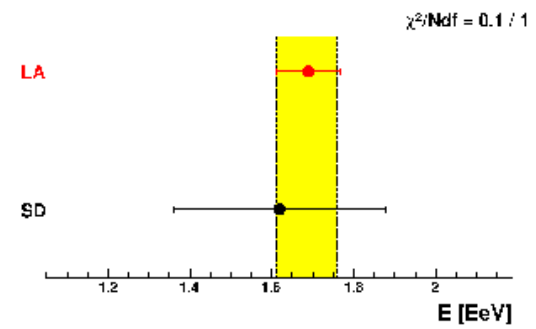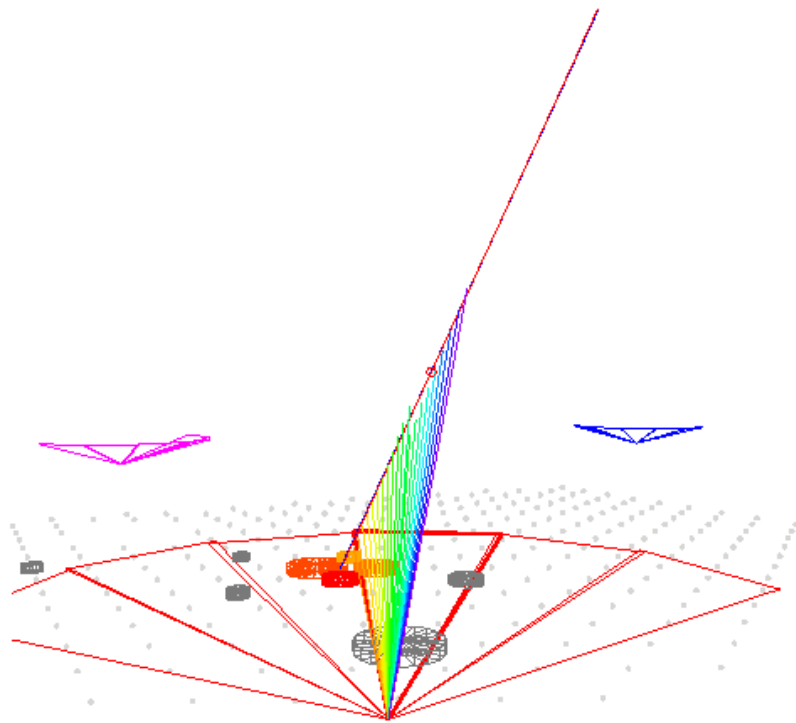
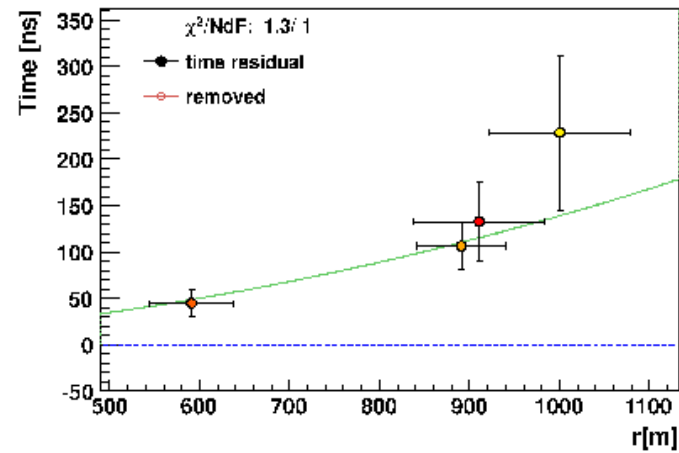Figure D.10: Hybrid Flagged Exotic: Overview Fixed.
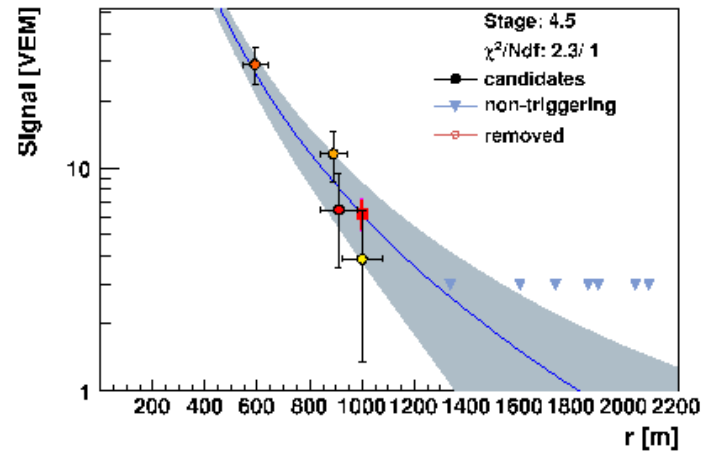
Figure D.11: Hybrid Flagged Exotic: Loma Amarilla Response.
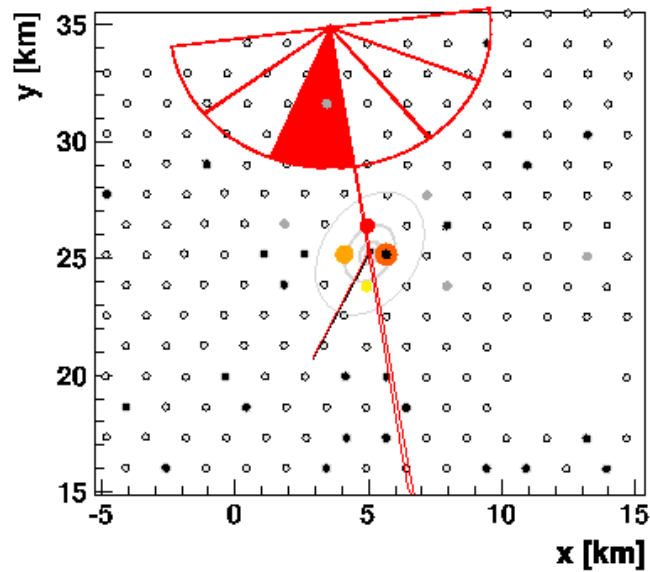
Figure D.12: Hybrid Flagged Exotic: SD Response.